IN-SITU MEASUREMENTS AND CALCULATION OF RADON GAS CONCENTRATION AND EXHALATION FROM A TAILINGS MINE DUMP

JOASH NYAKONDO ONGORI

Thesis presented in fulfilment of the requirements for the degree of Doctor Philosophiae in the Department of Physics at the University of the Western Cape, South Africa.

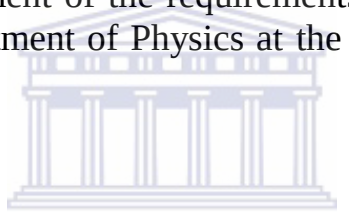

Supervisors:

Prof. R. Lindsay,
Department of Physics,
University of the Western Cape.

Prof. R.T. Newman,
Department of Physics,
Stellenbosch University.

July 2013

DECLARATION

I, the undersigned, declare that the work contained in this thesis, **In-situ measurements and calculation of radon gas concentration and exhalation from a tailings mine dump**, is my original work and has not previously in its entirety or part been submitted at any University for a degree, and that all the sources I have used or quoted have been indicated and acknowledged by complete references.

Joash Nyakondo Ongori July 2013

Signature: ……

IN-SITU MEASUREMENTS AND CALCULATION OF RADON GAS CONCENTRATION AND EXHALATION FROM A TAILINGS MINE DUMP

Joash Nyakondo Ongori

KEYWORDS

Activity concentration (uranium, potassium and thorium)

Alpha-spectrometry

Diffusion-Advection

Electret ion chambers

Gamma-ray spectrometry

MEDUSA γ-ray detector system

Natural radioactivity

Radon exhalation

Radon gas concentration

Uranium-tailings

IN-SITU MEASUREMENTS AND CALCULATION OF RADON GAS CONCENTRATION AND EXHALATION FROM A TAILINGS MINE DUMP

Joash Nyakondo Ongori

Department of Physics, University of the Western Cape, Private Bag X17, Bellville, South Africa.

ABSTRACT

In Africa as well as in the world, South Africa plays an important role in the mining industry which dates back almost 120 years. Mining activities in South Africa mainly take place in Gauteng Province. Every year millions of tons of rocks are taken from underground, milled and processed to extract gold. Uranium is one of the minerals which is mined as a by-product of gold. The uranium bearing tailings are then placed on large dumps which are usually one or more kilometres in diameter in the environment. There are approximately 250 gold mine tailings dumps covering a total area of about 7000 ha. These gold mine tailings dumps contain considerable amounts of radium (^{226}Ra) and have therefore been identified as large sources of radon (^{222}Rn). Radon release from these tailings dumps pose health concerns for the surrounding communities.

This study reports on the ^{222}Rn soil-gas concentrations and exhalations measurements which were conducted at a non-operational mine dump (Kloof) which belongs to Carletonville Gold Field, Witwatersrand, South Africa.

Radon soil-gas concentrations were measured using a continuous radon monitor (the Durridge RAD7). The radon soil gas concentration levels were measured at depths starting from 30 cm below ground/air interface up to 110 cm at intervals of 20 cm. These radon soil-gas measurements were performed at five different spots on the mine dump. The concentrations recorded ranged from 26 ± 1 to 472 ± 23 kBq·m^{-3}. Furthermore, thirty four soil samples were taken from these spots for laboratory-based measurement. The soil samples were collected in the depth range 0-30 cm and measured using the low-background Hyper Pure Germanium (HPGe) γ-ray detector available at the Environmental Radioactivity Laboratory (ERL), iThemba LABS, Western Cape Province. The weighted average activity concentrations in the soils samples were 308 ± 7 Bq·kg^{-1}, 255 ± 5 Bq·kg^{-1} and 18 ± 1 Bq·kg^{-1} for ^{238}U, ^{40}K and ^{232}Th, respectively.

The activity concentration of ^{40}K and the decay series of ^{238}U and ^{232}Th for the top 30 cm of the accessible parts of the mine dump were measured using the MEDUSA

(**M**ulti-**E**lement **D**etector for **U**nderwater **S**ediment **A**ctivity) γ-ray detection system which was mounted on the front of a 4×4 vehicle, 0.6 m off the ground. The spectra acquired by the MEDUSA system were analysed and the activity concentrations were extracted using the Full Spectrum Analysis approach. The average activity concentrations obtained were 259 ± 75 Bq·kg^{-1} for ^{40}K, 309 ± 40 Bq·kg^{-1} for ^{238}U series and 18 ± 5 Bq·kg^{-1} for ^{232}Th series for 2002 survey while 260 ± 75 Bq·kg^{-1} for ^{40}K, 310 ± 40 Bq·kg^{-1} for ^{238}U series and 20 ± 5 Bq·kg^{-1} for ^{232}Th series were recorded for 2010 survey.

Moreover, a novel technique by means of the MEDUSA γ-ray detection system was utilised to map radon exhalation from the Kloof mine dump. In this technique the ^{214}Bi concentration in the top 30 cm of the dump, which is used as a proxy for the ^{238}U or ^{226}Ra concentration, is measured even though there is not secular equilibrium between the radium and bismuth because radon has escaped. The actual activity concentrations of ^{40}K and ^{226}Ra are obtained from soil samples which were collected, sealed and measured in the laboratory settings after attaining secular equilibrium since radon gas does not escape.

By comparing the ratios of the activity concentrations of the ^{214}Bi obtained in the field using the MEDUSA γ-ray detector system to the activity concentrations of the ^{214}Bi obtained in the laboratory using the HPGe γ-ray detector system yields a reasonable radon exhalation for a particular location in the mine dump. In this case it is assumed that the ^{40}K and ^{232}Th series activity concentrations are not or hardly affected by radon exhalation. By applying this new technique an average normalised radon flux of 0.12 ± 0.02 and 0.12 ± 0.02 Bq·m^{-2}·s^{-1} were obtained for 2002 and 2010 surveys, respectively. The electrets and the IAEA standard formula were also utilised to calculated radon fluxes yielding 0.06 ± 0.02 and 0.12 ± 0.02 Bq·m^{-2}·s^{-1} respectively.

The new technique gives a reasonable estimate of the radon flux based on measuring gamma rays which is not tedious when a large area needs to be covered. Unlike other large scale models which require averaging of parameters and a collection of hundreds of soil samples, this technique requires few soil samples which are used to calibrate the system and after that radon fluxes are extracted.

ACKNOWLEDGEMENTS

I would like to take this opportunity to thank the following people, institutions and my family for their priceless support throughout this journey when I embarked on this study:

Prof. Robbie Lindsay and Prof. Richard Newman (my supervisors), for their invaluable support that they have provided me which includes technical discussions as well as their financial support.

Prof. De Meijer for his technical suggestions at the beginning of this study.

Dr. Peane Maleka and Nelly Maleka, I thank you for your constant encouragement and the technical help that you have extended to me at all times.

The former staff members (Hlatshwayo Israel, Lungi and Taki) of the ERL (Environmental Radioactivity Laboratory), iThemba LABS, Western Cape, I appreciate your contribution since I started this project.

Sive Noncolela, thank you for working tirelessly at the mine dump.

The UWC Physics department for the kind support and assistance you have provided me since I became part of the department.

This project was also possible because the Gold field accepted that we conduct our research at Kloof mine dump, as such I thank Zama Zituta and the whole company for accepting us to conduct our research at one of the mine dumps.

I also thank the NRF for the financial assistance during the project.

My family including W. Ombongi, Jerusa, Moraa, Kemunto, Jacky, Everline, Dennis, Ben, Vednah, Dorsilla, Nadia and Danny, all your patience, encouragement and support is highly appreciated. *Mbuya mono, Nyasae abaseseni.*

Finally, to all those who have contributed towards my well-being directly or indirectly, thank you very much.

CONTENTS

LIST OF FIGURES

LIST OF TABLES

Chapter 1

Introduction

1.1 Overview of mining in South Africa

Mining in South Africa can be traced back to 1867 when a diamond was discovered on the banks of the Orange River. In 1871, the prospectors who came for the diamond rush discovered the first concentrations of gold at Eersteling, south of Polokwane (Pietersburg) in the Limpopo Province. In 1886 with the discovery of gold in the Witwatersrand, another rush for gold was set off to the region [GDACE, 2008; Wikipedia1, 2012].

South Africa plays an important role as a mining country not only in Africa but also in the world, due to the variety and the quantity of mineral resources it produces. With the exception of crude oil and commercially viable bauxite (the principal ore of aluminium) which are not available in adequate amounts [GDACE, 2008], there are more than 65 minerals which are known to occur within South Africa. Just to mention a few examples, the economic mineral deposits currently mined in Gauteng province include aggregates (sand and crushed stone), brick and fire clay, dolomite and limestone, fluorspar, silica, uranium, diamonds, gold, coal, manganese and platinum. The world's largest reserves of chrome, gold, vanadium, manganese and the platinum group metals (PGMs) are found in South Africa. Apart from the diamonds from Botswana and the Democratic Republic of Congo, uranium from Niger, copper and cobalt from Zambia and the Democratic Republic of Congo and phosphates from Morocco, South Africa is the leading producer of Africa's metals and minerals. For example in 2005, 78% of the world's platinum was produced in South Africa. It is estimated that 80% of the world's known manganese reserves and 72% of the world's known chromite ore reserves are in South Africa [Mbendi, 2012]. Although South Africa was surpassed as a leading gold producer by China in 2007, the US Geological Survey estimates that 210 metric tons of gold were produced in South Africa in 2009 [Mbendi, 2012]. Due to the quantity of gold

produced in South Africa it is ranked third after China and Australia and then it is followed by the United States. The details of gold mining and production in the world over the past 150 years are shown in Figure 1.1 [Mudd, 2007].

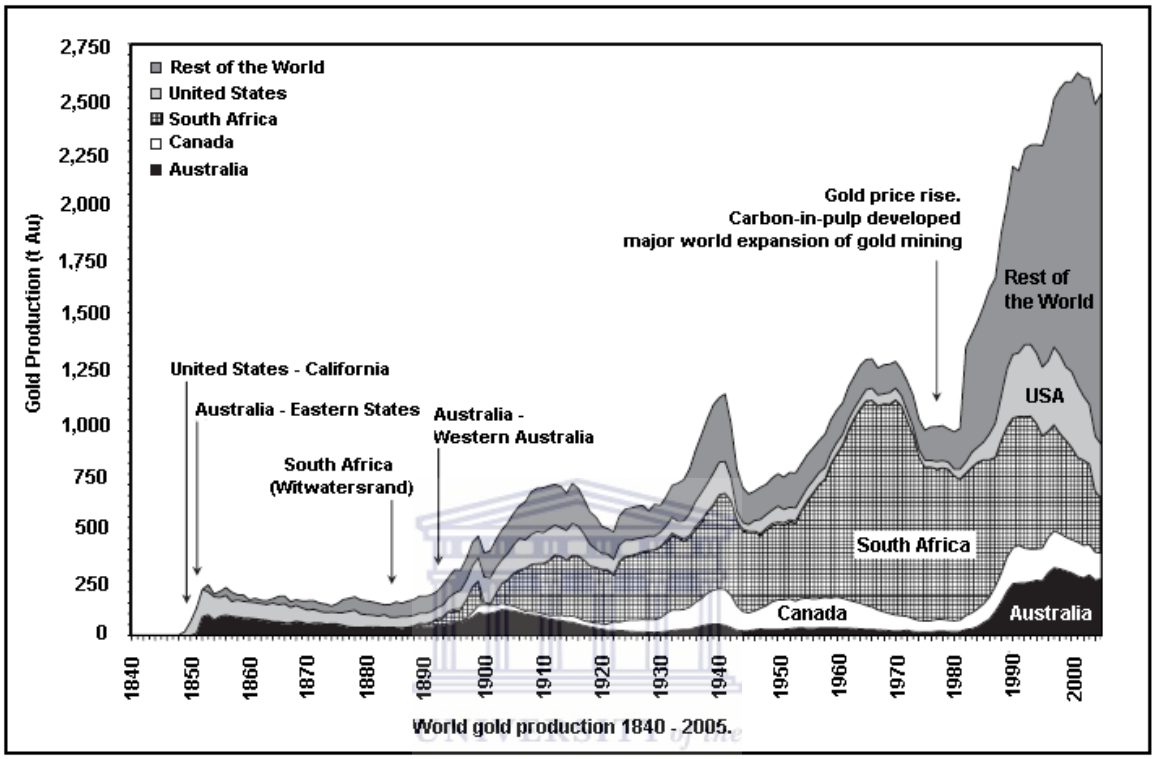

Figure 1.1: The world's gold production between 1840 and 2005 [Mudd, 2007].

It is estimated that the gold repository at Witwatersrand in South Africa has yielded over 47 000 tonnes of gold between 1886 and 2002 which represents between 33% and 40% of all gold ever produced [GDACE, 2008; Hartnady, 2009]. Figure 1.2 shows the locations where mining operations in the gold fields in the Witwatersrand region take place.

Of all mineral resources produced the process of dealing with uranium mining can be regarded special because uranium is radioactive, a property that other minerals which are mined do not exhibit. At present uranium mining is taking place in many countries worldwide. In Africa mining activities have increased in Niger, Mauritania, Zambia, Malawi, Gabon, Tanzania, South Africa, Namibia, and the Central African Republic. In some countries uranium exploration projects are underway. Uranium is radioactive which implies that over time it disintegrates releasing radiation to form new decay products

such as radium, radon, polonium, and lead (see Chapter 2, Figure 2.1). Radiation is considered to be harmful to people and animals. Consequently the process of dealing with uranium mining is considered more hazardous than the process of dealing with other minerals. In Gauteng Province (South Africa) uranium is mined as a by-product of gold. Uraninite (UO_2) and carnotite ($K_2(UO_2)_2(VO_4)_2 - 3H_2O$) uranium ore minerals are found in the Witwatersrand.

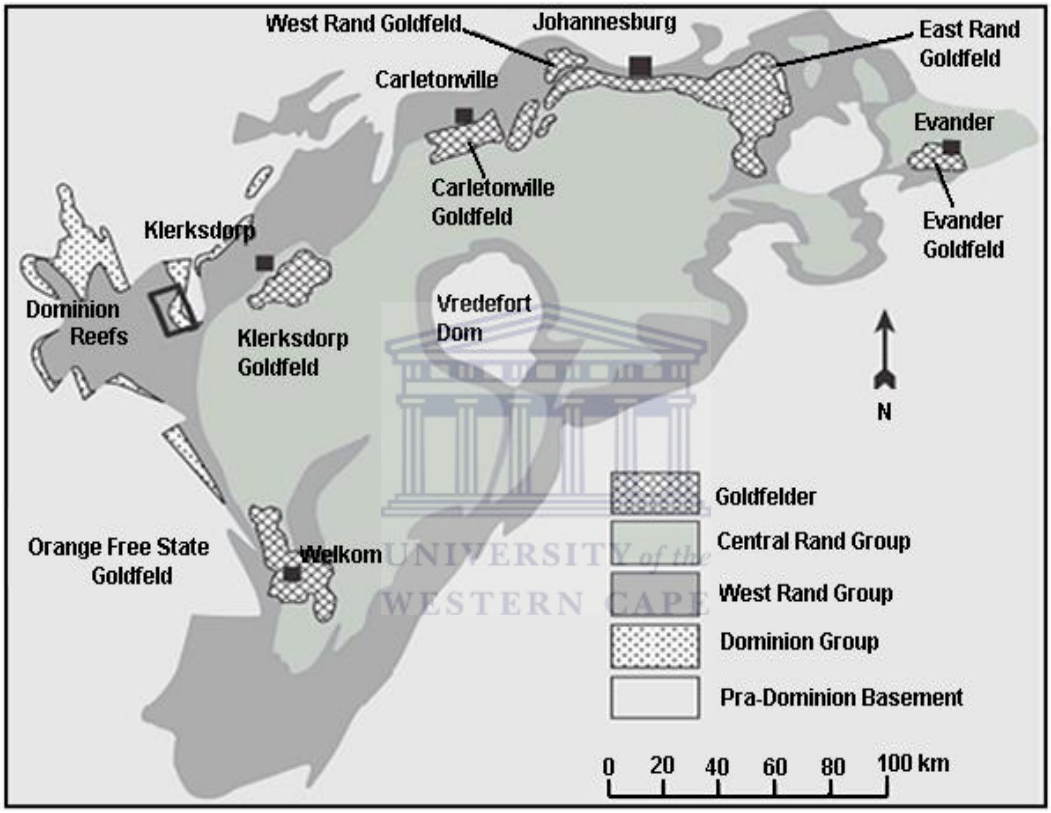

Figure 1.2: Map of the Witwatersrand area, indicating gold fields [GeoDZ, 2012].

Every year the gold-mining industry in South Africa extracts several millions of tons of rock from underground operations. The rocks are milled and processed to extract gold and after the extraction the uranium bearing tailings are disposed into waste storage sites referred to as tailings dumps. The tailing dumps contain materials of crushed rocks which are easily erodible. It is estimated that there are 7000 ha of such dumps and within its proximity a large population has settled [Lindsay et al, 2004a]. The settlements are inhabited by the mine workers who are given houses within the gold fields or the general public who are in the nearby formal or informal housing. Figure 1.3 shows a scene

encountered in Johannesburg where people live nearby gold mine dumps. Even more worrying is that we have thousands of people of an informal settlement living on a radioactive mine waste dump in Tudor Shaft in Krugersdorp waiting to be relocated [Bega, 2011]. Figure 1.4 shows the Tudor shaft informal settlement and the exposed mine waste dump where children are playing.

Figure 1.3: A picture of an old gold mine dump in Johannesburg [GDACE, 2008].

Figure 1.4: A picture showing the informal settlement in Tudor Shaft in Krugersdorp on the left and on the right children are playing barefoot on toxic and radioactive mine waste [Bega, 2011].

In South Africa and in many countries worldwide, tailings dumps of current and abandoned mines remain uncovered and unprotected from the environment and as a result a risk such as contamination of water and soil is possible due to the heavy metals they contain. For example it has been found that surface water, ground water, and even in drinking water in the Witwatersrand region contain elevated concentrations of uranium due to the mining activities [Winde, 2010]. As a result the Witwatersrand region is associated with the problem of acid mine drainage [Winde, 2010]. The toxic effects of exposure to the water (from uranium and other heavy metals) include cancers, birth defects, kidney failure and mental disorders. Because of the acidic nature of the water, it cannot be used either for animal or human consumption, or for agricultural purposes.

One of the radioactive substances found where mining activities take place is radon gas. Radon is the daughter product of radium which is found in the uranium series (see Chapter 2, Figure 2.1). Radon decays to form very small radioactive particles that attach themselves to dust particles which remain suspended in air. Consequently when the wind blows across the surface of the tailing material, dust is blown away. The dust particles contain radioactive substances which cause internal contamination in people and animals. When these particles are inhaled they irradiate the bronchi lining in the lung with alpha particles with a potential risk of causing lung cancer [BEIR VI, 1999].

A study is therefore necessary to investigate radon mobility in the tailings dump as well as the amount of radon released to the atmosphere from the tailings dump surface. According to the International Atomic Energy Agency technical report series No. 333 [IAEA, 1992], the release rate of radon from uranium bearing tailings is considered to be high especially during uranium mining, milling and tailings disposal operations. It is then essential that workers and the public be protected from these radon sources, both in the short and the long term.

The findings of a recent report assessing the mitigation measures of the negative impacts from uranium mines that the governments and industry are taking in Namibia, South Africa, and the Central African Republic, raise some serious concerns particularly on matters related to mining activities [Scheele, 2011]. The matters raised were not any

better for any of the three countries that were studied which necessitated the writers to conclude like this regarding South Africa,

> "… it is surprising that South Africa has no specialised institutions which have adequate knowledge on the impacts of (uranium) mining operations and can monitor, educate, and advise on all mining-related health and environmental issues".

1.2 Overview of radon

It was in 1900 that Owens and Rutherford discovered what was later recognized as thoron (^{220}Rn) when they observed erratic electrometer readings when measuring thorium salts. Later that year Friedrich Ernst Dorn found that radium salts emitted a radioactive gas which he called Radium Emanation which was later known as radon (^{222}Rn). Then in 1902 Rutherford and Soddy succeeded in condensing radon and five years later Soddy was able to show that radon was a member of the inert gas family [NCRP, 1988; Durrani & Ilic, 1997; Wikipedia2].

All isotopes of radon gas which are known are radioactive. Radon isotopes are produced in minerals by the radioactive decay of radium, which in itself is the product of a natural chain of decays that begin with the primordial actinium (^{235}U), thorium (^{232}Th), and uranium (^{238}U) series. The half-lives of ^{219}Rn ($t_{1/2} = 3.96$ s) from ^{235}U and ^{220}Rn ($t_{1/2} = 55.6$ s) from ^{232}Th are short and they therefore have a low abundance relative to ^{222}Rn ($t_{1/2} = 3.82$ days) from ^{238}U.

Radon gas is colourless, odourless and cannot be seen but can be detected with special equipment for instance the RAD7 detector [Durridge, 2000] (see Chapter 3 for details). At standard temperature and pressure, radon forms a monatomic gas with a density of 9.73 kg.m^{-3}. At room temperature radon is one of the heaviest gases and is the heaviest of the noble gases. Radon is chemically not very reactive [Wikipedia2; NCRP, 1988]. Radon is relatively soluble in water which transports it into some underground mines and into some homes where ground water (well water) is used instead of surface water.

For decades, radon remained a chemical curiosity even promoted sometimes as a "health-giving" gas at various spas [Appleton, 2005]. It was not until 1953 that it was understood that radon and its progeny are harmful to human health. Health hazards of radon and thoron are not mainly due to those isotopes directly, but due to the short-lived daughters that can be inhaled. Since radon's lifetime is long relative to breathing times, most of it that is inhaled is exhaled again, or becomes trapped in the lungs and later decays [Durrani & Ilic, 1997]. The short-lived daughter products of radon, ^{218}Po, ^{214}Pb, ^{214}Bi and ^{214}Po have such small half-lives that they probably decay through to the longer-lived ^{210}Pb before the lung can clear them. Due to that the alpha decays of ^{218}Po and ^{214}Po give the epithelial layer of the bronchi a substantial radiation dose. That is what is thought to be the cause of the elevated lung cancer rates among uranium miners as well as in animals subjected to measured exposures [Nero, 1989; Durrani & Ilic, 1997].

On the other hand radon gas is useful in physical sciences as a natural tracer. Since it can be transported within the earth, its water, and atmosphere; it can be used for a variety of geophysical, geochemical, hydrological, and atmospheric purposes. Some of the applications which utilise changes in radon concentrations in the earth include exploring for uranium and hydrocarbon deposits, studying gas flow and mixing in the atmosphere, recognizing fluid transport within the earth and attempting to predict seismic and volcanic events [Durrani & Ilic, 1997].

From the discussion above radon gas can be viewed both as a hazard and a help.

Human beings cannot totally avoid radon since it occurs naturally in the atmosphere; for that reason it is important to perform radon measurements which will play a role in monitoring human health and safety, both in homes and in the gold field mines in the case of South Africa.

1.3 Radon gas studies in South Africa

An interest to investigate radon arises due to the fact that it is mobile over large distances within the earth and in the atmosphere. Radon gas migrates from the source that is the uranium bearing tailings to the mine workers and the general public living around the tailings dumps. When the mine workers and the general public are exposed to large concentrations of radon it poses a health concern, because radon gas is considered to be a

significant source of ionizing radiation among those that are of natural origin [WHO, 2009]. It is well known that ionizing radiation can pose risks to human health. A summary of previous studies [BEIR VI, 1999; WHO, 2009] indicate that the lungs of human beings are susceptible to the carcinogenic effects of ionizing radiation.

In South Africa a fair amount of work has been done on radon although not all work can be found in the published literature. A number of studies can be identified. For instance:

Watterson et al. (1993) embarked on a project where they modified and came up with a direct method that could use activated carbon to measure radon concentration in the air. They hoped to establish the rate of radon emission from the tailing dumps, because the Council for Nuclear Safety (CNS - the forerunner of the National Nuclear Regulator) had reported that the levels of radon emission from certain tailings should be reduced. According to the author the procedure for the method turned out to be labour intensive even though preliminary results were obtained. It was labour intensive since exposure times of the order of 2 to 4 days were required to load carbon. A single measurement with the procedure could take the best part of a week. The method was not suitable to undertake a comprehensive experimental investigation into the rate of radon emission from tailings dumps.

Tsela & Brits (1998) conducted a theoretical study using the algorithm presented by the International Atomic Energy Agency [IAEA, 1992] to investigate the role of parameters such as the emanation coefficient and the diffusion coefficient in radon flux calculations. The authors did not investigate advective factors, thermal effects and pressure variation, since their effects average out and are hence expected to be negligible compared to diffusion. Through that investigation the authors concluded that the emanation coefficient must be determined with every radon flux, otherwise a typical value of 0.35 for South African tailings should be used. This is because a wrongly assumed value of the emanation coefficient results in an incorrect flux calculation.

Manutange (2002) measured radon exhalation from the Kloof mine dump using a "flow-through" method based on Electret ion chambers (EIC). The details about Electret ion chambers and the results obtained are given in Chapter 5, subsection 5.4.2. The study was carried out using the RadElec dynamic/active system which requires 24 hours per

measurement (see Chapter 5, Figure 5.16) and the RadElec passive system, which requires about 3 hours per measurement. The results obtained from that study indicate that the radon flux computed from the dynamic system were higher by almost a factor of 5 (in some cases) than the radon flux computed from the passive system.

Motlhabane (2003) measured the activity concentrations of ^{238}U series, ^{232}Th series and ^{40}K at Kloof mine dump using the MEDUSA gamma-ray detector system [De Meijer, 1998; Hendriks et al, 2001]. MEDUSA is an acronym for **M**ulti **E**lement **D**etector for **U**nderwater **S**ediment **A**ctivity. The activity concentration of the soil samples collected from the mine dump was determined in the laboratory using the Hyper Pure Germanium (HPGe) detector system. After the field and laboratory measurements were completed the standard formula [IAEA, 1992] was used to determine the radon flux. The average radon flux value calculated was 0.105 ± 0.023 Bq·m^{-2}·s^{-1}.

Speelman (2004) investigated the radon diffusion length on the Kloof mine dump by measuring radon in the soil gas using a continuous radon monitor (the RAD7). At depths of about 1.2 metres several hundreds of kBq·m^{-3} of radon soil gas concentration was measured. Moreover, in the study the electrets were incorporated to determine the radon emanation coefficient of the soil from Kloof mine dump. The emanation coefficient range obtained was between 0.13 and 0.39.

Lindsay et al (2004a, 2004b) carried out measurements to investigate the possibility of using a mobile γ-ray detector system (MEDUSA) to assess quantitatively the radon flux from a gold-mine dump by γ-ray mapping. Results obtained from that preliminary study indicated that it was possible to extract radon flux when laboratory-based measurements using the Hyper Pure Germanium (HPGe) detector and the field-based measurements using the MEDUSA technology were combined. These preliminary results obtained motivated the present study.

Manavhela (2007) carried out in-situ measurements of radon concentrations in soil gas at a site on the Cape Flats using a continuous radon monitor (the RAD7). At a depth of about 100 cm radon gas concentrations recorded were 11000 ± 800 Bq·m^{-3} and 26900 ± 1400 Bq·m^{-3} for two different points which were measured. Radon gas measurements were conducted in various seasons and from the results obtained, the author observed that radon concentrations were generally much lower during or after the

rainy season. In order to determine the activity concentration of the soil, the HPGe γ-ray detector system and the MEDUSA γ-ray detector system were used for laboratory and field measurements respectively.

Lindsay et al. (2008) measured the airborne radon (^{222}Rn) concentrations in the Paarl homes found about 50 km northeast of Cape Town in the Western Cape Province, South Africa. Electret ion chambers were used for measurements and the concentrations were found to vary between 28 and 465 Bq·m^{-3}.

Other work concerning radon measurements but not restricted to the ones mentioned above can be found in the internal reports prepared by the National Nuclear Regulator (NNR - http://www.nnr.co.za/) and The South African Nuclear Energy Corporation (Necsa - http://www.necsa.co.za/). The NNR is responsible for radiation protection so it is obliged to carry out monitoring programmes at all mines that deal with radioactive materials.

The main focus for this study is to determine the amount of radon released from the uranium bearing tailings from gold mining using a novel technique by means of the MEDUSA gamma-ray detector system [De Meijer, 1998; Hendriks et al., 2001]. The MEDUSA gamma-ray detector system has been used to determine the activity concentration of ^{238}U series, ^{232}Th series and ^{40}K, however in this study radon fluxes will be extracted from the activity concentration measured. As opposed to any of the existing methods which are laborious and time consuming, gamma-ray measurements are much easier and faster to carry out. There are several methods that have been used to quantify the amount of radon exhaled from the tailings dumps; for instance diffusion tubes, electrets, ionization chambers, scintillation cells, nuclear track detectors, activated charcoal detectors, closed box methods and others. Some of these methods are described in Chapter 5. Radiation specialists in South Africa have mainly used diffusion tubes, the electrets, and the closed box methods to assess the amount of radon released to the environment. Although radon exhalation results have been obtained there are some concerns that have been raised regarding these methods, for example:

(1) the design of some instruments and the procedure to be followed, can lead to unreliable results, for instance in the closed box or flow through-method, a container is placed on the exhaling ground, radon diffuses to the container and then

it is measured. The exhalation of the radon strongly depends on the small pressure differences so if you put your container in the hot sun and due to the temperature, the pressure will increase inside the container. This will eventually stop radon from diffusing into the container and probably cause radon to diffuse back to the exhaling ground. This method has been critiqued in the literature [Samuelsson, 1984].

(2) normally radon gas exhalation measurements using the existing methods are only carried out in a few selected locations in the study area and then the results are generalised for the entire study area. It is of great concern since factors such as the moisture content and porosity affect the diffusion coefficient of radon significantly thus they need to be taken into consideration otherwise unreliable results will be obtained.

(3) many of the devices that are used to measure radon flux require a period ranging from a few hours to days so that they can measure radon exhaling from the ground to the atmosphere. Some of these devices need special care to be effective. For instance electrets need to be handled with care to prevent them from discharging. Dust gathering on the Teflon of the electret or mistakenly touching it leads to discharging. Furthermore, they require at least four hours for a reliable measurement. The period required to obtain radon flux measurements can be extremely long besides the fact that the measurements are obtained from a few selected locations.

Because of some of those reasons, in this study the amount of radon exhaled will be mapped in a different way to the usual methods to circumvent those shortcomings, in the hope that an easier, faster and reliable way compared to the usual methods will be established.

1.4 Aims of the research project

The main aims of this work are to determine:

- the radon soil-gas concentration levels in-situ using a continuous radon monitor (the RAD7) [Durridge, 2000] and to compare the measurements to the radon gas concentrations obtained by modelling using Comsol Multiphysics [Comsol, 2008].

- the important factors controlling the release of radon from the uranium bearing tailings.
- the effective radon diffusion coefficient in-situ and compare it with the results obtained from the commonly used analytic expression.
- the radon fluxes using
  (1) the MEDUSA gamma ray detector system, the main aim of this thesis,
  (2) the electret devices for radon flux measurements (i.e. adapted H-chambers),
  (3) the standard formula [IAEA, 1992; UNSCEAR, 1982] and compare the results obtained.

1.5 Justification for the research project

Several studies have indicated that uranium and radium concentrations have an influence on radon concentrations in the atmosphere. As such it is expected that atmospheric radon concentrations will vary greatly over the oceans, soil or even the uranium bearing tailings. For instance a typical value for ^{238}U and ^{226}Ra in soil is about 40 $Bq.kg^{-1}$ which yields an average measured value of 17 $mBq \cdot m^{-2} \cdot s^{-1}$ for the exhalation or emanation rate or flux of radon from soil [NCRP, 1988]. However, note that the actual value will be influenced by the soil moisture content, porosity, temperature and barometric pressure changes at the time of the measurement. The uranium bearing tailings are considered to contain substantial amounts of ^{238}U and ^{226}Ra concentrations which will yield much higher radon fluxes.

This study will firstly attempt to map radon flux accurately from a non-operational tailings dump of Kloof gold mine. This will lead to an understanding on the factors that control the release of radon from the uranium bearing tailings. Furthermore, the results can be used to estimate the radon radiation doses that the communities surrounding the gold-mine tailings receive due to their exposure to the atmospheric radon concentrations.

Second, the application of this new technique involving the MEDUSA technology will allow comparison with results from other methods. A comparison to the other methods will reveal whether previous radon fluxes have been underestimated or overestimated.

Last but not least, the new technique will provide an alternative method to the known techniques which the National Nuclear Regulator (NNR) can consider when it wants to carry out monitoring programmes for radiation protection. Since the technique utilises the MEDUSA technology a large area can be covered in a short time, therefore the radon flux measurements obtained can be representative for the whole mine dump. Details of the MEDUSA set-up are contained in Chapter 4, while extracting radon flux is discussed in Chapter 5.

1.6 Kloof mine dump

Radon flux measurements were performed at the Kloof mine dump. The mine dump is non-operational and it belongs to the Carletonville Gold Field (see Figure 1.5 and Figure 1.6). Kloof mine dump lies on the north-western edge of the Witwatersrand basin, 35 km west of Johannesburg.

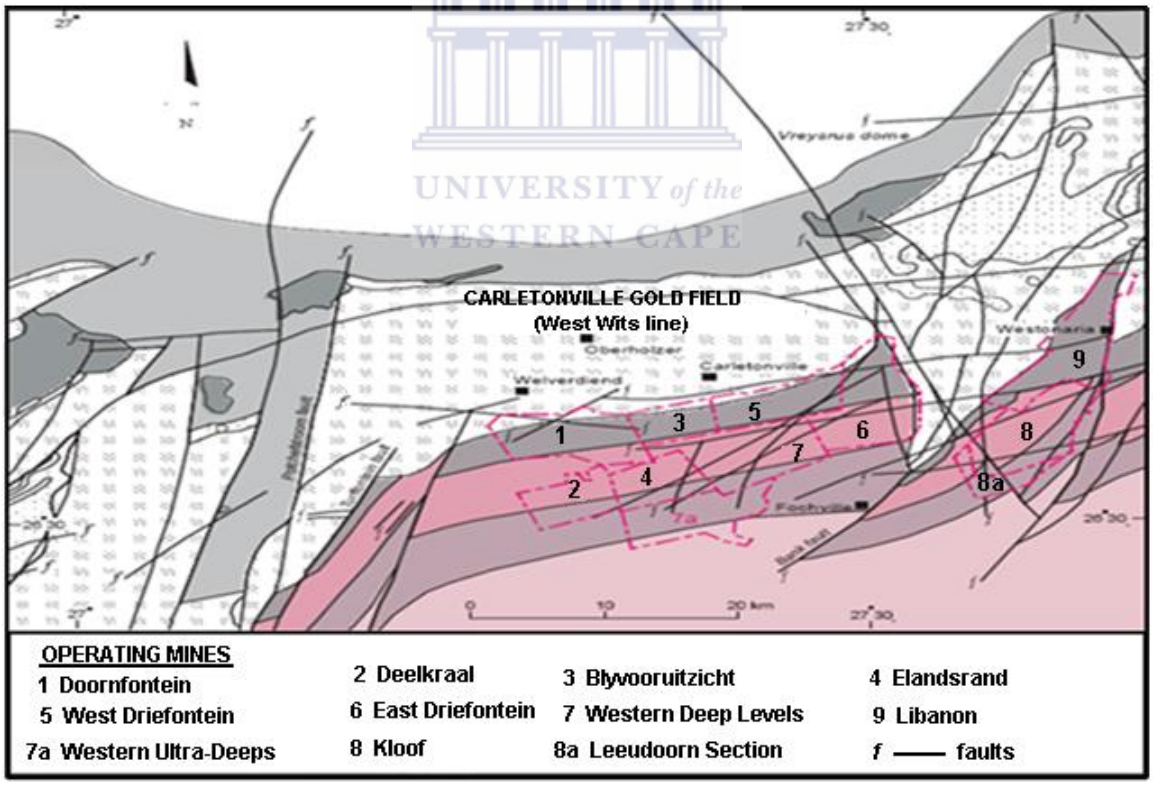

Figure 1.5: A map showing Carletonville Gold Field mines [GDACE, 2008].

To embark on conducting radon gas measurements at the Kloof mine dump will provide an opportunity to not only apply the new technique but also compare the results obtained

by other techniques which were applied by [Manutange, 2002; Motlhabane, 2003; Speelman, 2004].

Figure 1.6: (Top) A bird's eye view of Kloof mine dump [Google Earth, 2012]. (Below) Pictures of the vegetation on the mine dump. N stands for north.

1.7 The scope

In the current study the main focus will be on radon soil-gas measurements using a continuous radon monitor (the RAD7), radon soil-gas concentration modelling using Comsol Multiphysics and determining the amount of radon released from Kloof mine dump using the MEDUSA γ-ray detector system as well as using the electret devices and the standard formula [IAEA, 1992]. Note that in this work, after estimating the amount of

radon released to the atmosphere, the radiation doses that the general public and the mine workers receive due to radon will not be estimated. This can be done by applying standard plume models, for example the CAP88 (Clean Air Act Assessment Package-1988) computer model [Rosnick, 2007; EPA, 2012].

1.8 The thesis outline

The research that was conducted is reported in here under seven Chapters with each Chapter addressing a specific issue as depicted in Figure 1.7.

Chapter two will introduce some relevant background to radioactivity and radioactive decay. The techniques used in this study to detect gamma and alpha radiation will also be discussed.

Chapter three will discuss radon soil-gas concentration (given in $Bq \cdot m^{-3}$) measurements performed using the RAD7 from a depth range of about 30 cm to 110 cm to generate radon gas concentration profiles. The Chapter will also describe how Comsol Multiphysics was used to model radon soil-gas concentrations at various depths and then the results will be compared to the results obtained from the RAD7 measurements. After that a discussion will follow which will not only help to establish the amount of radon available in the pore spaces but also understand the transport mechanisms of radon gas through the ground and its eventual exhalation to the atmosphere.

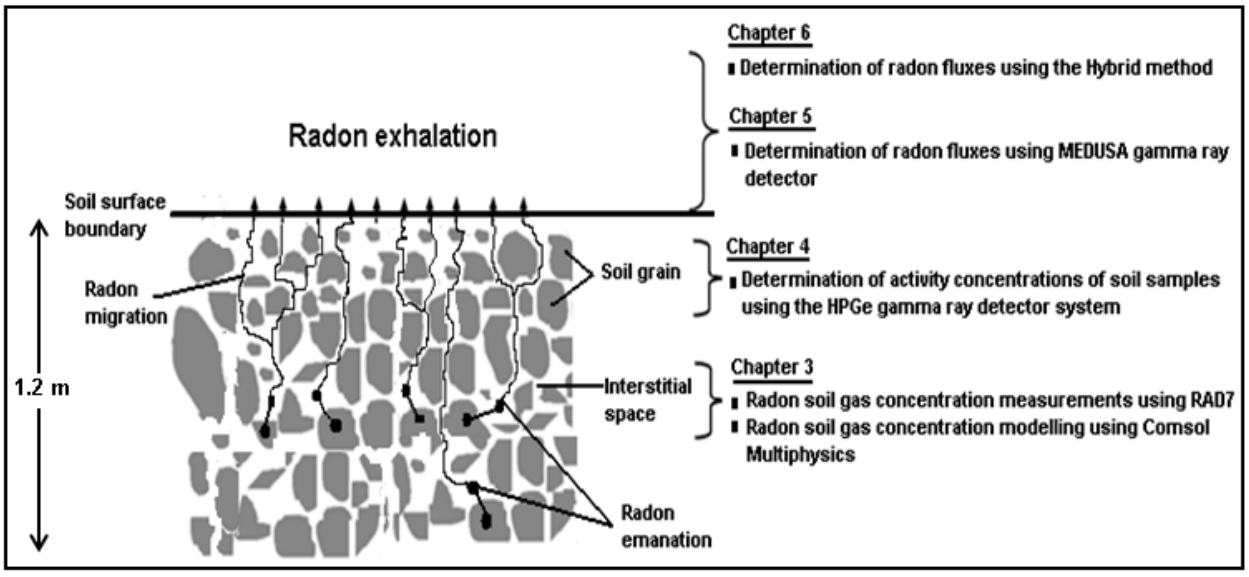

Figure 1.7: An illustration on what the Chapters ahead will discuss pertaining to the radon problem.

Chapter four will describe how the gamma-ray detectors were set-up and used to determine the activity concentrations of the radionuclides such as potassium, and the radionuclides in the decay series of uranium and thorium. In the laboratory the Hyper Pure Germanium (HPGe) detector was used, while the MEDUSA γ-ray detector was used for in-situ measurements. The activity concentration of the uranium bearing tailings will be established once the measurements are completed and analysed.

Chapter five will give an overview of the existing methods that have been used to determine radon flux. The discussion will proceed on to introduce the novel technique used to extract radon fluxes from the MEDUSA γ-ray detector measurements. It will be used in combination with the HPGe γ-ray detector.

Chapter six will discuss how radon fluxes will be determined using the hybrid method. The method has previously been used where the spectrum is manually divided into regions or windows and then analysed. The Full Spectrum Analysis [De Meijer, 1998; Hendriks et al, 2001] method and the Windows method based on regions-of-interest will be used to extract radon fluxes.

Chapter seven finally summarises, gives conclusions, recommendations and presents suggestions for further work.

Chapter 2

Background to Natural Radiation

2.1 Introduction

The subsequent sections in this Chapter give some relevant background related to radioactivity, radioactive decay, gamma-ray interactions with matter, gamma-ray measurements on soil samples and alpha measurements on soil gas.

2.2 Radioactivity

In 1896 Henri Becquerel discovered radioactivity when it was noticed that rays which emanated from uranium salts penetrated through paper and created an image on a photographic plate. Those rays were different from X-rays. This phenomenon where elements gave out rays spontaneously (without cause or stimulation) was referred to as radioactivity. Radioactivity is present everywhere in the environment and has been since the formation of the earth. Radioactivity in the environment can be categorised as [ISU, 2011];

- natural primordial radionuclides which are characterised by long half-lives often on the order of hundreds of million years and they date back to the time the earth was created. Examples for primordial radionuclides include uranium (^{238}U), thorium (^{232}Th) and potassium (^{40}K).
- cosmogenic radionuclides are formed as a result of interaction of cosmic rays with matter on or around the earth. The primary cosmic radiation consists of protons, plus some helium nuclei and heavy ions, with extremely high kinetic energies [Knoll, 2010]. Examples of some common cosmogenic radionuclides include carbon (^{14}C), tritium (^{3}H) and beryllium (^{7}Be).
- anthropogenic radionuclides are "man-made" radionuclides found in the environment through releases from nuclear power stations/facilities (e.g. Chernobyl and

Fukushima nuclear reactor accidents); through radioisotopes manufactured for medical imaging (e.g. ^{131}I with half-life = 8.04 days) and through fall-out from nuclear bombs (e.g. Nagasaki and Hiroshima). Other examples of anthropogenic radionuclides are ^{3}H, ^{90}Sr, ^{99}Tc, ^{129}I, ^{131}I, ^{137}Cs and ^{239}Pu.

Natural occurring radionuclides such as potassium (^{40}K), decay series of uranium (^{238}U) and thorium (^{232}Th) are present in soil, air and water, but in low activity concentrations. These naturally occurring radionuclides are unstable, consequently they decay to a more stable nuclei by emitting alpha (α) particles, beta (β) particles and high energy electromagnetic rays (gamma, γ-rays and X-rays). These emissions from the nuclei are the most common ones. There are three naturally occurring radioactive series but only the uranium series (Figure 2.1) and the thorium series (Figure 2.2) are displayed.

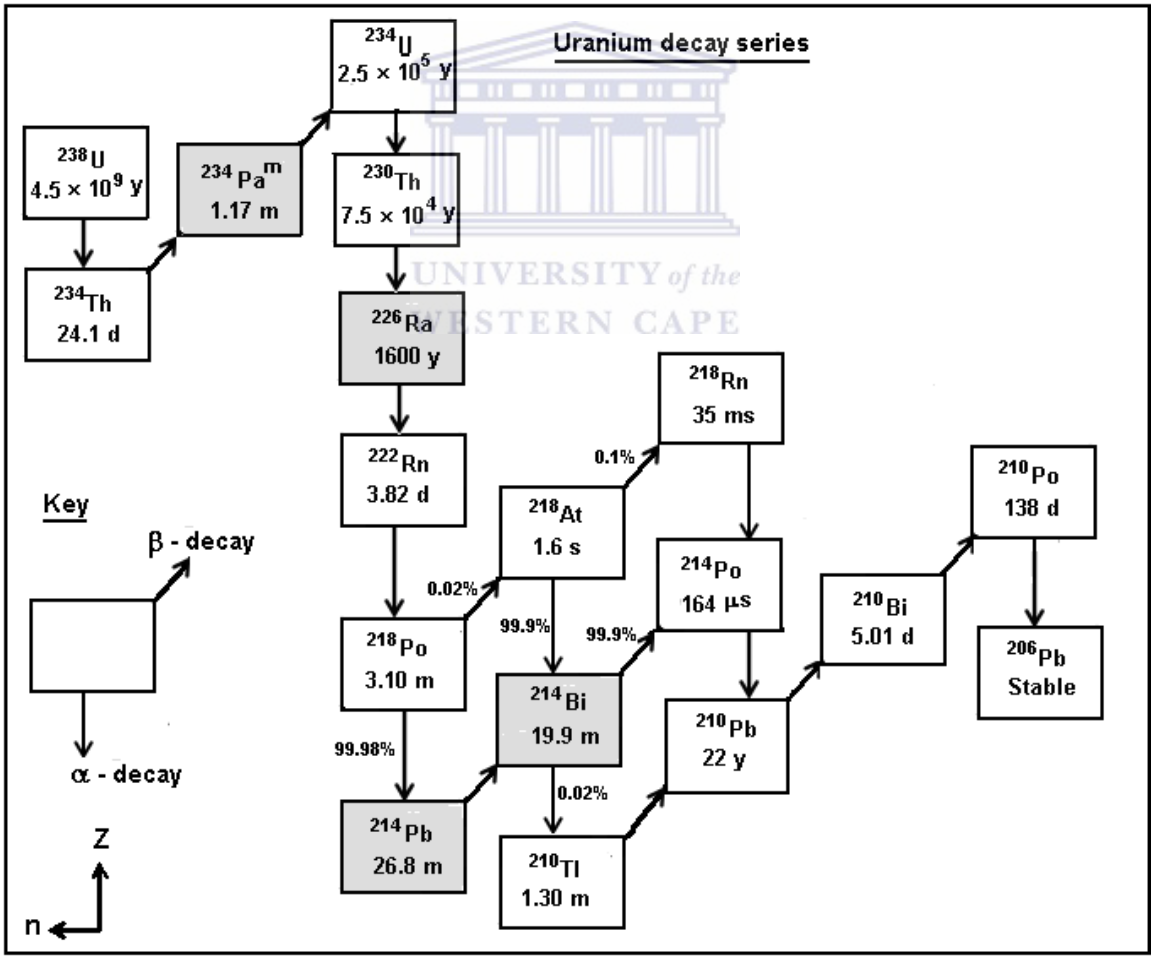

Figure 2.1: A schematic illustration of the uranium decay series. The half-life of each radionuclide in the series is indicated in years (y), days (d), minutes (m) and seconds (s). The grey box represents the γ-ray emitters [Krane, 1988].

The uranium series is considered to be significant because of radium (^{226}Ra) and radon (^{222}Rn) and it decays until it terminates in a stable isotope of lead (^{206}Pb). Radium whose half-life is 1.60×10^{3} years has been used widely in medicine and in industry. Radon with a half-life of 3.82 days is a noble gas with closed orbital-electron shells.

Since the half-life of radon is fairly long it can be transported large distances before it decays. So if there is a net flow of radon flux from a system, the whole activity measurement process is affected especially when post-radon radionuclides are measured to estimate ^{238}U activity. This results from the loss of radon which will be estimated using a novel technique which is discussed in Chapter 5. In brief the activity concentrations of the radon progeny (e.g. ^{214}Bi) will be measured in-situ using the MEDUSA γ-ray detector. Thereafter some soil samples will be collected and then taken to the laboratory for further analysis using the HPGe γ-ray detector to determine the activity concentrations of the radon progeny after they have attained secular equilibrium. Then the amount of radon released to the atmosphere will be quantified by comparing the in-situ activity concentrations extracted from the MEDUSA γ-ray detector to the activity concentrations of the soil sample determined using the HPGe γ-ray detector in the laboratory.

Figure 2.1 shows a phenomenon of branching at ^{214}Bi where 99.9% of the disintegrations go by β-emission. The emission characteristics of the two daughters are such that the series reunites at ^{210}Pb [Lapp, 1972].

The thorium series (Figure 2.2) originates in nature with ^{232}Th which is an alpha emitter with a half-life of 1.4×10^{10} years and ends at ^{208}Pb. Radon (^{220}Rn) gas whose half-life is 55.6 s is one of the progenies in the thorium chain. Very few ^{220}Rn atoms escape from the system because it has a very short half-life. So the chain can be considered to be in equilibrium, which implies that all active radionuclides in the chain, except where the chain branches, have basically equal activities. This chain branches at ^{212}Bi, which β-decays 64% of the time into ^{212}Po and 36% through alpha decay into ^{208}Tl. So by applying the correct decay branch fractions on the activity of ^{212}Bi the activities of ^{212}Po and ^{208}Tl can be worked out. One noticeable similarity between the

thorium and uranium series is that each has one gaseous member. In the thorium series branching occurs at ^{212}Bi in a way similar to that at ^{214}Bi in the uranium series.

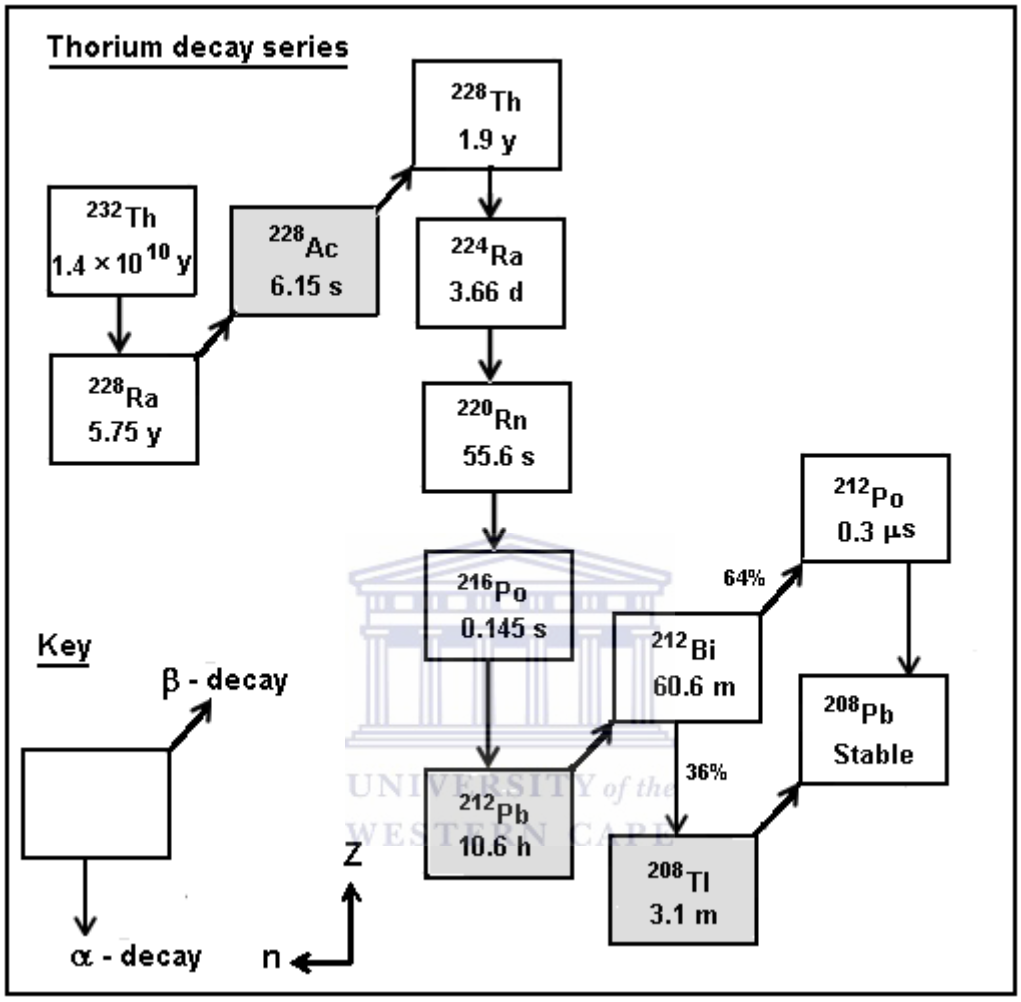

Figure 2.2: A schematic illustration of the thorium decay series. The half-life of each radionuclide in the series is indicated in years (y), days (d), minutes (m) and seconds (s). The grey box represents the γ-ray emitters [Krane, 1988].

From the uranium and thorium series, the nuclide in each chain decays by emitting α and/or β particles until a stable nuclide is reached. Of interest in this study is to detect and quantify nuclides which decay via gamma and alpha particle emissions.

An alpha particle emission is commonly the preferred mode of decay in many heavy nuclei, with $82 < Z \leq 92$, and artificially produced transuranic elements, $Z > 92$, in which the parent nucleus loses both mass and charge. An unstable nucleus that ejects an alpha particle will lose two protons and two neutrons.

Gamma decay occurs when the nucleus which is at an excited state (high energy) decays emitting high energy photons known as gamma rays as it decays to its ground state or to lower-lying excited states. The emitted gamma radiation is characterised by very short wavelength electromagnetic radiation which are highly energetic.

Last but not least, natural potassium contains 0.012% ^{40}K, which decays with a 1.26×10^{9} years half-life through the decay scheme shown in Figure 2.3. The sketch (Figure 2.3) illustrates the two modes through which potassium decays that is beta-minus (β^-) decay to ^{40}Ca and electron capture decay to an excited state of ^{40}Ar. Then the excited state of argon decays to the ground state through the emission of a 1.461 MeV γ-ray.

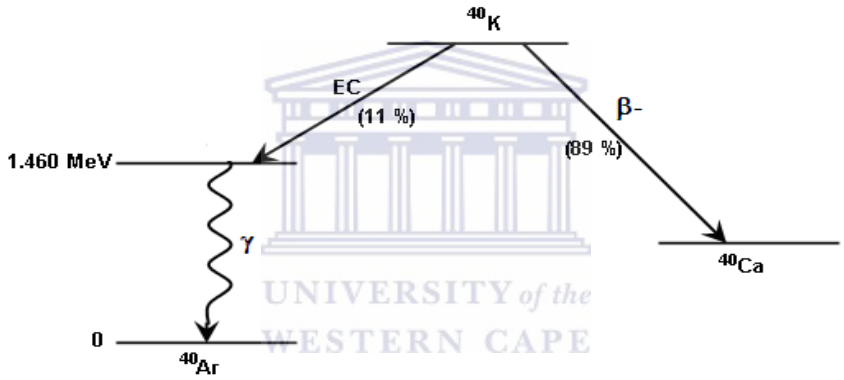

Figure 2.3: Schematic representation of the decay of ^{40}K. EC means electron capture.

2.3 Rate of radioactive decay of a nuclide

Since the process of radioactive decay is spontaneous and random, it is possible to establish how the nuclei will disintegrate with time. If N is the number of atoms present at time t for a radioactive nuclei sample, then the rate of decay is given by

$$\frac{dN}{dt} = -\lambda N_O e^{-\lambda t} = -\lambda N = -A \qquad (2.1)$$

where, N_O is the number of atoms present at time $t=0$, λ is the decay constant of the radionuclide (s^{-1}), t is the time (s) and A is the activity.

The minus sign indicates that N is decreasing with time. The decay rate, λN gives the activity (Bq) of the radionuclide. The activity is high when both the number of unstable nuclei and the decay constant are large.

The solution to equation (2.1) is

$$N(t) = N_O e^{-\lambda t} \tag{2.2}$$

where, $N(t)$ is the number of atoms present after time t (s).

An important relation between the decay constant and the half-life, $t_{1/2}$ is obtained by putting $N = N_O/2$ in equation (2.2) leading to

$$t_{1/2} = \frac{0.693}{\lambda} \tag{2.3}$$

The half-life of any radioactive nuclide refers to the time required for any amount of it to decay to one-half of its original activity [Lapp, 1972].

Again substituting equation (2.3) in (2.2) we get

$$N(t) = N_O e^{\left(\frac{-0.693t}{t_{1/2}}\right)} \tag{2.4}$$

Equation (2.4) implies that it is possible to determine the residual radioactivity at any elapsed time t if the original amount of radioactivity and the half-life are known.

In many cases a radioactive decay can take place where a parent nuclide (N_a) decays to a daughter nucleus (N_b) which itself disintegrates to another unstable nucleus and the chain continues on until it terminates in a stable isotope. Applying the radioactive decay law the equations become

$$\frac{dN_a}{dt} = -\lambda_a N_a \tag{2.5}$$

$$\frac{dN_b}{dt} = \lambda_a N_a - \lambda_b N_b \tag{2.6}$$

where, λ_a and λ_b are the decay constants of the parent nuclide and the daughter nuclide respectively. The solutions to equations (2.5) and (2.6) are

$$N_a(t) = N_a(0)e^{(-\lambda_a t)} \tag{2.7}$$

$$N_{b(t)} = N_a(0)\frac{\lambda_a}{\lambda_b - \lambda_a}\left[e^{(-\lambda_a t)} - e^{(-\lambda_b t)}\right] \tag{2.8}$$

At any time the ratio of any daughter to its immediate parent in the longer chain is given by:

$$\frac{\lambda_b N_b}{\lambda_a N_a} = \frac{\lambda_b}{\lambda_b - \lambda_a}\{1 - e^{[-(\lambda_b - \lambda_a)t]}\} \quad (2.9)$$

Equation (2.9) suggests that transient and secular equilibrium may be achieved depending on the half-life of the parent nuclide and the daughter nuclide. Transient equilibrium is achieved if $\lambda_b > \lambda_a$, then the ratio of the activities of daughter to parent is almost constant and greater than unity. A state of secular equilibrium is achieved if $\lambda_b >> \lambda_a$ and in that case the ratio of the activities of daughter to parent rapidly levels off to approximately one [Leo, 1987, Gilmore, 2008].

In practise when samples (soil or liquid) containing the ^{238}U and ^{232}Th series are measured in the laboratory using nuclear techniques, it can be assumed that they have reached secular equilibrium since the half-lives of the parents are very long. For example Kloof soil samples (see Chapter 4) were measured using the HPGe γ-ray detector in the laboratory after being stored for three weeks. In this case the activity concentrations of the radon progeny were used as a proxy to determine the activity concentration of the parent nuclide (^{238}U).

2.4 Interaction of gamma rays with matter

The mechanisms of interaction of gamma radiation with matter will be discussed in this section. There are a number of possible interaction mechanisms out of which only three main processes namely photoelectric absorption, Compton scattering, and pair production are significant in radiation measurements.

In the photoelectric absorption process, the gamma-ray photon interacts with one of the bound electrons and all of the photon energy is absorbed. An electron, in this case known as a photoelectron, is then ejected from its shell (see Figure 2.4) with an energy E_e approximately equal to

$$E_e = E_\gamma - E_b \quad (2.10)$$

where E_b is the binding energy (very very small compared to the photon energy; $E_b << E_\gamma$) and E_γ is the photon energy [Debertin, 2001; Gilmore, 2008; Knoll, 2010].

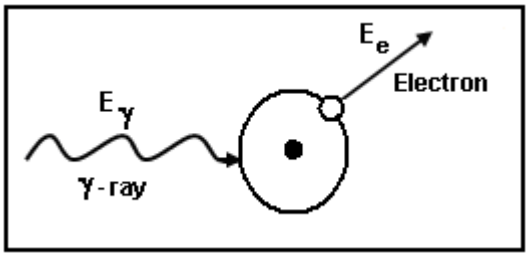

Figure 2.4: The Mechanism of photoelectric absorption [Gilmore, 2008].

Photoelectric absorption can not take place with an unbound electron because energy and momentum cannot be conserved. At relatively low energy the main mode of interaction for gamma rays (or X-rays) is by photoelectric process (see Figure 2.6).

The probability that a photon will undergo photoelectric absorption per atom over all ranges of E_γ and Z, can be expressed roughly as a cross section, τ as

$$\tau \cong \text{constant} \times \frac{Z^n}{E_\gamma^{3.5}} \tag{2.12}$$

where, n is within the range 4 to 5, depending upon the energy.

Equation (2.12) indicates that a high-Z material is very effective in the absorption of photons.

In the Compton scattering process, only a "portion" of the photon scatters from a nearly free atomic electron, resulting in a less energetic photon and a scattered electron carrying the energy lost by the photon. A schematic view of the process is shown in Figure 2.5.

From the conservation of linear momentum and total energy, the energies of the outgoing photon and electron are related to the angles at which they are emitted. From the symbols in the sketch the scattered photon energy can be expressed as

$$E_\gamma^{'} = \frac{E_\gamma}{1 + \frac{E_\gamma}{mc^2}(1 - \cos\theta)} \tag{2.13}$$

where, E_γ is the incident photon energy, $mc^2 = 0.511$ MeV, the rest-mass of the electron.

The recoil energy of the electron E_e is given by

$$E_e = E_\gamma - E_\gamma^{'}. \tag{2.14}$$

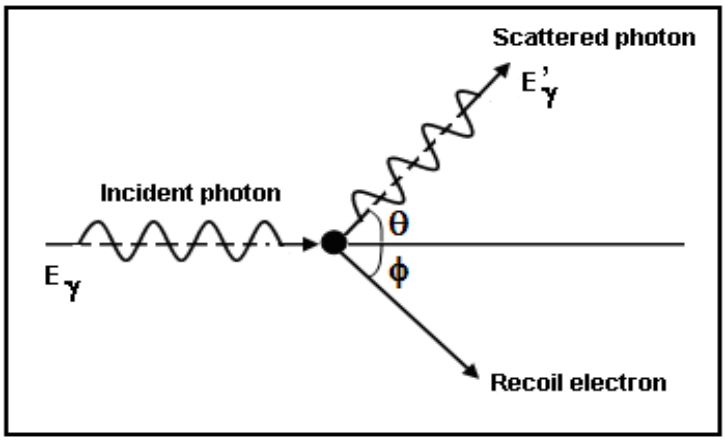

Figure 2.5: The geometry of Compton scattering.

The scattered photons range in energy from E_γ for $\theta = 0^0$ (forward scattering, corresponding to no interaction) to a minimum of roughly $mc^2/2 \approx 0.25\,MeV$ for $\theta = 180^0$ when the photon energy is large.

The probability for Compton scattering at an angle θ is predicted by the Klein-Nishina formula for the differential scattering cross section, $d\sigma/d\Omega$ per electron

$$\frac{d\sigma}{d\Omega} = Z\,r_o^2 \left(\frac{1}{1+\alpha(1-\cos\theta)}\right)^2 \left(\frac{1+\cos^2\theta}{2}\right)\left(1+\frac{\alpha^2(1-\cos\theta)^2}{(1+\cos^2\theta)[1+\alpha(1-\cos\theta)]}\right) \qquad (2.15)$$

where, $\alpha \equiv h\nu/m_0c^2$ and r_0 is the classical electron radius.

The Compton scattering absorption cross section, σ is given approximately by

$$\sigma = \text{constant} \times E_\gamma^{-1} \qquad (2.16)$$

The probability that the Compton process will take place decreases with energy and depends more on the density of the electrons in the medium rather than on the atomic number.

In the pair production process, the atom as a whole interacts with the gamma ray. The process takes place in the Coulomb field of the nucleus which results in the creation of an electron-positron pair. For this process to take place an energy threshold of $2mc^2 = 1.022$ MeV is required and the pair production cross section does not become important until E_γ exceeds several MeV. Pair-production becomes the main process for

photon energies $E_\gamma > 3$ MeV. Figure 2.6 illustrates the significance of the three processes described above for different absorber materials and gamma-ray energies.

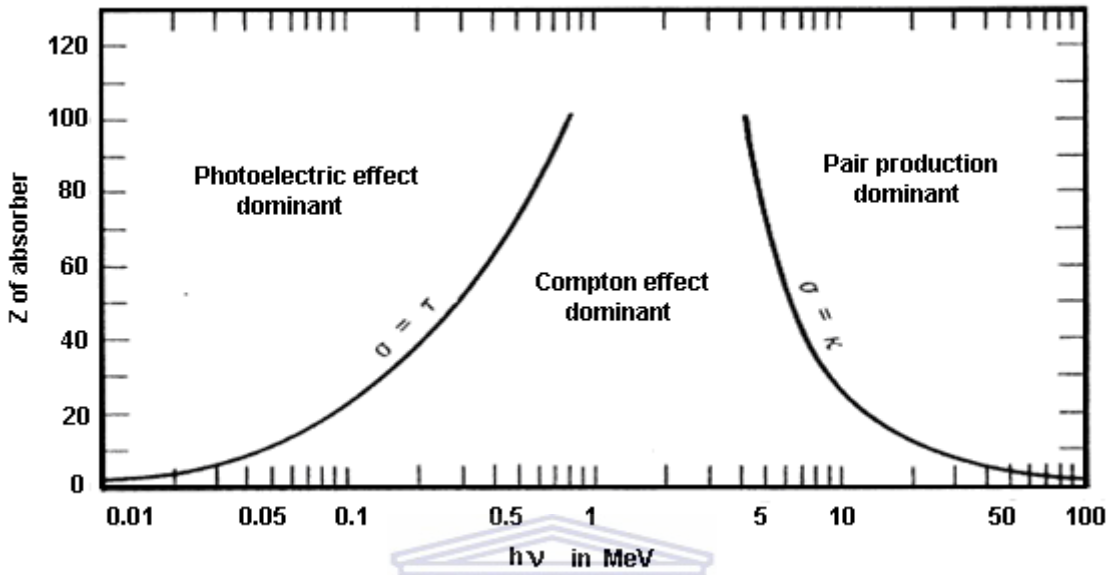

Figure 2.6: The relative importance of the three major types of γ-ray interaction. The lines show values of **Z** and **hν** for which the two neighbouring effects are just equal [Knoll, 2010].

So far the processes that have been mentioned involve the interaction of the photon with electrons but also note that other photon-interaction processes exist which might be less probable and less important in the energy range considered.

2.5 Gamma-ray spectrometry

This technique was utilised to identify and quantify the nuclide's activity concentration in the laboratory and in the field (in-situ). The technique is non-destructive, allows for multi-element analysis and can be applied to all types of samples (solids/liquids). Gamma-ray spectrometry is used extensively in laboratories worldwide for radioactivity measurement [Yucel, 1998; Croft, 1999; Daza, 2001; Melquiades, 2001; Khater, 2008; Misiak, 2011].

The Hyper Pure Germanium (HPGe) γ-ray detector available at the Environmental Radioactivity Laboratory (ERL), iThemba LABS Western Cape, South Africa was used for radiometric analysis of soil samples collected from the Kloof mine dump. Details of the HPGe γ-ray detector are given in Chapter 4, subsection 4.4.1. Two processes are

required when this technique is used to analyse samples. The first process involves identifying the various radionuclides in the soil samples as illustrated in Figure 2.7. The second process involves estimating the activity concentrations of the identified radionuclides. The process of estimating activity concentrations is discussed at length in Chapter 4, subsection 4.4.2.

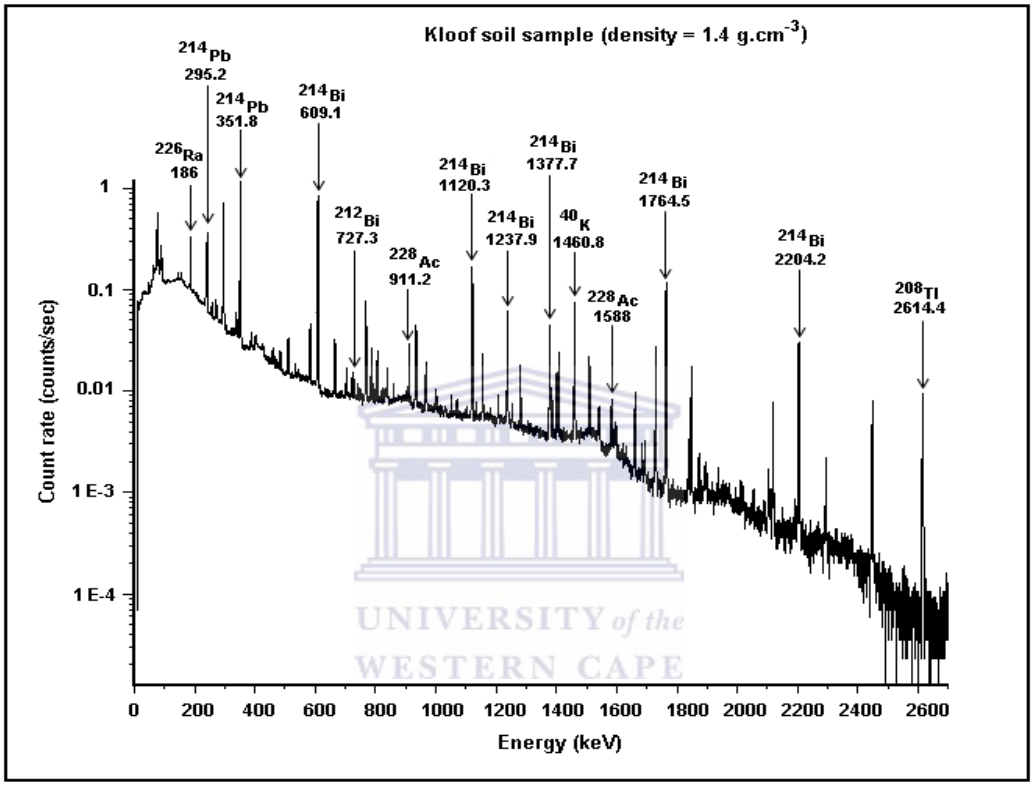

Figure 2.7: The process of identifying radionuclides in the spectrum obtained using the HPGe γ-ray detector.

γ-ray spectrometry can be employed to identify and estimate the activity concentrations of radionuclides in the ground directly at the field. Often, a portable sodium-iodide (NaI(Tl)) or a portable high purity germanium (HPGe) γ-ray detector is used with a multichannel analyzer for in-situ gamma-ray spectrometry. In-situ γ-ray spectrometry can be performed as either stationary or mobile measurements. By stationary is meant that the detector system is held above the ground and then the measurement is conducted at that position for a given period of time. Mobile measurements are performed either on foot or by a vehicle or by an aeroplane and they allow for the assessment of the activity concentration levels of radionuclides over a large area.

In this study, the MEDUSA (Multi Element Detector for Underwater Sediment Activity) γ-ray detector system was used to perform in-situ stationary and mobile measurements. The MEDUSA γ-ray detector system detects γ-rays associated with the radionuclides in the ^{238}U and ^{232}Th decay series as well as ^{40}K up to a depth of about 30 cm below the soil surface. This is due to self-absorption of the γ-rays within the soil.

The MEDUSA system was designed and developed by the Nuclear Geophysics Division (NGD) of the accelerator facility, Kernfysisch Versneller Instituut (KVI) at the University of Groningen (RUG) in the Netherlands [De Meijer, 1997; De Meijer, 1998]. The MEDUSA system was initially used to measure the activity concentrations of the natural radionuclides ^{40}K, ^{232}Th series and ^{238}U series in underwater environments [De Meijer et al., 1997; De Meijer, 1998; Hendriks et al., 2001; Venema et al., 2001]. The MEDUSA γ-ray detector used had a bismuth germanate (BGO) scintillator crystal. For the MEDUSA system available at iThemba LABS, the BGO γ-ray detector crystal was replaced by a cesium iodide crystal, CsI(Na). The CsI crystal has a more stable light output at variable temperatures compared to BGO detectors. Details for the MEDUSA set-up in the field and its accompanying components are given in Chapter 4, section 4.2. Figure 2.8 shows a typical MEDUSA spectrum being analysed using the MEDUSA Post Analysis (MPA) software (more details in subsection 4.2.3).

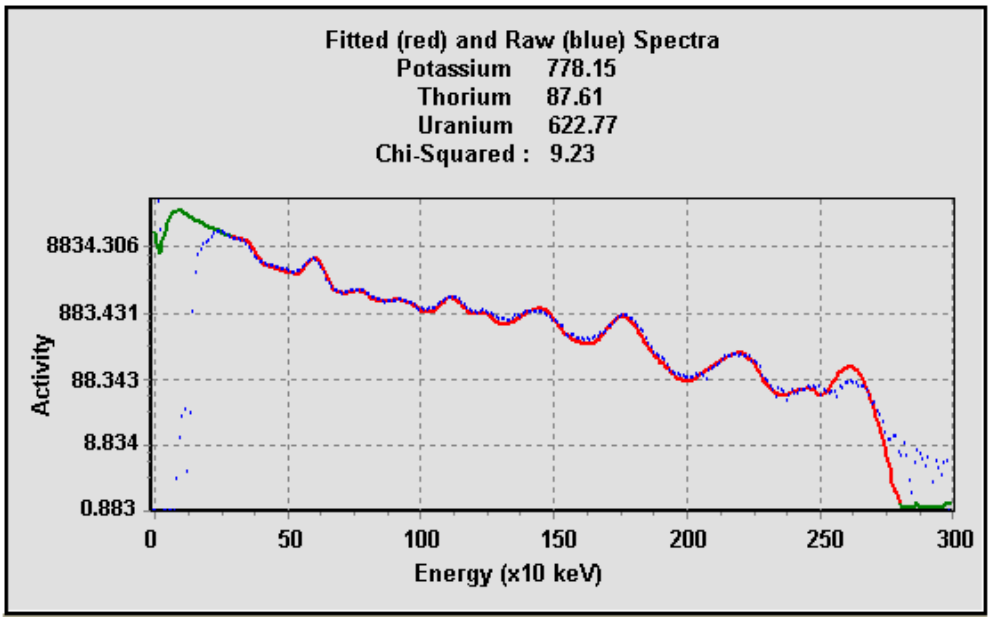

Figure 2.8: A typical MEDUSA spectrum showing the estimated activity concentrations of the radionuclides of ^{40}K and in the decay series of ^{238}U and ^{232}Th.

2.6 Alpha spectrometry

This technique was mainly used to determine the activity concentration of radon gas in soil air at the field. As mentioned earlier in Chapter 1, section 1.2, there are three radon isotopes namely ^{219}Rn, ^{220}Rn, and ^{222}Rn which exist as members of the primordial radioactive series of ^{235}U, ^{232}Th and ^{238}U, respectively. Note that ^{219}Rn (4 s) and ^{220}Rn (55 s) are not found in significant concentrations in the environment because their half-lives are relatively short as compared to ^{222}Rn (3.82 days).

There are several techniques discussed in the literature that are used to detect and measure radon gas in the soil [NCRP, 1988; Durrani & Ilic, 1997]. Not all techniques mentioned discuss the detection of radon by using alpha emissions except the following:

An alpha card system which provides a means for measuring radon in soil-gas. The alpha card is approximately 4.5 cm × 5 cm with a 2.5 cm diameter hole at the centre which is covered with a thin membrane. It is then put in an inverted cup and then deposited in the ground for period of 12 hours up to several days. During that period radon diffuses into the detection volume and then decays into its daughters which make an active deposit on the thin membrane. The alpha card is then retrieved from the field and read. Then silicon detectors which are sensitive to alpha particles only are used to measure the activity of radon in soil-gas. Note that this system is able to distinguish between radon and thoron by taking advantage of the fact that thoron daughter products have long half-lives compared to those of radon daughters.

Another way through which radon can be measured is by using the Solid State Nuclear Track Detectors (SSNTDs). In order for this method to work, it means that every detectable alpha particle must produce a single trail of damage in a SSNTD. After chemical enlargement the single trail turns into a narrow channel and is made visible under the microscope. SSNTDs display different sensitivities to heavy charged particles; however they are largely insensitive to beta and gamma rays. In other words, beta and gamma rays do not produce etchable individual tracks.

Schubert (2002) used an Alpha Guard PQ2000 system for radon measurement in air and soil gas in a column (1 m^2 × 2 m) consisting of a homogenous mixture of dry sand and uranium tailings. The measurements were intended to provide information on the radon transport under well defined conditions. The system allowed the simultaneous

monitoring of radon progenies using an alpha spectrometric detector with a sensitivity of 5 cpm at 100 $Bq \cdot m^{-3}$.

In this work, radon in soil-gas measurements were performed at the Kloof mine dump using a continuous radon monitor (RAD7). The RAD7 is a highly adaptable instrument which was designed to detect alpha particles only. Now referring back to the uranium decay series (see Figure 2.1), every nucleus of ^{222}Rn ultimately decays through the polonium-218 (^{218}Po), lead-214 (^{214}Pb), bismuth-214 (^{214}Bi), polonium-214 (^{214}Po), and lead-210 (^{210}Pb). With each transformation, the nucleus emits characteristic radiations: alpha particles, beta particles, or gamma rays, or combinations of these.

An alpha particle is released with energy of 5.49 MeV when a ^{222}Rn nucleus transforms to ^{218}Po which in turn releases alpha particle of energy 6.00 MeV. Furthermore, ^{214}Po nucleus decays emitting an alpha particle of energy 7.69 MeV. In brief the RAD7 measures alpha particles mainly from nuclei deposited on its detector and uses the 6.00 MeV α-decay from ^{218}Po to infer the ^{222}Rn concentration.

The RAD7 is capable of differentiating between radon and thoron as shown in Figure 2.9 based on the energy of the alpha particle released. In addition it is almost completely insensitive to beta or gamma radiation, so there will be no interference from beta-emitting gases or from gamma radiation fields. More details of the RAD7 are given in subsection 3.3.1.

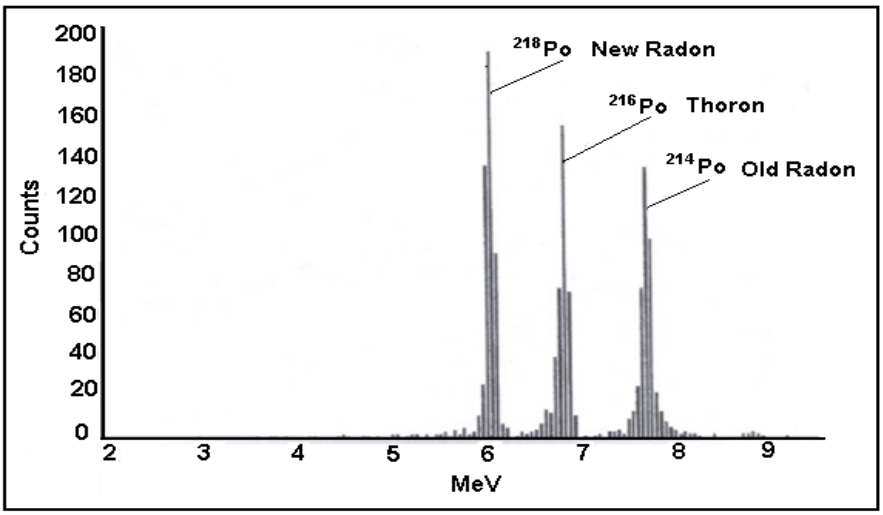

Figure 2.9: A high resolution image of the RAD7 spectrum.

2.7 Summary

An introduction to the relevant background information concerning natural radiation has been given. The main techniques, namely the gamma-ray spectrometry and the alpha spectrometry, have been introduced briefly. Details of the alpha spectrometry will be discussed in depth in Chapter 3 while Chapter 4 and 5 will focus on gamma-ray spectrometry.

Chapter 3

Transport of Radon Gas

3.1 Introduction

In this Chapter radon gas transport mechanisms will be explored. As shown in Figure 3.1, radon originates from the decay of radium whose parent radionuclide is uranium and once it emanates to the pore spaces it is available for transport and then it ends up in the environment. In the pore spaces the amount of radon available for transport will be measured using a RAD7 counter [Durridge, 2000] and later on in this Chapter Comsol Multiphysics [Comsol, 2008] will be used to predict the amount of radon in the pore spaces at various depths.

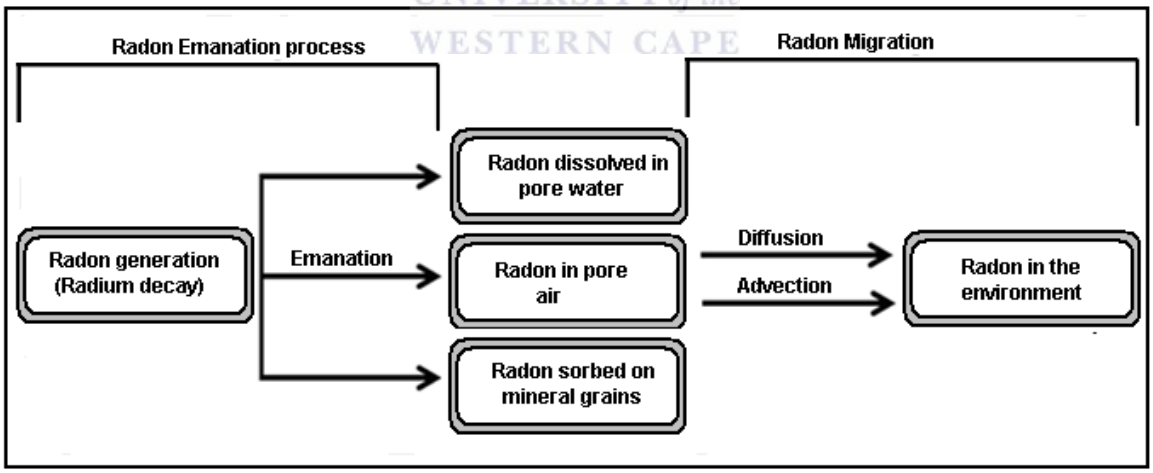

Figure 3.1: A sketch showing radon emanation and migration processes.

3.2 Radon transport mechanisms

Radon gas in soil pores migrate in the ground by diffusion; however it does not always involve any movement of the fluid (soil gas or ground water) in the pores, or by

advective flow of the fluid. Changes in air pressure, wind and even temperature influence air moving in the ground [Schumann, 1994; Åkerblom, 1997]. Some of the soil characteristics such as the permeability, degree of compaction and the water content also influence radon migration in the ground. Soil permeability is determined by the number, size, and degree of interconnection of pore spaces, which are controlled by the size, shape, and arrangement of the soil grains or aggregates. In this context soil gas permeability refers to how easily the gas, for instance radon, will flow through soil.

Schumann (1994) indicated that permeability is highest in coarse, well sorted and finer grained materials, whereas it is lowest in poorly sorted and finer grained materials where smaller grains can fill the void spaces between larger grains. Cracks and fissures in the soil also increase the soil's permeability [Schumann, 1994]. A wide spectrum of permeability values for different types of soils shown in Figure 3.2 has been reported by Nazaroff et al. (1988). The particle sizes for the various soil types are usually taken as 60-2000 μm for sand, 2-60 μm for silt and with a range less than 2 μm for clay.

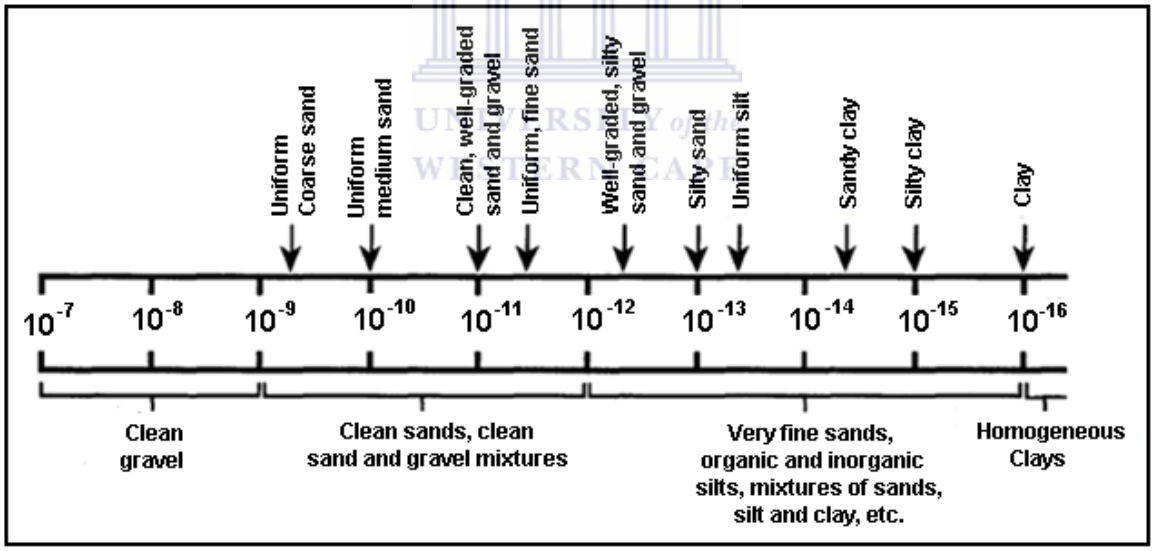

Figure 3.2: Typical soil permeability (m^2) values. From [Nazaroff et al., 1988].

If the pore spaces in the soil are completely filled with water, it hampers radon transport because water tends to block the soil pores and thereby reduce the radon gas permeability in the soil [Schumann, 1994]. If the moisture content of the soil is large enough such that a fraction of radon can dissolve in it, then radon gas mobility due to diffusion and

advection can be described by a combined general transport equation [Nazaroff et al., 1988] written as

$$\frac{1}{\varepsilon}\frac{\partial(C_{Rn}\varepsilon_g + C_w\varepsilon_w)}{\partial t} = \nabla\cdot D\nabla C_{Rn} - \nabla\cdot C_{Rn}\frac{v}{\varepsilon_g} + E\rho_s\frac{1-\varepsilon}{\varepsilon}C_{Ra}\lambda_{Rn} - \frac{1}{\varepsilon}\lambda_{Rn}(C_{Rn}\varepsilon_g + C_w\varepsilon_w) \tag{3.1}$$

where, ε is the soil porosity (dimensionless), ε_g is the gas porosity defined as the ratio between the gas filled volume of the soil pores and the total soil pore volume, ε_w is the water porosity, defined as the ratio between the water filled volume of the soil and the total soil pore volume, so that $\varepsilon = \varepsilon_g + \varepsilon_w$, C_{Rn} is the radon activity concentration in the gas filled volume of the soil pores, C_w is the radon activity concentration in the water filled pore volume of the soil, D is the effective diffusion coefficient ($m^2 \cdot s^{-1}$) corrected by the effect of the water content, v is the superficial velocity vector of soil gas ($m \cdot s^{-1}$), E is the emanation coefficient corrected by the effect of the water content, ρ_s is the density of the soil grains ($kg \cdot m^{-3}$), λ_{Rn} is the radon decay constant, and C_{Ra} is the radium activity concentration in the soil ($Bq \cdot kg^{-1}$).

The first term on the right hand side of equation (3.1) represents diffusion in the pore air, the second term, advection, the third term, radon generation and the fourth term, radon radioactive decay. Therefore the equation takes into account the moisture content of the soil. On the other hand if the soil has negligible moisture content then the equation may be written as

$$\frac{\partial C_{Rn}}{\partial t} = \nabla\cdot D\nabla C_{Rn} - \nabla\cdot C_{Rn}\frac{v}{\varepsilon} + E\rho_s\frac{1-\varepsilon}{\varepsilon}C_{Ra}\lambda_{Rn} - \lambda_{Rn}C_{Rn}. \tag{3.2}$$

Several radon transport equations that have been formulated can be found in the published literature. Some of the authors who have given radon transport equations include Loureiro (1987), Nazaroff et al. (1988), Rogers & Nielson (1991a) and Andersen (2000, 2001). All radon transport equations that have been suggested are almost the same with small differences which arise due to the assumptions that are made for example;

- neglecting radon adsorption on the surfaces of the soil grains
- in other cases the water content is neglected

- it is assumed that the superficial velocity vector is described by Darcy's Law
- it is assumed that soil gas is incompressible
- it is assumed that the soil is isotropic and homogeneous with respect to the diffusion coefficient, permeability, porosity, emanation coefficient, radium content, and bulk density

Due to those assumptions equation (3.2) may be written as

$$\frac{\partial(C_{Rn})}{\partial t} = D\nabla^2 C_{Rn} - v\nabla C_{Rn} - \lambda_{Rn} C_{Rn} + \lambda_{Rn} C_{\infty} \tag{3.3}$$

$$\text{where, } C_{\infty} = \frac{E\ C_{Ra}\ \rho_s\ (1-\varepsilon)}{\varepsilon} \tag{3.4}$$

As a result equation (3.3) provides an insight into radon transport in soil if three cases are analysed as follows [Antonopoulos-Domis, 2009].

Case 1: Pure diffusion model only

If the velocity in equation (3.3) is assumed to be constant and independent of the position in the soil, the equation reduces to a one-dimensional equation. If we also assume that the radon concentration is zero at the soil surface and that depth (z) in soil increases from the ground surface to deep down, the general solution of equation (3.3) that now reduces to a one-dimensional form at steady state (i.e. $\partial C/\partial t = 0$) is

$$C(z) = Ae^{-az} + Be^{(v/D+a)z} + C_{\infty} \tag{3.5}$$

where, A and B are constants which are determined by the boundary conditions and a is the positive root of the equation given below

$$Da^2 + va - \lambda = 0 \tag{3.6}$$

given by,

$$a = -\frac{v}{2D} + \left[\left(\frac{v}{2D}\right)^2 + \frac{\lambda}{D}\right]^{1/2}. \tag{3.7}$$

Applying the boundary and initial conditions which are $C(0) = 0$ and $\left.\frac{dC}{dz}\right|_{z=\infty} = 0$ at $z = \infty$, equation (3.5) becomes

$$C(z) = C_{\infty}(1 - e^{-az}) \tag{3.8}$$

In equation (3.8), C_∞ is given by equation (3.4) which is C at $z = \infty$.

Therefore in the case of a pure diffusion model, the velocity (v) in equation (3.3) is set to zero, and from equation (3.6) the concentration becomes

$$C(z) = C_\infty(1 - e^{-z/\ell_D}) \tag{3.9}$$

$$\text{where, } \ell_D = \left(\frac{D}{\lambda}\right)^{1/2}. \tag{3.10}$$

Equation 3.9 is the solution of the diffusion model and ℓ_D is called the diffusion length.

Case 2: Pure advection model only

Modelling of the pure advection process involves setting $D = 0$ in equation (3.3), thus from equation (3.6) it follows that the concentration will be

$$C(z) = C_\infty(1 - e^{-z/\ell_A}) \tag{3.11}$$

$$\text{where, } \ell_A = \frac{v}{\lambda}. \tag{3.12}$$

Note that the form of equation (3.11) is similar to that of equations (3.8) and (3.9) however the only difference is the characteristic "migration length", ℓ_A which is given in equation (3.12).

Case 3: Diffusion - Advection model

In the diffusion-advection model, the migration length is

$$\ell_{DA} = \frac{1}{a} \tag{3.13}$$

where, a is obtained from equation (3.7).

So the concentration will be

$$C(z) = C_\infty(1 - e^{-z/\ell_{DA}}). \tag{3.14}$$

The pure diffusion model, the pure advection model and the diffusion-advection model give the same form of $C(z)$ as shown by equations (3.9), (3.11) and (3.14) respectively. This could probably mean that the diffusion advection model can be substituted by a pure diffusion model, with an equivalent diffusion coefficient D_e, defined as

$$\left(\frac{\lambda}{D_e}\right)^{1/2} = a = -\frac{v}{2D} + \left[\left(\frac{v}{2D}\right)^2 + \frac{\lambda}{D}\right]^{1/2}. \quad (3.15)$$

The amount of radon available for transport from the ground beneath until it gets released to the atmosphere can be estimated by measuring the radon levels in the soil air at different depths. Consequently, the next section discusses how to estimate radon levels by measuring radon concentrations at different soil depths in-situ. Later on, in section 3.4, equations (3.9), (3.11) and (3.14) will be incorporated in Comsol Multiphysics which will be used as a tool to determine radon concentrations at different soil depths.

3.3 Radon gas concentration measurements at different soil depths

Research on determining the concentration of radon in soil air have been conducted and reported in the last 2-3 decades by amongst others the following authors, Bigu (1984), Speelman (2004), Manavhela (2007) and Antonopoulos-Domis (2009). For example Åkerblom & Mellander (1997) have reported that radon concentration in the soil air at shallow depth undergoes great change, at a depth of about 0.5 m the concentration is approximately 50 % of the equilibrium concentration and at about a metre it is normally about 70-80% of the equilibrium concentration, and more constant.

Radon concentration in soil air can be measured using various techniques that can detect radon, for example the nuclear emulsion, adsorption, solid scintillation, gamma spectrometry, solid-state nuclear track detectors, electrometer or electroscope, thermoluminescent phosphors, ionization chambers, electrets and solid state electronic detectors. Nearly all the techniques used in the field can also be used in the laboratory. A radon measurement can be carried out either passively or actively. A passive radon measurement implies that radon concentration is measured under natural conditions by allowing radon to diffuse to the detection volume. On the other hand an active radon measurement involves pumping of the radon gas into or through a detecting instrument.

In this work, the solid state detector equipment (RAD7, see the next subsection) and electrets were used to detect radon gas at the Kloof mine dump. The electrets detect radon gas passively while the solid state detector equipment (RAD7) monitors radon gas continuously. The details on the electrets will be discussed in subsection 5.4.2.

3.3.1 The Durridge RAD7^{TM} continuous radon monitor

The RAD7 from the Durridge Co., was used to monitor radon concentration in the soil air at the Kloof mine dump since it is portable, durable, sensitive and operates in a true, real-time continuous mode. In that mode RAD7 also monitors other factors such as temperature changes and relative humidity which may influence the radon concentration measurement during the measurement period.

Currently, various continuous radon monitors are available commercially. Continuous radon monitors work by detecting the alpha radiation, but not beta or gamma radiation. The scintillation cells or "Lucas cells", ionisation chambers and the solid state alpha detectors are the three types of alpha particle detectors that can be used to monitor radon gas.

The RAD7 instrument which is shown in Figure 3.3 uses a solid state alpha detector. A solid state detector is a semiconductor material which is usually silicon that converts alpha radiation directly to an electrical signal. This solid state device has the ability to determine the energy of each alpha particle electronically. Additionally, it enables one to differentiate between old radon, new radon, radon or thoron, and signal due to noise as one is able to establish the correct isotope (polonium-218 or polonium-214) which produced the radiation signal.

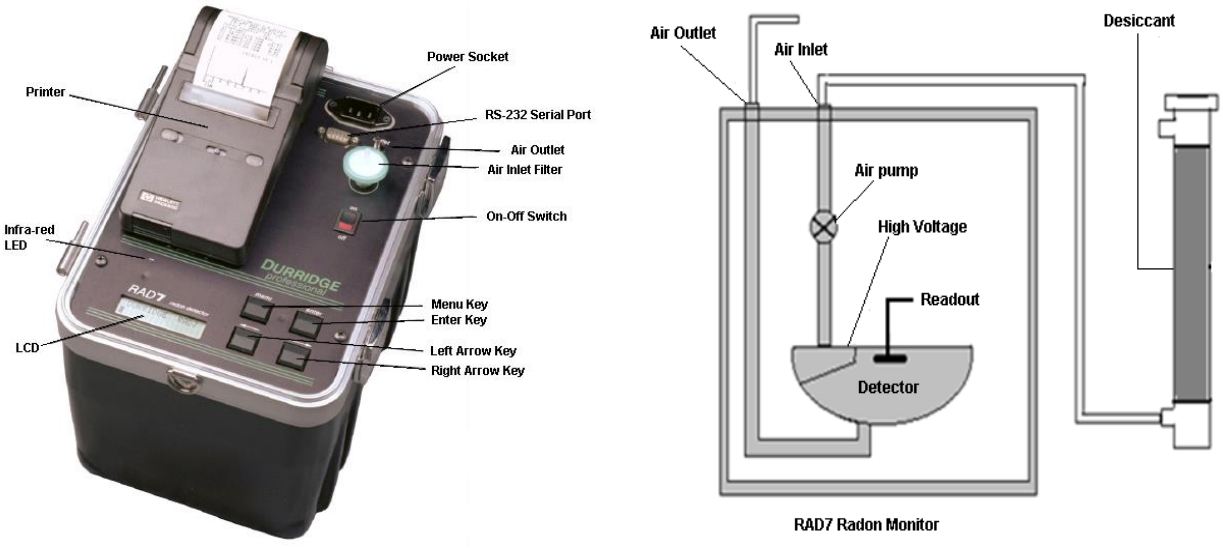

Figure 3.3: A picture of the RAD7 is shown on the left while the schematic diagram on the right shows the internal parts of the RAD7 [Durridge, 2000].

The RAD7 has a hemispherical internal sample cell with volume about 0.7 litres. The solid state ion-implanted silicon alpha detector is located at the centre of the hemisphere. The conductor inside the hemisphere is charged to a potential of 2000-2500 volts which creates an electric field throughout the cell. The RAD7 uses the high electric field to attract the positively charged polonium daughters, $^{218}Po^{+}$ (half-life = 3.10 min; alpha energy = 6.00 MeV), and $^{214}Po^{+}$ (half-life = 164 μs; alpha energy = 7.67 MeV), which are then counted as a measure of the radon concentration in air. The ^{218}Po nucleus has a short half-life and when it decays it has a 50% likelihood of entering the detector where an electrical signal is produced which leads to identifying the alpha particle. The electrical signal obtained by RAD7 is then amplified, filtered, and sorted. Subsequently, depending on the mode being used, the radon concentration is determined from the ^{218}Po (alpha energy = 6.00 MeV) signal and the thoron concentration is determined from the ^{216}Po (alpha energy = 6.78 MeV) signal. The succeeding longer-lived radon daughters are ignored.

Radon and thoron daughters that produce alpha particles with energy in the range of 6-9 MeV are measured as shown by the RAD7 spectrum in Figure 3.4.

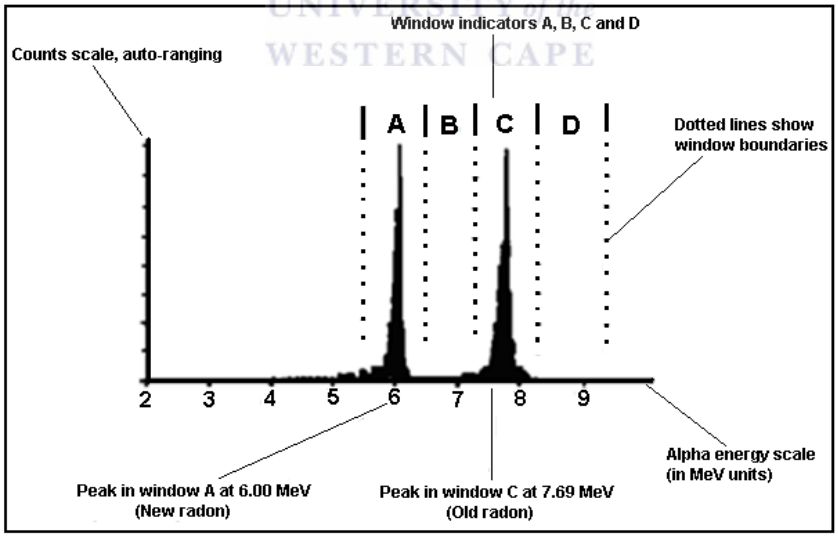

Figure 3.4: RAD7 spectrum and the energy windows.

The spectrum in RAD7 is grouped into 200 channels that correspond to 0.05 MeV per channel. In an ideal world the spectrum of a 6.00 MeV alpha emitter should look like a single needle-thin spike at just 6.00 MeV, however, the actual RAD7 spectrum shows a

broadened peak centred near 6.00 MeV with a tail that stretches into lower energy channels (see Figure 3.4). The peak widens due to high temperature which tends to increase the electronic noise in the detector and the amplifier while the tail stretches because the alpha particles enter the detector at different angles.

During analysis, the RAD7 utilises 8 separate "windows" which are labelled A to H; for instance window A, where ^{218}Po (alpha energy = 6.00 MeV) is found, lies between 5.40 and 6.40 MeV. The next step involves converting the raw spectral data to radon measurement which is achieved by taking all the counts in that energy range and dividing by the live-time (duration of active data collection). The RAD7 microprocessor performs all those tasks and stores the result in the memory which can then be retrieved for later use.

The RAD7 spectrum can be printed out but then it only contains the major windows A, B, C, and D. These major windows A, B, C and D contain the total counts from ^{218}Po (alpha energy = 6.00 MeV), ^{216}Po (alpha energy = 6.78 MeV), ^{214}Po (alpha energy = 7.69 MeV) and ^{212}Po (alpha energy = 8.78 MeV), respectively. Windows E-H are grouped together to form the composite window O (for “other”). This window O contains all the counts that did not go into the major windows A, B, C, and D.

In order to get accurate readings the background needs to be taken into account. Note that the background in the radon detector refers to the false counts that occur even in the absence of radon which might arise from the properties of the instrument or its components, other forms of radiation in the instrument's environment, or contamination of the instrument.

According to the manufacturer, RAD7 is considered to be less vulnerable to the background unlike other radon monitors; however there are problems that may crop up that the operator of the instrument must be aware of.

Firstly, the short lived radon and thoron daughters build up on the RAD7 solid state alpha detector and may continue for some time to produce alpha counts even after the radon and thoron gases have been removed from the instrument. This might pose a problem if one will try to measure a low radon sample immediately after a high radon sample. RAD7 overcomes this problem by changing the acquisition mode to SNIFF and

then start counting again. In that mode RAD7 is able to differentiate the different alpha-emitting daughters by their alpha energy.

Secondly, radon atoms can adsorb on or absorb into internal surfaces of the RAD7, on the inside of tubing or on desiccant granules. This problem can be overcome by the process of purging the instrument for 10 minutes until the levels are completely down to normal before a measurement can be performed.

Thirdly, after continual use of RAD7 for many years, the unavoidable build-up of the long-lived beta-emitter ^{210}Pb (half-life = 22 years) would result in increased ^{210}Po (energy = 5.3 MeV) levels with time, which could have a serious effect on background levels. The RAD7 is able to differentiate this isotope by its energy, and exclude it from all calculations.

3.3.2 Setup for radon soil gas measurements at the Kloof mine dump

RAD7 was used to monitor the levels of radon gas in the soil air at different depths in different spots at the mine dump. The concentration profiles of radon gas generated from the measurements can offer an insight into (1) predicting the amount of radon gas exhaling from the ground into the atmosphere and (2) deducing the possible factors that are affecting radon gas mobility in the ground.

Five different spots on the mine dump as displayed in Figure 3.5 were identified where radon soil gas measurements were done. The co-ordinates* of the five different spots which were selected with the aid of a GPS (Global Positioning System) and a previous map of the mine dump are given in Table 3.1. In addition to the RAD7 measurements, other systems such as the electrets, the HPGe γ-ray detector for soil samples and the MEDUSA γ-ray detector were also utilised for measurements. Details on the results from the electrets, the HPGe and the MEDUSA γ-ray detector systems will be given in Chapter 4 and 5.

* Co-ordinates are usually given in the format *xx^{0}yy.yy'* where *xx* and *yy.yy* correspond to degrees and minutes respectively see, Table 3.1, however it is not the case with the MEDUSA-software algorithm which gives the latitude and longitude in the format *xxyy.yy*, see Figure 3.5 and the other maps produced thereafter.

Table 3.1: The GPS co-ordinates where the radon soil gas measurements were conducted.

GPS co-ordinates for the Spots				
Spot 1	**Spot 2**	**Spot 3**	**Spot 4**	**Spot 5**
26^0 24.407′ S	26^0 24.699′ S	26^0 24.561′ S	26^0 24.861′ S	26^0 24.682′ S
27^0 36.831′ E	27^0 37.266′ E	27^0 37.355′ E	27^0 37.311′ E	27^0 36.988′ E

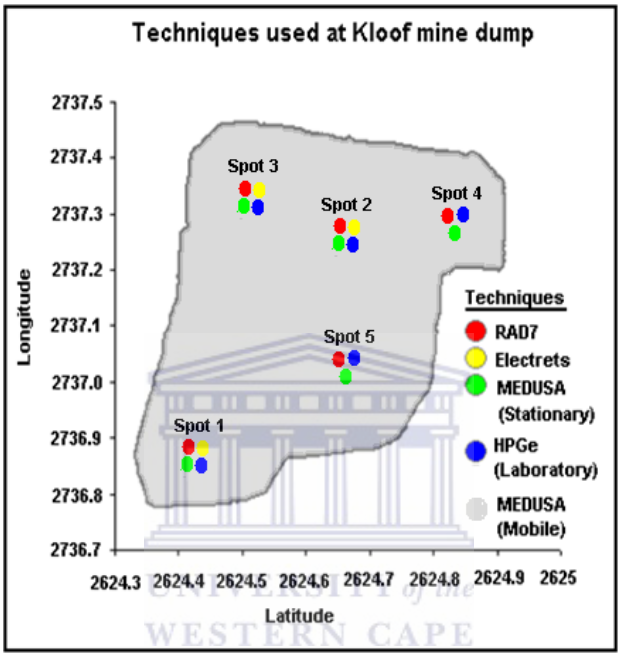

Figure 3.5: The spots which were identified for radon soil gas measurements.

The RAD7 instrument was used for soil gas measurements by first connecting it to its accompanying accessories which include the tube connectors, the desiccant column, inlet filter and the water trap bottle [Durridge, 2000]. Next a hollow soil gas probe was inserted slowly to the desired depth. The soil surrounding the probe was firmed using hands to ensure that there is a reasonable seal between the probe and the surrounding soil, so that air does not go down around the probe, to dilute the soil gas sample. At the top of the soil gas probe the screw connectors were wrapped with a Teflon tape to provide an air tight fit when it is hooked up to the RAD7. The in-situ setup of the RAD7 and its accompanying accessories is shown in Figure 3.6.

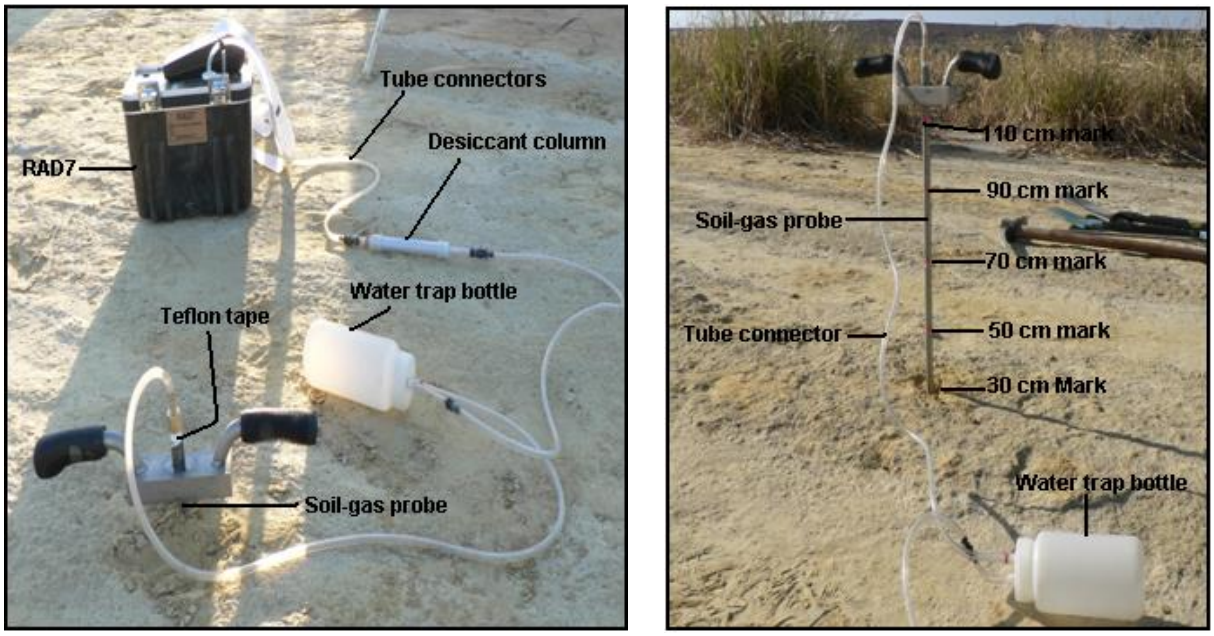

Figure 3.6: (Left) In-situ setup of RAD7 measuring radon gas at 110 cm. (Right) The picture indicates in-situ setup of RAD7 measuring radon gas at 30 cm.

A water trap bottle is connected to the top of the soil gas probe. In the process of conducting measurements the soil gas probe might be inserted in an area which is too damp or the water table is not too deep. In such circumstances water may be pumped up the soil gas probe and will get trapped in the water bottle. As a safety measure to ensure that the RAD7 instrument is not damaged, the soil gas probe will be withdrawn from that area.

To measure radon gas concentration, one has to set RAD7 to the right protocol and mode. RAD7 has standard preset protocols which include Sniff, 1-day, 2-day, Weeks (that is, indefinite), User (which lets you preset your own), Grab, Wat-40 and Wat-250 (for use with the RAD H_20), and Thoron.

The Grab protocol with the Sniff mode was used to measure radon soil gas concentration at the Kloof mine dump. Setting RAD7 to Grab protocol basically means that the RAD7 pump will run for five minutes to flush the cell detector's chamber and then stop. The RAD7 will wait for five more minutes, and then count for four 5-minute cycles. This measurement process takes 30 minutes for one depth measurement. Since the radon gas concentrations at Kloof mine dump are high, RAD7 was set to the Sniff mode so that the rapid change of radon concentration can be followed in the process of

performing a measurement. This is possible because RAD7 achieves rapid response to changing radon concentration levels by focusing on the ^{218}Po (half-life = 3.10 min; alpha energy = 6.00 MeV) alpha peak. Therefore radon gas concentration is calculated on the basis of that peak only. The internal air pump shown in Figure 3.3 pumps air at a rate of 1 L/min, however it is estimated that between 0.3 and 0.5 L/min of soil-gas is pumped. Before any measurement was done the RAD7 was purged for 10 minutes. This ensured that the cell's detector measurement chamber dried out to bring down the relative humidity to less than 10%.

At the Kloof mine dump, see Figure 3.5, radon soil gas concentration measurements at various depths were obtained from spot 1, 3, 4 and 5 starting from 0.30 m up to 1.1 m at depth intervals of 0.20 m. The length of the soil gas probe used was about 1.25 m therefore we could measure up to 1.1 m. RAD7 measures radon gas in Bq·m^{-3} and the concentrations that were measured are given in Table 3.2.

Table 3.2: Radon soil gas concentration (Bq·m^{-3}) and the average activity concentration (Bq·kg^{-1}) of soil at spots 1, 3, 4 and 5.

Depth (cm)	**Radon gas concentration** (Bq·m^{-3})			
	Spot 1	**Spot 3**	**Spot 4**	**Spot 5**
30	35900 ± 2680	26500 ± 1350	81400 ± 2410	52400 ± 1590
50	132000 ± 5150	90600 ± 5620	103000 ± 5240	67400 ± 5000
70	213000 ± 7240	295000 ± 16800	182000 ± 4940	84100 ± 1110
90	292000 ± 8550	400000 ± 14000	337000 ± 16200	169000 ± 6390
110	287000 ± 2790	420000 ± 21200	429000 ± 17400	472000 ± 23300
Average activity conc. ^{238}U series (Bq·kg^{-1})	282 ± 6	283 ± 6	341 ± 7	315 ± 7

Radon gas concentration measurements for less than 30 cm below the ground/air interface were not performed since it was thought that they might be affected by the meteorological changes which will introduce uncertainty when interpreting the results. Based on the concentrations measured as given in Table 3.2, the depth profile showing how radon gas concentrations vary with depth is presented in the figures that follow.

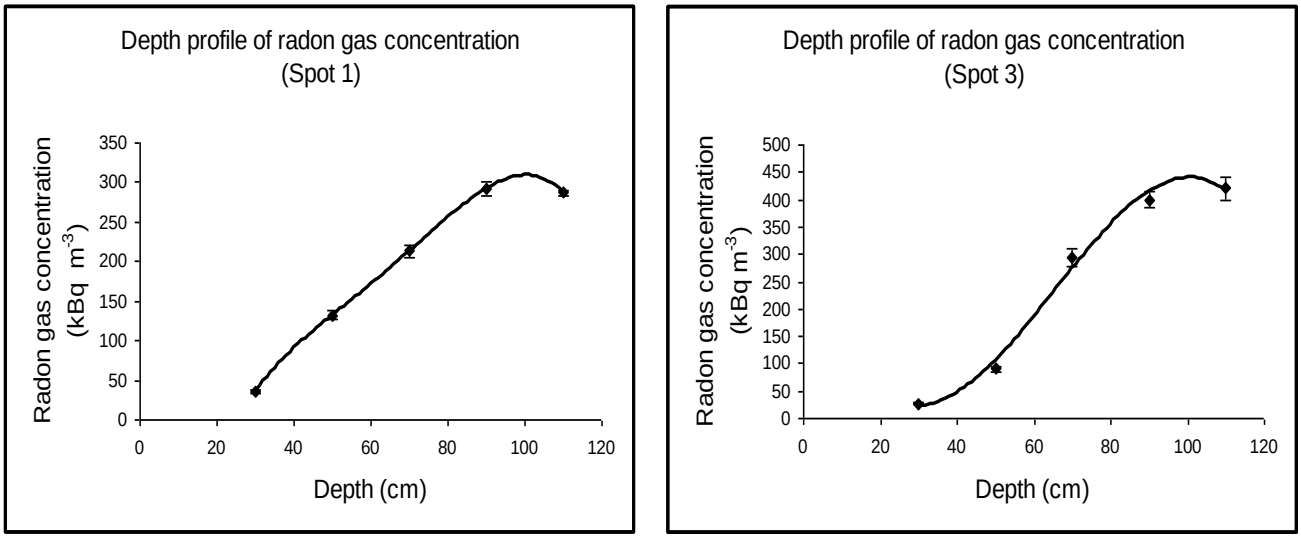

Figure 3.7: (Left) The graph shows radon soil gas concentration profile for spot 1. (Right) The graph shows radon soil gas concentration profile for spot 3. The solid lines are intended to "guide the eye ".

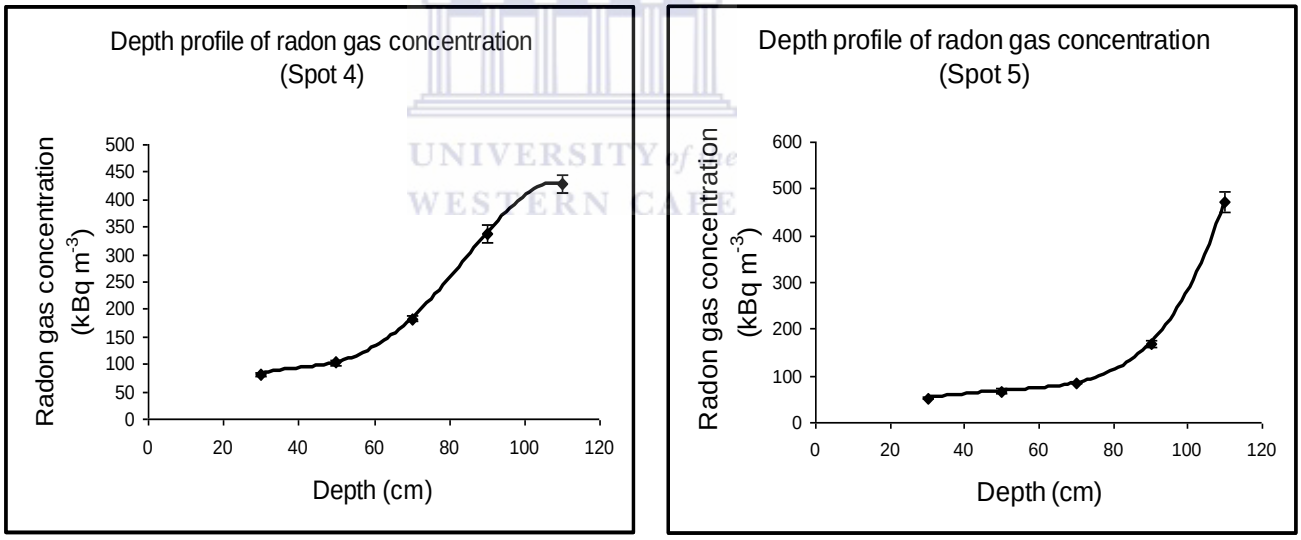

Figure 3.8: (Left) The graph shows radon soil gas concentration profile for spot 4. (Right) The graph shows radon soil gas concentration profile for spot 5. The solid lines are intended to "guide the eye ".

The curves above show how radon concentrations in soil air decrease towards the surface as a result of diffusion, but the curve on the right hand side of Figure 3.8, obtained from the measurements on spot 5, indicates a different trend compared to the other curves for spots 1, 3 and 4. The difference could be due to the pressure changes and the high wind speeds during that particular time when the measurements were being performed.

In actual fact the wind speeds were as high as 4.2 $m \cdot s^{-1}$ compared to the wind speeds in spot 1, 3 and 4 as revealed by Table 3.3 and Table 3.4. The wind speeds, the temperature (^0C), humidity (%), pressure (mb) and altitude (m) were monitored for one hour using a Kestrel 4000 pocket-sized weather station.

Table 3.3: The parameters recorded for spot 1 (on the left) and spot 3 (on the right) while radon soil gas concentrations were measured.

Spot 1			
Temp. (^0C)	Humidity (%)	Pressure (mb)	Wind speed ($m \cdot s^{-1}$)
31.8	11.0	842.6	0.0 - 1.4
30.5	10.8	842.4	0.5 - 1.5
31.2	10.7	842.2	0.0 - 1.0
32.3	10.2	842.1	0.0 - 0.7
30.7	10.4	841.5	0.6 - 1.2
30.8	10.2	841.7	0.0 - 0.8
30.9	09.3	841.4	0.0 - 1.5
31.2	11.5	841.3	1.5 - 2.4
28.8	12.3	841.1	1.4 - 2.4
29.7	11.4	841.2	0.7 - 1.0
28.3	11.7	841.1	1.4 - 1.9
28.4	12.6	841.0	0.3 - 1.0
27.4	14.0	840.8	0.4 - 1.6
25.1	13.1	841.0	0.5 - 2.5
-	-	-	-

Spot 3			
Temp. (^0C)	Humidity (%)	Pressure (mb)	Wind speed ($m \cdot s^{-1}$)
28.1	11.8	836.1	0.4 - 2.5
30.4	8.3	835.9	0.4 - 2.2
29.7	9.4	835.8	0.4 - 1.5
29.6	9.2	835.6	0.4 - 2.3
29.6	8.5	835.5	0.7 - 1.1
28.9	9.3	835.6	0.5 - 2.2
28.4	9.2	835.4	0.5 - 0.8
29.6	8.5	835.1	1.4 - 1.6
28.2	8.7	835.0	1.4 - 2.0
29	9.2	835.2	0.5 - 1.5
28.2	8.6	835.1	0.6 - 1.5
26.9	9.7	835.0	0.4 - 1.4
27.2	11.1	835.2	0.7 -1.5
26.2	10.7	835.2	0.0 - 0.7

Table 3.4: The parameters recorded for spot 4 (on the left) and spot 5 (on the right) while radon soil gas concentrations were measured.

Spot 4			
Temp. (^0C)	Humidity (%)	Pressure (mb)	Wind speed ($m \cdot s^{-1}$)
33.2	06.7	838.4	0.5 - 0.9
30.6	10.6	838.7	0.0 - 1.5
30.7	10.7	837.8	0.4 - 1.2
32.5	09.3	837.9	0.0 - 0.8
30.9	11.2	837.7	0.4 - 1.2
29.3	12.9	837.6	0.4 - 0.9
30.3	12.8	837.3	0.5 - 0.9
29.6	12.6	837.3	0.6 - 0.8
24.7	18.3	838.0	0.4 - 0.6
-	-	-	-

Spot 5			
Temp. (^0C)	Humidity (%)	Pressure (mb)	Wind speed ($m \cdot s^{-1}$)
21.1	42	842.6	1.3 - 4.2
21.9	35.6	842.7	2.7 - 4.1
23.6	31.6	840.3	2.1 - 3.8
23.2	34.8	840.3	2.2 - 3.1
23.5	34.5	840.3	1.9 - 2.8
23	38.1	840.5	1.9 - 3.8
22.8	38.3	840.4	2.1 - 3.7
21.9	42.7	840.7	1.9 - 3.6
21.7	45.0	840.7	2.2 - 3.8
20.0	51.1	840.7	1.9 - 2.6

At spot 2, the radon soil gas measurements were measured in a different way as portrayed by Figure 3.9. As opposed to performing measurements at various depths from shallow to deep, the measurements were done at the same depth 50 cm but at different spots within a radius of 80 cm. It was hoped that executing radon soil gas measurements in that way, will reveal some characteristics of radon transport when the concentration is compared within that locality.

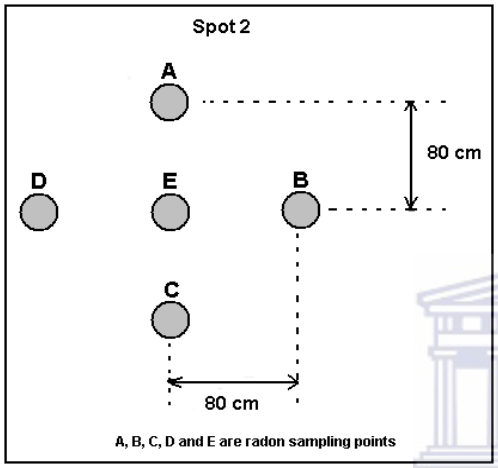

Figure 3.9: Design of sampling radon gas at spot 2.

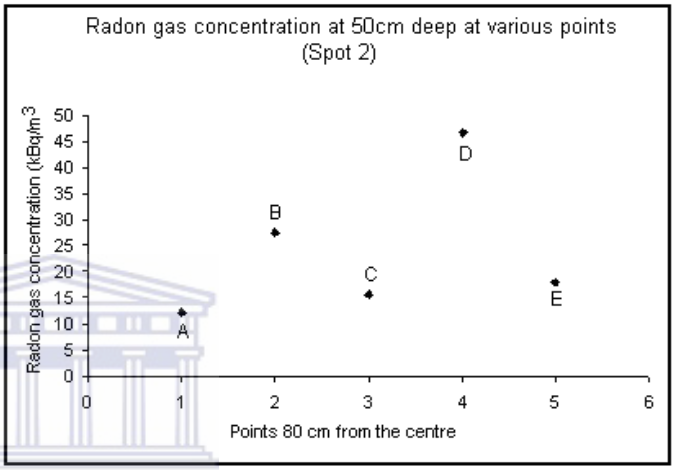

Figure 3.10: The graph shows the radon soil gas concentration profile for spot 2 recorded at the same depth.

Radon gas concentrations at spot 2 were found to vary between 12300 ± 543 $Bq \cdot m^{-3}$ and 46700 ± 1160 $Bq \cdot m^{-3}$ as illustrated by Figure 3.10. The temperature, relative humidity, pressure and wind speed did not vary significantly at spot 2, as shown in Table 3.5. The difference in radon concentration at that depth could probably suggest that within that radius the activity concentration of ^{226}Ra is not uniform as revealed from the results in Chapter 4 Table 4.7 Row 6-9 Column 4. Since there is a net flow of radon flux from the soil matrix it is not in secular equilibrium. The degree of soil compaction (porosity) could also influence the mobility of radon; hence it could have an effect on the amount of radon detected and possibly there is some leakage of air next to the probe.

Table 3.5: The parameters recorded for spot 2 while radon soil gas concentration was measured.

Spot 2			
Temp. (^{0}C)	Humidity (%)	Pressure (mb)	Wind speed ($m \cdot s^{-1}$)
31.6	12.3	840.1	0.0 - 1.2
30.3	13.8	839.6	0.5 - 1.6
29.0	12.9	839.8	0.3 - 2.5
29.9	12.5	839.0	0.3 - 0.6
30.7	9.5	838.8	0.0 - 1.1
29.3	12.1	838.7	0.5 - 1.2
30.4	13.5	838.6	0.0 - 0.9
27.5	13.5	838.5	0.4 - 1.8
27.8	13.5	838.4	0.0 - 0.6
28.5	11.5	838.3	0.4 - 1.6
27.8	9.4	838.4	0.4 - 0.7
25.6	12.4	838.7	0.4 - 0.9

When in-situ measurements are conducted, one must be aware of the background otherwise the results obtained might be exaggerated by the background. The background at the Kloof mine dump was dealt with as follows:

- when inserting the soil gas probe into the ground, the soil surrounding the probe was firmed to prevent any atmospheric radon as well as air on the mine dump from diffusing into the sampling point in the ground, and
- after each RAD7 30 minutes run at every depth the instrument was purged for 10 minutes and then the soil gas probe was hammered slowly further to another depth to begin another process of measurement. The RAD7 is capable of calculating the correct radon gas concentrations because it has the ability to distinguish the new radon at window A (^{218}Po) from the old radon at window C (^{214}Po) based on their different decay rates, see Figure 3.4.

After RAD7 measurements at every spot, a soil sample was dug out from a depth of 30 cm and 50 cm, weighed and packed in plastic bags to be transported to the laboratory for further analysis using the HPGe γ-ray detector to determine the radium (^{226}Ra) activity concentration present in the tailings at the mine dump. The procedure of determining the activity concentrations of a sample is given in subsection 4.4.2.

Radon gas concentrations in soil air have been measured to depths exceeding 1 m, for instance Bigu (1984) and Schubert (2002) have measured radon gas concentrations at depths up to 2 m and 5.7 m respectively. Yakovleva (2005) demonstrated that with only two measurements of the soil radon gas concentration at 0.35 m and at 0.70 m from the ground/air interface, one is able to determine a number of radon transport characteristics. A depth of about 1 m has proved to be most favoured for measurement [Durrani & Ilić, 1997].

3.4 Radon transport modelling

3.4.1 Introduction

The underlying processes involved in radon transport have necessitated several authors to investigate them not only by carrying out in-situ measurements but also by developing numerical models which are validated by laboratory experiments. For instance;

Loureiro (1987; 1990) developed a theoretical model to simulate (1) the generation and decay of radon within the soil; (2) its transport throughout the soil due to diffusion and convection induced by the pressure disturbance applied at a crack in the basement; (3) its entrance into the house through the crack; and (4) the resultant indoor radon concentration. Then two 3D finite difference programs called PRESSU and MASTRA were used to solve the equations of the models. PRESSU was used to calculate the pressure distribution within the soil as a result of the applied disturbance pressure at the crack; and the resultant velocity distribution of the soil gas throughout the soil matrix. MASTRA was used to solve the radon mass-transport equation, and to calculate the concentration distribution of radon in the soil gas within the whole soil.

Owczarski (1990) used the Rn3D model to estimate radon concentration profiles in soils beneath a two-dimensional slab-on-grade dwelling subjected to wind pressures. The findings from that study indicated that gravel showed significant changes in sub-slab concentrations as a result of wind pressures when you compare to other types of soil such as sand, silt, loam and clay.

The Rn3D model was developed by Holford (1994) to simulate gas flow and radon transport in variably saturated, non-isothermal porous media. The model can be applied in solving problems concerning radon transport in soil. The model can simulate both

steady-state or transient flow and transport in one-, two- or three-dimensions. The porous materials may be heterogeneous and anisotropic.

Kohl (1994) extended an existing coupled 3D transient model called FRACTure to model radon transport processes by simulating steady state pressure and radon concentration fields in the ground surrounding a cylindrical building. According to the author results obtained from numerical and analytic calculations showed an excellent agreement for a simple geometry.

Van der Spoel (1997; 1998; 1999) validated a numerical model for radon transport in soil measurements using a radon vessel at the Kernfysisch Versneller Institute in Groningen, The Netherlands. The study involved studying the diffusive and advective radon transport. According to the author calculations between the model developed and the experimental results showed a good correspondence with maximum deviations of less than 10%.

Andersen (2000) developed a numerical model known as RnMod3d. The model was for soil-gas and radon transport in porous media. It was used to study radon entry from soil into houses in response to indoor-outdoor pressure differences or changes in atmospheric pressure. In addition, it was also used for flux calculations of radon from the soil surface or to model radon exhalation from building materials such as concrete.

Schubert (2002) used a designed Gas Migration Simulator (GAMS) which was installed on an outdoor site and placed into the ground. The GAMS was filled with a homogenous mixture of quartz sand and uranium tailings. With probes installed at depths of 0, 5, 30, 70, 140, and 200 cm radon concentration was measured. Moreover, physical parameters such as the wind speed, the atmospheric pressure and the air temperature were also recorded using a mobile weather station.

It is clear that the models that have been proposed and used were geared towards solving the radon transport equation especially for radon predictions in houses. These models can be distinguished by the approach they use and the assumptions they make to solve the radon transport equation. The finite difference and the finite element approaches are the ones which are commonly utilised.

In this study Comsol Multiphysics software [Comsol, 2008] was applied in the modelling of radon migration in the mine dump soil to the ground/air interface. Details of the modelling process are given in the next subsection.

3.4.2 Radon transport modelling using Comsol Multiphysics

Comsol Multiphysics software [Comsol, 2008] is available commercially and it is commonly used for solving systems of time dependent or stationary second order partial differential equations in one, two, and three dimensions. The software has predefined application modes which act like templates which make it easier to model a large number of processes that we encounter for instance the transport phenomena. A single physics model can be extended to a Multiphysics model, hence solve the coupled physics phenomena simultaneously.

In the subsequent discussion strategies used to model in Comsol Multiphysics will be analysed, with great emphasis on radon gas diffusing through the mine dump soil which is regarded as being porous. Note that when modelling sometimes it is difficult to duplicate exactly the state of the porous material, however, results that are obtained will provide

- an understanding on the transport processes (diffusion and advection) of radon gas through the mine dump soil, and
- an understanding on how variations in parameters (pressure, moisture content etc) can affect the transport processes through soil.

Modelling successfully in Comsol Multiphysics requires the following steps:

Step 1: Modelling using the graphical user interface

Starting Comsol Multiphysics leads to the Model Navigator shown in Figure 3.11 which gives an option to select (1) the space dimension either 1D or 2D or 3D of the problem, (2) the application mode whether it is Comsol Multiphysics, AC/DC module, Acoustics module, Chemical Engineering module, Earth Science module, Heat Transfer module, MEMS module, RF module or Structural Mechanics module, (3) the name of the dependent variable(s), and (4) the type of the finite element to be used. The Multiphysics

button shown on the Model Navigator gives access to the more advanced features of Comsol Multiphysics.

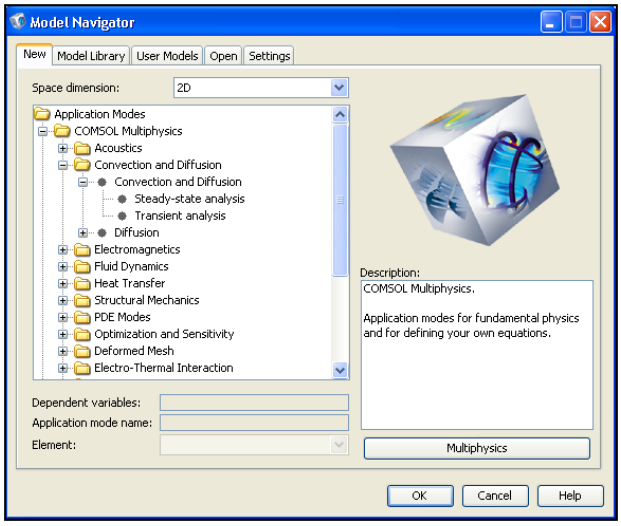

Figure 3.11: Comsol Multiphysics Model Navigator.

(i) Define your problem

The process of solving the problem at hand involves selecting the appropriate application mode which describes the phenomena or parts of the phenomena that is being investigated. Alternatively, if the phenomena can not be found in the list of ready-to-use applications, the system of equations used to solve the phenomena can be specified from the beginning in the PDE modes.

In this work, the ready-to-use Convection and Diffusion application mode of Comsol Multiphysics in combination with the Earth Science module were applied to simulate radon gas transport in the mine dump soil. After selecting and accepting the Convection and Diffusion application mode, a graphical window appeared where the domain was constructed, see Figure 3.12. The graphical window has the main menu which contains the steps to be followed when solving the problem. Below the main menu there are buttons which provide shortcuts to most important submenu items.

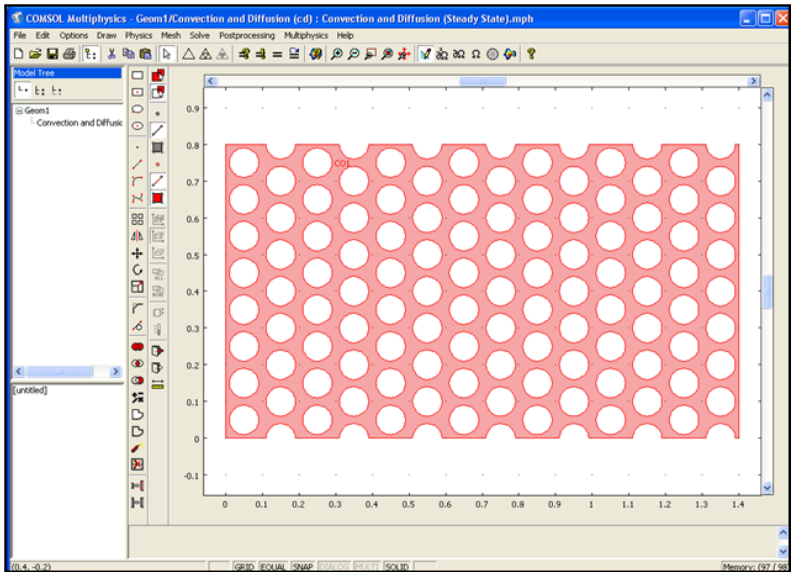

Figure 3.12: The graphical window for constructing the geometry of the problem.

The area where the domain is constructed is defined by the **Axes/Grid settings** found in the **Options** menu. The **Axes/Grid settings** dialog box enables for the x, y and z limits to be defined as well as the x, y and z spacing. The constants and their typical values that were required for radon gas transport modelling were defined in the **Constants** dialog box shown on the left of Figure 3.13 and given in Table 3.6. The constants include radon's generation rate, maximum radon concentration, effective diffusion coefficient, diffusion length, radon diffusivity in open air, density of water, porosity, radium activity concentration, emanation coefficient, dry bulk density, soil water content (%), initial concentration, decay constant and mass transfer.

Note that the values of some constants were determined either in the laboratory using the HPGe γ-ray detector system or in-situ using the MEDUSA γ-ray detector system. For example the diffusion coefficient was extracted from the in-situ measurements which were performed using the MEDUSA γ-ray detector system, while the bulk density of the mine dump soil, the radium content and emanation coefficient were determined in the laboratory. Details of determining these constants are given in Chapter 5.

Table 3.6: The parameters and values used in the simulation.

Parameter	Symbol	Value
Emanation coefficient	E	0.28
Dry bulk density	ρ_b	1530 ($kg{\cdot}m^{-3}$)
Specific density	ρ_s	2476 ($kg{\cdot}m^{-3}$)
Radium activity concentration	C_{Ra}	308 ($Bq\ kg^{-1}$)
Porosity	ε	0.38
Soil water content	M	17.6 (%)
Radon decay constant	λ_{Rn}	2.1×10^{-6} (s^{-1})
Maximum radon concentration	C_0	4.2×10^{5} ($Bq{\cdot}m^{-3}$)
Density of water	ρ_w	1000 ($kg{\cdot}m^{-3}$)
Radon diffusivity in open air	D_o	1.1×10^{-5} $m^2{\cdot}s^{-1}$
Water saturation in soil	S	0.71
Effective diffusion coefficient	D_e	3.5×10^{-7} $m^2{\cdot}s^{-1}$
Diffusion length (pure diffusion)	ℓ_D	0.4 m
Diffusion length (pure advection)	ℓ_A	0.48 m
Diffusion length (diffusion+advection)	ℓ_{DA}	0.74 m

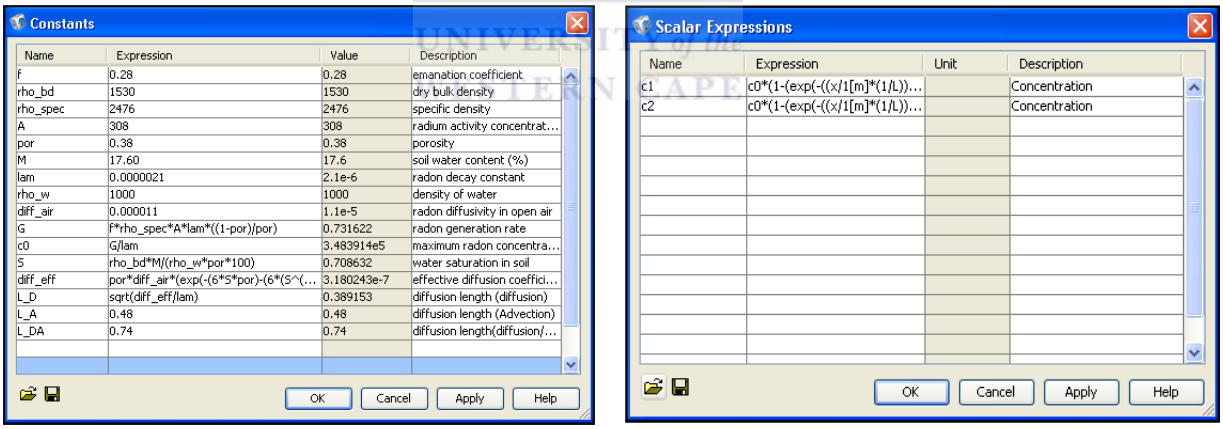

Figure 3.13: (Left) The Constants dialog box for defining the constants. (Right) The Scalar Expressions dialog box for defining the expressions used in solving the problem.

In a similar way, the expressions utilised to predict the radon gas concentration in the domain were specified in the **Scalar Expressions** dialog box which is accessed via the **Options** menu. Therefore, the expressions shown on the right side of Figure 3.13 correspond to equations (3.9), (3.11) and (3.14) which were discussed earlier in

section 3.2. The expressions reflect the pure diffusion, the pure advection model and the diffusion-advection model respectively.

After constructing the domain of the problem and specifying the constants and expressions to be used in the domain, the next step requires that the necessary Physics conditions be set to solve the problem.

Step 2: The Physics conditions

The 2D conceptual sketch illustrated by Figure 3.14 shows how the problem of determining the radon gas concentration in soil air at various depths was tackled. Radon gas is transported from deep down in the mine dump; in this case assume that it is from boundary 3 via the path indicated in pink until it ends up being released to the atmosphere which is above boundary 1. Note that the z-axis is chosen in the opposite direction compared to section 3.2 to conform to the software conventions. When the domain was constructed many boundaries were created, for instance the white circles representing the soil grains were constructed using boundaries, however, in solving this problem the Physics conditions were applied to boundary 1 and boundary 3 only. The conditions that were applied are as follows

- At boundary 1 ($z = L$), the disturbance pressure is 0 Pa and the radon concentration is set to 0. All pressures are given relative to the atmospheric pressure.
- At boundary 3 ($z = 0$), the disturbance pressure is $\Delta p\,(100\text{Pa})$ and the radon concentration is C_0 = 450 kBq·m^{-3}. C_0 is the initial radon concentration and it is already defined as a constant, see Figure 3.13 and Table 3.6.
- Boundaries 2 and 4 were closed for radon transport.

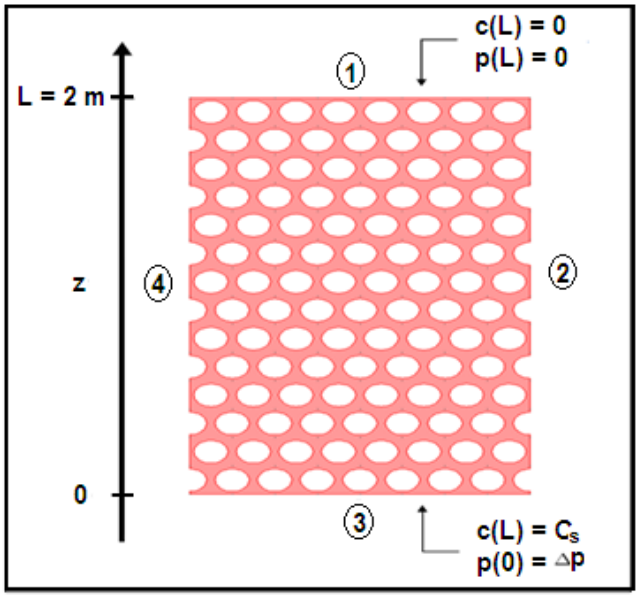

Figure 3.14: A sketch showing the boundaries and the conditions applied at the boundaries. Boundary 1 corresponds to the surface and 3 is deep down in the mine dump.

It is possible to input the subdomain and boundary conditions when modelling using this Convection and Diffusion application mode. This application mode simulates radon transport by convection and diffusion in the subdomain as given by

$$\nabla \cdot (-D\nabla c) = R - v \cdot \nabla c \qquad (3.16)$$

where, D is the effective diffusion coefficient ($m^2 \cdot s^{-1}$), c is the concentration ($mol \cdot m^{-3}$), R is the reaction rate ($mol \cdot m^{-3} \cdot s^{-1}$) and v is the velocity field. This equation essentially corresponds to equation (3.3).

The coefficients (D, c, R and v) of equation (3.16), see also equation (3.1) were specified in the **Subdomain Settings** dialog box shown on the left hand side of Figure 3.15 which pops up when accessed via the **Physics** menu.

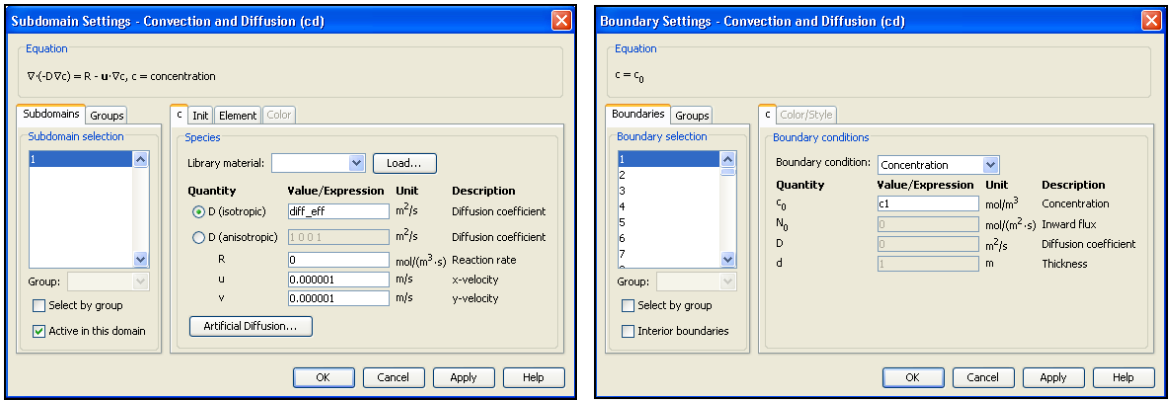

Figure 3.15: The Subdomain Settings dialog box (left) and the Boundary Settings dialog box (right) for entering the coefficients of convection and diffusion equation.

The convection and diffusion application mode supports artificial diffusion using isotropic diffusion, streamline diffusion and crosswind diffusion when any instability is encountered. Artificial diffusion eliminates any instability in the model without the need of refining the mesh; however, the final result obtained is altered. In this work artificial diffusion was not used. More details on the types of artificial diffusion are given in Comsol Multiphysics User's Guide [Comsol, 2008].

The boundary conditions that are available while simulating using the Convection and Diffusion application mode include: Concentration, Flux, Convective flux, thin boundary layer, Continuity, Flux discontinuity and Axis symmetry. The description concerning each boundary condition is summarised and given in Figure 3.16. The boundary conditions were specified in the **Boundary Settings** dialog box shown on the right hand side of Figure 3.15 which is found under the **Physics** menu. The domain is enclosed within the boundaries, therefore the correct boundary is identified first and then the boundary condition is set. For radon gas transport simulation the thin boundary layer, continuity and flux discontinuity boundary conditions were not relevant for this problem. So depending on the problem being solved and the geometry, some of the boundary conditions are not used at all.

Boundary Condition	Description
Concentration $c = c_0$	c_0 is a user-specified concentration
Flux $-n\cdot(-D\nabla c + cu) = N_0$	This boundary corresponds to total mass flux in or out of the domain depending on the user-specified flux expression.
Insulation/Symmetry $n\cdot(-D\nabla c + cu) = 0$	It describes the symmetry about an axis while the total mass flux across the boundary is zero.
Convective flux $n\cdot(-D\nabla c) = 0$	It assumes that mass is transported out of the domain by convection only, while the diffusive mass flux is zero across the boundary.
Thin boundary layer $n_1\cdot(-D\nabla c + cu)_1 = \frac{D}{d}(c_1 - c_2)$ $n_2\cdot(-D\nabla c + cu)_2 = \frac{D}{d}(c_2 - c_1)$	The thin boundary layer condition is used to model a thin layer of a material with a small diffusion coefficient compared to the adjacent domains. The layer has the thickness (d) and the diffusion coefficient (D)
Continuity $n\cdot(N_1 - N_2) = 0$	This boundary condition ensures that the total mass flux across two adjacent domains is constant.
Flux discontinuity $-n\cdot(N_1 - N_2) = N_0$	Represents a discontinuity in the mass flux across a border between parts in an assembly.
Axial symmetry $n\cdot(-D\nabla c + cu) = 0$	This boundary condition is identical to the insulation/symmetry condition. It is used for axisymmetric models using cylindrical coordinate systems.

Figure 3.16: Description of each boundary condition [Comsol, 2008].

In addition to the Convection and Diffusion application mode, the Earth Science module was applied to determine the velocity of radon gas through the domain. It was assumed that:

- the flow of radon gas to the ground/air interface is of the Darcy type
- the soil has a uniform temperature (natural convection in the soil is ignored)
- the pressure variations are small in comparison with the absolute pressure
- the fluid is incompressible.

The Earth Science Module's Darcy's Law application mode describes fluid flow through interstices in a porous medium by gradients in pressure and elevation potential.

The flow velocities in porous media are usually very low because the fluid loses substantial energy to frictional resistance within pores.

This module handles both time-dependent and stationary problems for 1D, 2D and 3D systems with axial symmetry for 1D and 2D. The fluid flow, heat transfer and solute transport are the main categories covered in physics. The fluid flow group of application modes estimates the pressure and velocity of fluids flowing within the interstices of the

porous medium. Fluid flow is described by either the Navier-Stokes equations or the Brinkman equations or the Darcy law. The heat transfer group of application modes estimates the temperature distribution in solids, fluids, and fluid-solid systems. Solute transport application modes characterise the fate and transport of individual or multiple and interacting chemical species for systems containing fluids. According to Darcy's law the governing equation is

$$v = -\frac{\kappa}{\eta}(\nabla P + \rho_f g \nabla D) \qquad (3.17)$$

In this equation, v is the Darcy velocity or specific discharge vector ($m \cdot s^{-1}$); κ is the permeability of the porous medium (m^2); η is the fluid's dynamic viscosity ($Pa \cdot s$); P is the fluid's pressure (Pa) and ρ_f is its density ($kg \cdot m^{-3}$); g is the gravitational acceleration ($m \cdot s^{-2}$); and ∇D is a unit vector in the direction over which g acts.

The permeability represents the resistance to flow over a representative volume consisting of many solid grains and pores. The constants in equation (3.17) were specified in the **Subdomain Settings** dialog box depicted on the left hand side of Figure 3.17. Those constants are utilised in the domain during fluid flow to determine the velocity of the flow.

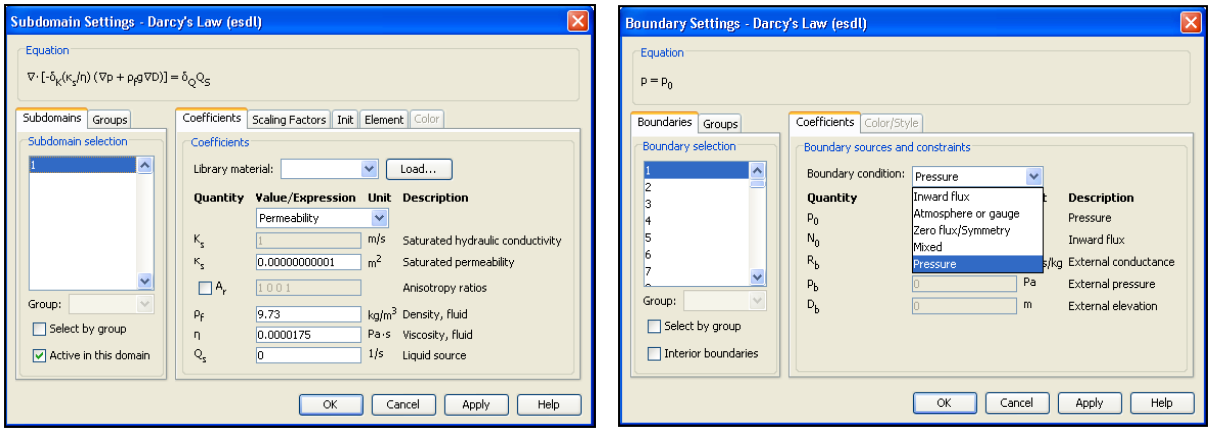

Figure 3.17: The Subdomain Settings dialog box (left) and the Boundary Settings dialog box (right) for entering the coefficients of the Darcy's law.

The Darcy's law application mode of the Earth Science module provides a number of boundary conditions which are needed to reach a solution to the problem being solved.

This requires initial conditions for transient or time- dependent problems. On the right hand side of Figure 3.17 a boundary condition is only ascribed after a boundary has been selected. Only relevant boundaries are ascribed boundary conditions and the description of the boundary conditions is given in Figure 3.18.

Boundary Condition	Description
Pressure $p = p_0$	p_0 is a user-specified pressure
Atmosphere or gauge $p = 0$	At a free surface, such as soil surface or surface of a lake, so the boundary condition for such a surface can be set to atmosphere or gauge
Inward flux $n \cdot \frac{K}{\eta}(\nabla p + \rho_f g \nabla D) = N_0$	This boundary condition corresponds to flow in or out of the domain. N_0 is an expression for the specified flux
Zero flux/Symmetry $n \cdot \frac{K}{\eta}(\nabla p + \rho_f g \nabla D) = 0$	Neumann condition, while the fluid flow is zero across the boundary, it still moves along it. This way the equation for the zero flux condition also describes symmetry about an axis.
Mixed $N = N_0 \quad R = R_b \quad p = p_b \quad D = D_b$ $n \cdot \frac{K}{\eta}(\nabla p + \rho_f g \nabla D) = N_0 + R_b (p_b - p + \rho_f g(D_b - D))$	Mixed boundary condition expression is used when the domain is connected to a larger body of liquid through a semi-pervious layer. p_b is external pressure, R_b is external conductance, D_b is external elevation and N_0 is inward flux.

Figure 3.18: Description of each boundary condition for pressure [Comsol, 2008].

Step 3: Meshing the problem domain

The geometric model shown in Figure 3.14 was meshed after specifying all the required constants in the subdomain and the boundary conditions. The domain was divided into small units of simple shapes as illustrated in Figure 3.19.

In Comsol Multiphysics mesh generation was achieved by selecting and clicking on **Initialize Mesh** which is accessed through the **Mesh** menu. The mesh generator also known as the free mesher is available in all space dimensions and it can be used to create free meshes for all types of geometry objects.

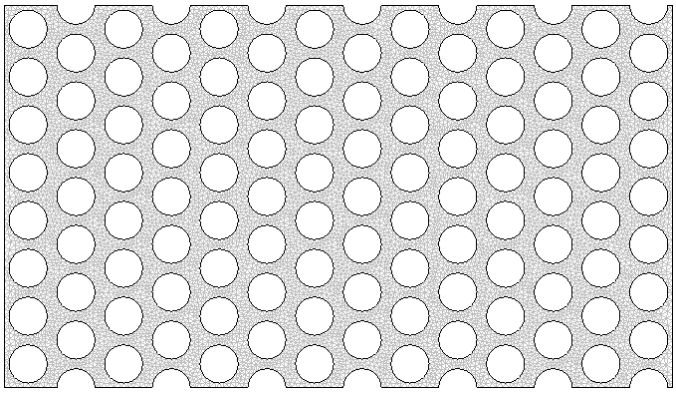

Figure 3.19: The meshed domain.

In 1D geometry, the mesh generator divides the subdomain intervals into smaller intervals (or mesh elements).

For a 2D geometry, the mesh generator divides the subdomain into triangular or quadrilateral mesh elements. The sides of the triangles or quadrilaterals elements created are called mesh edges and their corners are the mesh vertices. The elements created only represent an estimate of the original geometry, if the boundary is curved. Unlike a free mesh, a mapped mesh is structured in its pattern. A mapped quadrilateral mesh on a geometry is possible if the subdomain of the geometry are fairly regular in shape and do not contain holes.

In 3D the mesh generator divides the subdomain into tetrahedral, hexahedral, or prism mesh elements. The boundaries in the geometry are divided into triangular or quadrilateral boundary elements. A free mesh containing tetrahedral elements or a swept mesh containing prism elements or hexahedral elements can be created. A swept mesh is structured in the sweep direction and can be either structured or unstructured orthogonally to the sweep direction. Also, a 3D mesh can be created by extruding or revolving a 2D mesh. An extruded or revolved mesh is structured in the direction of the extrusion or revolution.

Note that with the assumptions used in this work the problem reduces to 1D.

Step 4: Solving the model

The next process after meshing the model depicted in Figure 3.19 was to solve the model. Comsol Multiphysics provides a variety of solvers for PDE based problems. The solver

types are given in Figure 3.20. The application modes in Comsol Multiphysics give possible analysis types such as stationary, eigenfrequency, transient, time-dependent, and parametric, to be used depending on the problem being solved.

In most cases the analysis type selects an appropriate solver; consequently it is not necessary to select the solver yourself. However, if you want to select the solver then you must know whether the problem at hand is stationary or time-dependent. The solver type can be specified in the **Solver Parameters** dialog box (Figure 3.21) which is accessed via the **Solve** menu.

Solver Type	Usage
Stationary	For linear or nonlinear stationary PDE problems
Time-dependent	For linear or nonlinear time-dependent PDE problems
Eigenvalue	For eigenvalue PDE problems
Parametric	For linear or nonlinear parameterized sets of stationary PDE problems
Stationary-segregated	For linear or nonlinear stationary Multiphysics PDE problems
Parametric segregated	For linear or nonlinear parameterized sets of stationary Multiphysics PDE problems
Adaptive	For linear or nonlinear stationary or eigenvalue PDE problems using adaptive mesh refinement

Figure 3.20: The description of the solver types.

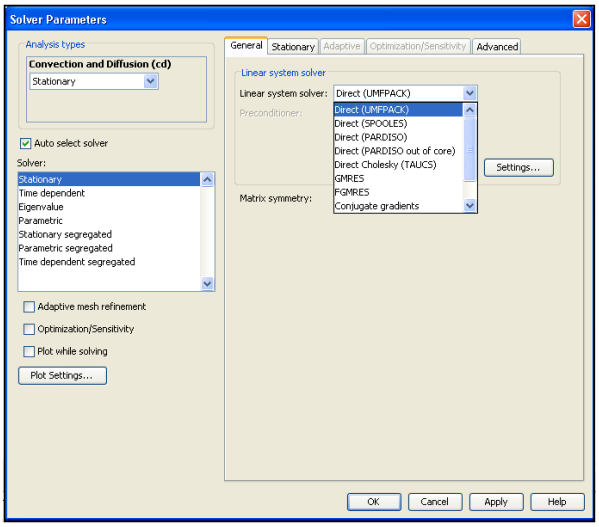

Figure 3.21: Solver parameters dialog box for specifying the solver.

Comsol Multiphysics can model both linear and nonlinear problems. Usually Comsol Multiphysics detects whether a model is linear or nonlinear automatically and after that an appropriate solver is selected. Figure 3.22 illustrates solvers and their usage that are available for the linear system. The solvers are categorised into two groups namely; direct solvers and iterative solvers.

Linear System Solver	Usage
Direct Solvers	
UMFPACK	Unsymmetric Multi Frontal Method. A direct solver for non symmetric systems
SPOOLES	Sparse Object Oriented Linear Equations Solver. A solver symmetric and non symmetric systems. It uses less memory than UMFPACK
PARDISO	Parallel sparse Direct linear Solver. A solver for symmetric and non symmetric systems. It uses less memory than UMFPACK.
TAUCS Cholesky	TAUCS is a C library of solvers for sparse linear algebra. It is a solver for symmetric, positive-definite systems.
Iterative Solvers	
GMRES	Generalized Minimum Residual Solver. It is used for non symmetric problems
FGMRES	Flexible Generalized Minimum Residual Solver. It is used for non symmetric problems. It can handle more general preconditioners. It uses more memory than GMRES
Conjugate gradients	A solver for symmetric positive definite problems
Geometric Multigrid	A solver for elliptic or parabolic problems

Figure 3.22: Direct and Iterative Linear system solvers [Comsol, 2008].

Step 5: Post processing and visualisation

To analyse results obtained from the solvers, Comsol Multiphysics provides many tools for post processing and visualisation including advanced graphics, data display and export functions, and a report generator. These tools can be accessed through the **Postprocessing** menu. For instance under the **Postprocessing** menu when the **Plot Parameters** is select and clicked, the dialog box displayed in Figure 3.23 appears.

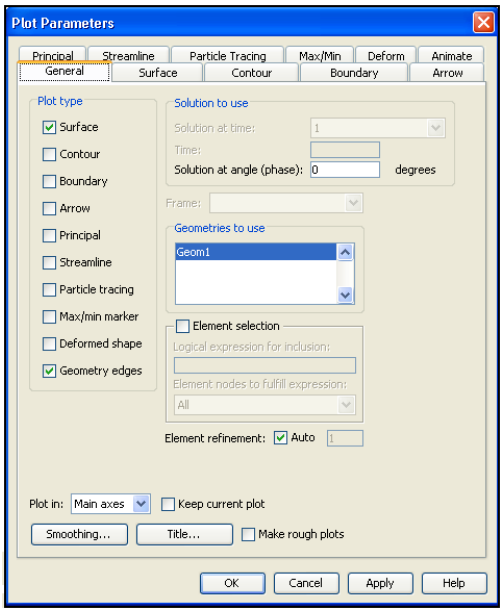

Figure 3.23: The Plot parameters dialog box for post processing and visualisation.

The **Cross-Section Plot Parameters** and the **Global variables Plot** which are available from the **Postprocessing** menu provide another option for analysing the results from the solvers. Cross-section plots can interpolate within a domain to extract mesh-independent plots, and the software can also extend these plots in time or along parametric solutions.

Note that the function values of the solution are not accessible via dialog boxes. Instead, one has to rely on the solution plot.

3.4.3 Radon gas concentrations obtained using Comsol Multiphysics

It was possible to calculate the radon concentration in the soil air at any given depth using equations (3.9), (3.11) and (3.14) for the diffusion, advection and for diffusion-advection models respectively. In this work the decay process of radon was not considered when radon is migrating. In order to model the transport process involving diffusion only the velocity of radon flow through the domain was set to zero and when the dominant process was through advection the diffusion coefficient of radon was set to zero. The velocity of radon flow was simulated using the Earth Science module which has the Darcy's flow application mode. A pressure of 100 Pa was used on the domain which resulted in a velocity of $1\times10^{-6}\,\mathrm{m\cdot s^{-1}}$. Figure 3.24 illustrates the curves obtained from the

depth profile of the radon concentrations, while Figure 3.25 shows the colour profile of the concentrations and the direction of flow of radon gas.

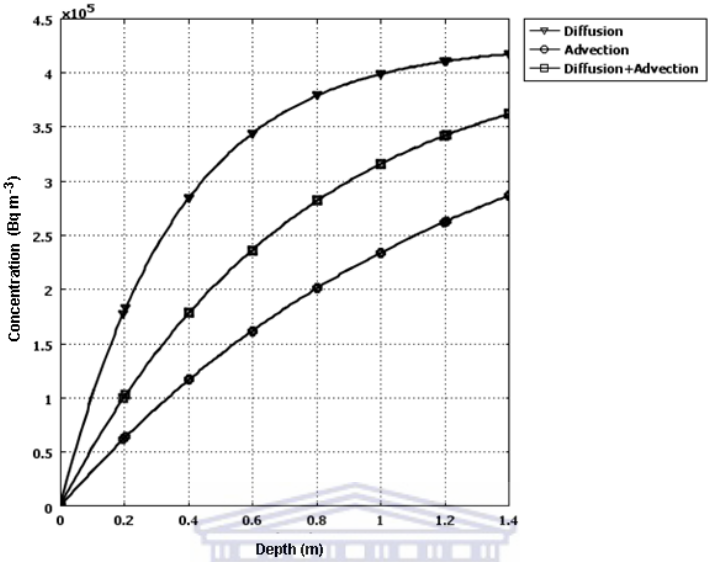

Figure 3.24: The graphs show radon soil gas concentrations calculated for various depths using Comsol Multiphysics software.

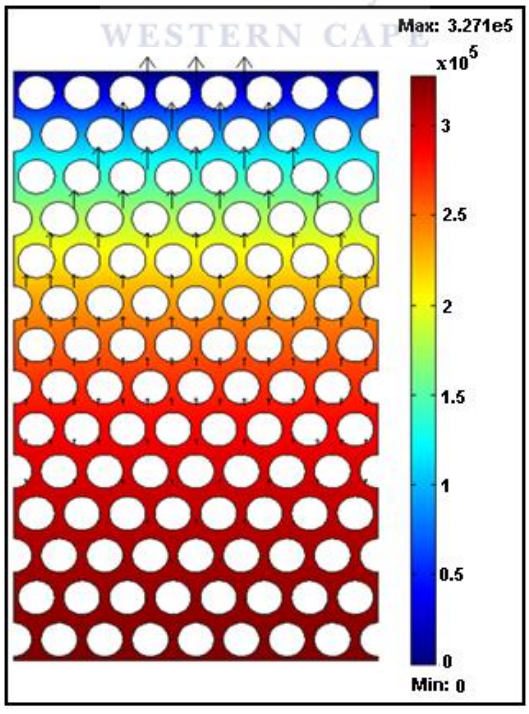

Figure 3.25: Radon gas concentration profile in the soil air.

3.5 Comparison of radon gas concentrations obtained using RAD7 and Comsol Multiphysics

Expressions such as equations (3.9), (3.11) and (3.14) were developed so that they can be used to predict the concentration levels of radon in the soil air. In reality when the results of the models are compared to the actual measurements carried out in the field, some differences are noticed. From Figure 3.26 the levels of radon concentration in the soil air for less than 30 cm that is closer to the ground/air interface measured using the RAD7 are much lower than the simulated concentrations using Comsol Multiphysics. The differences could be attributed to the different diffusion lengths. In the field at shallower depths closer to the ground/air interface radon is more permeable meaning that it can possibly migrate a large distance because moisture is reduced as opposed to deep depths where higher moisture reduce radon's permeability. As a result when the RAD7 is used to detect radon at shallower depths it records low levels because a large amount of radon has migrated and released to the atmosphere.

When the levels of radon concentration in the soil air are determined using Comsol Multiphysics it was assumed that the diffusion length is constant both at shallower and deep depths. The results obtained still indicate that the simulated concentrations are higher than the RAD7 measured concentrations even after using different diffusion lengths at the same time when calculating the concentrations. From the graphs of the models it is clear that a very short diffusion length causes a very rapid increase in radon gas in the soil with increasing depth. The differences that are noticed at depths less than 30 cm below the ground/air interface could be due to the differences in the material structures which are being compared. For this case it is difficult to duplicate exactly the soil structure found for the mine dump in a model. Another possibility is that the values at shallow depths may be reduced by some air being sucked down the outside of the soil probe from the atmosphere (see Figure 3.6).

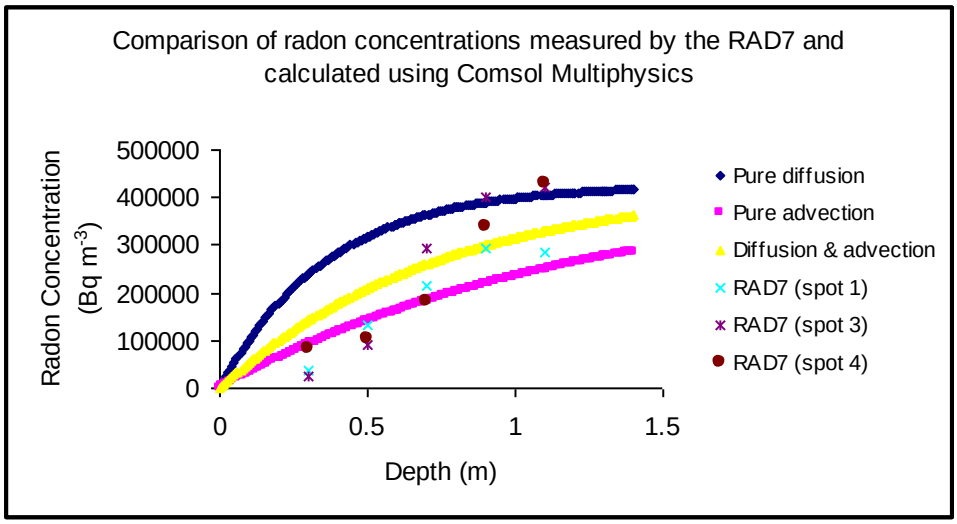

Figure 3.26: A graph showing a comparison between radon concentrations measured by the RAD7 and calculated using Comsol Multiphysics.

3.6 Conclusion

Radon gas concentration in the soil air has been modelled using Comsol Multiphysics and measured in the mine dump using the continuous radon monitor (the RAD7). The range of concentration measured using the RAD7 was between 26 ± 1 and 472 ± 23 kBq·m^{-3}. In other places radon concentrations in the soil air in mill tailings from uranium mining have been reported to be higher. For instance Bigu (1984) measured the mill tailings in a project carried out in Canada and found the concentrations to range from about 670 kBq·m^{-3} at 0.5 m to around 4 MBq·m^{-3} at 5.7 m.

Now that the levels of radon gas concentration in the soil air have been measured and modelled, the next Chapter will discuss the other technique (gamma-ray spectrometry) which was used to quantify the natural primordial radionuclides that are found in the mine dump. The activity concentrations will be estimated from the soil samples that were collected from the spots where radon soil gas measurements were conducted.

Chapter 4

Methodology: Field (MEDUSA) and laboratory (HPGe) measurements

4.1 Introduction

Natural occurring radionuclides are present everywhere, with variable concentrations. Nuclides can be either stable or unstable. The unstable radionuclides decay to stable or unstable products emitting alpha, beta or gamma radiation. Gamma-rays can easily be detected using γ-ray detector systems in the laboratory and in the field.

This chapter focuses on gamma-ray detector systems used for measurements in the laboratory and in the field, set-up of the detector systems and detailed analysis of the spectra acquired to determine the identity and quantity of gamma-ray emitters. Field measurements were conducted using the MEDUSA (**M**ulti-**E**lement **D**etector for **U**nderwater **S**ediment **A**ctivity) γ-ray detector system. The **H**yper **P**ure **Ge**rmanium (HPGe) γ-ray detector system was used for laboratory-based measurements.

The MEDUSA γ-ray detector system detector is discussed in the subsequent section and the HPGe in the later section of this Chapter.

4.2 MEDUSA γ-ray detector system

4.2.1 MEDUSA components

The MEDUSA γ-ray detector system available at the Environmental Radioactivity Laboratory (ERL) of iThemba LABS consists of a cesium iodide doped with sodium (CsI (Na)) detector crystal (15 cm long, 7 cm in diameter) which is encased in aluminium/stainless steel shown in Figure 4.1 as well as the probe, ALADIN (**A**NTARES **L**og **A**cquisition and **D**ata **In**terpretation system) box, the laptop computer and the Global Positioning System (GPS) device. The ALADIN interface box contains a data acquisition system and more details of the ALADIN can be found at www.antares-geo.de. Data accumulation, storage and analysis softwares are installed on the laptop computer. The

Garmin GPS 76 model was used to log-in the detector position (latitude, longitude and altitude).

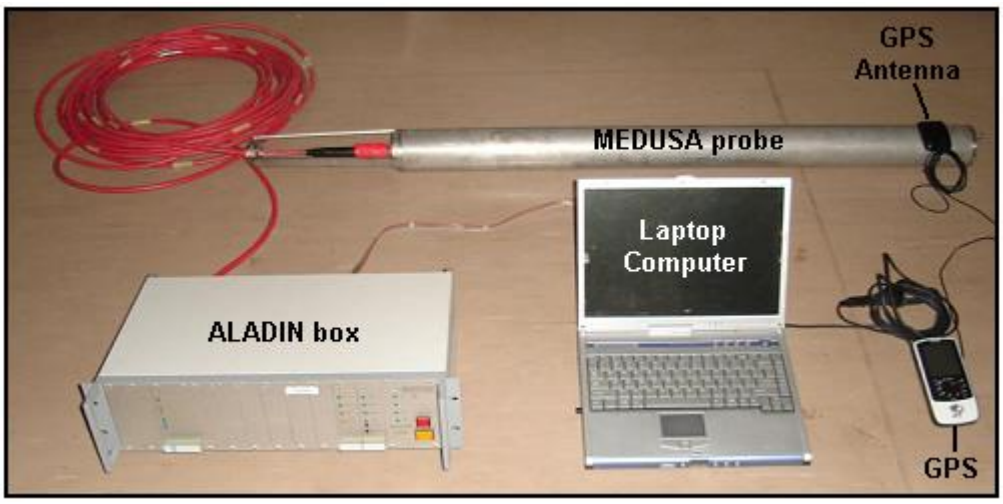

Figure 4.1: Components of the MEDUSA γ-ray detector system.

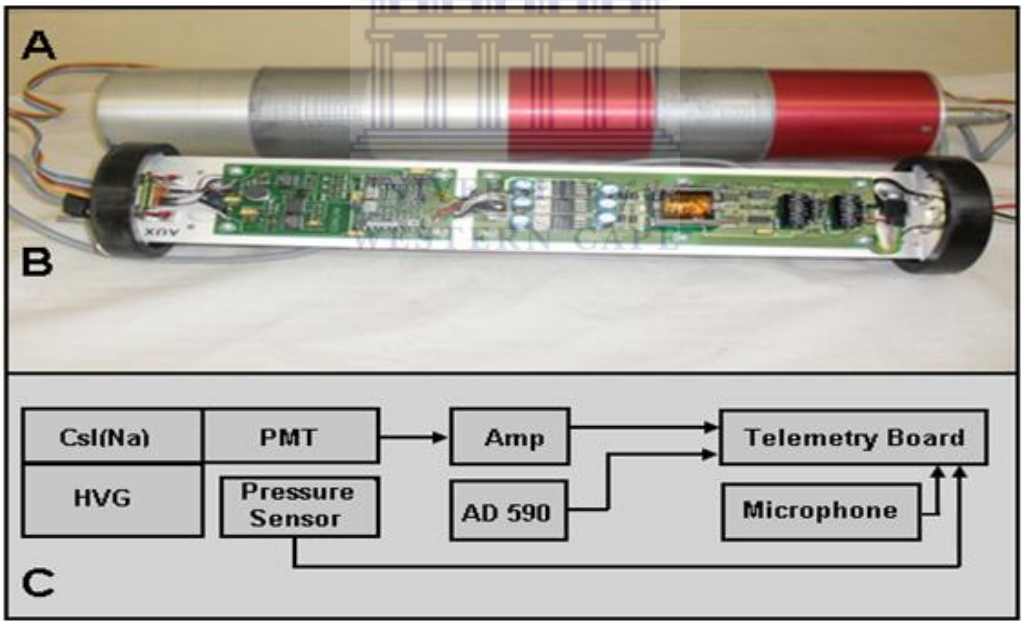

Figure 4.2: (a) MEDUSA (CsI (Na)) detector crystal picture (b) electronics components in the probe and (c) telemetry board showing other components.

The steel probe contains the (CsI (Na)) detector crystal, a photomultiplier tube (PMT), a Cockcroft Walton high-voltage generator (HVG), spectroscopic amplifier (Amp), temperature sensor (AD 590), pressure sensor, microphone and a telemetry board all shown in Figure 4.2 a-c. The output of the amplifier is sent to the telemetry board where

the detector signal, along with signals from a pressure sensor, temperature sensor and microphone, are digitized. The microphone data are used to infer the coarseness of the sediment over which the detector moves during underwater work. The detector unit is connected to an ALADIN interface box *via* an armoured co-axial cable.

4.2.2 MEDUSA field set-up

The MEDUSA γ-ray detector system of the ERL is used for in-situ radiometry. The system was mounted approximately 60 cm off the ground at the front of a 4×4 vehicle as seen in Figure 4.3.

Figure 4.3: The MEDUSA γ-ray detector system mounted on a 4×4 vehicle approximately 60 cm off the ground.

A detailed survey map for estimating surface activity concentrations of γ-ray emitting radionuclides can be achieved using this gamma ray spectrometry. This system has an advantage over portable systems in terms of larger surface coverage for a given time and cost, and over airborne systems for quick mobilization and improved resolution [IAEA, 2003].

MEDUSA field measurements were categorised as either stationary or mobile. The mode of data acquisition determined the category to be ascribed.

Stationary field measurements refer to data acquired while the MEDUSA γ-ray detector system is mounted as illustrated in Figure 4.3 and the vehicle is stationary on the spot for a period of 30-60 minutes. At Kloof mine dump stationary measurements were carried out at five spots on different days. A map (Figure 4.4, see also Figure 3.5) shows the five spots on the mine dump. A ridge across the mine dump divides it into two where one part is elevated compared to the other part. Spot 1 and spot 3 are on the higher part of the ridge and the rest of the spots on the lower part of the ridge. After every stationary field measurement was completed, soil samples were collected for further radiometric analysis using the ERL HPGe γ-ray detector system. Five soil samples were collected in the depth range 0-30 cm for every spot as follows: one soil sample beneath the detector and four peripheral samples (labelled a-d) at a distance of 80 cm from the centre as illustrated by Figure 4.5.

MEDUSA activity concentrations deduced from these stationary measurements will be used in conjunction with corresponding HPGe activity concentrations of samples collected from these spots to work out normalisation factors. Normalisation factors will be discussed in Chapter 5.

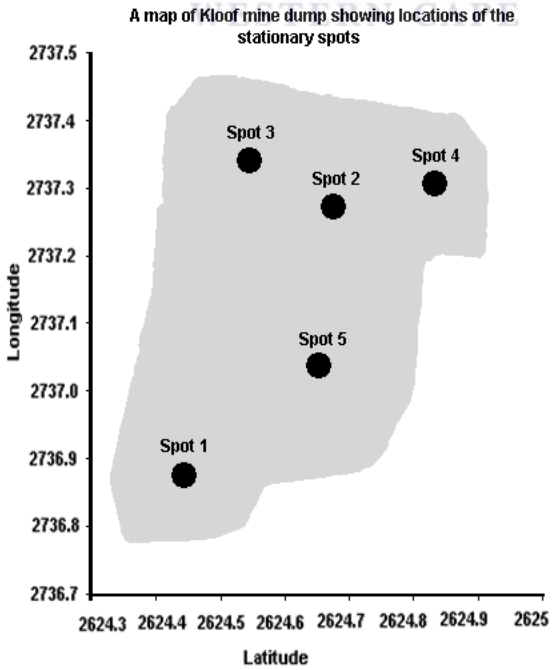

Figure 4.4: A map of Kloof mine dump showing five spots where stationary measurements were performed.

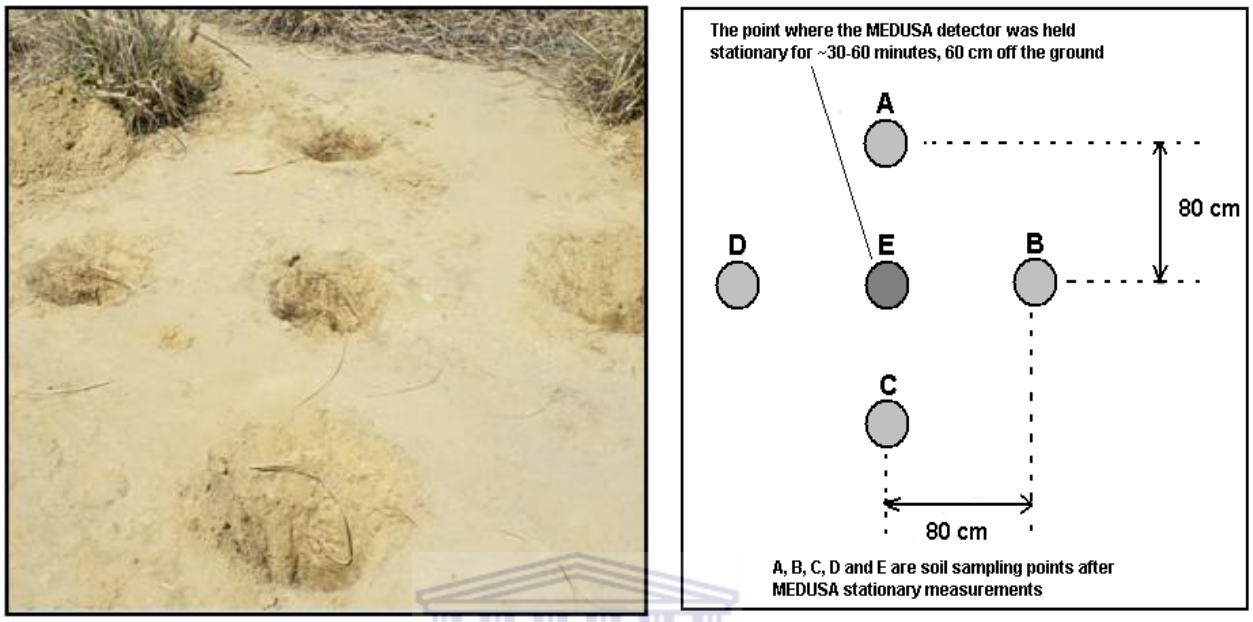

Figure 4.5: A sampling procedure in the field (Left) and a corresponding schematic design (Right) with more details.

Mobile field measurements refer to data acquired with the MEDUSA γ-ray detector system mounted on the 4×4 vehicle as shown in Figure 4.3, while transversing the dump at approximately 2 $m \cdot s^{-1}$. The spectra are recorded every 2 seconds and the MEDUSA γ-ray detector location is logged-in by the GPS for the given data.

MEDUSA stationary and mobile measurement data are analysed to identify and quantify the gamma emitters from the spectra. The next subsection discusses data analysis.

4.2.3 MEDUSA data processing

The procedure for analysing data acquired by the MEDUSA γ-ray detector system involves various software as indicated by the flowchart (Figure 4.6) and described below.

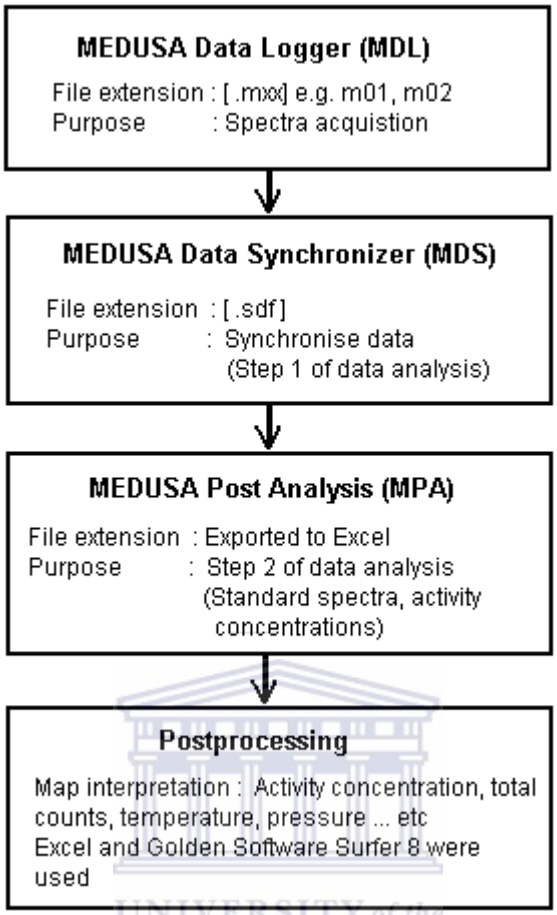

Figure 4.6: A flowchart showing the MEDUSA data analysis process.

MEDUSA Data Logger (MDL) captures and logs-in raw data and saves it in a file with an extension (.mxx) where xx refers to the number of files for instance .mo1, m02 etc. The first step in data analysis involves MEDUSA Data Synchronizer (MDS). As its name suggests the MDS accesses the files from the MDL and synchronizes the data. Data synchronization entails: (1) setting the synchronizer at the spectrum, (2) changing the digits of the latitude, longitude and the altitude to 4, 4 and 2 respectively and (3) setting the latitude, longitude and altitude at "average". Other parameters for instance pressure, sound, temperature total counts etc., are not changed and their action line reads "last known". The synchronizer is pressed to run and after a complete synchronization, data are saved in a new file format with an extension (.sdf). The subsequent analysis entails MEDUSA Post Analysis (MPA) software package owned by MEDUSA Exploration B.V.

in Groningen, the Netherlands. The MPA accesses data from the MDS. Next, extraction of activity concentrations using MPA requires the following:

4.2.3.1 Full Spectrum Analysis (FSA)

The spectra acquired are analysed using the Full Spectrum Analysis (FSA) method. This method uses almost all of the data present in the measured gamma spectrum as opposed to the traditional window methods. FSA applies a Chi-squared fitting algorithm to fit a set of "Standard Spectra" (see Figure 4.7) to the measured spectrum and a measured background spectrum [De Meijer, 1998; Hendriks, 2001]. The standard spectra refers to the response per unit time of a detector for a given geometry to the γ-rays emitted by a radionuclide with a concentration of one $Bq \cdot kg^{-1}$ [De Meijer, 1998]. A standard spectrum is specific to the uranium series, thorium series and potassium as shown in Figure 4.7.

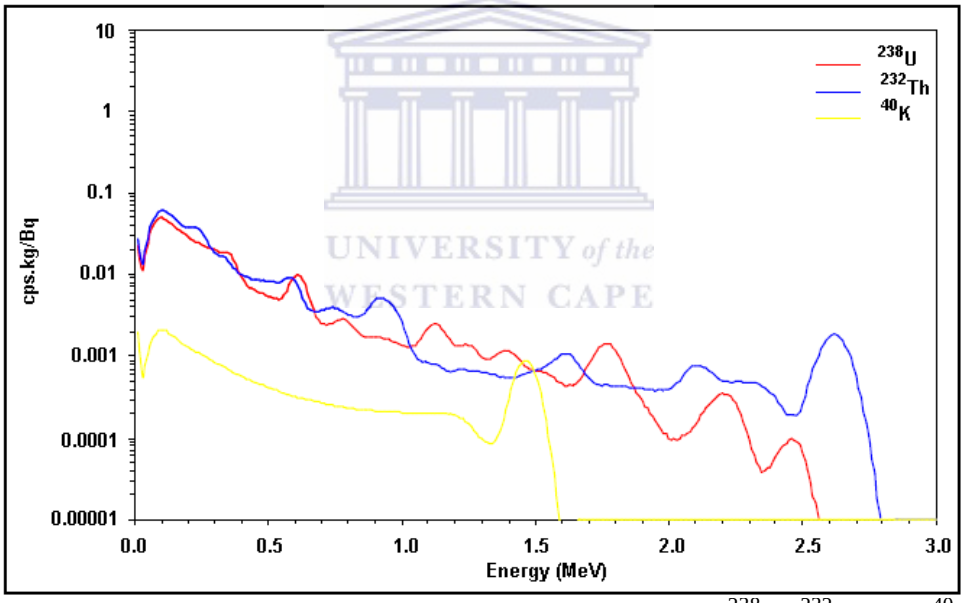

Figure 4.7: An example of a set of standard spectra for ^{238}U, ^{232}Th and ^{40}K [Mlwilo, 2010].

The standard spectra (^{40}K, ^{232}Th series and ^{238}U series) used in this work were obtained from Monte Carlo simulations with the MCNPX code [Hendriks, 2001; Maleka, 2012]. The MCNPX code was used to simulate flat-bed geometry with 30% soil porosity (50% filled with water and other 50% with air). The soil content was assumed to be mainly SiO_2.

In the FSA method, the measured spectrum $S(i)$ is regarded for each channel i, as the sum over all radionuclides of standard spectra $(X_j(i))$ multiplied by the activity concentration C_j plus a background $(Bg(i))$ component [De Meijer, 1998; Hendriks et al., 2001]:

$$S(i) = \sum_{j=1}^{M} C_j X_j(i) + Bg(i) \tag{4.1}$$

The index j sums from 1 to M, representing the number of radionuclides.

If for a certain geometry the standard spectra X_j and the background spectrum are known, a measured spectrum $S(i)$ can be analysed in terms of the standard spectra by optimising the fit to the spectra by finding the best C_j values in minimizing chi-squared (χ^2) procedure, by using the reduced χ_R^2 which is defined as:

$$\chi_R^2 = \frac{1}{N-M} \sum_{i=1}^{N} \frac{1}{\sigma^2(i)} \left[S(i) - \sum_{j=1}^{M} C_j X_j(i) - Bg(i) \right]^2 \tag{4.2}$$

where, N is the number of channels in the spectra and M is the number of standard spectra used (which is 3 in this case) or the number of radionuclides, i is the channel number of the spectrum and $\sigma^2(i)$ is the variance associated with the sample spectrum.

In addition to the standard spectra, a cosmic-ray background spectrum measured using the MEDUSA detector below the water-surface of Theewaterskloof (Twk) dam was used. The dam is located near Villiersdorp about 60 km from iThemba LABS Cape Town. A background spectrum can be defined as a spectrum measured initially without taking into account the radiation originating from the target source except the environment. It consists of the cosmic and internal background radiation from the detector.

The Full Spectrum Analysis method yields data which need to be stabilized as described below.

4.2.3.2 Stabilization process

Data stabilization refers to a process of shifting the energy spectra in such a way that they 'fit' with the standard spectra model. The measured energy spectra tend to shift due to inaccuracy of the Multichannel analyzer (MCA) and crystal, temperature change etc. The stabilization process corrects the position of the gamma peaks. For instance, the ^{40}K peak should be positioned at 1460 keV, the highest ^{232}Th peak should be found at about 2614 keV [Limburg, 2009]. This process is based on the least squares method which computes the lowest possible chi-squared. The stabilization process is said to be fitting when the reduced chi-squared is closest to unity, thereby considered the best. However, it is not always the case that the reduced chi-squared will be unity. Figure 4.8 displays an example of data stabilized with the best reduced chi-squared achieved for this particular analysis being 13.06. The window also shows the stabilization parameters and the activity concentrations of ^{40}K, ^{232}Th and ^{238}U.

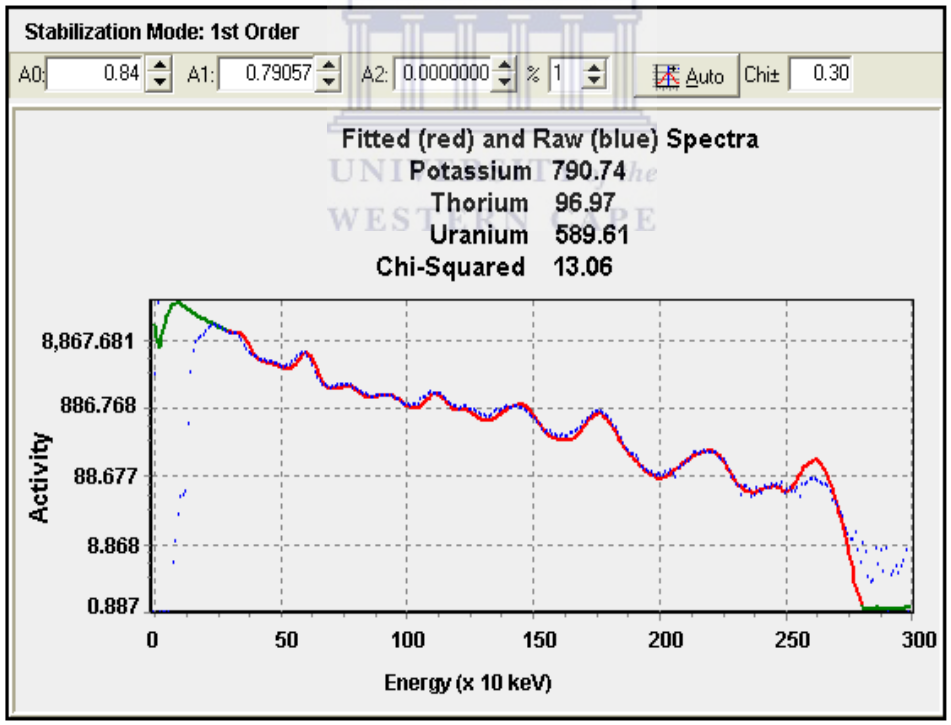

Figure 4.8: An example of stabilized data fit after measured data is fitted with standard spectra.

The parameters of stabilization of this fit are saved and also exported to Microsoft Excel. This constitutes the preliminary analysis. At this stage the detector total counts with their

exact location on the mine dump are extracted. Examples of these maps of the detector total counts are presented in Figure 4.9-4.10. The Maps on the left are produced using MPA software while the maps on the right are interpolated using Golden Software Surfer® 8 which correspond to the maps on the left. Details of the interpolation method are given in Appendix A. The totals counts plotted are for the 4×4 vehicle accessible areas while the grey parts represent the inaccessible areas due to the bushes on the mine dump. The Kloof mine dump was previously surveyed in 2002 using the MEDUSA γ-ray detector system and again in 2010, but this time a smaller surface area was covered.

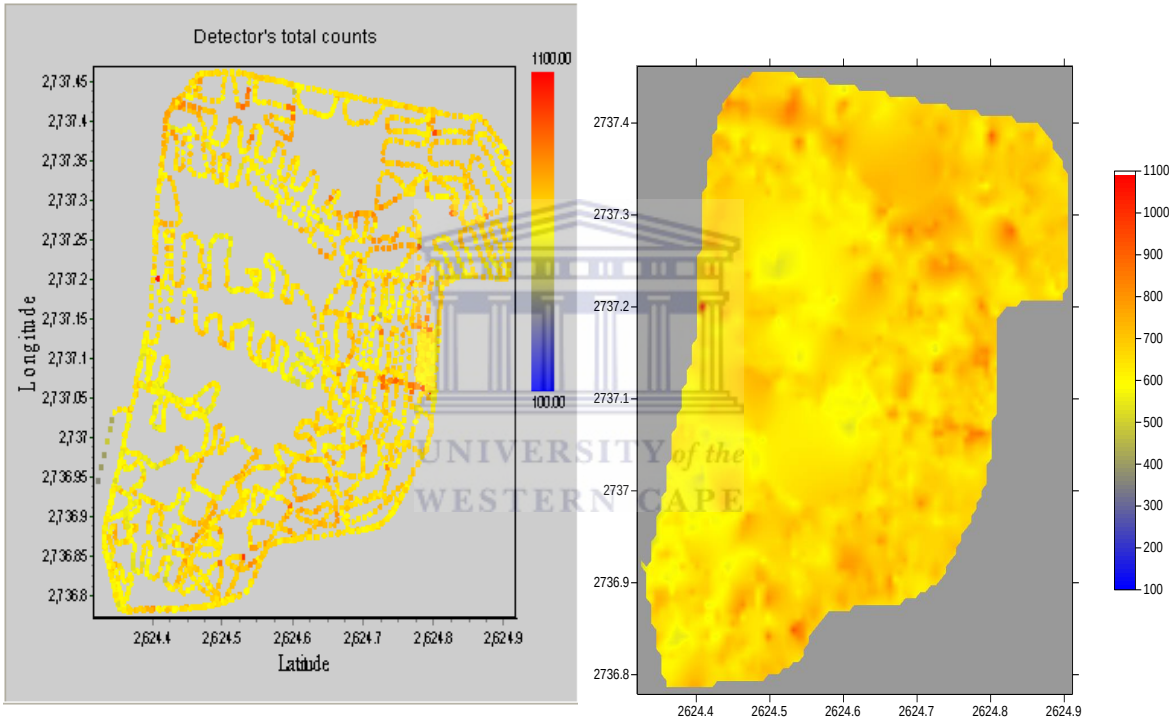

Figure 4.9: A map of the detector's total counts (left) recorded in 2002 survey and an interpolated map (right) of the total counts corresponding to the map on the left.

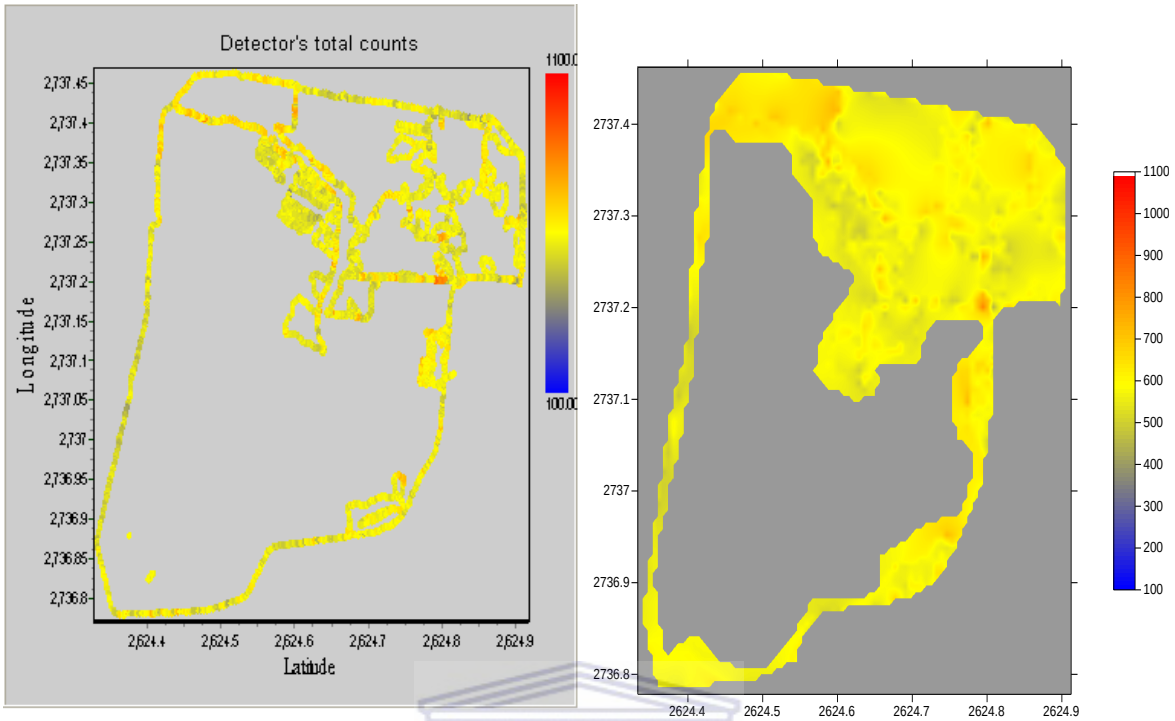

Figure 4.10: A map of the detector's total counts (left) recorded in 2010 survey and an interpolated map (right) of the total counts corresponding to the map on the left.

Next, detailed analysis can be achieved by operations from the "Data analysis" menu of the MPA software. First by selecting the log-files that you want to analyse and proceeding to perform an operation such as "Sum & Analyse" results achieved include: total activity (TC), standard deviation of TC, activity concentration (AC), chi-squared of fit, co-variances, and stabilization parameters. These are in addition to the detector total counts extracted earlier.

Similarly, using MPA and Golden Software Surfer® 8 software, three sets of maps of activity concentrations ($Bq \cdot kg^{-1}$) as estimated in 2002 and 2010 are displayed for individual radionuclides of ^{40}K, ^{232}Th and ^{238}U (see Figures 4.11-4.16). Maps produced by MPA are on the left and the interpolated maps using Golden Software Surfer® 8 corresponding to the maps on the left are on the right.

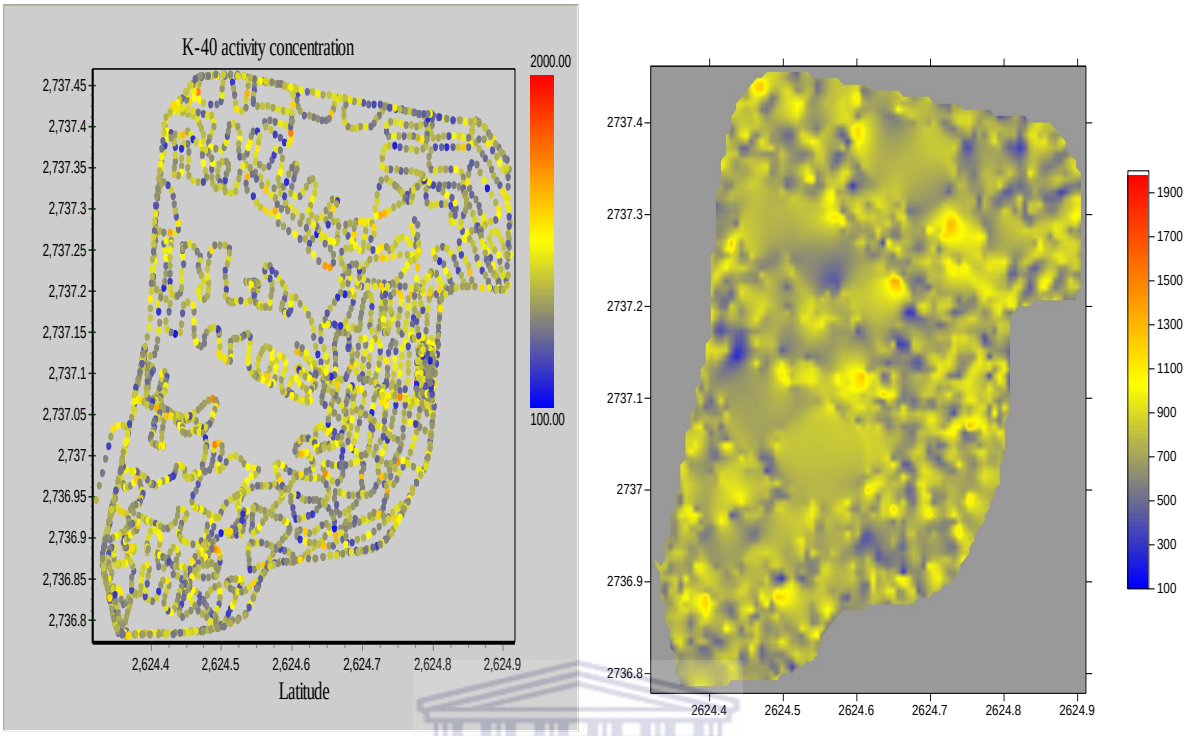

Figure 4.11: A map (left) showing ^{40}K activity concentration measured using the MEDUSA γ-ray detector during 2002 survey and an interpolated map (right) corresponding to the map on the left.

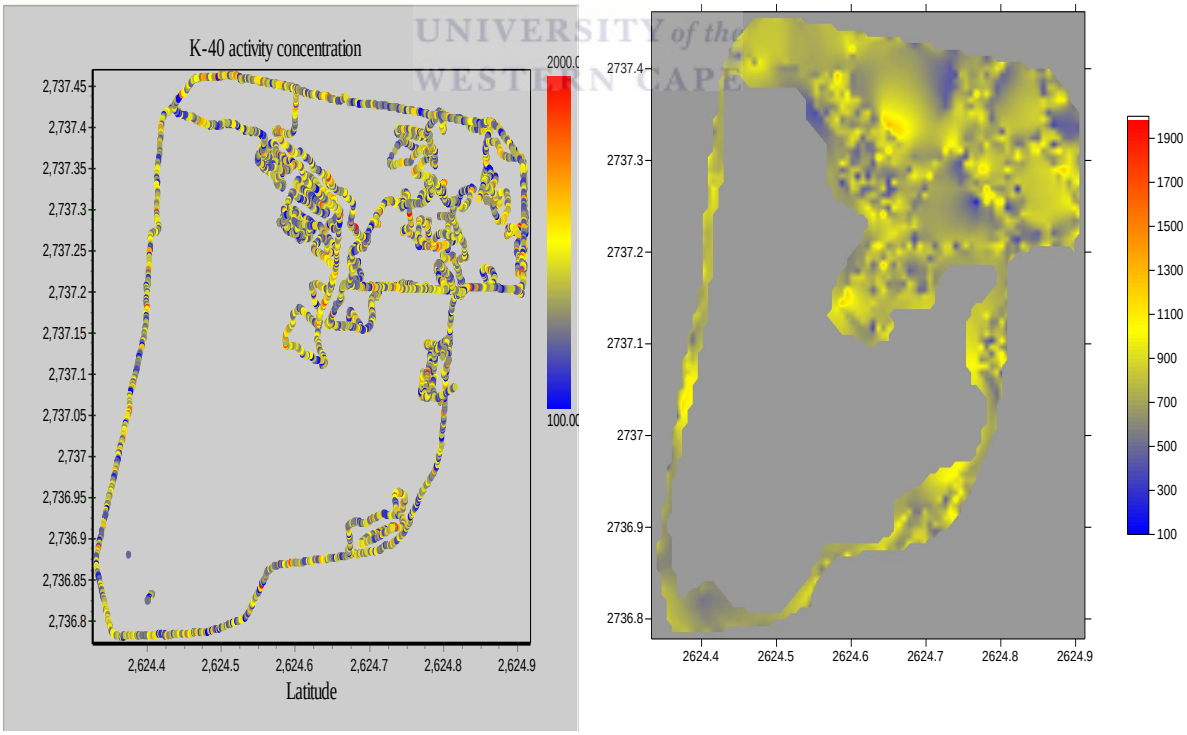

Figure 4.12: A map (left) showing ^{40}K activity concentration measured using the MEDUSA γ-ray detector during 2010 survey and an interpolated map (right) corresponding to the map on the left.

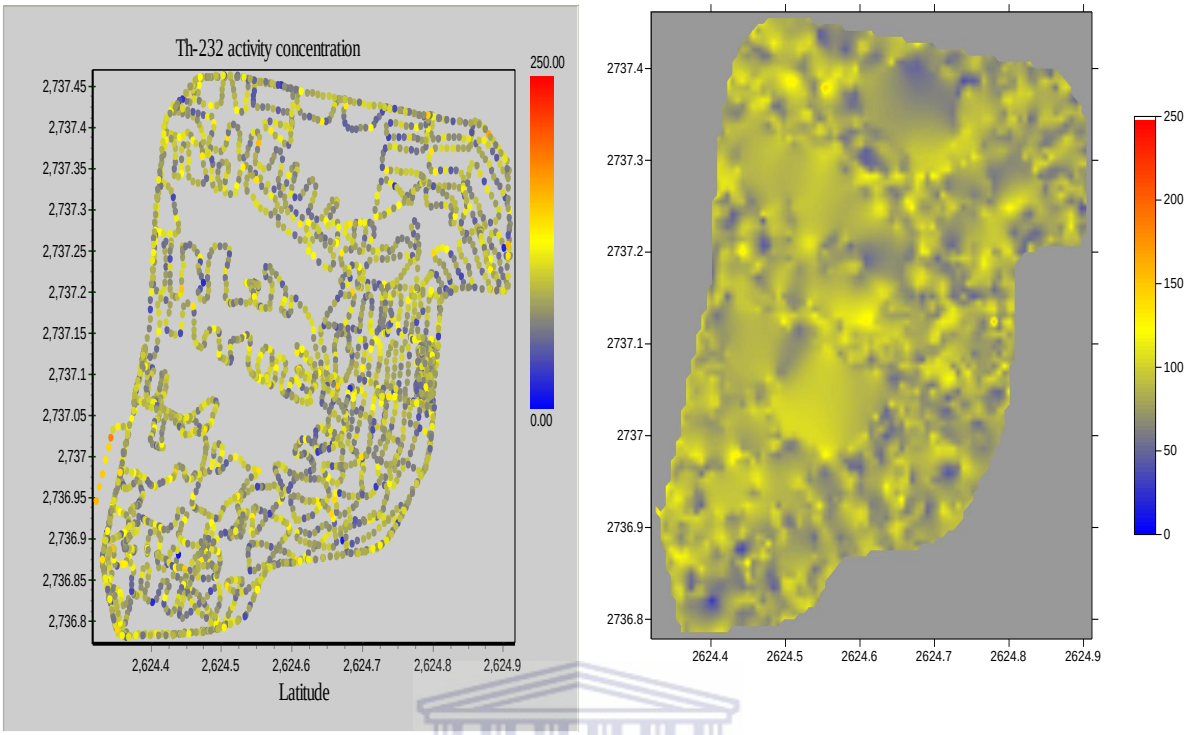

Figure 4.13: A map (left) showing ^{232}Th activity concentration measured using the MEDUSA γ-ray detector during 2002 survey and an interpolated map (right) corresponding to the map on the left.

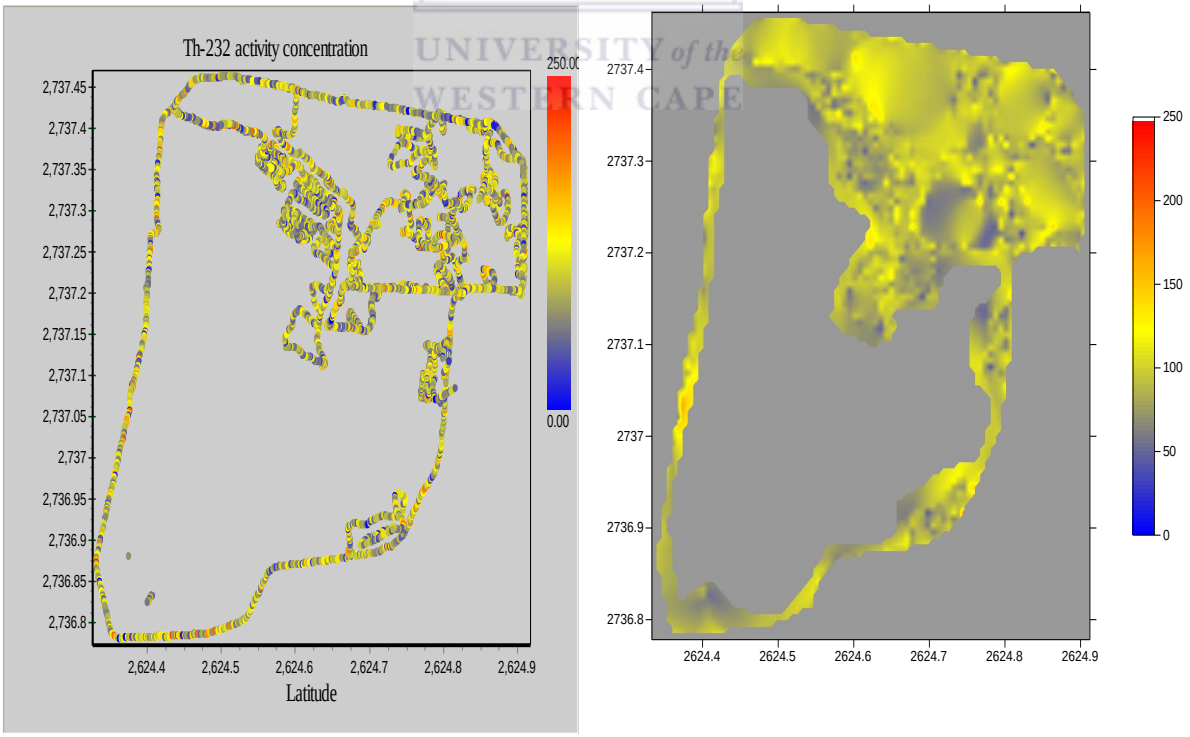

Figure 4.14: A map (left) showing ^{232}Th activity concentration measured using the MEDUSA γ-ray detector during 2010 survey and an interpolated map (right) corresponding to the map on the left.

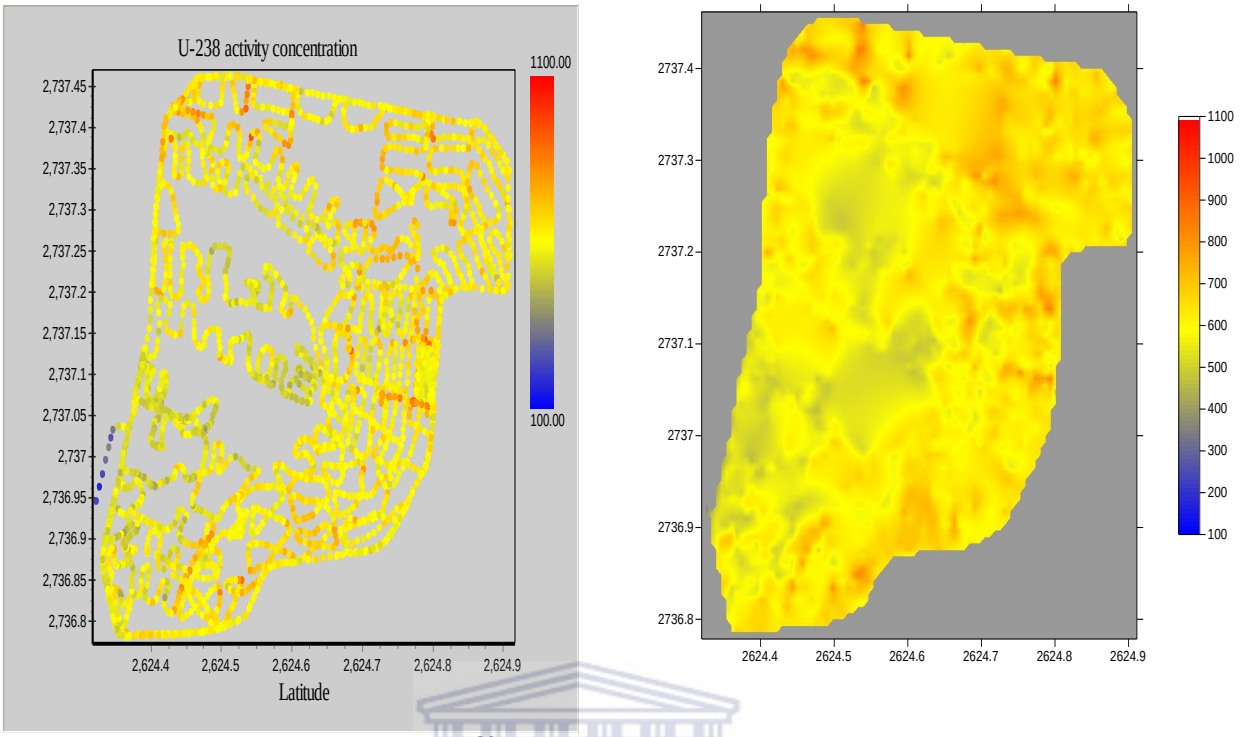

Figure 4.15: A map (left) showing ^{238}U activity concentration measured using the MEDUSA γ-ray detector during 2002 survey and an interpolated map (right) corresponding to the map on the left.

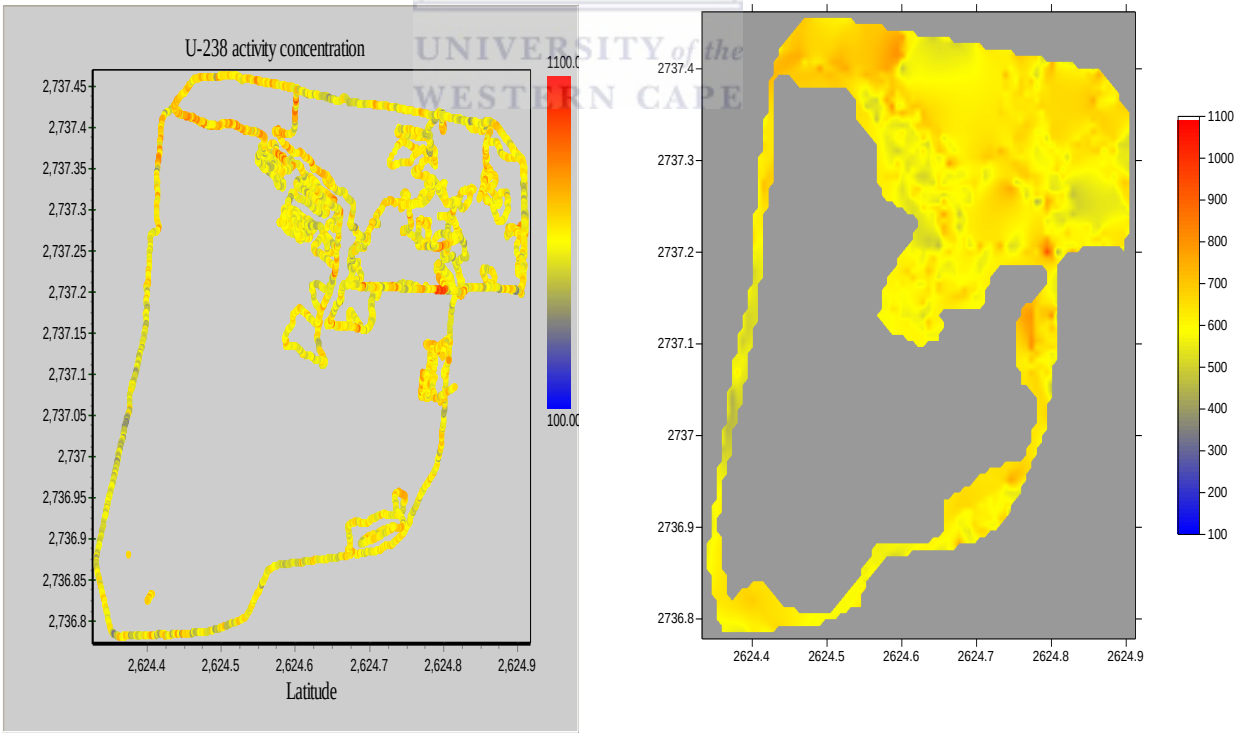

Figure 4.16: A map (left) showing ^{238}U activity concentration measured using the MEDUSA γ-ray detector during 2010 survey and an interpolated map (right) corresponding to the map on the left.

The maps (Figures 4.11-4.16) display activity concentrations extracted by the MPA software for ^{40}K and in the decay series of ^{238}U and ^{232}Th for the 2002 and 2010 surveys. Those activity concentrations were exported to Microsoft Excel for further analysis. The activity concentrations for ^{40}K, ^{232}Th and ^{238}U were then multiplied by an appropriate average normalisation factor given in Chapter 5 Table 5.4. The average activity concentrations obtained were 259 ± 75 Bq·kg^{-1} for ^{40}K, 309 ± 40 Bq·kg^{-1} for ^{238}U and 18 ± 5 Bq·kg^{-1} for ^{232}Th for 2002 survey while 260 ± 75 Bq·kg^{-1} for ^{40}K, 310 ± 40 Bq·kg^{-1} for ^{238}U and 20 ± 5 Bq·kg^{-1} for ^{232}Th were recorded for the 2010 survey. The reported uncertainty that is 29% for ^{40}K, 13% for ^{238}U and 29% for ^{232}Th represents the expanded uncertainty which is based on a standard uncertainty multiplied by a coverage factor k=1.645, providing a coverage probability of approximately 90%. The uncertainty was evaluated according to guides provided by ISO (1992), Bell (2001), UKAS (2007) and Gilmore (2008). Details of the uncertainty evaluation are given in Appendix B.

The sections above have introduced and discussed the MEDUSA γ-ray detector system which is used for in-situ gamma ray spectrometry and the data analysis methods used for MEDUSA stationary and mobile measurements. To complement MEDUSA field measurements, soil samples from five stationary spots (see Figure 4.4 and Figure 3.5) were taken for further radiometric analysis in the laboratory by means of a HPGe γ-ray detector system. In total thirty four soil samples were collected and in the next section preparation processes of the soil samples in readiness for measurement by the HPGe detector system will be discussed.

4.3 Soil sample preparation processes

Soil samples collected after digging out from the ground were weighed immediately and sealed tightly in Ziploc® polythene bags and later transported to the Environmental Radiation Laboratory (ERL) at iThemba LABS. Before the actual gamma ray measurement by the HPGe γ-ray detector system, the soil samples were dried, crushed and sieved as described in detail below.

4.3.1 Sample drying

Samples were transferred from Ziploc® polythene bags into pre-weighed glass trays. The wet masses of soil samples were recorded. Afterwards the soil samples were dried in the oven (Labotec EcoTherm) overnight at 105^0C to remove moisture. The samples were removed and left to cool down and their dry masses were recorded. Moisture content for each soil sample was calculated by the expression below after subtracting the mass of each glass tray,

$$S = 1 - \frac{M_{dry}}{M_{wet}} \tag{4.3}$$

where, S is the moisture content, M_{wet} and M_{dry} represents the wet and dry mass of each soil sample respectively. The moisture contents and the exact location where soil samples were collected are given in Table 4.2. The naming convention for the soil sample codes adapted is explained using one example as shown in Table 4.1.

Table 4.1: The naming convention of the Kloof soil samples.

KS52A (30 cm)					
K	**S**	**5**	**2**	**A**	**30cm**
Kloof	Soil sample	The spot where the soil sample was collected, in this case spot number 5. Spot numbers ranged from 1 to 5.	The second soil sample to be picked at spot 5.	**A** refers to north, **B** for east, **C** for south & **D** for west ~80 cm from the detector where the soil sample was collected.	Refers to the depth at which the second soil sample was collected at spot 5.

Table 4.2: The moisture content and the location of the soil samples from the mine dump.

Spots		Sample ID	Co-ordinates		Moisture (%)
			Latitude	Longitude	
Spot 1	1	KS11(30 cm)	26°24.407 S	27°36.831 E	5.0
	2	KS12(30 cm)	26°24.407 S	27°36.831 E	4.3
	3	KS13(45 cm)	26°24.407 S	27°36.831 E	11.4
Spot 2	4	KS21(30 cm)	26°24.700 S	27°37.266 E	8.0
	5	KS21(50 cm)	26°24.700 S	27°37.266 E	8.5
	6	KS22(50 cm)	26°24.701 S	27°37.267 E	9.6
	7	KS23(50 cm)	26°24.699 S	27°37.266 E	8.6
	8	KS24(50 cm)	26°24.699 S	27°37.267 E	9.1
	9	KS25(50 cm)	26°24.701 S	27°37.265 E	8.6
Spot 3	10	KS31 A(30cm)	-	-	9.7
	11	KS31 B(30cm)	-	-	9.7
	12	KS31 C(30cm)	-	-	9.8
	13	KS31 D(30cm)	-	-	10.4
	14	KS31(30 cm)	26°24.561 S	27°37.355 E	10.4
	15	KS31(50 cm)	26°24.561 S	27°37.355 E	13.5
	16	KS32(50 cm)	26°24.558 S	27°37.357 E	14.0
	17	KS33(50 cm)	26°24.561 S	27°37.359 E	14.4
Spot 4	18	KS41 A(30cm)	-	-	9.3
	19	KS41 B(30cm)	-	-	7.6
	20	KS41 C(30cm)	-	-	9.4
	21	KS41 D(30cm)	-	-	9.1
	22	KS41(30 cm)	26°24.861 S	27°37.311 E	9.9
	23	KS41.1(50 cm)	26°24.861 S	27°37.311 E	9.1
	24	KS41.2(50 cm)	26°24.861 S	27°37.311 E	10.4
	25	KS42(50 cm)	26°24.862 S	27°37.310 E	10.0
	26	KS43(50cm)	26°24.859 S	27°37.309 E	7.2
	27	KS44(cylinder)	26°24.861 S	27°37.307 E	8.6
Spot 5	28	KS51(50cm)	26°24.684 S	27°36.987 E	15
	29	KS52 A(30cm)	-	-	7.5
	30	KS52 B(30cm)	-	-	7.2
	31	KS52 C(30cm)	-	-	7.8
	32	KS52 D(30cm)	-	-	8.3
	33	KS52(30cm)	26°24.682 S	27°36.988 E	8.5
	34	KS52(50cm)	26°24.682 S	27°36.988 E	11.2

4.3.2 Sample crushing and sieving

The dry soil samples were further processed to obtain homogenous soil samples. By using a pestle and mortar soil samples were crushed and then sieved through a mesh of 1-mm diameter holes. Grains larger than 1 mm were again crushed and sieved. During this process organic material, some stones and lumps which could not be crushed were removed. Next, sieved soil samples were transferred into pre-weighed empty Marinelli beakers, filled up to the l000 cm^3 mark and weighed. The mass of the soil sample in each Marinelli beaker was calculated by subtracting the mass of the pre-weighed empty Marinelli beaker from the filled Marinelli beaker. A pre-weighed copper lid of 2 mm thickness which acts as an extra lid was placed on the surface of the soil sample inside the Marinelli beaker. A white silicon sealant (Bostik) was applied on the edge of the copper lid and attached to the inside wall of the Marinelli beaker. The copper lid prevents radon leaking out of the Marinelli beaker. After that the Marinelli beaker lid was placed back and silicon sealant applied once again on the outside to hold the lid firmly (see Figure 4.17).

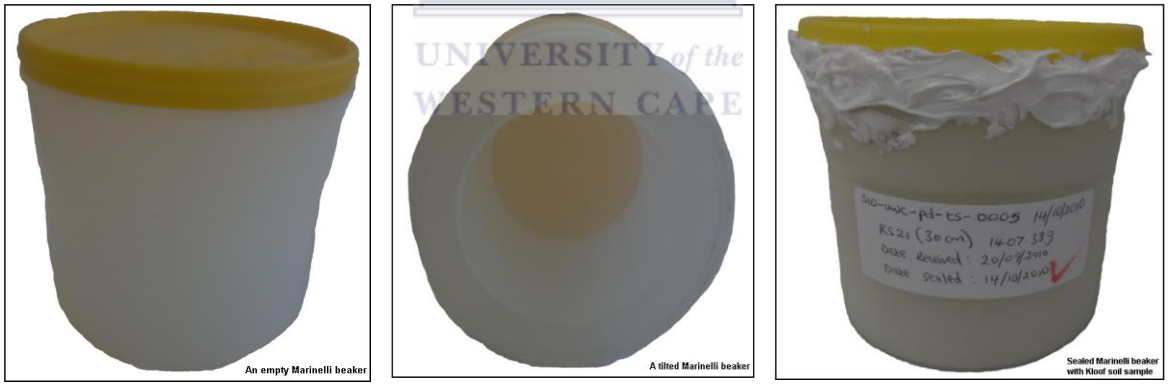

Figure 4.17: A Marinelli beaker used with the HPGe detector system at an upright position (left), tilted position (centre) and a filled, labelled and sealed one (right).

The soil samples were then stored for at least 21 days so as to attain secular equilibrium between the γ-emitters in the uranium (mainly ^{226}Ra, ^{214}Bi and ^{214}Pb) and thorium (^{228}Ac, ^{208}Tl and ^{212}Pb) decay series. Secular equilibrium means that activity concentration of the parent radionuclide will be ascribed to the progenies. After 21 days the soil samples were each measured for 24 hours using the HPGe γ-ray detector system so as to identify and quantify the various radionuclides present in the soil samples. Moreover, a background

spectrum measured for about 230400 seconds (~ 3 days) using a Marinelli beaker filled with ultra pure water was used for data analysis.

4.4 Hyper Pure Germanium (HPGe) detector

4.4.1 Overview of the HPGe detector system

Soil sample preparation processes paves the way for the radiometric analysis using the HPGe γ-ray detector system. This system is extensively used worldwide in laboratories for radioactivity measurement [Yucel, 1998; Croft, 1999; Daza, 2001; Melquiades, 2001; Khater, 2008; Misiak, 2011]. This system can be applied to all types of samples (solids/liquids), it is non-destructive and it allows for multi-elements analysis.

The HPGe system available at the ERL is a closed-end coaxial Canberra *p*-type detector; model GC 4520 with a built-in preamplifier. The detector crystal has a diameter of 62.5 mm and a length of 59.0 mm, with a 45 % relative efficiency and 2.1 keV FWHM energy resolution at the 1.33 MeV γ-line of ^{60}Co. The detector crystal is enclosed in a lead castle, approximately 10 cm thick cladded with a 2.0 mm thick copper inner lining for shielding against background radiation. The copper lining surrounding the detector absorbs any X-rays emanating from the lead [Debertin, 2001]. The HPGe crystal is supported in a rigid cryostat with liquid nitrogen dewar to reduce thermal conductivity between the crystal and the surrounding air. The ERL HPGe liquid nitrogen dewar is routinely filled with the liquid once a week. The detector is operated at 77K liquid nitrogen temperatures to prevent thermally-induced leakage currents which would result from its small band gap (0.7 eV) [Leo, 1987; Knoll, 2010].

The other components of the ERL HPGe system are the detector castle, detector bias supply (SILENA model 7716), preamplifier (model 2002CSL), amplifier (model ORTEC 572) and ATOMKI Palmtop Multichannel Analyzer (model MCA 8k-01) and desktop computer as shown in Figure 4.18.

Figure 4.18: A picture showing the set-up of the HPGe detector system comprising of the lead castle, the liquid nitrogen dewar and the other components of the system.

The ERL HPGe detector operates at a bias voltage of +3500 volts. A bias supply provides the voltage needed to collect all the charges formed in the detector as a result of radiation interaction with the detector material. The amplifier will then shape and increase (in size) the voltage pulse from the preamplifier. The pulses from the amplifier are collected and sorted by the ATOMKI Palmtop Multichannel Analyzer (MCA), which consists of an ADC (analog-to-digital converter), a digital spectrum stabilizer (DSS), single channel analyzer (SCA) and multi-channel scaler (MCS). The ADC produces a digital code (or number) at its output that is proportional to an analog voltage supplied to its input [Knoll, 2010]. All the digitized pulse heights are stored as a spectrum file containing counts and channels.

For this study the ATOMKI Palmtop MCA system was used for data acquisition and γ-spectral analysis. The Palmtop MCA (MCA 8k-01) is from the Institute of Nuclear Research of the Hungarian Academy of Sciences (ATOMKI), 2005.

4.4.2 Activity concentrations determination

The peak or window analysis method was used to analyse the HPGe acquired spectra.
In this method the ATOMKI Palmtop software was used to set the regions-of-interest (ROIs) manually around the photopeak of the gamma lines of interest. Then the software with its in-built algorithm calculates the net counts and its uncertainty.

The net counts in the photopeak area and their uncertainties are then used to calculate the activity concentrations A ($Bq \cdot kg^{-1}$) of a gamma-emitting radionuclide in the soil samples using this expression:

$$A\ (Bq/kg) = \frac{C_{net}}{Br \cdot \varepsilon \cdot t_s \cdot m} \tag{4.4}$$

where, C_{net} represent the full-energy peak content corrected for continuum contribution given as

$$C_{net} = C_s - \frac{t_s}{t_b} C_b \tag{4.5}$$

C_s is the net peak area in the sample spectrum, C_b is the corresponding net peak area in the background spectrum, t_s is the live time of the sample spectrum collection in seconds, t_b is the live time of the background spectrum collection in seconds, Br is the branching ratio (that is the percentage of the decay of the nuclide that will proceed via the emission of a particular gamma-ray), ε is the photopeak detection efficiency and m (in kg) the sample mass.

To determine the activity concentration of any radionuclide accurately, the photopeak detection efficiency (ε) for a given sample geometry is required which is discussed in the next subsubsection.

4.4.2.1 Gamma-ray detection efficiency

The photopeak detection efficiency was determined using the following two approaches:

(1) The relative efficiency approach

This approach which is described by Croft (1999) and used by Newman (2008) entailed using Kloof soil samples and potassium chloride (KCl) powder. The photopeak detection efficiency for each of the thirty four soil samples collected was measured and appropriate gamma lines due to the decay of the ^{238}U series and ^{232}Th series were analysed. As depicted by Table 4.3, six γ-ray lines for ^{238}U and five γ-ray lines for ^{232}Th were used for analysis. These lines are abundant enough to be detected and isolated from other lines in the spectrum. The 1460 keV gamma line of ^{40}K was analysed from a KCl powder source. After that, a relative photopeak efficiency curve for each soil sample was generated. In principle, 34 relative efficiency curves were generated from the 34 soil samples.

Table 4.3: Uranium, thorium and potassium γ-ray lines used and their associated branching ratios [Firestone, 1996].

Nuclide	Energy (keV)	Branching ratios
^{238}U series	295	0.185
	352	0.358
	609	0.448
	1120	0.148
	1237	0.059
	1377	0.04
	2204	0.05
^{232}Th series	238	0.433
	338	0.113
	583	0.304
	727	0.066
	794	0.046
	911	0.266
	2614	0.359
^{40}K	1460	0.107

Next, the relative efficiency curves were scaled to equal the measured absolute photopeak efficiency (ε) at 1460 keV found by using the KCl source and this yielded the absolute photopeak efficiency (ε) for every soil sample. The volume of these soil samples sealed in Marinelli beakers and the KCl source was 1000 cm^3. Note that to get an accurate absolute photopeak efficiency (ε) at 1460 keV for ^{40}K when using the KCl source, the concentration of the ^{40}K in KCl needs to be determined as discussed later in this subsection. A step-by-step process explaining how to generate absolute photopeak efficiency curves from this approach is illustrated hereafter using one soil sample. In a similar way the process was applied to the rest of the remaining thirty three soil samples.

1. To begin with, each spectrum of the 34 soil samples was analysed using the Palmtop MCA software.
2. Regions of interest (ROIs) were set around the peaks of interest according to the γ-ray lines in Table 4.3, in that way counts (C_s) in peak area and live time (t_s) were obtained. The natural logarithms $(\ln E)$ of the γ-ray lines were computed.
3. The counts (C_s) were corrected for background spectrum to obtain net counts (C_{net}) using equation (4.5).
4. The ratios of net counts (C_{net}) to the corresponding branching ratio (Br) were calculated.
5. The relative efficiencies of ^{238}U and ^{232}Th were determined by normalising the ratio of the photopeak counts for each γ-ray energy to its associated branching ratios with the 352 keV line in the ^{238}U series and 338 keV line in the ^{232}Th series respectively. At 352 keV and 338 keV lines relative efficiencies were assumed to be unity.
6. The natural logarithm of ^{238}U relative efficiencies in step 5 was calculated.
7. A graph of natural logarithm of ^{238}U relative efficiencies (step 6) versus energy E (keV) was plotted and a linear fit was used to determine parameters a_1 and b_1 as shown on Figure 4.19. This method is based on the assumption that the efficiency in this energy region has a power law dependence on the energy (see equation (4.7)).

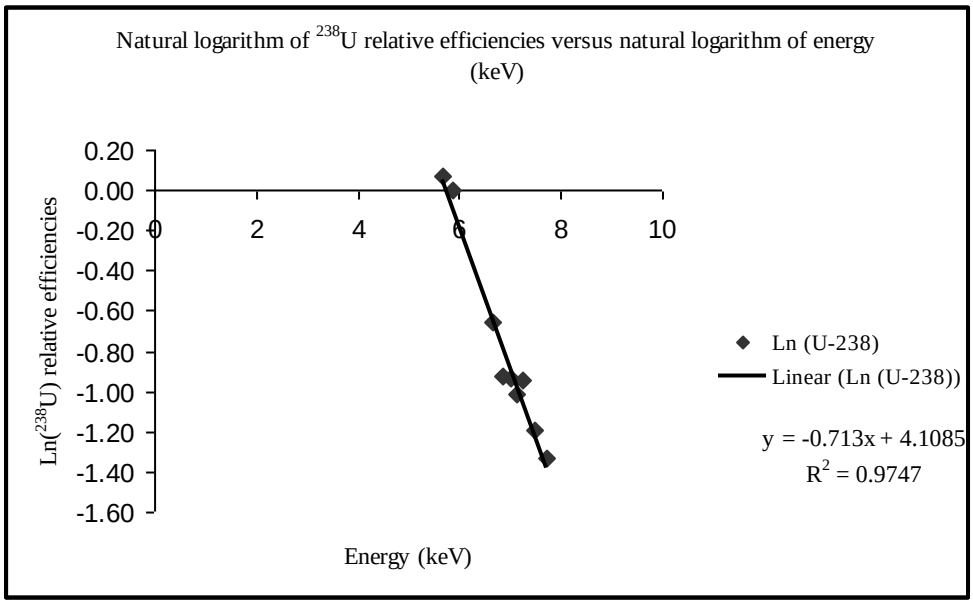

Figure 4.19: A graph of natural logarithm of ^{238}U relative efficiencies.

The equation of the graph can then be represented as follows:

$$\ln \varepsilon = \ln a_1 + b_1 \ln\left[\frac{E}{E_o}\right] \tag{4.6}$$

where, E_o = 1 MeV, E ranges from 186-2204 keV, a_1 and b_1 are dimensionless fit parameters.

8. The relative efficiencies of ^{232}Th (from step 5) were normalised by a factor calculated using this power-law relationship:

$$\varepsilon_{det}(E) = a \times \left(\frac{E}{E_o}\right)^b \tag{4.7}$$

where, E = 338 keV, E_o = 1 MeV, while a and b, refer to a_1 and b_1 respectively (step 7).

9. The new normalised relative efficiency for ^{232}Th was calculated by multiplying the factor obtained in step 8 at E (338 keV), with the relative efficiencies obtained in step 5. For ^{238}U the new normalised relative efficiency was given by equation (4.7) where E (keV) refers to the gamma lines in ^{238}U decay series, parameters a and b, refer to a_1 and b_1 respectively (step 7). Thus far new normalised relative efficiencies have been determined as illustrated in Figure 4.20.

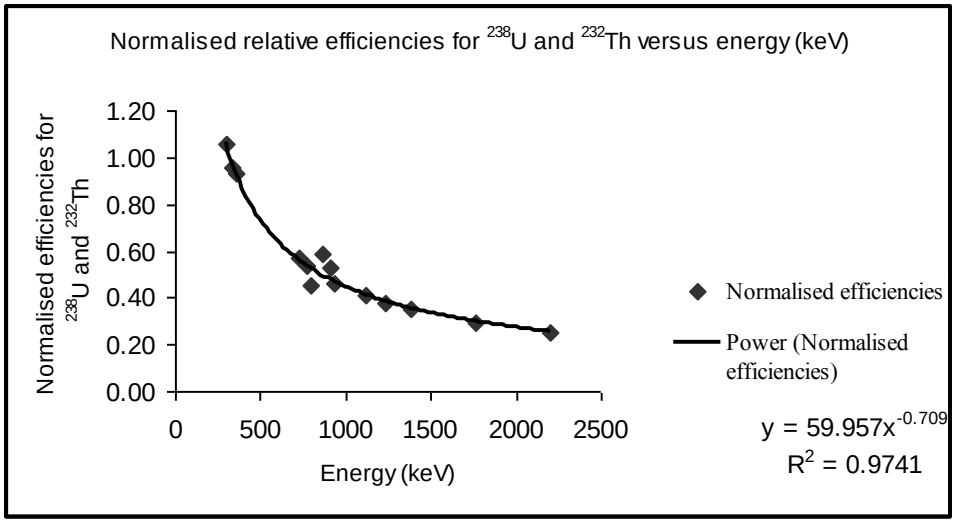

Figure 4.20: Normalised relative efficiencies for ^{238}U and ^{232}Th.

10. After this the natural logarithm of the new relative efficiencies from step 9 for ^{238}U and ^{232}Th was computed.
11. A graph of the natural logarithm of the new relative efficiencies (step 10) against natural logarithm of energy (step 2) was plotted. From the straight line graph new parameters a_2 and b_2 were extracted, refer Figure 4.21.

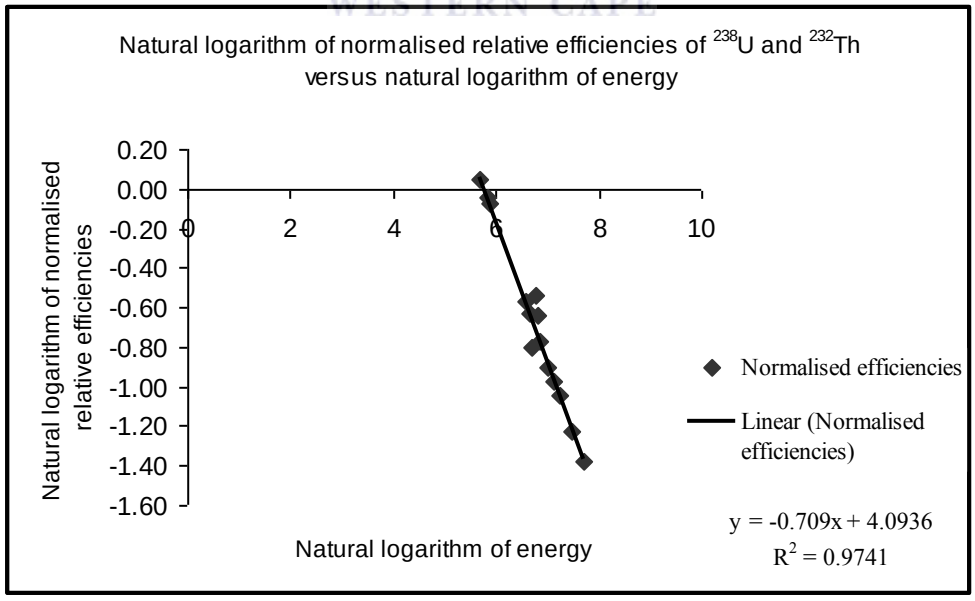

Figure 4.21: Natural logarithm of normalized relative efficiencies of ^{238}U and ^{232}Th.

12. The final relative efficiency was computed using equation (4.7) for ^{238}U, ^{232}Th and ^{40}K, where, E (keV) represents the gamma line, a and b, refer to a_2 and b_2 respectively (step 11). Note that all along the relative efficiency of ^{40}K had been excluded in the analysis but at this stage it will be included. The final efficiencies are shown in Figure 4.22.

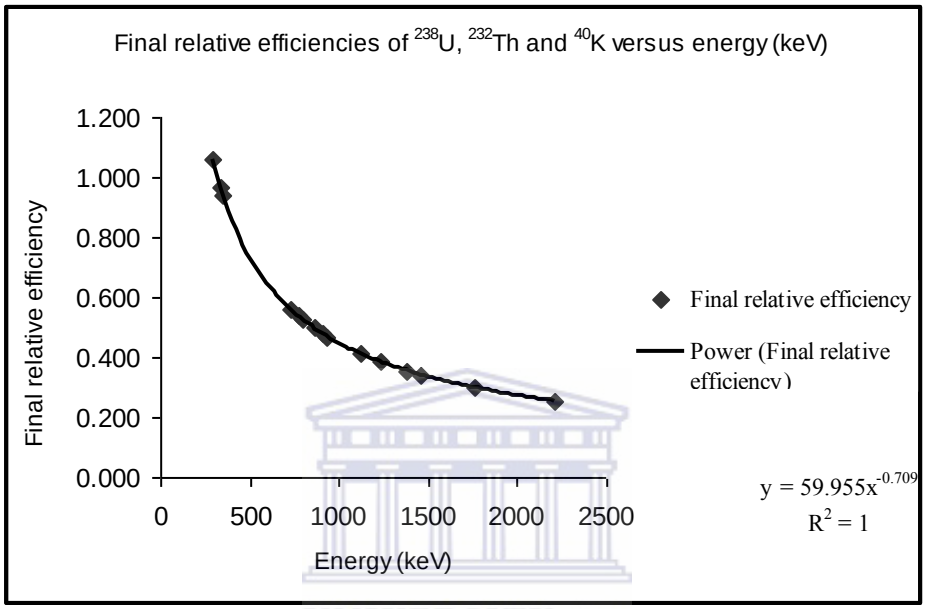

Figure 4.22: Final relative efficiencies of ^{238}U, ^{232}Th and ^{40}K.

13. Next the absolute efficiency of ^{40}K in KCl powder is determined by re-arranging equation (4.4) after computing the activity concentration of ^{40}K as discussed below.
14. Determine the scaling factor (K_f) to convert the final relative efficiencies in step 12 to absolute photopeak efficiencies. The scaling factor is given by the ratio of the value of ^{40}K in KCl powder (step 13) to the value of relative efficiency (step 12) of ^{40}K in soil samples that is:

$$K_f = \frac{\varepsilon_{Abs}(^{40}K)}{\varepsilon_{Rel}(^{40}K)} \qquad (4.8)$$

15. Finally, the absolute efficiencies are obtained by multiplying the final relative efficiencies obtained in step 12 by the scaling factor (K_f). All the steps described culminate in generating the absolute photopeak efficiency curve as illustrated in Figure 4.23. From the power-law relationship given on the graph, a and b parameters are extracted and used for interpolation purposes for any other gamma line energies

which were not initially used to determine the absolute photopeak efficiency. Since thirty four samples were analysed, 34 absolute photopeak efficiency curves were generated leading to 34 sets of parameters a and b. The average of the parameters a and b is 1.55 ± 0.07 and -0.71 ± 0.01 respectively, as shown in Table 4.4.

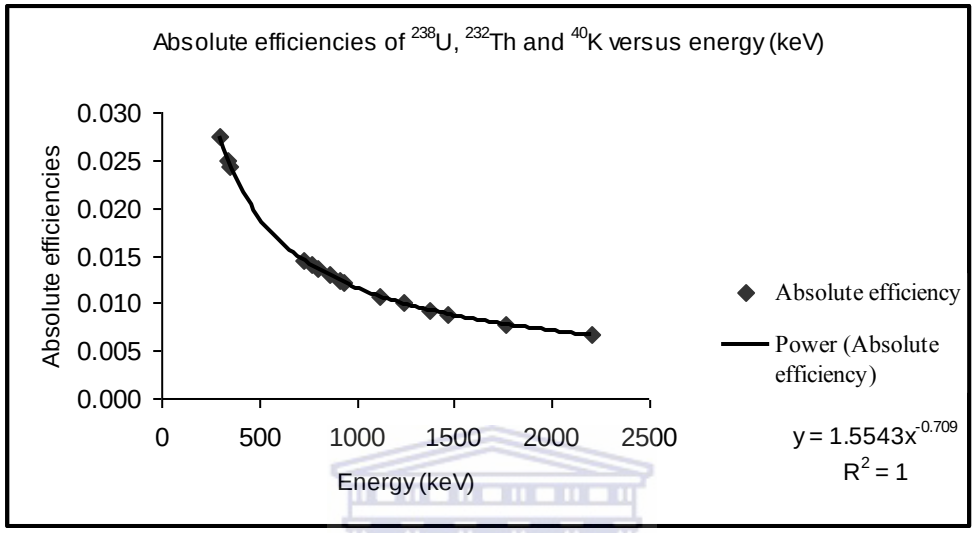

Figure 4.23: Absolute photopeak efficiencies of ^{238}U, ^{232}Th and ^{40}K.

Table 4.4: Parameters a and b generated from absolute photopeak efficiency curves of Kloof soil samples.

Spots		Sample Code	Parameters	
			a	b
Spot 1	1	KS12 (30cm)	1.5521	-0.7088
	2	KS11(30cm)	1.5589	-0.7094
	3	KS13(45cm)	1.5871	-0.7119
Spot 2	4	KS21(30cm)	1.7022	-0.7215
	5	KS21(50cm)	1.4770	-0.7020
	6	KS22(50cm)	1.4377	-0.6983
	7	KS23(50cm)	1.5852	-0.7117
	8	KS24(50cm)	1.5130	-0.7053
	9	KS25(50cm)	1.7237	-0.7232
Spot 3	10	KS31(30cm)	1.5817	-0.7114
	11	KS31(50cm)	1.4651	-0.7009
	12	KS31A(30cm)	1.4673	-0.7011
	13	KS31B(30cm)	1.5174	-0.7057
	14	KS31C(30cm)	1.5285	-0.7067
	15	KS31D(30cm)	1.6249	-0.7151
	16	KS32(50cm)	1.5064	-0.7047
	17	KS33(50cm)	1.6214	-0.7148
Spot 4	18	KS41(30cm)	1.5487	-0.7085
	19	KS41.1(50cm)	1.5207	-0.7060
	20	KS41.2(50cm)	1.4770	-0.7020
	21	KS41A(30cm)	1.5273	-0.7066
	22	KS41B(30cm)	1.6730	-0.7191
	23	KS41C(30cm)	1.5698	-0.7104
	24	KS41D(30cm)	1.4961	-0.7038
	25	KS42(50cm)	1.6500	-0.7172
	26	KS43(50cm)	1.4976	-0.7039
	27	KS44(Cylinder)	1.4653	-0.7009
Spot 5	28	KS51(50cm)	1.5219	-0.7061
	29	KS52(30cm)	1.5679	-0.7102
	30	KS52(50cm)	1.5543	-0.7090
	31	KS52A(30cm)	1.5020	-0.7043
	32	KS52B(30cm)	1.5285	-0.7067
	33	KS52C(30cm)	1.6074	-0.7136
	34	KS52D(30cm)	1.4803	-0.7023
Average			**1.5482**	**-0.7083**

As mentioned earlier, a ^{40}K activity concentration from the KCl powder needs to be established. KCl powder was obtained from Merck company (99.5% purity) sealed in a Marinelli beaker weighing 1.291 kg. The concentration (A) will be given by

$$A = \lambda N \tag{4.9}$$

where, λ is the decay constant of ^{40}K which is given by

$$\lambda = \frac{\ln 2}{t_{1/2}} \tag{4.10}$$

where, $t_{1/2}$ is the half-life of ^{40}K ($4.027 \times 10^{16} \pm 0.63\%$) seconds [Firestone, 1996].

N is the number of ^{40}K nuclei in the KCl sample which is calculated as follows,

$$N = n \times N_A \times a \tag{4.11}$$

where, n is the number of moles of ^{40}K, N_A (6.02×10^{23} atoms/mol) is Avogadro's number and a ($1.17 \times 10^{-4} \pm 0.85\%$ is the natural abundance of ^{40}K) in KCl. The number of moles (n) is related to the mass (m) and molar mass (M) as follows,

$$n = \frac{m}{M} \tag{4.12}$$

The molar mass of KCl is 74.551 g/mol. Thus, the ^{40}K activity concentration in KCl powder was found to be 16258 Bq·kg^{-1}.

Moreover, re-arranging equation (4.4) and extracting other parameters (live time of 3600s and 71422 net counts) from the HPGe measured spectrum of KCl, the ^{40}K absolute efficiency, $\varepsilon_{Abs}(^{40}K)$ was found to be 0.0089. On the other hand the ^{40}K relative efficiencies, $\varepsilon_{Rel}(^{40}K)$ ranged from 0.3206 - 0.3542 for the thirty four soil samples. As a result of the variation in relative efficiencies the scaling factors K_f also ranged from 0.0250 - 0.0277.

Besides this relative efficiency approach, the IAEA reference materials and KCl powder were used to determine the absolute photopeak efficiencies as discussed below:

(2) IAEA reference materials approach

In this approach the IAEA (International Atomic Energy Agency) reference materials RGU-1, uranium ore and RGTh-1, thorium ore; and potassium chloride powder, from the company Merck (99.5% purity) were used to work out the absolute photopeak

efficiencies. The IAEA reference materials approach assumes that the densities and hence the absorption of the samples and the reference materials are the same. On the other hand the relative efficiency approach has the advantage that absorption differences are taken into account although we assume that the absorption at 1460 keV is the same for the samples and the KCl.

The activity concentrations and masses of the IAEA reference materials and the powder from Merck are given in Table 4.5. These reference materials and the KCl powder are sealed in Marinelli beakers each with a volume of 1000 cm^3. The soil samples measured and the reference materials have the same geometry and volume. The reference materials and the KCl powder were first measured using the HPGe detector.

Table 4.5: The activity concentrations and masses of the IAEA reference materials and the powder from Merck.

IAEA Reference Materials	**Activity Concentration** ($Bq \cdot kg^{-1}$)	**Mass** (kg)
^{238}U	4940	1.41
^{232}Th	3250	1.36
^{40}K	16258	1.29

Next, using 6 γ-ray lines from the ^{238}U series, 3 γ-ray lines from the ^{232}Th series and the 1460 keV γ-ray line for ^{40}K (see Table 4.3), absolute photopeak efficiencies were calculated by re-arranging equation (4.4). Other parameters of that expression are extracted from the measured HPGe spectrum for the reference materials and the powder. The efficiency derived in this particular way is considered to be the absolute photopeak efficiency since the reference materials activity concentration is known, whereas the ^{40}K activity concentration in the KCl powder can be determined accurately.

Figure 4.24 shows a graph of absolute photopeak efficiencies fitted with a power-law relationship obtained from the reference materials and the KCl powder.

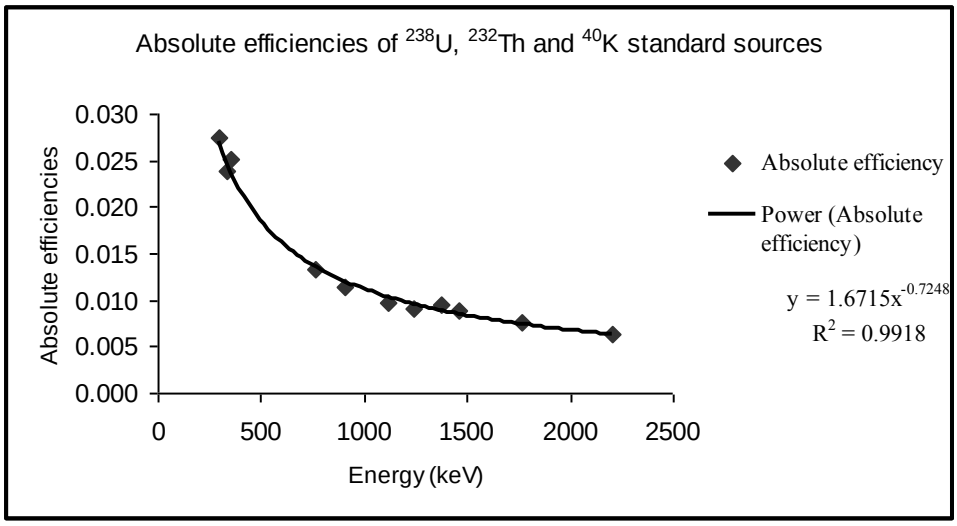

Figure 4.24: Absolute efficiencies determined using the IAEA reference materials and the KCl powder.

The two approaches above have highlighted on how to parameterize the detector efficiency for γ-rays over the energy range 186 – 2204 keV assuming a power-law relationship. The parameters (a and b) for the power law can be extracted from the equation given on the graph shown in Figure 4.23 for the relative efficiency approach and in a similar way for the IAEA reference materials approach using Figure 4.24. The absolute photopeak efficiencies obtained from these two approaches indicate a good agreement as depicted in Figure 4.25 and by Table 4.6.

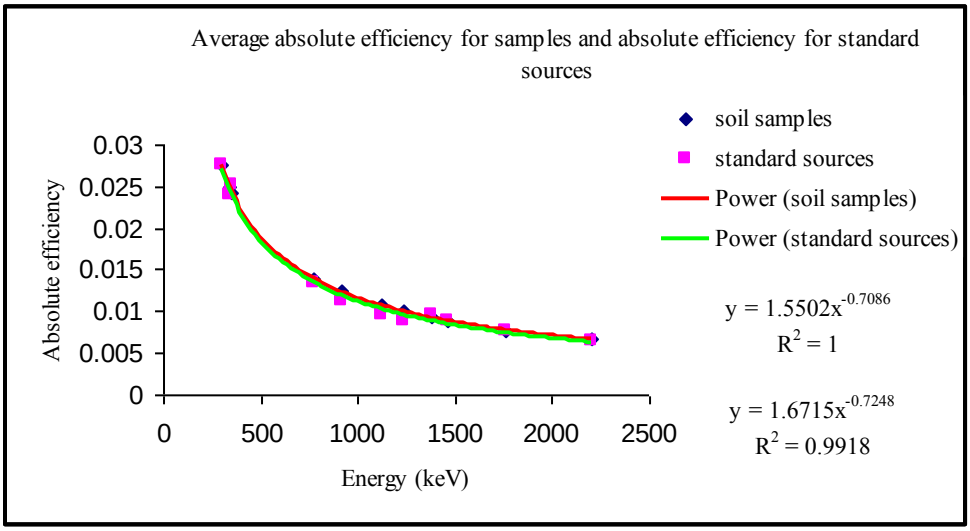

Figure 4.25: A comparison between the absolute efficiencies of the IAEA reference materials approach with the relative efficiency approach.

Table 4.6: A comparison between the absolute efficiencies of the IAEA reference materials approach with the other approach of soil samples plus KCl.

Nuclide	Energy (keV)	Average Absolute efficiency (soil samples + KCl)	Absolute Efficiency (IAEA reference materials)
^{238}U series	295	0.0275	0.0275
	352	0.0243	0.0251
	768	0.0140	0.0134
	1120	0.0107	0.0097
	1238	0.0100	0.0090
	1377	0.0092	0.0095
	1764	0.0078	0.0076
	2204	0.0066	0.0064
^{232}Th series	338	0.0250	0.0240
	911	0.0124	0.0113
^{40}K	1460	0.0089	0.0089

The reference materials, KCl powder and soil samples used for the approaches were considered to have the same density. The density of the reference materials were 1.4 kg·m^{-3} for ^{238}U, 1.4 kg·m^{-3} for ^{232}Th, and 1.3 kg·m^{-3} for ^{40}K. The average soil samples density was about 1.4 kg·m^{-3} see Table 4.7. For this reason and from the good agreement of the two approaches (Figure 4.25), it was considered not necessary to correct for density because any of the approaches would yield the expected results. Note that sample measurements with extremely different densities have variations in the detector response due to self attenuation effects [Croft, 1999; Damon, 2005; Quindos, 2006].

At this stage after establishing the absolute photopeak efficiencies, it is now possible to accurately determine the activity concentrations of the soil samples using equation 4.4. Table 4.7 presents a summary of ^{238}U, ^{232}Th and ^{40}K activity concentrations.

Table 4.7: The activity concentration (^{238}U, ^{232}Th and ^{40}K) of the soil samples with their masses.

Spots		Sample Code	Mass (g)	Activity concentrations (Bq·kg^{-1})		
				^{238}U series	^{232}Th series	^{40}K
Spot 1	1	KS12 (30cm)	1422.91	294 ± 14	15 ± 1	229 ± 11
	2	KS11(30cm)	1414.69	273 ± 13	13 ± 1	209 ± 10
	3	KS13(45cm)	1414.69	280 ± 13	18 ± 1	248 ± 12
Spot 2	4	KS21(30cm)	1407.38	323 ± 15	18 ± 1	254 ± 12
	5	KS21(50cm)	1404.24	323 ± 15	17 ± 1	245 ± 11
	6	KS22(50cm)	1395.05	311 ± 15	19 ± 1	253 ± 12
	7	KS23(50cm)	1405.96	308 ± 14	17 ± 1	247 ± 12
	8	KS24(50cm)	1408.04	303 ± 14	15 ± 1	244 ± 11
	9	KS25(50cm)	1403.98	306 ± 14	20 ± 1	252 ± 12
Spot 3	10	KS32(50cm)	1403.38	341 ± 16	20 ± 1	291 ± 14
	11	KS31(30cm)	1402.82	292 ± 14	16 ± 1	272 ± 13
	12	KS31(50cm)	1414.61	345 ± 16	21 ± 1	287 ± 13
	13	KS31A(30cm)	1429.49	273 ± 13	15 ± 1	249 ± 12
	14	KS31B(30cm)	1411.43	279 ± 13	17 ± 1	262 ± 12
	15	KS31C(30cm)	1406.97	282 ± 13	18 ± 1	263 ± 12
	16	KS31D(30cm)	1438.11	288 ± 14	16 ± 1	262 ± 12
	17	KS33(50cm)	1406.29	351 ± 16	21 ± 1	300 ± 14
Spot 4	18	KS41(30cm)	1406.48	340 ± 16	17 ± 1	250 ± 12
	19	KS41.1(50cm)	1409.06	245 ± 12	17 ± 1	233 ± 11
	20	KS41.2(50cm)	1421.82	261 ± 12	18 ± 1	247 ± 12
	21	KS41B(30cm)	1414.02	350 ± 16	18 ± 1	256 ± 12
	22	KS41A(30cm)	1411.52	338 ± 16	18 ± 1	243 ± 11
	23	KS41C(30cm)	1428.53	343 ± 16	18 ± 1	252 ± 12
	24	KS41D(30cm)	1413.73	336 ± 16	18 ± 1	255 ± 12
	25	KS42(50cm)	1412.94	249 ± 12	18 ± 1	236 ± 11
	26	KS43(50cm)	1408.40	255 ± 12	17 ± 1	237 ± 11
	27	KS44(Cylinder)	1477.88	240 ± 11	17 ± 1	227 ± 11
Spot 5	28	KS51(50cm)	1404.09	339 ± 16	20 ± 1	287 ± 13
	29	KS52(50cm)	1414.71	354 ± 17	17 ± 1	260 ± 12
	30	KS52(30cm)	1419.56	311 ± 15	17 ± 1	250 ± 12
	31	KS52A(30cm)	1411.73	308 ± 14	19 ± 1	257 ± 12
	32	KS52B(30cm)	1415.84	310 ± 15	16 ± 1	250 ± 12
	33	KS52C(30cm)	1429.60	322 ± 15	19 ± 1	254 ± 12
	34	KS52D(30cm)	1427.66	323 ± 15	19 ± 1	259 ± 12
Weighted Average			**1415.22**	**308 ± 7**	**18 ± 1**	**255 ± 5**

The weighted average activity concentrations as determined using the HPGe γ-ray detector system were 308 ± 7 Bq·kg^{-1}, 18 ± 1 Bq·kg^{-1} and 255 ± 5 Bq·kg^{-1} for ^{238}U series, ^{232}Th series and ^{40}K respectively.

4.5 Verification of the two approaches

A reference IAEA-375 soil sample was measured and using the appropriate γ-ray lines from the ^{238}U series, the ^{232}Th series and ^{40}K, the activity concentrations were derived and recorded as shown in the Table 4.8. The absolute efficiencies for various gamma lines were interpolated using the power law relationship of equation (4.7), with 1.55 ± 0.07 and -0.709 ± 0.006 as a and b parameters, respectively.

Table 4.8: Intercomparison of the activity concentration measured using the ERL HPGe γ-ray detector with the IAEA certified values on IAEA-375 soil sample.

Radionuclide	**IAEA certified values** (Bq·kg^{-1})	**ERL measured values** (Bq·kg^{-1})
^{238}U	18 - 22	17 - 19
^{232}Th	20.1 - 21.3	20 - 22
^{40}K	417 - 432	400 - 438

When the activity concentration values measured using the ERL HPGe γ-ray detector system are compared to the expected IAEA certified values for the IAEA-375 soil sample, it was found that the ERL measured activity concentrations are within an error margin of 10% for ^{238}U, 1% for ^{232}Th and 1% for ^{40}K from the expected certified values. This implies that the methods used for determining the activity concentrations are consistent.

4.6 Summary

This chapter has described how measurements were conducted using an in-situ detector (MEDUSA) and a laboratory-based detector (HPGe). The set-up of the detectors has been provided and activity concentrations extractions have been discussed. MEDUSA activity concentrations have been presented by plots while HPGe activity concentrations have been tabulated with the weighted average activity concentrations of the soil samples being 308 ± 7 Bq·kg^{-1}, 18 ± 1 Bq·kg^{-1} and 255 ± 5 Bq·kg^{-1} for ^{238}U series, ^{232}Th series and ^{40}K respectively.

Up to this stage two sets of data have been generated, that is one by the MEDUSA γ-ray detector system and the other by the HPGe γ-ray detector system. The next chapter will explain how the two sets of data will complement each other to determine radon exhalation from Kloof mine dump.

Chapter 5

Radon Exhalation

5.1 Introduction

A brief description on the general processes involving radon emanation, transport and exhalation will be provided, followed by a detailed account of radon exhalation (flux).

The radon exhalation discussion will encompass techniques used for measurements and the typical values of radon flux obtained by other researchers. A novel technique will be discussed which was deployed at Kloof mine dump for measurements as well as other techniques namely the Electret Ion Chamber (EIC) and the International Atomic Energy Agency (IAEA) methods which will be used to validate it.

5.2 Radon emanation and transport

5.2.1 Radon emanation general

Radon emanation refers to the processes by which radon atoms escape from a given material. Emanation power or coefficient of emanation is defined as the ratio of the number of radon atoms that escape from a quantity of material to the total number of atoms formed by radioactive decay of radium in the material in unit time [NCRP, 1988]. Various materials have different emanation coefficients that vary from 0.02 for recent lavas to 0.7 for well developed fine grained soil. Uranium mill tailings emanation coefficients vary from 0.03 to 0.5 with an average value of 0.25 [IAEA, 1992].

In the soil, radon emanates from soil grains after it is released by the decay of radium. As depicted in Figure 5.1, not all of the radon atoms generated by the radium contained in a rock or soil grain is actually released into pore spaces. After radium decay one of the four scenarios portrayed as (A-A′, B-B′, C-C′ and E-E′) can happen to the radon released.

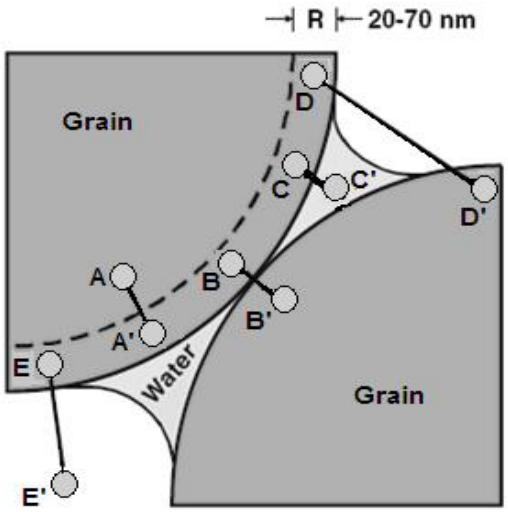

Figure 5.1: Radon atom recoils: A-A′ inside same mineral grain; B-B′ from one mineral to adjacent mineral; C-C′ from mineral to water; D-D′ from mineral through air to adjacent mineral; E-E′ from mineral to air. Adapted from [Mudd, 2008].

A-A′ indicates the influence of grain sizes on the newly formed radon due to its recoil when its parent ^{226}Ra decays. If the grains are much larger than the recoil range in the grains, then it means that new radon atoms cannot escape from the grains in which they originate. If pore spaces are much smaller than the recoil range then the resulting recoil paths do not terminate in the pores (see B-B′). However, if the pores are filled with water the range of the recoil atom is only about 0.1μm, and the probability that it will stop in the pore is greatly increased (C-C′). Therefore, water presence surrounding a soil particle increases the direct recoil fraction of emanation power. The emanation coefficient has to be measured for each material being studied. The effect of moisture on emanation power will be discussed further in subsubsection 5.3.1.2 below.

The process indicated by E-E′ is the only one that directly leads to radon in the air in the pore space.

5.2.2 Radon transport

Radon moves basically by (1) molecular/atomic diffusion through pore fluids (gases and/or liquids) as a result of the concentration gradient, which is described by Fick's Law or (2) advective transport. Advective transport as described by Darcy's Law occurs when the pore fluids move through the soil pores under the influence of an external driving force such as a pressure gradient, which may or may not be present in a given situation [NCRP, 1988; Durrani & Ilic, 1997]. Figure 5.2 shows the process of radon emanating to the pore space, migrating and exhaling from the soil surface boundary.

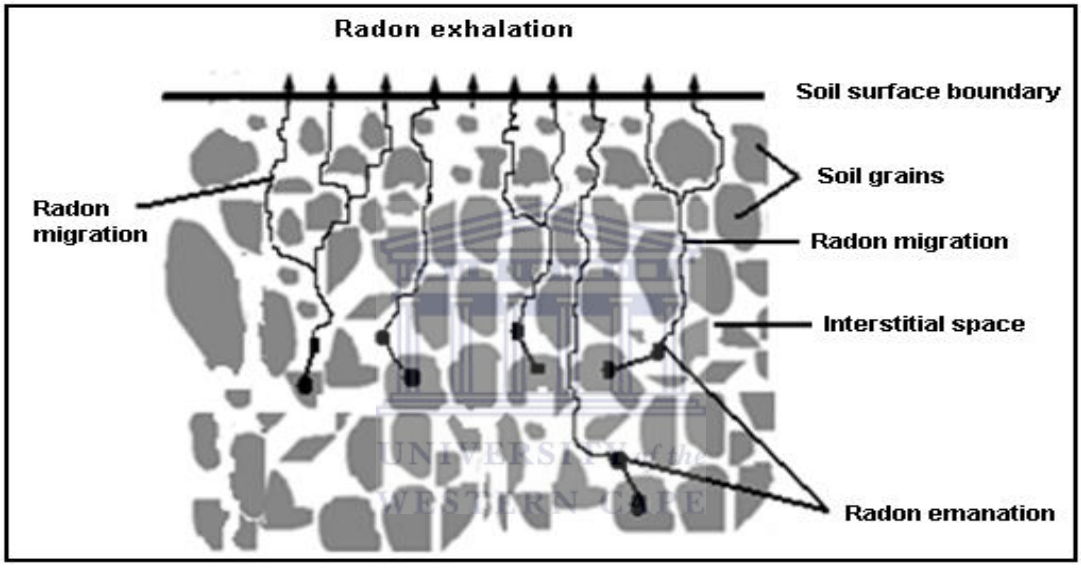

Figure 5.2: Radon emanation, migration and exhalation.

5.3 Radon (^{222}Rn) exhalation

Radon exhalation refers to the transfer of ^{222}Rn from the soil surface boundary to the atmosphere. Before radon is released to the environment, it first emanates from the solid grain (as described in subsection 5.2.1 above) in which it is formed which is characterised by the radon emanation coefficient and next, due to concentration or pressure driven forces, it migrates into the atmosphere. Radon releases are quantified by the radon flux, F in ($Bq \cdot m^{-2} \cdot s^{-1}$). This refers to the transfer rate per unit area of radon from source or any solid substance to the atmosphere [NCRP, 1988; IAEA, 1992].

5.3.1 Radon flux measurements

Several researchers worldwide have reported their radon flux measurements. The common themes discussed in these reports include: the techniques deployed, materials used (e.g. soil, cement. building materials, rocks, granite or uranium tailings), factors influencing the radon exhalation process and the typical flux values measured. A summary of these themes is hereafter provided.

5.3.1.1 Flux measurement techniques

Radon flux measurements can be done either in the laboratory or in the field by applying the following methods [NCRP, 1988; IAEA, 1992; Durrani & Ilic, 1997]:

(i) Accumulation method

A container of volume ranging up to 220 L, with one side open is placed on the surface to measure radon concentration inside the container. This is done at some selected time or at intervals over a period of several hours. The accumulation time should be short compared with the 3.82 d half-life of ^{222}Rn. Then radon exhalation rate is calculated from the accumulated chamber sample geometry and radon concentration [Stranden, 1983].

Recently, Hosoda (2007) has conducted measurements of radon and thoron exhalation rates from the ground surface simultaneously using an accumulator chamber of an area of 1200 cm^2 connected to a ZnS (Ag) scintillator which is connected to a photomultiplier tube, pulse counting part, scaler and timer.

(ii) Flow-through method

In this method a flow-through technique is utilised to continuously remove air in the accumulation container and as a result radon concentration buildup in the container with time is prevented. Note that the air flow rate should be sufficiently high to prevent buildup of radon concentration in the air, but the flow rate should not be too high otherwise radon concentration will be low leading to an inaccurate flux rate. By applying this method radon concentration inside the container is proportional to the flux rate and the surface area of the container in contact with the surface.

(iii) Adsorption method

This is also referred to as the ROAC (Radon On Activated Charcoal) method. A plastic can containing a few grams of an adsorption medium such as activated charcoal is placed in the ground, with its lid open, and left for a few days ranging from 4 to 12 days. After that the plastic can is retrieved and the lid closed. Next, gamma activity of the trapped daughters ^{214}Pb and ^{214}Bi is measured by means of a scintillation counter. If there is no gas leakage from the plastic can, then the radioactivity of the entrapped radon decreases according to the laws of radioactivity. In addition, the radon amount can also be determined by desorbing it into a scintillation liquid and thereafter counting the α and β activity by liquid scintillation counting.

(iv) Vertical profile method

This method is basically applied to large areas which require aircraft or balloons for sampling after assuming several conditions. So it follows that the total amount of radon in a vertical air column of fixed area represents the radon that has been exhaled by the same area of soil.

(v) Soil concentration gradient method

An estimate of radon flux can be inferred if soil radon concentration gradient is established. This is possible under stable pressure conditions as well as when there is no interference from rain and wind. Moreover, this requires that radon diffusion is constant and radon concentration in soil be determined as the soil-air interface is approached [Clements, 1974]. An indication of the time-averaged gradient of radon concentration using concentrations of ^{210}Pb in the surface layers of soil has been demonstrated by Schery (1984). Fleischer (1980) used solid state nuclear track detector (SSNTD) techniques to determine soil radon gradients.

(vi) Diffusion tube method

This method was developed in South Africa. In this method two tubes, one open at the top and the other one closed are pushed into the ground. A measurement of the radon gas in the tubes could then be used to extract the radon flux. To the best of our knowledge,

this method is not used in practise any longer even though it was approved by the National Nuclear Regulator [Lindsay, 2012].

(vii) Large scale measurements

These methods which have just been discussed require direct measurements and for most they turn out to be labour-intensive. They also measure only at one point per measurement. Currently, there are other methods that are utilised to map radon flux indirectly over large scales. This has been possible owing to the improved knowledge about parameters related to radon flux, which has led to radon flux maps being generated on large scales as discussed below.

On a European scale, Szegvary (2007) predicted an average regional ^{222}Rn flux by determining an empirical linear relation between the radon flux and the terrestrial gamma dose rate (GDR) which was automatically monitored in 25 European countries. From this model the radon flux value was 28.3 ± 3.6 mBq·m^{-2}·s^{-1} and the radon flux value measured was 27.7 ± 4.7 mBq·m^{-2}·s^{-1} for South Finland. Szegvary (2007) noted that an increasing soil moisture reduced gas diffusivity and the rate of ^{222}Rn flux, however it also decreased the GDR through increased shielding of photons.

In China annual and the seasonal radon flux densities from the soil surface of 1099 sites have been estimated by Zhuo (2008). Digital maps of the ^{222}Rn flux density were generated after linking a database of soil ^{226}Ra content and a global ecosystems database. As a result an area-weighted annual average ^{222}Rn flux density from the soil surface across China was estimated to be 29.7 ± 9.4 mBq·m^{-2}·s^{-1}. This model that was deployed had been used by Zhuo (2006) at 20 sites around East Asia to estimate seasonal and annual ^{222}Rn flux densities from semi-infinite and homogeneous soil.

In Australia, Griffiths (2010) produced a detailed time-dependent map of radon flux density for the land surface. Radon flux density was calculated from a simple model utilising data from national gamma-ray aerial surveys, modelled soil moisture, and maps of soil properties. The mean radon flux density was found to be 24.1 ± 2.2 mBq·m^{-2}·s^{-1}. Other researchers that have mapped radon flux indirectly are shown in Table 5.1.

In this study a method that measures the radon flux fairly accurately on an area of around 1 km^2 is developed without the need for collecting hundreds of samples or many

individual flux measurements. The purpose is to get a detailed map not based on average parameters as in the indirect methods discussed above.

Table 5.1: A summary of the indirect methods that have been used to map radon flux.

Method	Principle	Region	^{222}Rn Flux ($mBq \cdot m^{-2} \cdot s^{-1}$)	Reference
Radon map	TRACHGEO	France	52.0	Ielsch et al. (2002)
Gamma dose rate	Empirical relation with gamma dose	Finland	27.7	Szegvary et al. (2007)
A simple model	Empirical relation with datasets	East Asia	18.0	Goto et al. (2008)
A simple model	Empirical relation with datasets	China	29.7	Zhuo et al. (2008)
A simple model	Empirical relation with datasets	Australia	24.1	Griffiths et al (2010)
Radon map	Bayesian method	India	33.0	Hirao et al (2010)
Comparison of measurements	Continuous and integrated techniques	Spain	11.1-25.0	Grossi et al (2011)

5.3.1.2 Factors influencing radon releases

^{222}Rn exhalation from the soil surface interface is influenced by physical factors such as the ^{226}Ra activity concentration and its distribution in soil grains; soil grain size; soil porosity, soil moisture; atmospheric pressure, wind speed, rainfall and temperature [Lawrence, 2009]. The effects of these physical factors are highlighted in the follow-up discussions.

(i) Soil moisture

Soil moisture is a weather-related parameter affecting both radon generation and transport and therefore it affects soil-gas radon concentrations. At low to moderate soil moisture levels, ^{222}Rn emanation into soil pores is increased (as discussed in subsection 5.2.1) whereas it is reduced at higher levels of soil moisture. Moreover, ^{222}Rn transport is generally reduced by high soil moisture because water tends to block soil pores, reducing the gas permeability of the soil [Schumann, 1994]. In dry soil, ^{222}Rn atoms can travel about one meter by diffusion, but it may migrate only 1-2 cm in saturated soil during the same time period [Tanner, 1980].

Grasty (1997) measured ^{222}Rn concentration at various depths for a soil under three different soil moisture conditions as shown in Figure 5.3. It can be concluded that at a depth of about 10 cm, ^{222}Rn concentration reaches its maximum value under saturated conditions whereas under dry conditions, almost all the ^{222}Rn is lost from the soil down.

Strong & Levins (1982) demonstrated the effect of moisture on the ^{222}Rn emanation coefficient for a sample of uranium mill tailings content using uranium ore tailings as shown in Figure 5.4 and concluded that radon flux from tailings increases with moisture content up to a maximum, corresponding to the appearance of interstitial water due to the increase of the emanation coefficient.

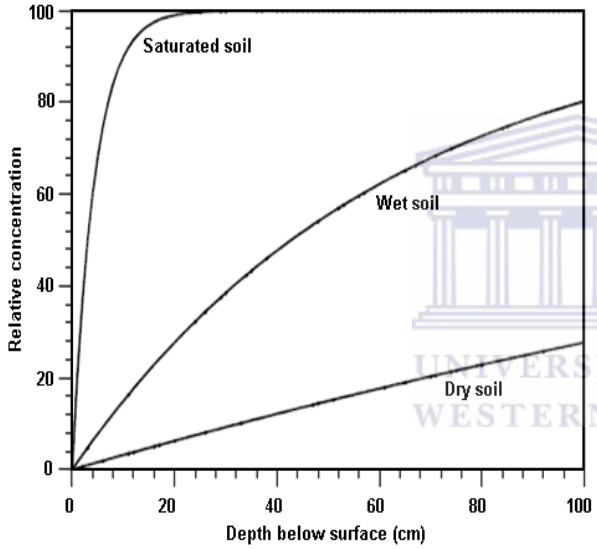

Figure 5.3: Effect of soil moisture on radon concentration with depth [Grasty, 1997].

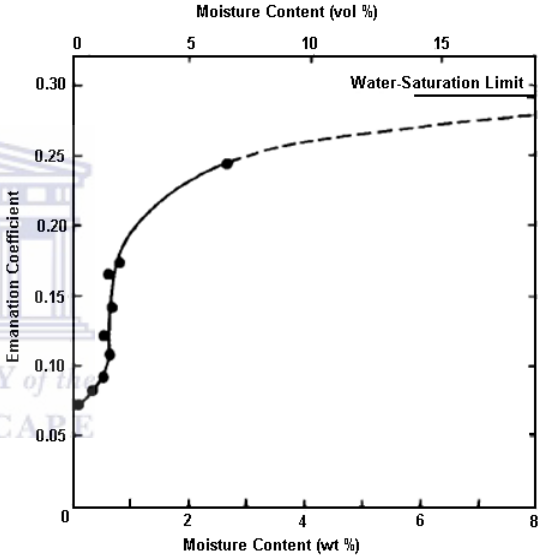

Figure 5.4: Effect of moisture content on ^{222}Rn emanation coefficient for a sample of uranium mill tailings [Strong, 1982].

Other reported work on the impact of soil moisture or precipitation on ^{222}Rn soil gas concentration and exhalation can be found in Tanner (1980), Straden (1984), Nazaroff et al. (1988), Schery (1989), Shweikani (1995), Grasty (1997), Van der Spoel (1997), Jha (2000); Ferry (2001) and Lawrence (2005; 2009).

(ii) Atmospheric pressure

Barometric pressure is another important parameter which influences radon exhalation. Soil gas radon concentrations are significantly changed when there are changes in barometric pressure. It has been noted that when pressure falls it tends to draw soil gas

out of the ground thereby increasing the radon concentration in the near-surface layers. Conversely, high barometric pressure forces atmospheric air into the soil, diluting the near-surface soil gas and driving radon deeper into the soil [Clements, 1974; Janssens, 1984; Schery, 1984; Jha, 2000]. Clements (1974) noted that pressure changes of about 1-2% associated with the passage of weather fronts could produce changes of 20-60% in the radon flux, depending on the rate of change of pressure and its duration. However, from a designed model of diffusion and pressure induced transport, Clements (1974) observed that diffusion remained the predominant migration mechanism.

(iii) Temperature

Information found in the literature concerning the influence of temperature on radon exhalation seems to be conflicting. Some authors are of the view that temperature has little or no effect on soil gas radon content. Schumann (1988) found that soil-gas radon concentrations correlate with changes in soil temperature and, to a lesser extent, with air temperature changes. Other investigators [Schery, 1983; Straden, 1984; Nazaroff 1992; Zhuo, 2006; Sahoo, 2010] have estimated the dependence of the radon exhalation rate on the soil temperature. It has been noted that when the soil temperature increased, the exhalation rate increased. Straden (1984) observed that an increase of temperature from 5 to 22^{0}C increased radon exhalation rates in soil and shale samples by 50-200 %.

Temperature changes are often but not always related to pressure changes. As noted above, radon exhalation is strongly influenced by pressure changes. Hence temperature variation does not have a clear effect since it is not always linked to pressure changes.

(iv) Wind speed

Wind blowing across irregular soil surfaces, causes air turbulence which leads to soil gas being drawn upward from deep down [Pearson, 1966; Schumann, 1994]. Jha (2000) studied the influence of wind speed on exhalation rates and reported that the wind speed variations from the region studied are not strong enough to cause any considerable change in the exhalation rate. Furthermore, they postulated that extreme wind speeds would only produce minor variations in exhalation rate through depletion of soil gas from the upper layers of the ground.

(v) Porosity

An increase in the porosity of the medium leads to an increase in radon exhalation rate. When soil grains are close to each other the path of radon atoms in the pore space is restricted, whereas if the porosity is increased so does the exhalation rate [Shweikani, 1995; Hosoda, 2007].

(vi) Grain size

It is generally thought that the variation of the grain size is inversely proportional to the radon exhalation rate [Shweikani, 1995; Hosoda, 2007]. However, there have been conflicting results that indicate that the effect of particle size on the emanation coefficient is very dependent on the mineralogical characteristics [IAEA, 1992].

5.3.1.3 Typical values of radon flux

Radon flux values have been determined from materials such as soil, cement, building materials, rocks, and uranium tailings. In addition to that, surface flux densities from the ocean and land have also been examined. Even though the land surface flux density varies in space and time, it is the dominant source of radon when compared to the ocean surface flux.

The United Nations Scientific Committee on the effects of Atomic Radiation [UNSCEAR, 1982] has reported that flux rates for uranium tailings are much higher than radon flux rates for a variety of soil types. The uranium tailings flux rates range between 0.03 $Bq \cdot m^{-2} \cdot s^{-1}$ and 10.2 $Bq \cdot m^{-2} \cdot s^{-1}$. Table 5.2 displays values obtained for exhalation rates of various materials in different regions of the world.

Table 5.2: The exhalation rate of various materials in different regions of the world. Adapted and modified from [Hassan, 2009].

Material	Region (Country)	Exhalation rate ($mBq \cdot m^{-2} \cdot s^{-1}$)	Reference
Building materials	India	0.30 - 88	Sahoo (2007)
Cement	Israel	0.1 - 0.5	Kovler (2005)
Cement	Turkey	1.4 - 100	Turhan (2008)
Concrete	Taiwan	0.1 - 0.4	Chen (1993)
Concrete	Netherlands	6 - 16	De Jong (1996)
Concrete	Hong Kong, China	3.8 - 27	Chao (1999)
Concrete	USA	28	Ingersoll (1983a)
Granite	Taiwan	0.02 - 0.29	Chen (1993)
Granite	Egypt	0.01 - 0.19	Arafa (2004)
Soil	San Jose, USA	78	Ingersoll (1983b)
Soil	Norway	9100	Stranden (1984)
Soil	Finland	53 - 130	Markkanen (1992)
Soil	Mean world value	15 - 230	UNSCEAR (1982)
Soil	New Mexico	32 ± 4.1	Schery (1984)
Soil	Australia	22 ± 5.0)	Schery (1989)
Soil	North America	40 - 480	Graustein (1990)
Soil	Netherlands	0.45 ± 0.02	Aldenkamp (1992)
Soil	Slovenia	20	Brajnik (1992)
Soil	Spain	38 ± 2.0	Escobar (1999)
Uranium tailings	Spain	1700 ± 40	Escobar (1999)
Uranium tailings	Nabarlek, Australia	6500	Bollhofer (2003)
Uranium tailings	India	3740	Sahoo (2010)

So far, a general review on radon exhalation has been given. In the next section the discussion on radon exhalation continues with specific emphasis on the technique that was utilised to extract radon exhalation rates at Kloof mine dump.

5.4 Radon exhalation measurements at Kloof mine dump

An alternative to the direct methods (see subsubsection 5.3.1.1) was investigated for ^{222}Rn exhalation measurements. Some of these methods are limited to conducting measurements on a small scale and if large scale measurements are required then it becomes tedious and labour intensive and in the end they only provide information for a particular location. Moreover, these methods have their own shortcomings such that their measurements are prone to a number of uncertainties, like back-diffusion and

uncontrollable advection due to pressure differences induced by temperatures or wind. Because of these shortcomings some of these methods have been critiqued [Samuelsson, 1984].

In this study, radon exhalation values were extracted after utilising the MEDUSA technology [De Meijer, 1998; Hendriks et al., 2001]. Later these radon exhalation values will be compared with values obtained from Electret Ion Chamber (EIC) measurements and an expression given by the IAEA. Each of these techniques is discussed below.

5.4.1 Radon exhalation measurement using MEDUSA γ-ray detector

(i) General

In Chapter 4, details about acquiring data using the MEDUSA γ-ray detector system and processing of MEDUSA data were discussed at length. The MEDUSA γ-ray detector system has been used previously to measure the presence of radionuclides in various conditions and activity concentrations determined thereafter [De Meijer, 1998; Venema, 2001; Motlhabane, 2003; Hlatshwayo, 2009; Talha, 2009; Mlwilo, 2010]. Moreover, in this study the MEDUSA γ-ray detector system will be used to extract radon fluxes from the Kloof mine dump. The residues at the mine dump contain high concentration of ^{238}U after gold extraction and traces of other two naturally radioactive nuclides, ^{232}Th and ^{40}K when compared to the concentration of normal soil or rocks.

In brief, uranium occurs naturally with the following radioisotopes ^{238}U and ^{235}U that have different half-lives. Both decay leading to stable isotopes of lead (see for example Figure 2.1). Naturally occurring uranium contains approximately 99.28% of ^{238}U and 0.72% of ^{235}U [Firestone, 1996]. Thorium occurs naturally as the radioisotope ^{232}Th. Its decay products are unstable until the stable isotope ^{208}Pb, see the decay chain in Figure 2.2. ^{40}K is the only radioactive isotope of potassium and its abundance is about 0.012 % in natural potassium. ^{40}K nuclei decay, 11% branching ratio by electron capture (see Figure 2.3) to an excited state of ^{40}Ar, which subsequently decay to ground state by emitting a single gamma-ray photon with energy of 1.46 MeV.

Note that neither ^{238}U nor ^{232}Th emit gamma rays, therefore the gamma-ray emissions from their radioactive daughter products are relied upon to estimate their concentrations [Minty, 1997a; IAEA, 2003].

In the field, disequilibrium in the ^{238}U decay series is common. Disequilibrium occurs when one or more decay products are completely or partially removed or added to the system. The estimates of ^{238}U concentration from gamma ray spectrometry rely on the abundance of ^{214}Bi and ^{214}Pb isotopes which are radon progenies. They occur far down in the radioactive decay chain (see Figure 2.1) and require equilibrium conditions that are not present in the field. So this means that any field measurement with the MEDUSA detector system will yield activity concentrations after radon has escaped leading to lower apparent ^{238}U activity concentration. The more radon escapes the lower the apparent ^{238}U concentration. The ^{238}U gamma ray measurement obtained reflects the effective radon loss over the last hour or so, since ^{214}Bi and ^{214}Pb half-lives are in the order of 20 minutes. Note that for gamma-rays emitted by radionuclides above ^{226}Ra, they cannot be detected easily in the field, only possible in a laboratory-based setup.

On the other hand in the field, the ^{232}Th decay series is almost always in equilibrium and this is due to the fact that the half-life (55.6 s) of thoron (^{220}Rn) is too short to escape before decay. In the ^{238}U decay series, the half-life (3.82 d) of radon (^{222}Rn) is long enough to allow radon to escape before it can decay. As a consequence of radon loss, it is possible to map the radon exhalation for the mine dump as discussed below.

(ii) Radon exhalation expression

The usual expression for the exhalation of radon from the mine dump can be derived from equation (3.3) if we assume a steady state situation and reduce the problem to a one dimensional diffusion problem in the z-direction. This leads to (see also Appendix C)

$$J = D_e \varepsilon \frac{\partial C}{\partial z} \tag{5.1}$$

where, J is the upward flux of radon activity concentration at $z = 0$, the surface of the mine dump, C is the radon activity concentration in the pore space, D_e is the effective diffusion coefficient and ε is the porosity. This equation is Fick's first law of diffusion [Crank, 1975].

The expression for the radon concentration as derived for diffusion in equation (3.9), or also (3.11) or (3.14), leads to

$$J = \frac{D_e \varepsilon C_\infty}{\ell} = \frac{D_e E C_{Ra} \rho_b}{\ell} = \ell \lambda E C_{Ra} \rho_b \quad (5.2)$$

from equation (3.4) and (3.10) where λ_{Rn} is the radon decay constant, C_{Ra} is the radium activity concentration, E is the emanation coefficient, ρ_b is the dry bulk density, ℓ is the diffusion length and C^∞ is the volumetric concentration of radon in the pore space at large depth.

This equation agrees with the IAEA expression given in IAEA (1992).

In order to extract the radon exhalation from the MEDUSA γ-ray detector measurement, consider the counts seen in the detector, I, compared to what the counts would have been if there was no radon escape, I_H. The radon flux will clearly be proportional to the difference between these two values,

$$J \alpha (I_H - I) = I_H \cdot \left(1 - \frac{I}{I_H}\right) \quad (5.3)$$

The counts in the field are known, but the equilibrium counts are obviously not measured. However, the thorium and potassium equilibrium counts are known as well as the laboratory equilibrium measurements for these two as well as the uranium series since the samples are sealed and only counted after three weeks.

The activity concentration of ^{40}K, ^{238}U series and ^{232}Th series are extracted from the measured data in the field using the Full Spectrum Analysis method. Consequently to extract the radon flux values from the measured data, we have to be aware that in an ideal world the standard spectrum used during Full Spectrum Analysis is perfect for ^{238}U and ^{40}K.

Then it can be shown (Appendix C),

$$^{238}U_M = {}^{238}U_H \cdot \left(1 - \frac{E \mu \ell}{1 + \mu \ell}\right) \quad (5.4)$$

and

$$^{40}K_M = {}^{40}K_H \quad (5.5)$$

where, $^{238}U_M$ represents uranium disequilibrium activity concentration measured by the MEDUSA γ-ray detector, $^{238}U_H$ represents the uranium equilibrium activity concentration measured by the HPGe γ-ray detector, $^{40}K_M$ represents the potassium

activity concentration measured by the MEDUSA γ-ray detector, $^{40}K_H$ represents the potassium activity concentration measured by the HPGe γ-ray detector, E is the emanation coefficient, ℓ is the diffusion length (≈ 0.4 m) and μ is the attenuation coefficient, see more details in Appendix C.

Since the standard spectra are all normalised in a similar manner with the same factor (N_f), then

$$^{238}U_M = {}^{238}U_H \times N_f \cdot \left(1 - \frac{E\,\mu\,\ell}{1+\mu\,\ell}\right) \tag{5.6}$$

$$^{40}K_M = N_f \times {}^{40}K_H \tag{5.7}$$

Combining equation (5.6) and (5.7) results in

$$\frac{^{238}U_M}{^{40}K_M} = \frac{^{238}U_H}{^{40}K_H} \cdot \left(1 - \frac{E\,\mu\,\ell}{1+\mu\,\ell}\right) \tag{5.8}$$

and then,

$$1 - \frac{^{238}U_M/^{40}K_M}{^{238}U_H/^{40}K_H} = \frac{E\,\mu\,\ell}{1+\mu\,\ell} \tag{5.9}$$

In our case it is found that due to the normalisation of the standard spectra, the individual normalisation factors for ^{238}U series, ^{232}Th series and ^{40}K are different. The normalisation factors are presented in (iii) below. Thus,

$$^{238}U_M = {}^{238}U_H \times \frac{1}{N_f^U} \cdot \left(1 - \frac{E\,\mu\,\ell}{1+\mu\,\ell}\right) \tag{5.10}$$

$$^{40}K_M = {}^{40}K_H \times \frac{1}{N_f^K} \tag{5.11}$$

where, N_f^U and N_f^K represent ^{238}U and ^{40}K normalisation factors respectively.

Combining equation (5.10) and (5.11) results in

$$1 - \frac{^{238}U_M/^{40}K_M}{^{238}U_H/^{40}K_H} \cdot \frac{N_f^U}{N_f^K} = \frac{E\,\mu\,\ell}{1+\mu\,\ell} \tag{5.12}$$

Now, since the counts are proportional to the radon concentrations, we can rewrite equation (5.3) and (5.4) and say that the flux can be found by,

$$J \ \alpha \ {}^{238}U_H \cdot \left[1 - \left(\frac{{}^{238}U_M / {}^{40}K_M}{{}^{238}U_H / {}^{40}K_H} \cdot \frac{N_f^U}{N_f^K} \right) \right] \qquad (5.13)$$

In this equation we are dividing by the ^{40}K values to compensate for the normalisation as discussed in (iii) below.

In the same way, radon flux can be extracted when the activity concentration of ^{238}U series and ^{232}Th series are considered. This stems from the fact that ^{40}K and ^{232}Th activity concentrations are not affected by radon exhalation which means that they are independent of radon escape (loss), so the flux can be determined as follows,

$$J \ \alpha \ {}^{238}U_H \cdot \left[1 - \left(\frac{{}^{238}U_M / {}^{232}Th_M}{{}^{238}U_H / {}^{232}Th_H} \cdot \frac{N_f^U}{N_f^{Th}} \right) \right] \qquad (5.14)$$

where, $^{232}Th_M$ represent the thorium activity concentration measured by the MEDUSA γ-ray detector, $^{232}Th_H$ represent the thorium activity concentration measured by the HPGe γ-ray detector and N_f^{Th} is the thorium normalisation factor.

Equations (5.13) and (5.14) present a new way of determining radon exhalation using ratios by combining field and laboratory measurements. Unless otherwise stated this technique will henceforth be referred to as **ME**DUSA **L**aboratory **T**echnique (MELT).

MELT can be applied successfully to calculate radon exhalation if:

- Normalisation factors between MEDUSA and HPGE γ-ray detectors are established,
- Moisture content for the field (MEDUSA) activity concentrations is taken into account, and
- Normalisation constants for the radon flux are established.

In principle, we have discussed in Chapter 4 how we used two γ-ray detectors to acquire data, one using the field-based MEDUSA system and the other laboratory-based HPGe system. The flow chart displayed in Figure 5.5 shows a step-by-step process of determining radon exhalation and the step where MELT is applied. Data acquired using the MEDUSA γ-ray system were categorised as MEDUSA stationary or MEDUSA mobile depending on the mode of acquisition. The MEDUSA mobile data is illustrated on the left hand side of the flow chart while MEDUSA stationary data is illustrated on the right hand side. The activity concentration of the ^{238}U series, ^{232}Th series and ^{40}K

extracted using (1) the MEDUSA γ-ray system at the stationary spots and (2) the HPGe γ-ray system on the soil samples collected from the stationary spots reveal the origin of very useful information such as normalisation factors, moisture correction factors and radon flux normalisation constants (see Figure 5.5, step 5). This information is extracted by comparing MEDUSA stationary data directly with the corresponding HPGe data obtained from the stationary spots shown in Figure 3.5 and Figure 4.4 on the mine dump. The normalisation factors, moisture correction factors and radon flux normalisation constants were extracted as follows:

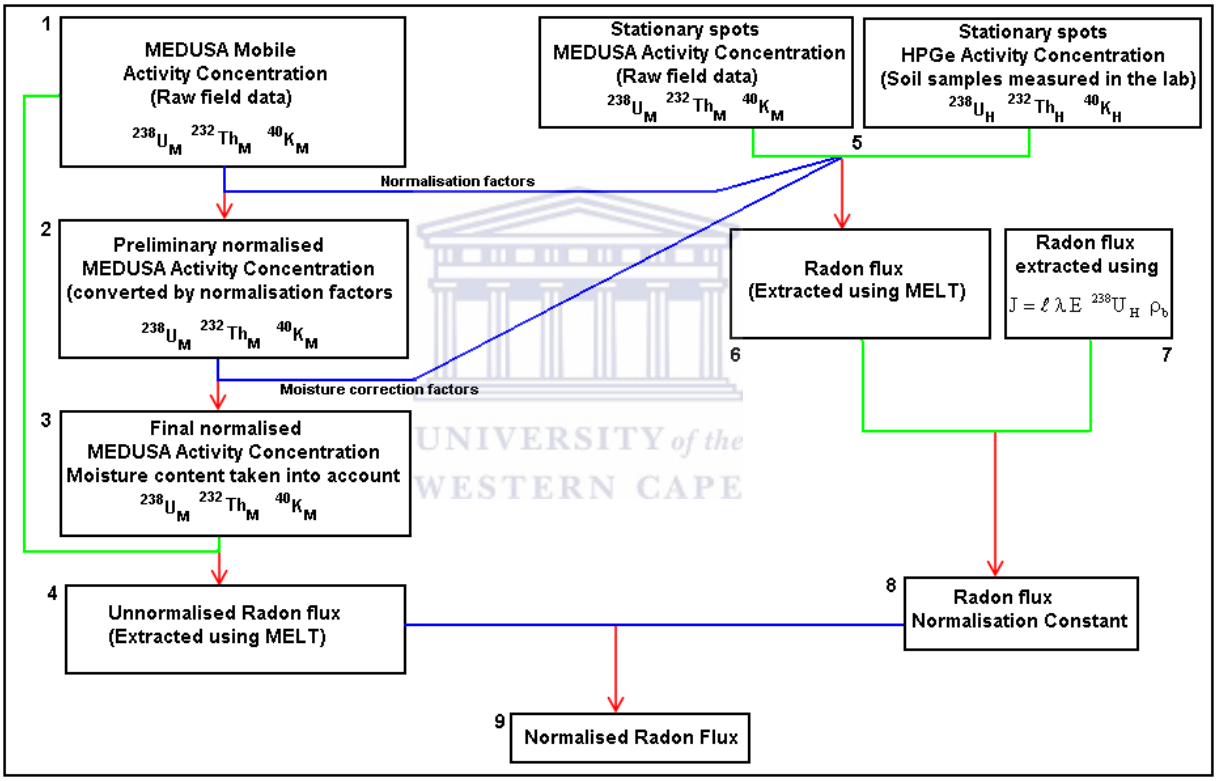

Figure 5.5: A flow chart indicating the steps for calculating radon exhalation applying MELT. Blue lines indicate normalisation and moisture correction factors obtained from stationary spots. Green lines indicate data manipulation. The red lines indicate the results after data manipulation. The numbers indicated on the flow chart are intended to guide during the discussion after this.

(iii) MEDUSA and HPGe normalisation factors

As previously shown in Figure 4.4, five spots on the mine dump were used as calibration points. MEDUSA stationary measurements at those spots lasted for 30-60 minutes, and thereafter data were processed separately using MEDUSA Post Analysis (MPA)

software. HPGe data were obtained from 25 soil samples which were collected around the five spots on the mine dump. The soil samples were processed as discussed in Chapter 4 and later measured to determine the equilibrium activity concentrations of ^{238}U, ^{232}Th and ^{40}K. Next, the ratios for the radionuclides (^{238}U, ^{232}Th and ^{40}K) were used to determine the normalisation factors (N_f); by taking the average equilibrium activity concentrations of soil samples from the HPGe measurements and dividing by the activity concentrations from the MEDUSA measurements. This can also be expressed as:

$$N_f = \frac{AC_{HPGe}}{AC_{MEDUSA}} \tag{5.15}$$

where, AC_{HPGe} and AC_{MEDUSA} represent the activity concentrations of each radionuclide (^{238}U, ^{232}Th and ^{40}K) from the HPGe and MEDUSA, respectively.

These normalisation factors are required since the standard spectra are calculated for a standard soil that will not have similar absorption coefficients as the soil on the mine dump and may not include all the light gathering characteristics of the detector.

The activity concentrations which were measured in the field using the MEDUSA γ-ray detector system and in the laboratory using the HPGe γ-ray detector system on the soil samples collected from the stationary spots are presented in Table 5.3. In addition the table shows the normalisation factors for each radionuclide (^{238}U, ^{232}Th and ^{40}K) and the moisture content (%) computed from the soil samples collected at the stationary spots.

Table 5.3: The HPGe and the MEDUSA activity concentrations, the normalisation factors and the moisture content (S) derived from the stationary spots.

	HPGe Activity concentrations ($Bq \cdot kg^{-1}$)			**MEDUSA Activity concentrations** ($Bq \cdot kg^{-1}$)			**Normalisation factor** N_f (Dimensionless)			**S** (%)
	^{238}U	^{232}Th	^{40}K	^{238}U	^{232}Th	^{40}K	^{238}U	^{232}Th	^{40}K	
KS21(50cm)	323 ± 15	17 ± 1	245 ± 11							8.5
KS22(50cm)	311 ± 15	19 ± 1	253 ± 12							9.6
KS23(50cm)	308 ± 14	17 ± 1	247 ± 12							8.6
KS24(50cm)	303 ± 14	15 ± 1	244 ± 11							9.1
KS25(50cm)	306 ± 14	20 ± 1	252 ± 12							8.6
Average	**310 ± 6**	**17 ± 1**	**248 ± 5**	**620±80**	**90±11**	**700± 85**	**0.50**	**0.20**	**0.36**	**8.9**
KS31(30cm)	292 ± 14	16 ± 1	272 ± 13							10.4
KS31A(30cm)	273 ± 13	15 ± 1	249 ± 12							9.7
KS31B(30cm)	279 ± 13	17 ± 1	262 ± 12							9.7
KS31C(30cm)	282 ± 13	18 ± 1	263 ± 12							9.8
KS31D(30cm)	288 ± 14	16 ± 1	262 ± 12							10.4
Average	**282 ± 6**	**17 ± 1**	**261 ± 5**	**510±60**	**80±10**	**660± 80**	**0.56**	**0.21**	**0.40**	**10.0**
KS41(30cm)	340 ± 16	17 ± 1	250 ± 12							9.9
KS41A(30cm)	338 ± 16	18 ± 1	243 ± 11							9.3
KS41B(30cm)	350 ± 16	18 ± 1	256 ± 12							7.6
KS41C(30cm)	343 ± 16	18 ± 1	252 ± 12							9.4
KS41D(30cm)	336 ± 16	18 ± 1	255 ± 12							9.1
Average	**341 ± 7**	**18 ± 1**	**251 ± 5**	**570±70**	**85±10**	**690± 85**	**0.60**	**0.21**	**0.37**	**9.1**
KS52(30cm)	311 ± 15	17 ± 1	250 ± 12							8.5
KS52A(30cm)	308 ± 14	19 ± 1	257 ± 12							7.5
KS52B(30cm)	310 ± 15	16 ± 1	250 ± 12							7.2
KS52C(30cm)	322 ± 15	19 ± 1	254 ± 12							7.8
KS52D(30cm)	323 ± 15	19 ± 1	259 ± 12							8.3
Average	**315 ± 7**	**18 ± 1**	**254 ± 5**	**610±75**	**90±11**	**750± 90**	**0.52**	**0.21**	**0.34**	**7.9**

Note that the HPGE calculated activity concentrations are presented for every sampling spot (5-samples) whereas the MEDUSA determined activity concentration is represented by a single data point. An averaged value for each of the radionuclides was deduced at every spot when analyzing using the MEDUSA Post Analysis software. So for every spot the weighted average activity concentration of each radionuclide which was measured by the HPGe was considered, and then compared to the activity concentration which was measured by MEDUSA.

Therefore, the averaged normalisation factors are 0.54 ± 0.05, 0.36 ± 0.03 and 0.21 ± 0.01 for ^{238}U, ^{40}K and ^{232}Th, respectively (see Table 5.4).

Table 5.4: A summary of the normalisation factors for each radionuclide.

Stationary spot	Normalisation factors (N_f)		
	^{238}U	^{40}K	^{232}Th
2	0.50	0.36	0.20
3	0.56	0.40	0.21
4	0.60	0.37	0.21
5	0.52	0.34	0.21
Average	**0.54 ± 0.05**	**0.36 ± 0.03**	**0.21 ± 0.01**

Of interest from Table 5.4 is the normalisation factor of ^{238}U and ^{232}Th. As previously mentioned ^{40}K is not affected by radon exhalation, so if the ^{40}K normalisation factor is considered to be correct then we expect that ^{238}U and ^{232}Th normalisation factors should be larger than 0.36. Even though ^{232}Th activity concentration is considered to be in equilibrium because the half-life of thoron (^{220}Rn) is too short to escape before it decays, its normalisation factor is lower compared to the normalisation factor of ^{40}K. The normalisation factor could be lower than 0.36 ± 0.03 due to a poor fit as at the region 2614 keV the standard spectra and the measured data do not fit well (see Figure 4.8 and Figure 6.1). This often happens for the nuclide with the lowest concentration since the automated fitting routine in the Full Spectrum Analysis [De Meijer, 1998; Hendriks et al., 2001] will adjust its value to compensate for the many continuum points and not to the peaks.

Although in the field the activity concentration ascribed to the ^{238}U after measuring the ^{214}Bi activity concentration using the MEDUSA γ-ray detector is different from when it is measured in the laboratory using the HPGe γ-ray detector, due to ^{222}Rn escape and wrongly normalised standard spectrum. The average ^{238}U series normalisation factor (N_f) shown in Table 5.4 was used for converting the field activity concentrations into absolute concentrations.

These normalisation factors derived from the field stationary measurements (MEDUSA) and the laboratory measurements (HPGe) of soil samples at the stationary

spots (see Figure 5.5, step 5) are used to convert MEDUSA mobile activity concentrations (see step 1) for each radionuclide into absolute activity concentrations. This is achieved by multiplying the average normalisation factors (Table 5.4) with the corresponding MEDUSA mobile activity concentrations, for instance each ^{238}U activity concentration is multiplied by 0.54 and that is applied to all 4005 data points which were measured in 2002 and to all 7961 data points which were measured in 2010. The same procedure is applied to ^{40}K activity concentration where it is first multiplied by 0.36 for all 4005 data points which were measured in 2002 and for all 7961 data points which were measured in 2010. Finally a similar procedure is applied for ^{232}Th activity concentrations. After the conversions, preliminary normalised MEDUSA activity concentrations (indicated as step 2) are obtained.

As discussed earlier, soil moisture is a parameter which influences radon gas concentration and exhalation to a large extent (see subsubsection 5.3.1.2 above), for that reason this factor needs to be taken into account in calculating the correct activity concentrations of radionuclides as explained next.

(iv) Moisture correction factors

Soil moisture can be a source of error if not taken into account when processing data acquired during gamma ray surveying; this is because it has significant effect on the radon emanation coefficient and exhalation [Grasty, 1997; Van der Spoel, 1997].

Moisture content was accounted for by analysing 25 soil samples which were collected from around five stationary spots. A total of 25 moisture content percentages were determined using equation (4.3) and presented in Table 5.3.

In addition, the difference between the activity concentration of a moist soil sample and an oven dried soil sample was investigated. The difference in the activity concentration was worked out from a large soil sample which was dug out at spot 4. The soil sample was thoroughly mixed and divided into three equal portions. Two portions of the soil samples were placed in separate plastic bags, weighed and labelled KS41.1 (50 cm) and KS41.2 (50 cm). The other portion of the soil sample was immediately placed in the Marinelli beaker, weighed, sealed and labelled KS41.3 (Beaker). With the exception of the soil sample placed in the beaker, the other two soil samples were analysed as

discussed in sections 4.3-4.4. The soil sample, already in the beaker did not require any processing apart from storing it for three weeks to attain secular equilibrium in the ^{238}U series so as to deduce the activity concentrations. Table 5.5 presents the details.

Table 5.5: The measured activity concentration of a dry and wet soil sample from spot 4. The difference indicates the change caused by the moisture.

Sample Code	**Mass** (g)	**Activity concentration** (Bq·kg^{-1})			**Moisture** (%)
		^{238}U series	**^{232}Th series**	**^{40}K**	
KS41.1(50cm)	1409.06	245 ± 12	17 ± 1	233 ± 11	9.1
KS41.2(50cm)	1421.82	261 ± 12	18 ± 1	247 ± 12	10.4
Average	1415.44	**253 ± 12**	**18 ± 1**	**240 ± 12**	**9.8**
KS41.3 (Beaker)	1354.64	**224 ± 12**	**16 ± 1**	**223 ± 12**	-

The comparison between the average of the activity concentration of the two samples, KS41.1 (50 cm) and KS41.2 (50 cm) which were processed in the laboratory and the soil sample placed in the beaker, KS41.3 (Beaker) show a difference of about 9%. That percent difference is almost the same as what was obtained when the average moisture percent of KS41.1 (50 cm) and KS41.2 (50 cm) was calculated.

The conclusion drawn above agrees very well with models such as the ones given by De Groot (2009). Therefore, De Groot's (2009) models will be adapted to determine the moisture correction factors and thereafter correct the preliminary normalised activity concentrations depicted in Figure 5.5, step 2. In brief, according to the model, if a radionuclide j in the soil sample is considered, then the activity concentration C (Bq·kg^{-1}) will be given by:

$$C_j = \frac{A_j}{m} \tag{5.16}$$

where, A_j(Bq) is the activity and m (kg) the mass of a volume unit of soil sample. Further, assuming that mineral grains only within the soil sample contain radionuclides, then the activity concentrations for a dry soil sample will be given by:

$$C_j^{dry} = \frac{A_j}{m_{dry}} \tag{5.17}$$

where, m_{dry} represent mass of dry solids.

On the other hand if the pores in the soil sample contain water, A_j remains unchanged but the mass per unit volume increases and consequently the activity concentrations in the bulk soil sample decrease, so it can also be expressed as:

$$C_j^{wet} = \frac{A_j}{m_{wet}} \tag{5.18}$$

where, m_{wet} represent mass of the wet soil sample.

Combining equation (5.17) and (5.18) yields another expression which is

$$C_j^{wet} = C_j^{dry} \frac{m_{dry}}{m_{wet}} \tag{5.19}$$

The term (m_{dry} / m_{wet}) gives the mass of solid material with respect to the total mass of the wet soil sample. It is related to the mass of water with respect to the total mass of the soil sample, which is the absolute water content (w_a). The absolute water content can be determined from soil samples by taking the mass of the sample before (m_{wet}) and after (m_{dry}) drying and then applying equation (4.3).

Thus, C^{wet} and C^{dry} can be expressed as

$$C_j^{wet} = (1 - w_a)\ C_j^{dry} \tag{5.20}$$

Therefore, equation (5.20) suggests that an estimation of the wet activity concentrations, C^{wet} can be calculated from the dry activity concentrations, C^{dry} and vice versa. This can be applied to correct the activity concentrations of all measured environmental radionuclides. However, it does not take into account a small extra effect due to the difference in mass-attenuation coefficients of water and soil. To account for this extra effect, a correction factor θ is introduced on the right hand side of equation (5.20) which becomes [De Groot, 2009]

$$C_j^{wet} = (1 - (1+\theta)\ w_a)\ C_j^{dry} \tag{5.21}$$

This correction factor θ is radionuclide specific and it can be derived from the slopes of the linear graphs of Figures 5.6 a-c. The graphs have been generated by plotting moisture

content (%) against MEDUSA stationary activity concentration for each radionuclide. In so doing some assumptions were made that:

- The mine dump is considered fairly homogeneous; that is it only contains residues from rocks after extraction of gold. Otherwise if there are any other foreign deposits (sand, soil, quartz) on some parts of the mine dump, then it could have an effect on the attenuation coefficient.
- MEDUSA activity concentration extracted from any point in the mine dump will not vary much from MEDUSA activity concentration within a radius of 80cm. This assumption is hypothesized after analyzing the five HPGe activity concentrations obtained from the stationary spots as indicated by Table 5.3.

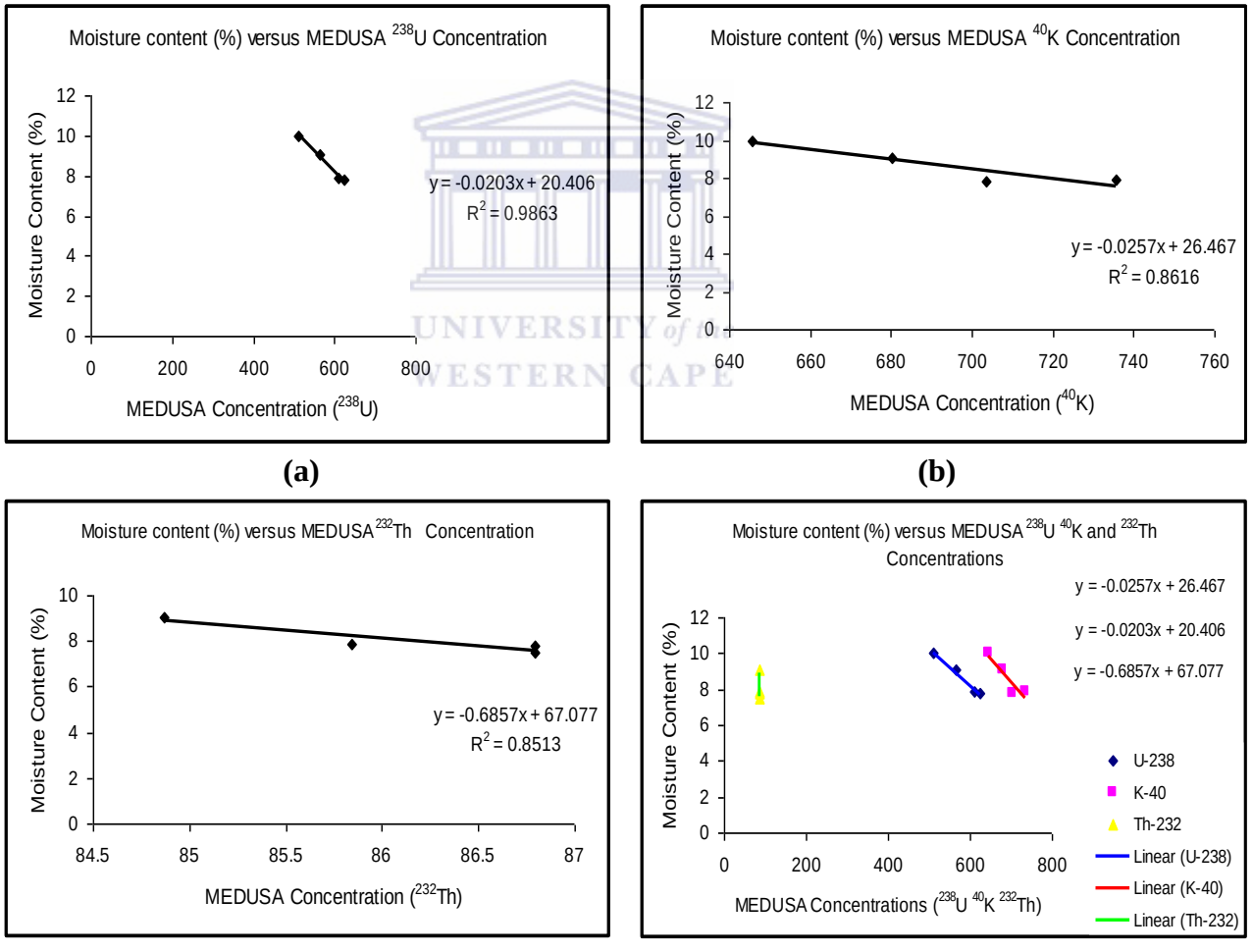

Figure 5.6 (a - c): Graphs of moisture content versus MEDUSA activity concentration at the stationary spots for ^{238}U, ^{232}Th and ^{40}K. Graph (d) represent a combination of all graphs (a-c).

Figure 5.6d presents a clear picture that the slope of ^{238}U (blue line) and ^{40}K (red line) are almost the same while ^{232}Th (green line) is different. The difference arises when fitting the standard spectra and measured data using the Full Spectrum Analysis (FSA) method. From Figure 4.8 it can be noted that the ^{238}U (1764 keV) and ^{40}K (1460 keV) regions, the standard spectra and measured data fit quite well, unlike ^{232}Th at 2614 keV.

Similarly, three linear equations (5.22-5.24) for ^{238}U, ^{40}K and ^{232}Th respectively, were generated from which the correction factor θ (slope) was extracted and applied to equation (5.20)

$$y^{U} = -0.0203x + 20.41 \tag{5.22}$$

$$y^{K} = -0.0257x + 26.47 \tag{5.23}$$

$$y^{Th} = -0.6857x + 67.08 \tag{5.24}$$

These equations (5.22-5.24) were used to predict the moisture correction factors for each radionuclide at every point in the field where MEDUSA measurements were done apart from the stationary spots. The equations were applied to 4005 data points obtained in 2002 survey and 7961 data points for the 2010 survey.

Next, the final normalised activity concentrations, F_{AC}, (indicated as step 3) for each radionuclide were generated from the preliminary normalised activity concentrations, P_{AC}, (indicated as step 2) by using the following expressions:

$$F_{AC}^{U} = P_{AC}^{U} \times \left(1 - \frac{y^{U}}{100}\right) \tag{5.25}$$

$$F_{AC}^{K} = P_{AC}^{K} \times \left(1 - \frac{y^{K}}{100}\right) \tag{5.26}$$

$$F_{AC}^{Th} = P_{AC}^{Th} \times \left(1 - \frac{y^{Th}}{100}\right) \tag{5.27}$$

where, P_{AC}^{U}, P_{AC}^{K} and P_{AC}^{Th} represent the preliminary normalised activity concentration of ^{238}U, ^{40}K and ^{232}Th, obtained when the MEDUSA activity concentration measured in the field is multiplied by the average normalisation factor of 0.54, 0.36 and 0.21, respectively. The parameters y^{U}, y^{K} and y^{Th} represent the moisture content in

percentage obtained for ^{238}U, ^{40}K and ^{232}Th using equation (5.22), (5.23) and (5.24), respectively.

Thus far, necessary corrections have been made therefore, radon flux values can be computed by applying MELT (equations 5.13-5.14). According to the MELT, the field disequilibrium activity concentrations for the radionuclides refer to the raw MEDUSA mobile data depicted in Figure 5.5 Step 1 and the laboratory equilibrium activity concentrations refer to the final normalised activity concentrations (indicated as step 3). After applying MELT to 4005 (2002 survey) and 7961 (2010 survey) data points, radon flux values are determined and indicated as step 4 in Figure 5.5, but then the values need to be normalised as discussed next.

(v) Normalisation of radon flux

MELT yields unnormalised radon fluxes at every point in the mine dump where the MEDUSA γ-ray detector system was used for measurements. Flux normalisation constants are first computed and then applied to the unnormalised radon flux. The normalisation flux constants are derived from MEDUSA stationary measurements (indicated as step 5) and the process of determining the constants is as follows:

- **Radon flux normalisation constant using ^{238}U and ^{232}Th activity concentrations**

Firstly, the unnormalised radon flux was calculated using equation (5.14), indicated as step 6. In equation (5.14), the field activity concentrations refer to the raw MEDUSA stationary activity concentrations which originate from the stationary spots and the equilibrium concentrations refer to the corresponding average HPGe activity concentrations of soil samples collected from the stationary spots (depicted as step 5). Here the moisture correction is not required since the soil samples have been oven dried. The unnormalised radon flux obtained using equation (5.14) from the stationary spots is shown in Table 5.6.

Table 5.6: Determining the radon flux normalisation constant using ^{238}U and ^{232}Th activity concentrations.

Spot	Average HPGe activity concentration		MEDUSA activity concentration		† 'Unnormalised' Flux (UF)	* 'Theoretical' Flux (TF)	Normalisation constant (TF / UF)
	^{238}U	^{232}Th	^{238}U	^{232}Th			
2	310 ± 6	17 ± 1	620 ± 80	90 ± 11	270	0.11	0.00041
3	282 ± 6	17 ±1	510 ± 60	80 ± 10	240	0.10	0.00042
4	341 ± 7	18 ±1	570 ± 70	85 ± 10	294	0.12	0.00042
5	315 ± 7	18 ±1	610 ± 75	90 ± 11	265	0.11	0.00043
Average							**0.00042**

†Unnormalised flux calculated using equation (5.14).
*Theoretical flux calculated using equation (5.2).

Secondly, the theoretical radon flux at the stationary spots was calculated using equation (5.2). According to equation (5.2) the radon decay constant, the diffusion length, the emanation coefficient, the radium content and the soil bulk density are required as the input parameters. These parameters were extracted from measurements done either in the field or determined in the laboratory. The diffusion length ($\ell \approx 40\,\text{cm}$) was extracted from the radon gas concentration (Bq·m^{-3}) measured in the mine dump using the RAD7 at various depths (see Table 3.2). Extracting the diffusion length entailed using equation (3.4) and (3.9). The emanation coefficient (E) was found to be 0.28. This value was determined in the laboratory using a cylindrical soil sample placed in a sealable accumulator jar together with electrets (see Figure 5.19) as discussed in subsubsection 5.4.3.2. The bulk density of the soil sample was determined in the laboratory and a value of about 1500 kg·m^{-3} was found (see details in subsubsection 5.4.3.2). Moreover, the laboratory-based HPGe γ-ray detector was utilised to analyse the activity concentration of the radium content in the soil samples. Sections 4.3 and 4.4 highlights the processes involved in determining the activity concentration using the HPGe γ-ray detector. Table 5.6 shows the weighted average values of the radium content at the stationary spots. Given that the half-life of radon gas (^{222}Rn) is 3.82 days, radon decay constant (λ) was computed using equation (2.3) yielding a value of $2.1\times10^{-6}\ \text{s}^{-1}$. The theoretical radon flux value computed was about 0.11 Bq·m^{-2}·s^{-1} as seen in Table 5.6 and depicted as step 7 in Figure 5.5.

Up to this stage, it is possible to compute the radon flux normalisation constant which is required to normalise the radon flux obtained earlier on (indicated as step 4). The ratio of the theoretical radon flux calculated using equation (5.2) to the unnormalised radon flux calculated using equation (5.14) gives the radon flux normalisation constants presented in Table 5.6. The table shows four radon flux normalisation constants since four stationary spots were considered. An average value of 4.2×10^{-4} kg·m^{-2}·s^{-1} was computed. This value was used to normalise, the unnormalised radon fluxes (indicated as step 4) obtained when MEDUSA mobile data is processed by utilising the ^{238}U and ^{232}Th activity concentrations.

- **Radon flux normalisation constant using ^{238}U and ^{40}K activity concentrations**

In a similar way, the procedure described above was repeated using equation (5.13) to determine the average radon flux normalisation constant when using ^{238}U and ^{40}K activity concentrations. An average value of 6.4×10^{-4} kg·m^{-2}·s^{-1} as shown in Table 5.7 was computed. This value was used to normalise, the unnormalised radon fluxes (indicated as step 4) obtained when MEDUSA mobile data is processed by utilising the ^{238}U and ^{40}K activity concentrations.

Table 5.7: Determining the radon flux normalisation constant using ^{238}U and ^{40}K activity concentrations.

Spot	Average HPGe activity concentration		MEDUSA activity concentration		† 'Unnormalised' Flux (UF)	* 'Theoretical' Flux (TF)	Normalisation constant (TF / UF)
	^{238}U	^{40}K	^{238}U	^{40}K			
2	310 ± 6	248 ± 12	620 ± 80	700 ± 85	187	0.11	0.00060
3	282 ± 6	262 ± 12	510 ± 60	660 ± 80	145	0.10	0.00070
4	341 ± 7	251 ± 12	570 ± 70	690 ± 85	202	0.12	0.00061
5	315 ± 7	254 ± 12	610 ± 75	750 ± 90	175	0.11	0.00065
Average							**0.00064**

†Unnormalised flux calculated using equation (5.13).
*Theoretical flux calculated using equation (5.2).

Note that the theoretical flux is computed using equation (5.2) with the input parameters given above. Since the same parameters are utilised, a similar theoretical

radon flux value of about 0.11 Bq·m^{-2}·s^{-1} is obtained as shown in Table 5.7 and depicted as step 7 in Figure 5.5. The two radon flux normalisation constants (4.2×10^{-4} and 6.4×10^{-4} kg·m^{-2}·s^{-1}) that have been obtained by using the MEDUSA stationary data and the HPGe data from the soil samples collected at the stationary spots are now depicted as step 8.

Finally, normalised radon fluxes (indicated as step 9) are obtained when unnormalised radon fluxes (step 4) are multiplied by the appropriate radon flux normalisation constant. The unnormalised radon fluxes originate from the MEDUSA mobile measurements (indicated as step 1). For instance, to normalise radon flux values calculated using MELT (equation 5.13), the values are multiplied by 6.4×10^{-4} kg·m^{-2}·s^{-1}, while the values calculated using MELT (equation 5.14) are multiplied by 4.2×10^{-4} kg·m^{-2}·s^{-1}.

Apart from determining the radon flux from the ground beneath the MEDUSA γ-ray detector, the Electret ion chamber method as explained in subsubsection 5.4.2.3 was used to measure atmospheric radon concentration. This radon present in the atmosphere was assumed to be there since radon is a gas which is dispersed from all parts of the mine dump to the area where measurements were done. As a result an average radon gas concentration value of about 70 Bq·m^{-3} was determined (see subsubsection 5.4.2.3). This radon concentration will give a small contribution to the MEDUSA spectrum since it has to be compared to the soil activity value of about 300 Bq·kg^{-1} which corresponds to about (300×1500) Bq·m^{-3} of soil concentration. The density of Kloof soil was found to be about 1500 kg·m^{-3}, see subsubsection 5.4.3.2. In conclusion, the atmospheric radon gas concentration was deemed to be too low to have any significant effect on the radon flux values extracted using MELT; as such no correction was made for radon gas concentration in air.

From the discussion above it is clear that two sets of normalised radon fluxes were generated where one is through the application of equation (5.13) and the other via equation (5.14). As expected the radon flux values obtained after normalisation by utilising MELT (equation 5.13 and 5.14) are within the same range as seen from the average radon flux values presented in Table 5.8. The average radon flux values were

computed by using 4005 data points for 2002 survey and 7961 data points for 2010 survey.

Table 5.8: The average radon flux values obtained using MELT when Kloof mine dump was measured in 2002 and 2010.

Survey year	**MELT method**	**Range of radon flux values** ($Bq \cdot m^{-2} \cdot s^{-1}$)	**Average radon flux values** ($Bq \cdot m^{-2} \cdot s^{-1}$)
2002	Equation (5.13)	0.03 - 0.20	0.11 ± 0.03
	Equation (5.14)	0.02 - 0.21	0.12 ± 0.02
2010	Equation (5.13)	0.04 - 0.21	0.12 ± 0.03
	Equation (5.14)	0.04 - 0.22	0.12 ± 0.03

Furthermore, the radon flux values are also presented in tri-colour maps (Figures 5.7-5.8) and Gaussian distributions (Figures 5.9-5.10). The blue, yellow and red colours indicate low, average and high radon flux values, respectively. Note that on the mine dump for the surface areas which were not covered due to the bushes, the radon flux values were interpolated using the Natural Neighbour gridding method provided by the Golden Software Surfer®8 [Golden Software, 2002]. The maps shown in Figure 5.7 represent interpolated maps generated after radon flux values have been calculated by using equation (5.13) and equation (5.14) for the 2002 survey. Similarly, Figure 5.8 represent interpolated maps generated after radon flux values have been calculated by using equation (5.13) and equation (5.14) for the 2010 survey.

As compared to the 2002 survey when a large area was covered, the area covered for the 2010 survey was smaller (see Chapter 4, Figure 4.9-4.10) hence one part of the Kloof mine dump was blanked. Therefore the interpolated radon flux for that area was not computed. The blanked area is shown as the grey area within the colour maps in Figure 5.8.

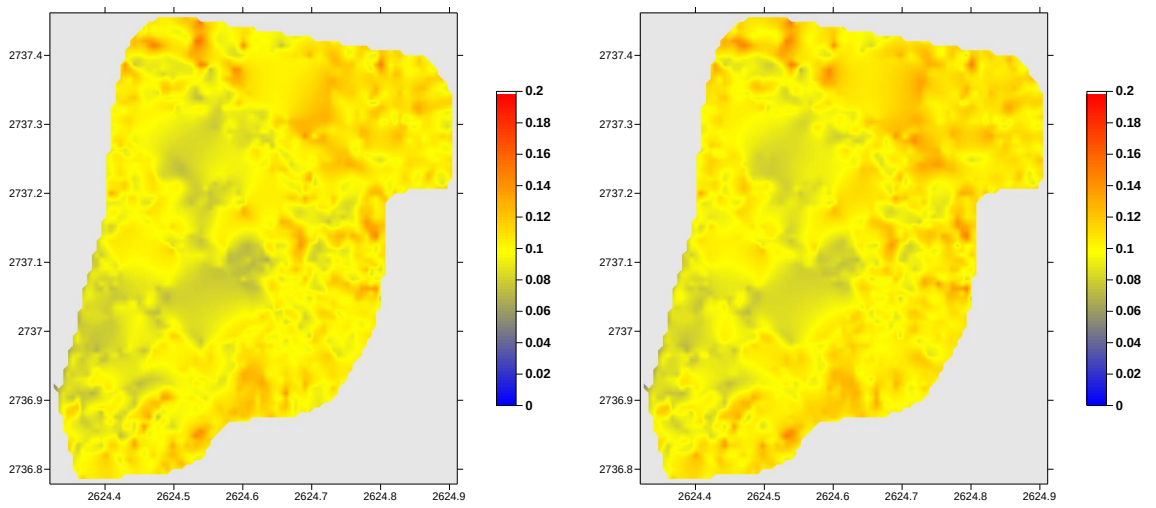

Figure 5.7: Interpolated maps generated showing radon flux values after utilising equation 5.13 (left) and equation 5.14 (right) for the 2002 survey.

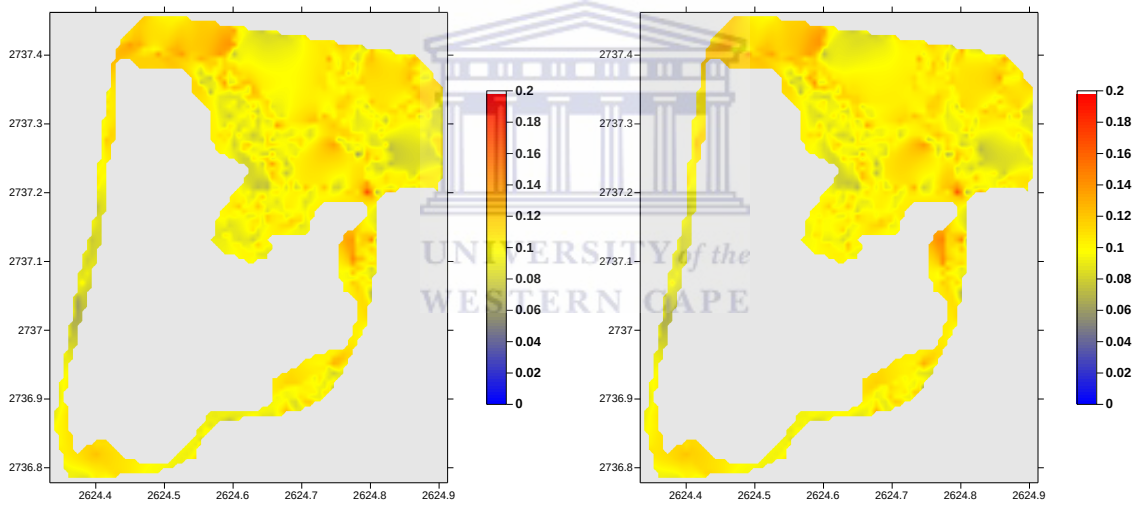

Figure 5.8: Interpolated maps generated showing radon flux values after utilising equation 5.13 (left) and equation 5.14 (right) for the 2010 survey.

Both Gaussian distributions (Figure 5.9) show a comparison of the radon flux values computed using equation (5.13) and equation (5.14) for 2002 survey on the LHS and for 2010 survey on the RHS. Moreover, the Gaussian distributions (Figure 5.10) show a comparison of the radon flux values computed using equation (5.13) on the LHS and equation (5.14) on the RHS for the 2002 and 2010 surveys.

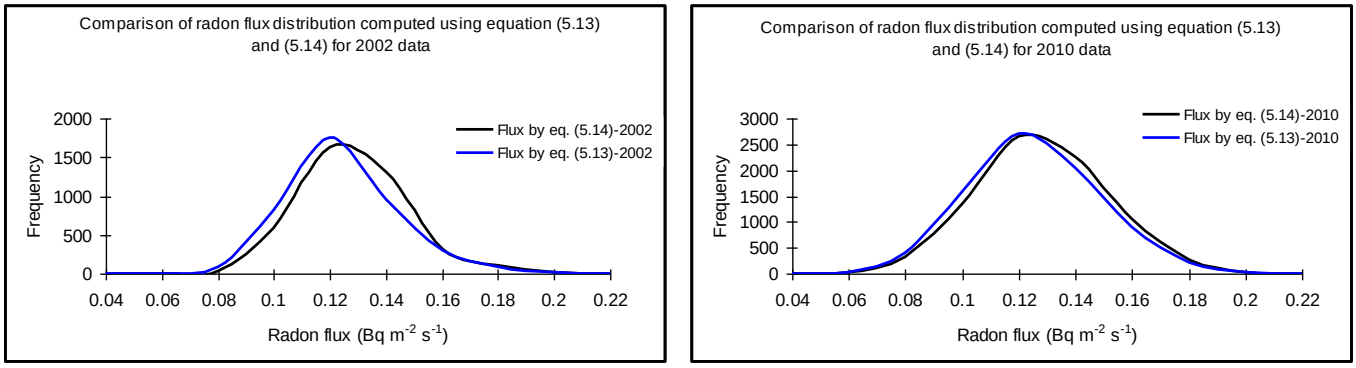

Figure 5.9: The graphs are showing radon flux values computed using equation (5.13) and (5.14) for the 2002 survey (left) and for the 2010 survey on the right.

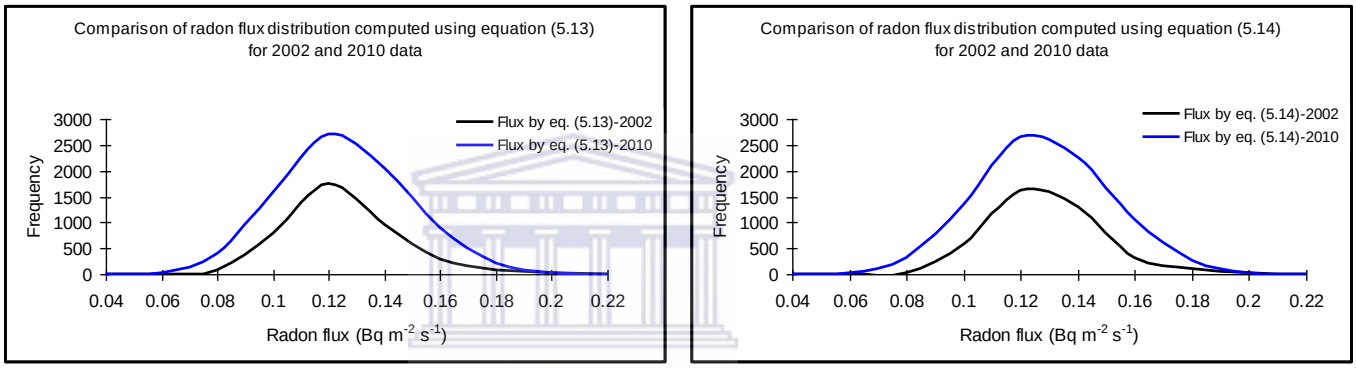

Figure 5.10: The graphs are showing radon flux values computed using equation (5.13) only (left) and equation (5.14) only (right) for the 2002 and 2010 surveys.

(Vi) Determining radon flux without taking moisture into account

Another way of extracting radon flux values is by comparing directly the ratios of the activity concentrations measured by the MEDUSA γ-ray detector in the field to the average activity concentration of the thirty four soil samples obtained from the mine dump measured using the HPGe γ-ray detector. In brief, the average activity concentrations of the thirty four soil samples measured using the HPGe γ-ray detector were 308 ± 14 Bq·kg^{-1} for ^{238}U series, 255 ± 12 Bq·kg^{-1} for ^{40}K and 18 ± 1 Bq·kg^{-1} for ^{232}Th series, see more details in subsection 4.4.2. Consequently, the radon flux values are worked out by using equations (5.13) and (5.14) where one must use the actual field activity concentrations measured using the MEDUSA γ-ray detector (indicated as step 1 in Figure 5.5) and the appropriate HPGe γ-ray detector average activity concentrations

given above. The radon flux calculated this way yields unnormalised radon flux values which do not take into account the need for the normalisation factors and the moisture content. Next, the unnormalised radon flux values obtained are multiplied by the average normalisation flux constant; in this case 6.4×10^{-4} and 4.2×10^{-4} $kg\cdot m^{-2}\cdot s^{-1}$ are used when equation (5.13) and equation (5.14) are applied, respectively. The normalisation flux constants were discussed in subsection 5.4.1. The average normalised radon flux values obtained are presented in Table 5.9 and Table 5.10.

Table 5.9: A comparison of radon flux values calculated using equation (5.5) when the normalisation factors and moisture content are (1) ignored and (2) taken into account.

Description	**Flux calculated equation 5.13** (Normalisation factors and moisture content ignored)		**Flux calculated using equation 5.13** (Normalisation factors and moisture content are taken into account)	
Year of survey	2002	2010	2002	2010
Data points captured using the MEDUSA	4005	7961	4005	7961
Data points discarded	604	2113	0	0
Data points utilised	85%	73%	100%	100%
Flux ($Bq\cdot m^{-2}\cdot s^{-1}$)	0.11 ± 0.01	0.13 ± 0.02	0.10 ± 0.01	0.11 ± 0.02

Table 5.10: A comparison of radon flux values calculated using equation (5.7) when the normalisation factors and moisture content are (1) ignored and (2) taken into account.

Description	**Flux calculated equation 5.14** (Normalisation factors and moisture content ignored)		**Flux calculated using equation 5.14** (Normalisation factors and moisture content are taken into account)	
Year of survey	2002	2010	2002	2010
Data points captured using the MEDUSA	4005	7961	4005	7961
Data points discarded	65	522	0	0
Data points utilised	98%	93%	100%	100%
Flux ($Bq\cdot m^{-2}\cdot s^{-1}$)	0.09 ± 0.02	0.10 ± 0.02	0.10 ± 0.02	0.10 ± 0.02

A closer look at Table 5.9-5.10 shows that the radon flux values obtained are within the calculated uncertainties whether the moisture content was ignored or taken into account. The result shows that the effect of moisture is not very large when the moisture content is around 10%.

5.4.2 Radon exhalation measurement using the Electret Ion Chamber (EIC) method

5.4.2.1 Description of the E-PERM method and equipment

An E-PERM (**E**lectret **P**assive **E**nvironmental **R**adon **M**onitor), also known as an **E**lectret **I**on **C**hamber (EIC), is a passive integrating ionization device requiring no batteries or power to function. The E-PERM Systems are used around the world for measuring short-term, long-term radon/thoron concentrations in air, radon in water, radon in soil and radon flux from surfaces and mill tailings [Kotrappa, 1988; Kotrappa, 1994; Kotrappa, 1996; Kotrappa, 2000]. The EIC for monitoring radon [Kotrappa, 1990] consists of three components:

(1) Electret

This is an electrostatically charged disk of Teflon. The electret disk is protected in a plastic cap which can be screwed into the electrically conductive E-PERM chamber. The positively charged electret produces an electrostatic field within the chamber, which attracts the negative ions generated by the radiation emitted by the radon and radon decay products as they undergo radioactive decay in the chamber. When the ions collect on the surface of the electret, they cause the surface voltage of the electret to decrease. The loss of surface voltage on the electret and the exposure period is used to calculate the average radon concentration in the place where the electrets were placed during exposure.

There are two types of electrets with different characteristics [Kotrappa, 1990; Rad Elec Inc., 1994 (http://radelec.com//)]. Short-term electrets (used in this work) have a high sensitivity and the less sensitive electrets are used for long-term measurements. The short and long-term electrets shown in Figure 5.11 have a usable voltage range from about 750 volts to about 200 volts. Several measurements can be made within that voltage range.

Figure 5.11: A picture of short-term and long-term electrets.

(2) An Electret Ion Chamber (EIC)

An EIC is made of a conductive plastic into which an electret can be loaded. During the decay of radon, ions are generated in the air, and since the volume of the electrically conductive chamber is fixed, the ions collect on a charged electret as a means of measuring the radiation. Figure 5.12 shows the three types of chambers (S, L and adapted H-chambers) that are available commercially from RadElec, Inc. The three types of chambers differ in their chamber volume.

Figure 5.12: A picture of a closed S-chamber on the left, L-chamber in the middle and the H-chamber on the right. The latter is shown in the adapted form used for flux measurements.

The S chamber which has a volume of about 210 ml is designed with an on-off mechanism that works with a spring-activated cap on top to enable air and radon to diffuse into the chamber during the exposure period. The S chamber can either be loaded with long or short-term electrets. The L chamber has a volume of about 50 ml and it can

either be loaded with a long or short-term electret. The H chamber is dome shaped, with a volume of about 1000 ml. It is the most sensitive to radon and it is used with short-term electrets [Rad Elec Inc., 1994].

(3) The Electret reader

This is an electronic instrument used for measuring the surface potential (voltage) of an electret. The surface voltage of the electret is measured with this special non-contact voltmeter called a SPER (**S**urface **P**otential **E**lectret **R**eader). Rad Elec Inc. has two types of electret readers that are commercially available namely: SPER-1 and SPER-2. The reader can measure surface potentials up to 1999 Volts. The picture of the electret readers is shown in Figure 5.13.

Figure 5.13: A picture of the electret readers namely SPER-2 (left) and SPER-1 (right).

A radon measurement always involves taking two voltage readings namely; an initial reading (I) before the exposure and a final reading (F) after the exposure. The difference of the voltage and the exposure time (T) information can then be converted into the radon concentration using an experimentally derived calibration factor for the chamber and electret combination. A small correction for background gamma radiation is also required. When conducting E-PERM measurements, physical factors such as temperature variations and relative humidity found in the environment hardly affect the measurements.

5.4.2.2 Radon exhalation measurement using H-chamber at Kloof mine dump

Radon exhalation at Kloof mine dump was measured using the H chambers adapted for flux measurements loaded with short-term electrets. These chambers have four filtered outlets to prevent radon accumulation; consequently radon diffusing back to the dump does not arise. When conducting radon flux measurements, a pair of H chambers is used simultaneously placed side by side. The initial voltages of the electrets were read using the SPER-1 voltmeter before exposure and then screwed onto the two H chambers. They were then gently placed and pressed on the exhaling surface. The chambers are structurally similar except that one of the chambers has a thin aluminium sheet which is in between the exhaling surface and the electret screwed at the top covering the Tyvek window that allows radon to pass freely. This chamber with an aluminium sheet is herein referred to as the "blank" (see Figure 5.14, chamber B). The purpose of the aluminium sheet is to prevent radon diffusing from the exhaling surface to the chamber; hence the voltage discharge is due to the environmental gamma radiation and environmental radon. Figure 5.14 shows a schematic representation of measuring radon flux from the ground.

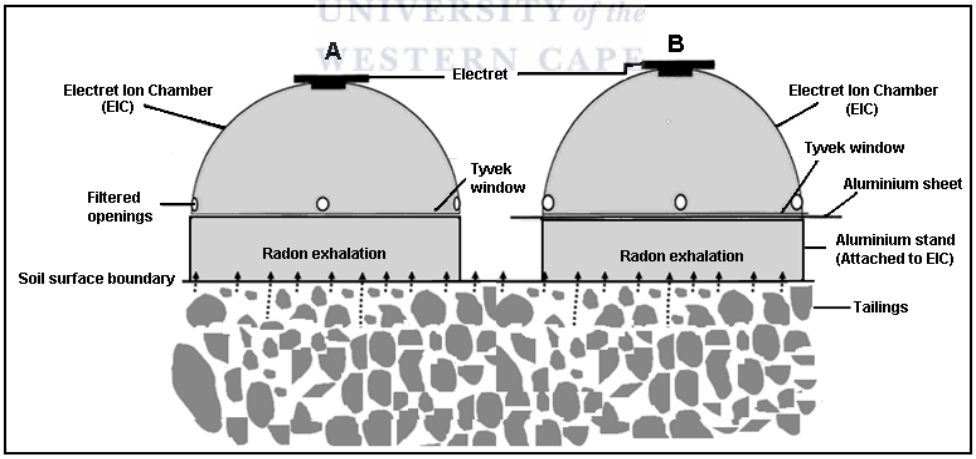

Figure 5.14: A schematic representation of measuring radon flux from the ground. The Chamber A allows radon and the Chamber B stops radon.

The radon monitoring chamber A allows radon to diffuse to the chamber from the mine dump surface because it does not have an aluminium sheet while the blank chamber B prevents (blocked by the aluminium sheet) radon from diffusing to the chamber.

Inside the chamber a semi-equilibrium radon concentration is established which is regarded as representative of the flux from the exhaling surface. Note that due to the equilibrium between the radon from the exhaling surface and radon in the outside air through the vents, the flux exhalation from the exhaling surface is not disturbed. Therefore, measuring the semi-equilibrium radon concentration gives a measure of the radon flux and this is given by the discharge rate of the electret screwed at the top of the chamber. The discharge rate (D_{Rate}) is basically the voltage drop divided by the exposure time (t) in hours and this is expressed as:

$$D_{Rate} = \frac{V_i - V_f}{t} \tag{5.28}$$

$$CF = (10.4 \pm 1.0) \times LCC \tag{5.29}$$

$$LCC = 0.7727 + 0.0004568 \times \frac{V_i + V_f}{2} \tag{5.30}$$

$$Flux = \frac{D_{Rate}}{CF} \tag{5.31}$$

where, V_i is the initial electret voltage in volts, V_f is the final electret voltage in volts, t is the exposure time in hours, LCC is the linearity correction coefficient, CF is the Calibration factor and D_{Rate} is the voltage discharge rate in volts per hour ($v \cdot h^{-1}$).

Equations (5.28-5.31) were applied to the blank and radon monitor chambers separately. The radon monitor chamber measures flux due to the contribution from radon, environmental gamma and environmental radon. On the other hand the blank chamber measures environmental gamma and environmental radon. The difference between the radon monitor chamber flux and the blank chamber gives radon flux from the ground. The net flux calculated is in flux units. The flux units are converted to SI units, $Bq \cdot m^{-2} \cdot s^{-1}$ by multiplying by 0.037 [Rad Elec Inc., 1994].

At Kloof mine dump, it was intended that electrets were to be deployed at every spot where MEDUSA stationary measurements were performed. This could provide a way to compare measurements between the two techniques. Due to practical issues, only three spots were monitored for radon fluxes using the electrets out of five spots where

MEDUSA stationary measurements were made. Radon fluxes measured using electrets at those three spots (see Figure 3.5) are presented in Table 5.11.

Table 5.11: Radon flux values measured using electrets at the three spots at the mine dump.

Spot	**Description**	**V_i** (volts)	**V_f** (volts)	**Time** (hrs)	**Discharge rate** ($v \cdot h^{-1}$)	**Flux units**	**Net flux units**	**Flux** ($Bq \cdot m^{-2} \cdot s^{-1}$)
3	Blank	570	562	8.93	0.971	0.090	0.003	**0.081 ± 0.009**
	Monitor	543	337	8.93	23.000	2.281	2.191	
3	Blank	301	291	8.93	1.120	0.119	0.004	**0.056 ± 0.006**
	Monitor	300	166	8.93	15.43	1.645	1.527	
2	Blank	578	573	5.42	0.984	0.091	0.003	**0.068 ± 0.008**
	Monitor	668	554	5.42	20.972	1.917	1.826	
2	Blank	307	302	5.42	0.923	0.097	0.004	**0.069 ± 0.008**
	Monitor	406	303	5.42	19.065	1.961	1.864	
2	Blank	677	672	4.3	1.163	0.103	0.004	**0.039 ± 0.005**
	Monitor	635	581	4.3	12.636	1.157	1.053	
2	Blank	313	308	4.3	1.085	0.114	0.004	**0.019 ± 0.002**
	Monitor	435	408	4.3	6.357	0.633	0.519	
1	Blank	684	678	4.1	1.545	0.137	0.005	**0.034 ± 0.005**
	Monitor	689	641	4.1	11.707	1.046	0.909	
1	Blank	317	313	4.1	1.057	0.111	0.004	**0.037 ± 0.005**
	Monitor	483	437	4.1	11.220	1.098	0.987	

Stationary spot 2 was measured twice; the first set of flux values obtained were 0.019 $Bq \cdot m^{-2} \cdot s^{-1}$ and 0.039 $Bq \cdot m^{-2} \cdot s^{-1}$ and the second set of values were 0.069 $Bq \cdot m^{-2} \cdot s^{-1}$ and 0.068 $Bq \cdot m^{-2} \cdot s^{-1}$. The difference might have been due to radon leaking from the sides of the chambers since it was noticed that the electret flux monitors were not firmly placed in

the exhaling ground when they were being collected. The second set of radon flux values was considered to be more trustworthy.

In 2002 an extensive study of radon exhalation from Kloof mine dump was carried out using the RadElec passive and dynamic methods [Manatunge, 2002]. Passive EICs (Electret ion Chambers) namely H-chambers loaded with short-term electrets were utilised. The same procedures for deploying and calculating radon flux discussed above for radon monitor and blank chambers were applied. During that study all radon monitor and blank chambers were exposed for a period ranging from 2.5 to 3 hours. After data analysis it was found that the radon flux ranged from 0.008 to 0.108 $Bq \cdot m^{-2} \cdot s^{-1}$ with an average of 0.062 ± 0.010 $Bq \cdot m^{-2} \cdot s^{-1}$. On the same mine dump in 2010, radon flux measured ranged between 0.034 and 0.081 $Bq \cdot m^{-2} \cdot s^{-1}$ with an average of 0.057 ± 0.019 $Bq \cdot m^{-2} \cdot s^{-1}$. Figure 5.15 displays the values of radon flux measured in 2002 and 2010 surveys. The radon flux values for 2010 survey are enclosed in the grey circles.

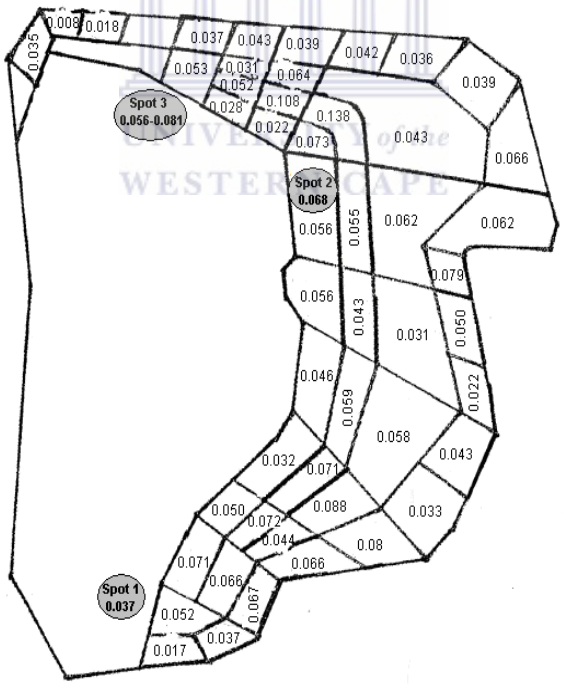

Figure 5.15: A comparison of radon exhalation values measured using H-chambers during the 2002 survey [Manatunge, 2002]. The enclosed grey circles show measurements using the H-chambers during the 2010 survey.

In addition to the passive method, Manatunge (2002) deployed a dynamic system to determine radon flux at Kloof mine dump. The dynamic system setup which was used is shown in Figure 5.16 and parts of the system were: a 12 V rechargeable battery, an aluminium box with one open end and two nozzles on the opposite ends, an air pump with an adjustable airflow, two S chambers, electrets and an electret reader. This system was used to determine radon exhalation for a period of 24 hours and during that time S-chambers with long term electrets were utilised. Radon fluxes were determined using a different CF (calibration factor) and LCC (Linearity Correction Coefficient) which can be found in the reference manual [Rad Elec Inc., 1994].

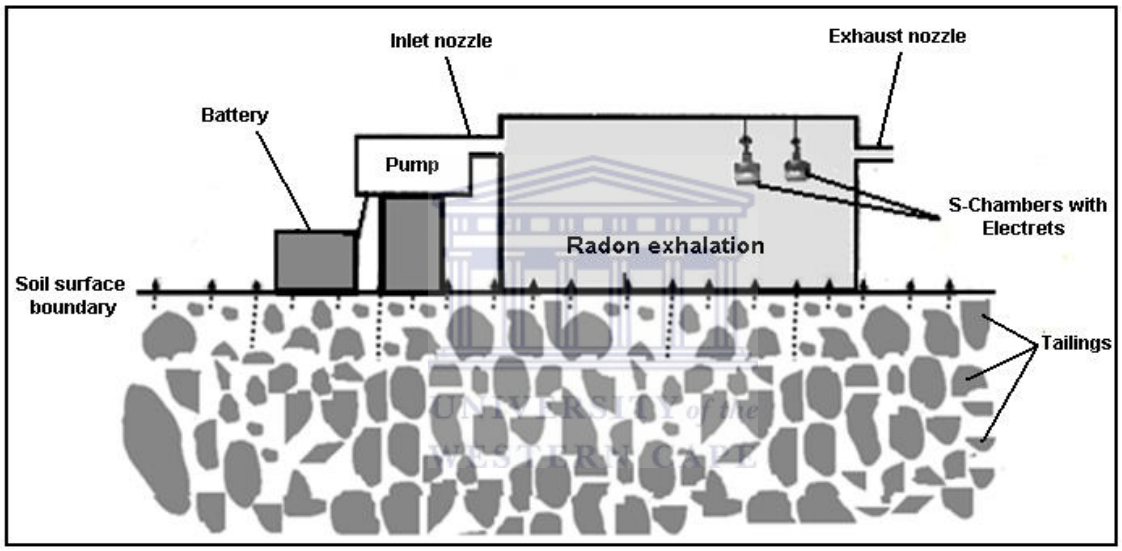

Figure 5.16: A schematic diagram of the dynamic system which was used for radon flux measurement by Manatunge (2002).

The range of the radon flux values was between 0.04 and 0.20 $Bq \cdot m^{-2} \cdot s^{-1}$ with an average of 0.12 ± 0.05 $Bq \cdot m^{-2} \cdot s^{-1}$. A summary of the radon flux values measured using the dynamic system and the location where the measurements were carried out is displayed by Figure 5.17. On the same map the radon flux values measured using the H-chambers during the 2010 survey are enclosed in grey circles for the three spots.

A comparison of the radon flux values obtained by Manatunge (2002) and the radon flux values measured during the 2010 survey are very close especially at the three spots that were investigated; see Figure 5.15 and Figure 5.17 at spot 2. The radon flux values obtained using the adapted H-chamber are found to be lower than the radon flux values

extracted from the MEDUSA γ-ray detector (see Table 7.3). The low radon flux values for the adapted H-chambers could be due to the systematic uncertainties since the chambers are placed on the exhaling ground surface to measure radon flux from a small area of about 215 cm^2.

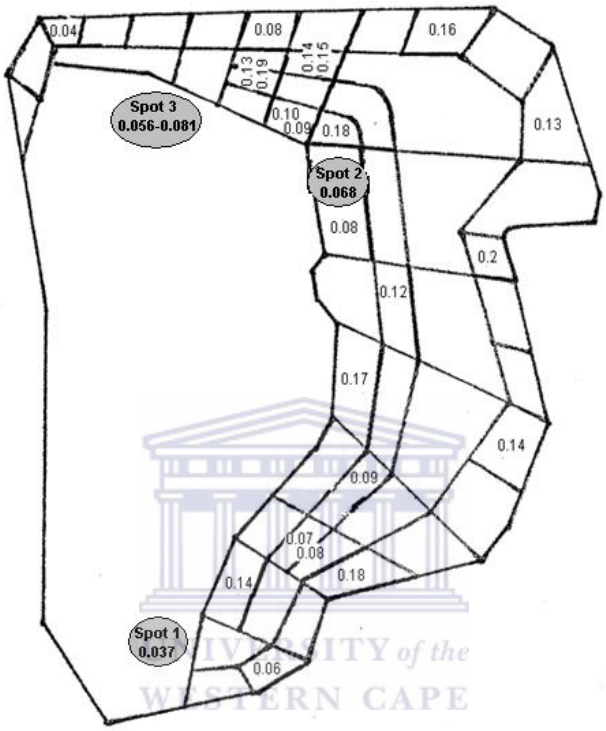

Figure 5.17: Results of the radon flux values measured using the dynamic system [Manatunge, 2002]. The enclosed grey circles show measurements using the H-chambers during the 2010 survey.

5.4.2.3 Atmospheric radon concentrations

Some component of the background radiation consists of radon which is due to the atmospheric radon and its daughters. Radon daughter products in the atmosphere contribute to the count rate in the uranium window when the MEDUSA system is used. This in turn introduces errors especially when estimating the uranium concentration. In previous airborne surveys the radon background component has been removed by one or a combination of these techniques:

(1) Spectral ratio technique

The technique is applied when the low energy ^{214}Bi photo peak at 0.609 MeV and high energy ^{214}Bi peak at 1.76 MeV is monitored. The ratio between the counts in each of these photopeak gives the relative contribution of atmospheric radon and in-ground. The photopeak at the low energy experiences less attenuation relative to the one at high energy photopeak [Minty et al., 1997b].

(2) Upward looking detector technique

This technique involves monitoring the background radiation using an upward looking detector which is partially shielded from ground radiation. The uranium window (downward looking detector) is corrected for the radon contribution using count rates recorded by the upward looking detector [Minty et al., 1997b].

The upward looking detector method and the spectral ratio method require dedicated calibrations. Another challenge which needs to be overcome is when analysing ^{214}Bi photopeak at 0.609 MeV and ^{137}Cs which occurs at 0.662 MeV with respect to the resolution of common detectors.

(3) Use of ^{214}Pb photopeak for radon removal

Jurza (2005) suggested a technique that makes use of the low energy photopeaks of ^{214}Pb. The technique utilises the Principal Component Method to establish a good quality Compton continuum to separate peaks of ^{214}Pb. Then the count rate in the window around ^{214}Pb photopeaks which has only minor interference from the thorium series is estimated.

(4) Online radon air concentration calculator

Radon air concentration can be estimated using an online uranium mill tailings radon flux calculator which is found at http://www.wise-uranium.org/ctb.html?unit=c [WISE, 2012]. Besides the general properties of the tailings (e.g. the activity concentration of ^{226}Ra) the online calculator requires specific properties of the tailings once zoning has been done. The tailings are zoned as either being submerged or being saturated or being unsaturated. The online calculator has been utilised to estimate radon air concentration near the Piñon Ridge tailings, in Colorado USA [Golder Associates Inc., 2010].

In this study an alternative, simple and straightforward method was applied to estimate atmospheric radon concentration at Kloof mine dump. This method involves extracting the atmospheric radon concentration from the adapted H-chambers which were placed in three spots where MEDUSA stationary measurements were done; see Figure 3.5 and Figure 5.15. Two H-chambers depicted in Figure 5.18 were placed next to each other about 3 m from the MEDUSA γ-ray detector. One chamber (A) was monitoring radon from the exhaling surface of the mine dump while the blank chamber (B) was monitoring the environmental gamma and environmental radon; more details are given in subsubsection 5.4.2.2. In order to determine the concentration of radon gas in the atmosphere (see Figure 5.18) the blank chamber (B) was analysed. Since the blank chamber has an aluminium sheet, radon gas is blocked from diffusing from the exhaling ground into the chamber. Therefore radon gas will get into the chamber via the filtered openings of the blank H-chamber and that radon gas is assumed to have been present in the air or dispersed from other parts of the mine dump. So by applying equation (E.1) and (E.3) given in Appendix E, radon gas concentration present in the air can be deduced. The average radon gas concentration was found to be 105 ± 30 Bq·m^{-3} before subtracting the contribution due to gamma radiation as shown in Table 5.12. However, after the background subtraction the atmospheric radon gas concentration was about 70 Bq·m^{-3}.

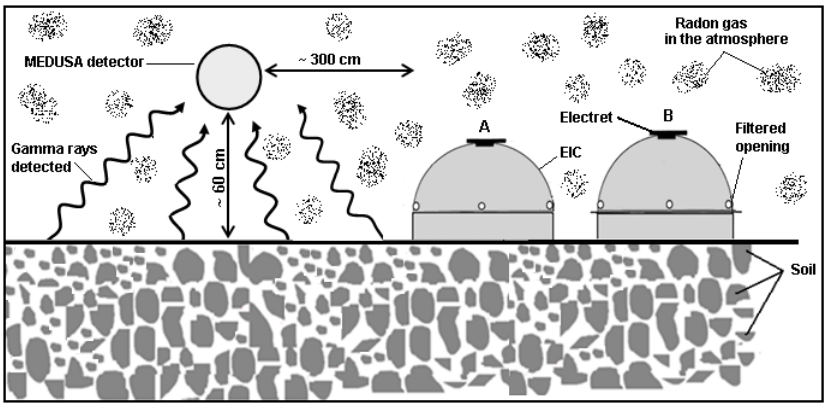

Figure 5.18: Determining the atmospheric radon concentration using the adapted blank H-chamber.

Table 5.12: The radon concentration values extracted using the adapted blank H-chamber.

Spot	V_i (volts)	V_f (volts)	Time (hrs)	Discharge rate ($v \cdot h^{-1}$)	Radon Conc. ($Bq \cdot m^{-3}$)
3	570	562	8.93	0.971	89 ± 17
3	301	291	8.93	1.120	116 ± 19
2	578	573	5.42	0.984	89 ± 24
2	307	302	5.42	0.923	95 ± 27
2	677	672	4.3	1.163	101 ± 29
2	313	308	4.3	1.085	112 ± 34
1	684	678	4.1	1.545	134 ± 30
1	317	313	4.1	1.057	109 ± 35
Average					**105 ± 30**

The atmospheric radon gas concentration found will make a very small contribution to the MEDUSA spectrum. The contribution is considered small when it is compared to the measured radon soil gas concentration which was found to range from a few thousands to hundred thousands of $Bq \cdot m^{-3}$ as Table 3.2 shows. Therefore the effect of atmospheric of radon gas concentration on the MEDUSA γ-ray measurements was believed to be very small; as a result it was not considered when the final normalised radon flux values (see Figure 5.5 step 9) were calculated.

5.4.3 Radon exhalation calculation using the IAEA expression

5.4.3.1 Radon flux at the surface of a tailing mine dump

An algorithm presented by the International Atomic Energy Agency (IAEA) relates radon flux, F ($Bq \cdot m^2 \cdot s^{-1}$) to the radium content, C_{Ra} ($Bq \cdot kg^{-1}$); bulk density, ρ_b ($kg \cdot m^{-3}$); emanation coefficient, E (dimensionless); radon decay constant, λ (s^{-1}) and effective diffusion coefficient, D ($m^2 \cdot s^{-1}$). These factors are quantitatively related and mathematical expressions are provided to calculate radon releases from bare and covered tailings.

The IAEA (1992) report suggests that if the tailings dam is regarded as homogeneous and of thickness above 2m, then the flux is given by:

$$F = C_{Ra}\, \rho_b\, E \sqrt{\lambda D} \tag{5.32}$$

Equation 5.32 presents main factors directly affecting radon releases. The values for these factors are normally obtained by direct measurement and if measurements are not done, estimates using empirical relationships that are found in the literature are made to deduce the values.

5.4.3.2 Estimation for input parameters and variables

(1) Radium content (C_{Ra})

In order to apply equation (5.32) the radium activity concentration value used was derived from the average uranium activity concentration. The average value for the activity concentration was obtained from 34 soil samples collected from 5 spots in the field. The soil samples were processed by sieving them and storing them for three weeks to attain secular equilibrium and then they were measured using the HPGe detector system as discussed in section 4.3. The average radium activity concentration computed was 308 ± 14 Bq·kg^{-1}.

(2) Dry bulk density (ρ_b)

A solid soil sample from Kloof mine dump was chipped carefully and placed in a measuring beaker. The dry cylindrical soil sample inside the measuring beaker was 6.41 cm in height and 7.97 cm in diameter, weighing 487.9 g. The dry bulk density was calculated using this expression:

$$\rho_b = \frac{m}{v} \tag{5.33}$$

where ρ_b is the dry bulk density, m is the mass of the dry sample and v is the total volume of soil and air (cm^3). The average dry bulk density obtained from the expression above was 1.50 ± 0.16 g·cm^{-3}.

(3) Soil particle density (ρ_s)

Soil particle density refers to the density of the soil particles only. On the other hand bulk density encompasses the total volume of the solid particles (mineral and organic) together

with the pore spaces where air and water are found in the soil. Soil particle density was measured using the following procedure:

A soil sample was placed in an empty pre-weighed graduated cylinder (M_{cyl}). The total mass of the soil sample and the graduated cylinder ($M_{soil+cyl}$) was recorded. The mass of soil (M_{soil}) was obtained by subtracting M_{cyl} from $M_{soil+cyl}$. Water was added to the graduated cylinder containing the soil sample until the soil was saturated and after that the mass ($M_{water+soil+cyl}$) recorded. It was then left to stand for 3 hours. The difference between $M_{water+soil+cyl}$ and $M_{soil+cyl}$, gave the mass of water (M_{water}) added. Since the density of water is 1 g/cm^3, the volume of water (V_{water}) added was computed by dividing M_{water} by the density of water. Next the volume on the graduated cylinder was read and recorded. This volume represents the total volume ($V_{soil+water}$) of the soil sample plus the amount of water that was added. The volume of the soil sample V_{soil} was determined by subtracting V_{water} from $V_{soil+water}$. Finally, the soil particle density was calculated as:

$$\text{Soil Particle density}\,(\rho_s) = \frac{M_{soil}\ (\text{Mass of soil})}{V_{soil}\ (\text{Volume of soil})} \tag{5.34}$$

The average soil particle density calculated by the method described above was 2.50 ± 0.27 g·cm^{-3} which is in close agreement to the density of SiO_2 which is equal to 2.6 g·cm^{-3}.

(4) Porosity (ε)

The term porosity refers to the fraction of pore space of the soil. Usually the pore spaces are occupied by fluids (water and air). Porosity can be deduced from the dry bulk and soil particle densities using the mathematical expression below:

$$\text{Porosity} = 1 - \left(\frac{\text{Dry bulk density}}{\text{Soil particle density}} \right) \tag{5.35}$$

With a dry bulk density of 1.5 ± 0.16 g cm^{-3} and soil particle density of 2.5 ± 0.27 g·cm^{-3}, a value of 0.38 ± 0.04 was obtained.

(5) Emanation coefficient (E)

The emanation coefficient is defined as the fraction of radon atoms generated which escape the solid phase in which they are formed and are free to diffuse through the bulk

medium. The emanation coefficient is also referred to as the emanation fraction or the emanating power. The emanation coefficient varies with a number of parameters for instance the fluid filling inter-grain pore space, the particle size, uranium mineralogy and uranium ore grade [IAEA, 1992]. An investigation to determine the emanation coefficient was performed at the Physics Department of the University of Western Cape using a sealable glass jar, an Electret ion Chamber (S-Chamber), a short-term electret and a solid cylindrical Kloof soil sample measuring 6.41 cm in height and 7.97 cm in diameter, weighing 487.9 g as shown in Figure 5.19.

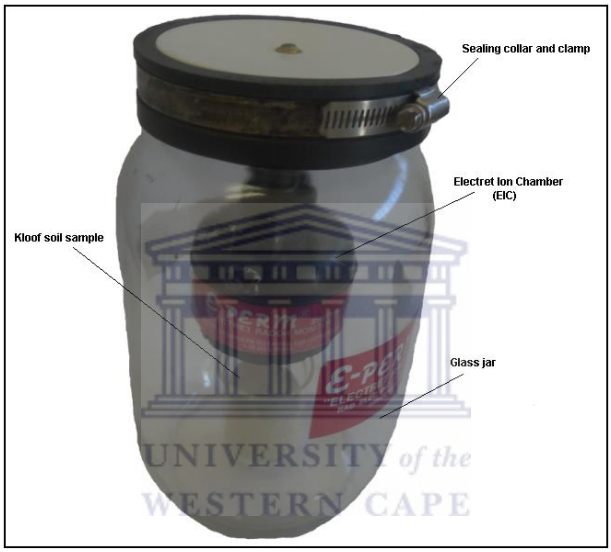

Figure 5.19: A picture showing the set-up for measuring the emanation coefficient of radon using a solid cylindrical Kloof soil sample in a sealable glass jar.

To estimate the radon emanation coefficient entails determining the radium content (C_{Ra}) in the mine dump soil samples and radon escaping from ^{226}Ra bearing soil. The HPGe γ-ray detector system is utilised to quantify the radium content (C_{Ra}) and in this case an average value of 308 Bq·kg^{-1} was calculated for Kloof mine dump soil (see subsubsection 4.4.2.1). On the other hand, the E-PERM technology [Kotrappa, 1994; Rad Elec Inc., 1994; Collé, 1995; Kotrappa, 2009] uses a direct method called the Radon Emanating ^{226}Ra Concentration (RnERaC) to make measurements in Bq·kg^{-1} of the emanating part. The RnERaC is the concentration of that fraction of ^{226}Ra in the soil which is emitting radon, so it does not refer to the radionuclide concentration of ^{226}Ra.

The expression used to determine the RnERaC is given below with other details in Appendix D:

$$\text{RnERaC} = \frac{C_{Rn} V_a}{m}\left[1 - \frac{(1 - e^{-\lambda T_a})}{\lambda T_a}\right]^{-1} \tag{5.36}$$

where, C_{Rn} is the radon activity in $Bq \cdot kg^{-1}$, m is the mass of the soil sample in grams, V_a is the air volume in the accumulator jar in litres, λ is the decay constant of radon per day and T_a is the accumulation time in days.

The ratio of the RnERaC and C_{Ra} gives the radon emanation coefficient (E) as follows:

$$E = \frac{\text{RnERaC}}{C_{Ra}} \tag{5.37}$$

The radon emanation coefficient estimated using the sealable glass jar (Figure 5.19) is 0.28 ± 0.03 for the oven dried solid cylindrical soil sample. Table 5.13 and Figure 5.20 display radon emanation coefficients of the solid cylindrical soil sample at various moisture percentages. This sample is small enough so that all the radon that enters the pore space is assumed to escape.

Table 5.13: Emanation Coefficients of a cylindrical soil sample at various moisture percentages.

Mass (g)	**Moisture** (%)	**Time** (days)	***Radon Conc.** ($Bq \cdot m^{-3}$)	**RnERaC**	**Emanation Coefficient**
160.3	29.69	0.83	213	71	0.23 ± 0.02
156.3	26.46	0.83	303	103	0.33 ± 0.03
151.9	22.90	0.83	239	84	0.27 ± 0.03
147.4	19.26	0.83	239	86	0.28 ± 0.03
143.3	15.94	0.83	240	89	0.29 ± 0.03
137.4	11.17	0.83	229	88	0.29 ± 0.03
123.6	0	0.90	199	85	0.28 ± 0.03

Accumulator jar volume = 3.8 litres, Radon decay constant = 0.1813 per day, Dry mass = 123.6 g. *Radon concentration calculated using Equation (E.1) and (E.2) given in Appendix E.

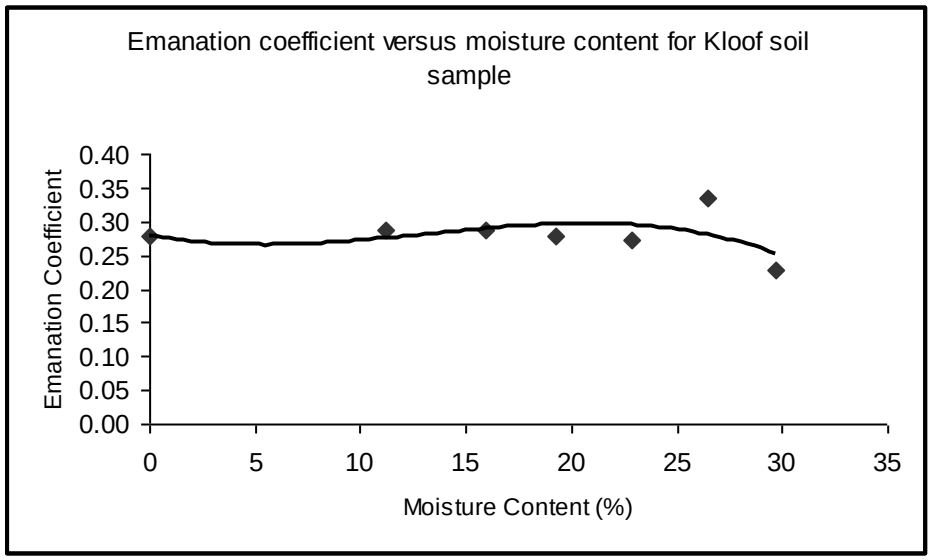

Figure 5.20: A graph showing the emanation coefficient of a cylindrical soil sample at various moisture percentages. The solid line is intended to "guide the eye ".

The emanation coefficient value obtained above is within the range of between 0.13 and 0.39 that Speelman (2004) determined from a series of similar experiments. The radon emanation coefficient experiments by Speelman (2004) were performed using soil samples weighing 30-40 grams from Kloof mine dump which were put in the sealable glass jar using a Petri dish.

According to the IAEA (1992) emanation coefficients for mill tailings generally range from 0.03 to 0.5. If specific measurements of the emanation coefficient are not made then a value of 0.35 can be used.

(6) Radon diffusion coefficient (D)

The molecular or atom diffusion behaviour of radon gas within the pore space of material can be described by Fick's law, which states that the flux density of the diffusing substance is linearly proportional to its concentration gradient. This corresponds to the first term on the right hand side of equation (3.2) for time independent conditions. Fick's law can be expressed as follows:

$$J = -D_o \nabla C \qquad (5.38)$$

where, J is a vector representing the density flux of radon activity ($Bq \cdot m^{-2} \cdot s^{-1}$), ∇C is a vector representing the gradient of radon activity concentration in the air ($Bq \cdot m^{-3}$) and D_o is the diffusion coefficient of radon in open air ($m^2 \cdot s^{-1}$).

In porous, media like soil, Fick's equation can be written in four different ways depending on whether the bulk or pore volume is used to define the concentration and whether the bulk or pore area is used to define the flux density. Because of these different ways of describing the radon diffusion coefficient in soil, it has led to some confusion in selecting and using parameters since the symbols and nomenclature used have not been standardized [Nazaroff et al, 1988].

In the literature two distinct ways of defining the diffusion coefficient of radon have been adopted that is: (1) D_e is the effective radon diffusion coefficient and (2) D is the bulk radon diffusion coefficient. The effective radon diffusion coefficient, D_e, is defined from Fick's equation as the ratio of the effective flux density of radon activity across the pore area, to the gradient of the radon activity concentration in the pore or interstitial space. The bulk radon diffusion coefficient, D, is defined as the ratio of the diffusive flux of radon activity across a geometric or superficial area of the medium to the gradient of the radon activity concentration in the pore space. In soil, the bulk radon diffusion coefficient, D, and the effective radon diffusion coefficient, D_e, are associated by the soil porosity, ε, according to the following expression:

$$D = \varepsilon D_e \ . \tag{5.39}$$

Radon diffusion coefficients can be measured either in the field [Culot, 1976; Gadd, 1995; Jarzemba, 1996] or in the laboratory [Rogers & Nielson, 1991b; Nielson et al., 1994; Van der Spoel, 1998; Oufni, 2003]. In most cases, laboratory methods are frequently used to determine the radon diffusion coefficient in porous media and particularly in soil materials and if laboratory methods are used then they are based on the solution of the mass balance equation that represents the diffusion process in a one-dimensional configuration [EAD, 2011].

It has been noted that soil moisture content has an influence on the effective diffusion coefficient of radon in soil [Rogers & Nielson, 1991b; Van der Spoel, 1998]. Van der Spoel (1998) measured the diffusion coefficient as function of moisture content for 14

experiments and came up with an alternative empirical function that almost resembles equation (5.40), below.

Rogers & Nielson (1991b) proposed an expression based on over a thousand laboratory measurements of radon gas diffusion in recompacted soils [Nielson et al., 1994] relating the diffusion coefficient, soil porosity and the water saturation content as follows:

$$D = \varepsilon D_o \exp(-6S\varepsilon - 6S^{14\varepsilon}) \tag{5.40}$$

where, $D_o = 1.1\times10^{-5}\ m^2\cdot s^{-1}$ is the radon diffusivity in open air, ε is the soil porosity, and S is the water saturation in the soil (or the fraction of pore space filled with water, also called the saturation ratio). The water saturation in the soil, S, is estimated using this expression [Nielson et al., 1994]:

$$S = \frac{\rho M_w}{\rho_w \varepsilon} \times \frac{1}{100} \tag{5.41}$$

where, ρ is the dry bulk density ($kg\cdot m^{-3}$) of Kloof soil, M_w and ρ_w are soil water content (dry weight percent) and density of water ($kg\cdot m^{-3}$) respectively.

In this study the soil porosity and soil moisture content values were determined in the laboratory; it was possible to deduce the radon diffusion coefficient (D) by applying the mathematical expression given by equation (5.40). The diffusion coefficient (D) was estimated to be about $3.5\times10^{-7}\ m^2\cdot s^{-1}$. This radon diffusion coefficient value is in good agreement with a previous estimated value of $4.2\times10^{-7}\ m^2\cdot s^{-1}$ for the Kloof mine dump [Motlhabane, 2003].

Up to now all parameters that are required to estimate the radon flux from the mine dump surface as per equation (5.32) have been discussed. Therefore applying the values of those parameters in equation (5.32), the average radon flux value for Kloof mine dump is deduced to be $0.11\pm0.02\ Bq\cdot m^{-2}\cdot s^{-1}$. Tables 5.14-5.15 present the parameters used and the results obtained.

Table 5.14: The values of the parameters (radium content, dry bulk density, emanation coefficient and diffusion coefficient) used in equation (5.32).

Radon Decay λ (s^{-1})	**Diffusion Coefficient** **D** ($m^2 \cdot s^{-1}$)	**Emanation Coefficient** **E**	**Dry bulk density** ρ_b ($kg \cdot m^{-3}$)	**Radium Content** C_{Ra} ($Bq \cdot kg^{-1}$)	**Constant Factor** $M = E\ \rho_b \sqrt{(\lambda\ D)}$
2.10×10^{-06}	3.51×10^{-07}	0.28	1530	308	3.65×10^{-4}

Table 5.15: The average radon flux values obtained using the IAEA expression (equation 5.32) when the mine dump was measured in 2002 and 2010.

Year of survey	**Range of radon flux values** ($Bq \cdot m^{-2} \cdot s^{-1}$)	**Average radon flux values** ($Bq \cdot m^{-2} \cdot s^{-1}$)
2002	0.03 - 0.20	0.12 ± 0.02
2010	0.04 - 0.20	0.12 ± 0.02

A constant factor, M, is given in Table 5.14. The constant factor represents the product of the emanation coefficient, the dry soil bulk density, and the square root of radon decay constant and the diffusion coefficient which is 3.65×10^{-4} $kg \cdot m^{-2} \cdot s^{-1}$. Sahoo (2010) measured radon flux values at 40 gridded locations from a uranium tailings pile at Singbhum shear zone in Jharkhand state of India. A constant factor of about 8.3×10^{-4} $kg \cdot m^{-2} \cdot s^{-1}$ was extracted from the slope of a linear fit between the radon flux values measured and the radium values of the uranium tailings. Assuming a constant factor of 3.65×10^{-4} $kg \cdot m^{-2} \cdot s^{-1}$ for Kloof mine dump, radon flux values were computed using equation (5.32) where the radium activity concentration refers to the final normalised activity concentration of uranium (indicated as step 3 in Figure 5.5). The radon flux values calculated are presented in Figure 5.21-5.22 after interpolation has been done using the Golden Software Surfer® 8 [Golden, 2002].

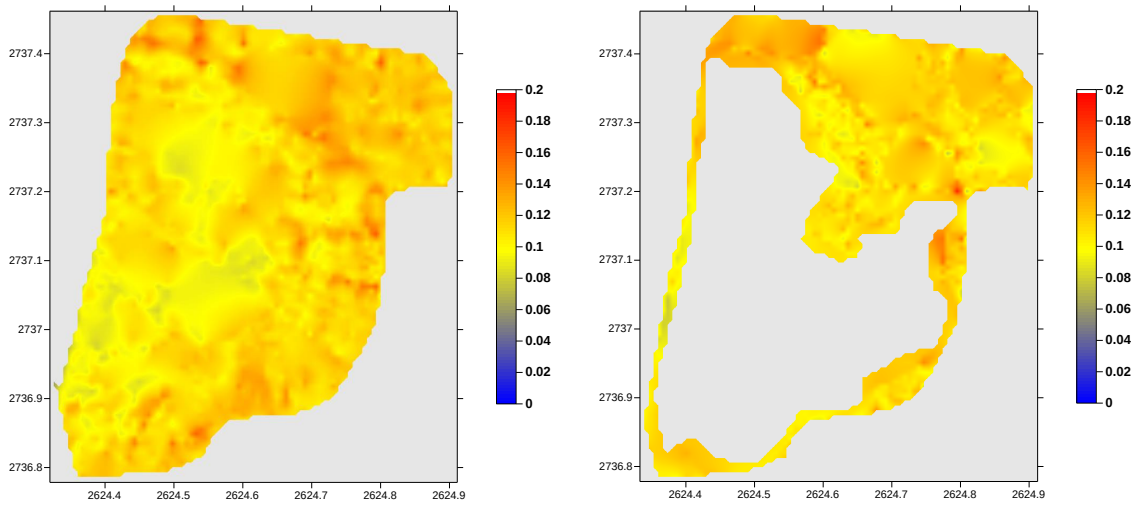

Figure 5.21: Interpolated maps generated showing radon flux values after utilising equation (5.32) on both 2002 survey (left) and 2010 survey (right).

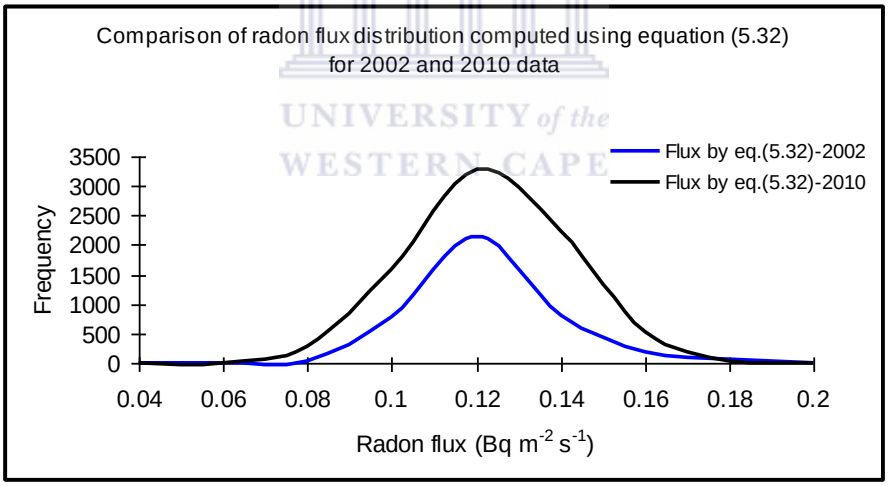

Figure 5.22: A comparison of radon flux distribution calculated using the standard formula (equation 5.32) for 2002 and 2010 surveys.

5.5 Discussion and Conclusion

Amongst the available techniques, the electrets with the adapted H-chambers, the standard formula (equation 5.32) given in IAEA (1992) and the new alternative method (MELT-equation 5.13 and 5.14) have been used in this study to assess quantitatively the radon flux values. The average radon flux value obtained while utilising the electrets with the adapted H-chambers was 0.06 ± 0.02 Bq·m^{-2}·s^{-1}. This radon flux value is lower than the values obtained using MELT or the standard formula (see Table 7.3 and Figure 7.2). It is believed that the radon flux values could be lower because the measuring device is placed on the ground surface of the mine dump but then it covers only a small area of about 215 cm^2, hence the device is prone to systematic uncertainties.

The MELT yield an average radon flux value of 0.12 ± 0.02 Bq·m^{-2}·s^{-1} when it is applied (see Table 5.8 and Table 7.3). Given that equation (5.13) and equation (5.14) use ^{40}K and ^{232}Th respectively, we believe that it yields better results because some correction is made for differences of attenuation. The average radon flux value obtained when the standard formula is utilised is 0.12 ± 0.02 Bq·m^{-2}·s^{-1}.

A comparison is presented (Figure 5.23-5.24) showing the distribution of radon flux values when the standard formula (equation 5.32) and MELT are used. It was found that 63% of the data points for the 2002 survey give radon flux values between 0.1 and 0.14 Bq·m^{-2}·s^{-1} when MELT is applied compared to 72% of the data points when the standard formula is used. For the 2010 survey, 79% of the data points give radon flux values between 0.1 and 0.14 Bq·m^{-2}·s^{-1} when MELT is applied as compared to 89% of the data points when the standard formula is used. Clearly, it indicates that more data points (~10% more) result in radon flux values between 0.1 and 0.14 Bq·m^{-2}·s^{-1} when the standard formula is compared to MELT. This leads to radon flux values being distributed around the average value 0.12 ± 0.02 Bq·m^{-2}·s^{-1} for both 2002 and 2010 surveys when the standard formula is utilised whereas a normal distribution is seen leading to the distribution of radon flux values around the linear dependency (see Figure 7.3-7.4). Table 5.16 shows the differences between MELT (equation 5.13 and 5.14) and the IAEA standard formula (equation 5.32) methods.

A new method (MELT) has been applied to determine radon exhalation from a large area (approximately 2 km^2) on the Kloof mine dump. The new method includes the absorption differences by using the ^{40}K or ^{232}Th series values at the individual points. Radon flux values obtained using MELT (see Table 5.8), the Electret Ion Chamber method and the IAEA expression (see Table 5.15) agree quite well which implies that the new method (MELT) can produce reliable results on a large scale.

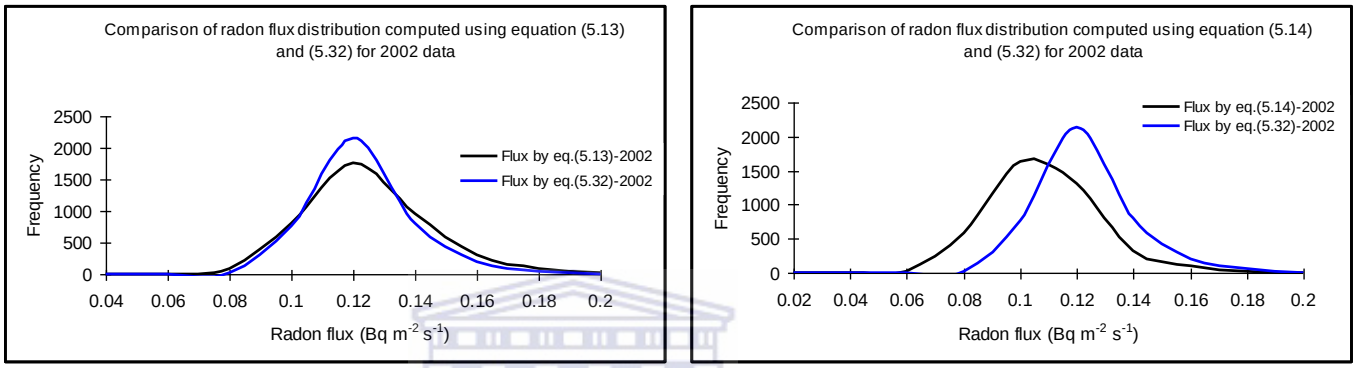

Figure 5.23: A comparison of radon flux distribution calculated using equation 5.13 (left) and equation 5.14 (right) with radon flux calculated using equation (5.32) for 2002 data.

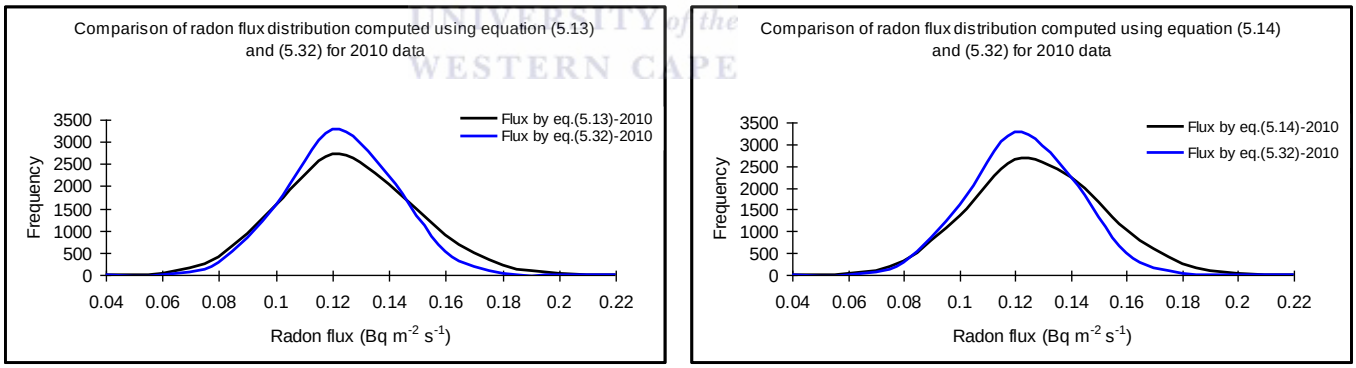

Figure 5.24: A comparison of radon flux distribution calculated using equation 5.13 (left) and equation 5.14 (right) with radon flux calculated using equation (5.32) for 2010 data.

Table 5.16: The differences between MELT (equation 5.13 and 5.14) and the IAEA standard formula (equation 5.32) methods.

MELT Flux calculated using equation (5.13) and (5.14) $J = {}^{238}U_H \cdot \left[1 - \left(\frac{{}^{238}U_M / {}^{40}K_M}{{}^{238}U_H / {}^{40}K_H} \cdot \frac{N_f^U}{N_f^K} \right)\right]$	**IAEA standard formula** Flux calculated using equation (5.32) $F = C_{Ra}\, \rho_b\, E \sqrt{\lambda D}$
1. In order to get the unnormalised radon flux value, the ratio between the field activity concentration and the equilibrium activity concentration is worked out, and then it is subtracted from unity. The fraction obtained is then multiplied by the equilibrium activity concentration of ^{238}U series. The equilibrium activity concentration for the 4005 and 7961 data points for the 2002 and 2010 surveys, respectively were estimated using normalisation factors, as discussed in subsection 5.4.1 (iii-iv). The unnormalised radon flux is then multiplied by a radon flux normalisation constant to normalise it.	- The radon flux value is obtained by multiplying the equilibrium activity concentration of ^{238}U series, the dry bulk density, emanation coefficient and the square root of radon decay constant and the diffusion coefficient. The equilibrium activity concentration for the data points for the 2002 and 2010 surveys were estimated using normalisation factors, as discussed in subsection 5.4.1 (iii-iv).
2. Radon flux normalisation constant is required to normalise the unnormalised flux. Therefore equation (5.2) together with equation (5.13) and (5.14) were used to determine the radon flux normalisation constant. Equation (5.2) requires the diffusion length, the emanation coefficient, the bulk density, the radium content and the decay constant of radon as the input parameters. These parameters were extracted from measurements done either in the field or at the laboratory.	- Radon flux normalisation constant is not required, however according to equation (5.32) the effective diffusion coefficient is required. Equation (5.40) together with equation (5.41) was used to determine the diffusion coefficient. Parameters like soil porosity, the water content percentage and the bulk density required for equation (5.40) and (5.41) were determined in the laboratory.
3. The results obtained indicate that the flux is distributed around the linear dependence when the uranium activity concentration is correlated with the radon flux see Figure 7.3-7.4. The correlation reflects that there is spatial variation.	- The results obtained indicate a linearlised correlation as it is expected between the uranium activity concentration and the radon flux.
4. The normalisation factors and moisture correction factors were used to estimate the equilibrium activity concentration as it could be measured by the HPGe detector. Equations (5.22-5.24) were used to predict the moisture content in the field.	- The moisture content at the stationary spots was determined from soil samples collected. Then by relating the moisture content and the MEDUSA activity concentration (see Figure 5.6a-d) at the stationary spots linear models were developed.

Chapter 6

The Hybrid Method

6.1 Introduction

The laboratory-based HPGe and the MEDUSA γ-ray detector systems have been used to analyse the activity concentrations of the natural radionuclides namely ^{238}U, ^{40}K and ^{232}Th. The traditional windows method was utilised to quantify the activity concentrations from the HPGe spectra while the Full Spectrum Analysis (FSA) method [De Meijer, 1998; Hendriks et al., 2001] was utilised to analyse the MEDUSA spectra. A detailed account on the procedures and interpretation of the data is described in Chapter 4. In addition, Chapter 5 has illustrated how to extract radon fluxes from Kloof mine dump by applying a new technique referred to in this study as the MELT (**ME**DUSA **L**aboratory **T**echnique).

The analysis in Chapter 5 showed that different normalisation factors in the FSA fits are needed for ^{40}K, ^{232}Th series and ^{238}U series as presented in Table 5.3. This indicates that the soil used in the model to create the standard spectra for use in the FSA method, had different absorption characteristics to the real soil on the mine dump or that the FSA fit is not good. The FSA fits tend to get the radionuclide with the lowest concentration wrong in order to fit the continuum better as discussed before. In order to investigate the FSA fit, another approach is used in this Chapter referred to as the hybrid method. The hybrid approach will be used in this Chapter and the flux values extracted in this way will be compared to the radon flux values obtained in Chapter 5.

6.2 Spectral analysis using the traditional Windows and FSA methods

In the traditional windows method regions of interest in a photopeak are defined manually, then the activity concentrations of radionuclides are determined by summing the intensity of the spectrum found in those peaks. The expression for computing the activity concentrations is given by equation (4.4). Although, the windows method is

mostly utilised for γ-ray radiometric analysis, it has its own shortcomings since it utilises a limited amount of spectral information in the actual analysis. Another shortcoming is that it applies the stripping factors when determining the contributions of radiation from one radionuclide into the peak of another radionuclide. The application of these stripping factors leads to propagation of uncertainties [Limburg, 2009].

As opposed to the windows method, the Full Spectrum Analysis (FSA) method incorporates almost all of the spectral data present in the measured gamma spectrum to extract activity concentrations of radionuclides from the γ-ray spectra. In FSA, a chi-squared minimization algorithm is used to fit a set of "Standard Spectra" to the measured spectrum and measured background which yields multiplication factors which are used to reconstruct the measured spectrum from the standard spectra. Then the activity concentrations are extracted [De Meijer, 1998; Hendriks et al., 2001].

6.3 Spectral analysis using the Hybrid Method

The Hybrid method basically incorporates the advantages of the FSA and the traditional windows method to analyse the γ-ray spectrum. The hybrid method estimates the continuum contributions by using the wide, nuclide dominated windows and the standard spectra[†] of the γ-ray spectrum [Talha, 2009; Mlwilo, 2010; Maleka, 2010].

The analysis using the hybrid method begins by dividing the γ-ray spectrum into four distinct energy regions in the range of 1.3-3.0 MeV. Figure 6.1 illustrates those regions where region I represents the cosmic background region and it is set between 2.75 MeV and 3.0 MeV. Region II represents thorium region and it mainly contains the ^{208}Tl peak (^{232}Th series) as well as the background. It is set between 2.40 MeV and 2.75 MeV. Next, region III which represents the uranium region is between 1.60 MeV and 2.40 MeV. It mainly contains two ^{214}Bi peaks, some ^{232}Th and the background. Lastly, region IV represents the potassium region in an interval between 1.3 MeV and 1.60 MeV. Region IV mainly contains ^{40}K, some ^{232}Th and^{238}U peaks as well as the background. After defining these regions, the ^{40}K radionuclide and the other radionuclides in the decay

[†] Standard spectra – represent the response of the detector in a given geometry to the activity concentration of 1 Bq·kg^{-1} of a given radionuclide.

series of ^{232}Th and ^{238}U are analysed within that range starting from region I [Talha, 2009; Maleka, 2010].

Just like in the traditional windows method and the FSA method, the background spectrum is also incorporated in the analysis of the measured spectrum. A background spectrum measured using the MEDUSA system near the surface of Theewaterskloof (Twk) Dam, situated near Villiersdorp about 60 km from iThemba LABS, Cape Town was used. The cosmic ray spectrum and the Theewaterskloof (Twk) spectrum are assumed to have the same shape.

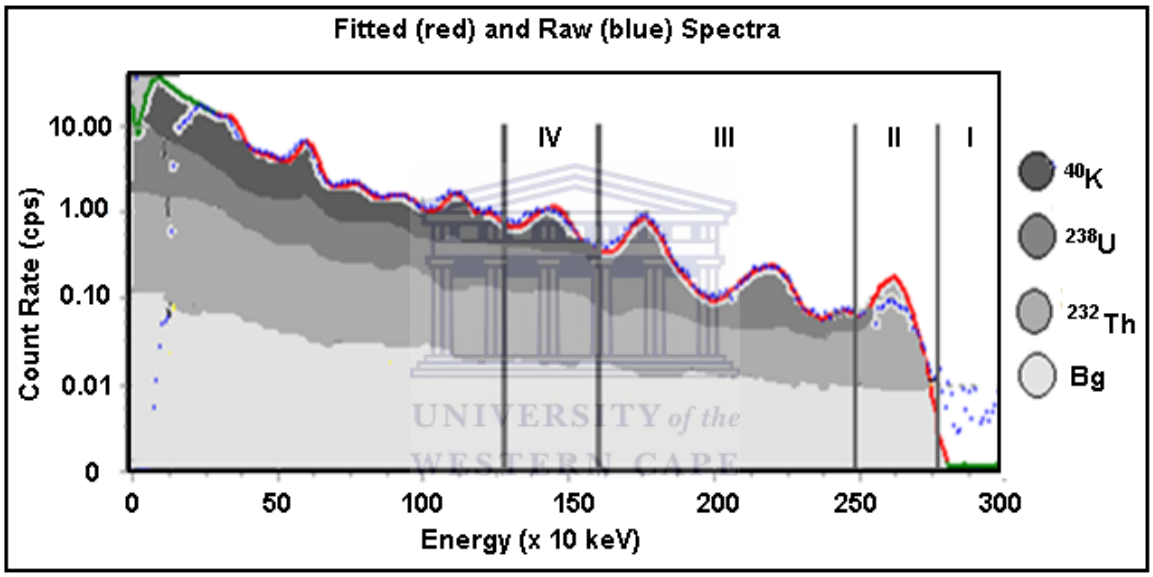

Figure 6.1: Regions showing the energy intervals used to analyse the activity concentrations using the hybrid method. Bg means background.

In region I when the count rates (CR) of the real spectrum (CR_I^S) and that of Theewaterskloof (Twk) spectrum (CR_I^{Twk}) are compared they may vary by a factor of κ_c that is:

$$\kappa_c = \frac{CR_I^S}{CR_I^{Twk}} \tag{6.1}$$

In region II, the count rate CR_{II}^S contains the contributions from the background and the decay of ^{232}Th and therefore the net count rate, $CR_{II}^{net}(^{232}Th)$ in that region can be expressed as:

$$CR_{II}^{net}(^{232}Th) = CR_{II}^{S} - (\kappa_c \times CR_{II}^{Twk}) \quad (6.2)$$

where, CR_{II}^{Twk} refers to the background contribution in region II and κ_c is the background correction factor of equation (6.1). Using the net count rate in equation (6.2) the effective ^{232}Th activity concentration, A_{Th} is calculated by dividing the net count rate in region II by the count rate of the simulated standard spectrum of thorium ($CR_{II}^{SS(^{232}Th)}$) in region II, which is corrected by the ratio factor, κ_f. The ratio factor will be discussed in the next section.

$$A_{Th}\kappa_f = \frac{CR_{II}^{net}(^{232}Th)}{CR_{II}^{SS(^{232}Th)}} \quad (6.3)$$

Clearly, equation (6.3) demonstrates the combination between the count rates from region II (window method) and the count rates from the FSA method (simulated standard spectrum) in determining the effective ^{232}Th activity concentration, A_{Th} and due to this combination the method is referred to as the hybrid method.

This implies that the effective ^{232}Th activity concentration, A_{Th} for regions II, III and IV can be derived using the following expressions:

$$A_{Th}\kappa_f = \frac{CR_{II}^{net}(^{232}Th)}{CR_{II}^{SS(^{232}Th)}} = \frac{CR_{III}^{net}(^{232}Th)}{CR_{III}^{SS(^{232}Th)}} = \frac{CR_{IV}^{net}(^{232}Th)}{CR_{IV}^{SS(^{232}Th)}} \quad (6.4)$$

The net count rate of uranium, $CR_{III}^{net}(^{238}U)$ contribution in region III is given by;

$$CR_{III}^{net}(^{238}U) = CR_{III}^{S} - (\kappa_C \times CR_{III}^{Twk} + A_{Th} \times \kappa_f \times CR_{III}^{SS(^{232}Th)}) \quad (6.5)$$

where, CR_{III}^{S} is the count rate of uranium in region III, CR_{III}^{Twk} is the count rate of the Twk spectrum in region III and $CR_{III}^{SS(^{232}Th)}$ is the count rate of the simulated standard spectrum of thorium in region III.

Then the effective ^{238}U activity concentration, A_U is achieved by dividing the net count rate for uranium, $CR_{III}^{net}(^{238}U)$ in region III by the simulated standard spectrum of

uranium, $CR_{III}^{SS(^{238}U)}$, which is corrected by the ratio factor, κ_f. In a similar way as equation (6.4) the effective ^{238}U activity concentration, A_U is expressed as:

$$A_U \kappa_f = \frac{CR_{III}^{net}(^{238}U)}{CR_{III}^{SS(^{238}U)}} = \frac{CR_{II}^{net}(^{238}U)}{CR_{II}^{SS(^{238}U)}} = \frac{CR_{IV}^{net}(^{238}U)}{CR_{IV}^{SS(^{238}U)}} \qquad (6.6)$$

Finally, the net count rate, $CR_{IV}^{net}(^{40}K)$ of potassium in region IV is given by;

$$CR_{1V}^{net}(^{40}K) = CR_{IV}^{S} - (\kappa_C \times CR_{IV}^{Twk} + A_{Th} \times \kappa_f \times CR_{IV}^{SS(^{232}Th)} + A_U \times \kappa_f \times CR_{IV}^{SS(^{238}U)}) \qquad (6.7)$$

where, CR_{IV}^{S} is the potassium count rate in region IV, CR_{IV}^{Twk} is the count rate of the Twk spectrum in region IV, $CR_{IV}^{SS(^{232}Th)}$ is the count rate of the simulated standard spectrum of thorium in region IV and $CR_{IV}^{SS(^{238}U)}$ is the count rate of the simulated standard spectrum of uranium in region IV.

The effective ^{40}K activity concentration, A_K is then computed by dividing the net count rate in region IV by the simulated standard spectrum of potassium, $CR_{IV}^{SS(^{40}K)}$, which is corrected by the ratio factor, κ_f. The expression for the effective ^{40}K activity concentration, A_K is given as;

$$A_K \kappa_f = \frac{CR_{IV}^{net}(^{40}K)}{CR_{IV}^{SS(^{40}K)}} \qquad (6.8)$$

6.4 Determining the ratio of the MEDUSA (FSA) to the hybrid activity concentration

The main purpose of this Chapter is to see if the activity concentrations extracted using the hybrid approach is different to the concentrations obtained with the FSA approach used in Chapter 5. To make this comparison clearer, the respective activity concentrations (A_{Th}, A_U, A_K) extracted using the MEDUSA (FSA) will be inserted on the left hand side of equations (6.3), (6.6) and (6.8) so that the ratios (κ_f) will give the ratio between the FSA and hybrid methods. During data analysis the FSA method [De Meijer, 1998; Hendriks et al., 2001] utilises the simulated standard spectra of ^{238}U, ^{232}Th and ^{40}K as well as the measured spectra, consequently not all properties are accounted for when a

simulated spectra is generated. Finding the ratio will eliminate some of the problems such as the light collection properties of the detector system and the efficiency of the photomultiplier tube.

The ratios were determined as follows: Firstly, five columns of count rates were set up in Microsoft Excel. The columns represented the MEDUSA spectrum for spot 2, the simulated standard spectra for ^{232}Th, ^{238}U, ^{40}K and the background spectrum (in this case Theewaterskloof spectrum).

Secondly, since a spectrum contains more than one region (see Figure 6.1), region II (the thorium region) was first identified from the columns containing the simulated standard spectrum for ^{232}Th and the MEDUSA spectrum for spot 2. Next, the count rate of the simulated standard spectrum of thorium ($CR_{II}^{SS(^{232}Th)}$) and the net count rate, $CR_{II}^{net}(^{232}Th)$ for ^{232}Th (region II) were determined. The net count rates were calculated using equations (6.1) and 6.2).

Thirdly, according to equation (6.3) the ratio of the net count rate ($CR_{II}^{net}(^{232}Th)$) to the count rate of the simulated standard spectrum of thorium ($CR_{II}^{SS(^{232}Th)}$), effectively the hybrid activity concentration was used to find the ratio (κ_f) between the MEDUSA (FSA) and the hybrid activity concentration. Since spot 2 was considered first, the same process was repeated for spots 3, 4 and 5 yielding the ratios shown in Table 6.1. Moreover, a similar procedure was applied to derive the ratios for region III (the uranium region) and region IV (the potassium region) by utilising equations (6.6) and (6.8) respectively for all spots. Table 6.1 shows the ratios obtained with an average value of 0.84 for the thorium region, 0.97 for the uranium region and 0.98 for the potassium region.

Table 6.1: The MEDUSA activity concentrations and the detector calibration factors extracted from the stationary spots.

Spots	MEDUSA (FSA) Activity Concentrations (Bq·kg^{-1})			Ratios (κ_f)		
	^{238}U	^{40}K	^{232}Th	^{238}U	^{40}K	^{232}Th
2	620	700	90	0.97	0.97	0.83
3	510	660	80	0.97	0.96	0.81
4	570	690	85	0.97	1.00	0.82
5	610	750	90	0.96	0.99	0.91
Average				**0.97**	**0.98**	**0.84**

Lastly, based on the average ratios that have been found, the hybrid activity concentrations were calculated relative to the activity concentrations extracted from the MEDUSA using the FSA method for all spots. This method provided easy comparison between the hybrid and the MEDUSA (FSA) activity concentrations. The hybrid activity concentrations were found to be slightly lower than the MEDUSA (FSA) activity concentrations, even though the ratios seemed to be close to unity. Table 6.2 presents the activity concentrations derived for the spots using the hybrid method, the FSA method (MEDUSA) and the windows method (HPGe) which measured the activity concentration of the soil samples collected from the spots in the laboratory.

Table 6.2: A comparison of the hybrid, MEDUSA (FSA) and HPGe activity concentrations for ^{232}Th series, ^{238}U series and ^{40}K at the stationary spots.

Spots	Hybrid Activity Concentration (Bq·kg^{-1})			MEDUSA (FSA) Activity Concentration (Bq·kg^{-1})			HPGe Activity Concentration (Bq·kg^{-1})		
	^{238}U	^{40}K	^{232}Th	^{238}U	^{40}K	^{232}Th	^{238}U	^{40}K	^{232}Th
2	600±70	685±80	80±10	620±80	700±85	90±11	310±6	248±5	17±1
3	495±60	650±75	70±8	510±60	660±80	80±10	282±6	262±5	17±1
4	555±70	680±80	70±8	570±70	690±85	85±10	341±7	251±5	18±1
5	590±70	735±90	80±10	610±75	750±90	90±11	315±7	254±5	18±1

- The hybrid activity concentrations calculated using equations (6.3), (6.6) and (6.8) using ratios of 0.84, 0.97 and 0.98 respectively.
- The HPGe and MEDUSA activity concentrations were determined using the traditional windows and FSA methods respectively (see Chapter 4).

Given that another analysis has been completed using the hybrid method, it is evident that another set of data has been generated from the stationary spots where the MEDUSA stationary measurements were carried out. The new set of data will be re-processed with an ultimate aim of extracting radon fluxes using the MEDUSA γ-ray detector system. The procedure to extract radon fluxes using the MEDUSA γ-ray detector was discussed in subsection 5.4.1.

The only alteration will be replacing the MEDUSA stationary activity concentrations with the hybrid activity concentrations which have been computed. However, the HPGe activity concentrations and the MEDUSA mobile concentrations will remain the same. So, that alteration occurs in step 5 depicted in Figure 5.5. To extract radon flux values, normalisation factors between the hybrid method and the HPGe activity concentrations at the stationary spots ought to be established first. Thereafter, other factors like moisture correction factors and radon flux normalisation factors will be considered. The ensuing discussion will focus on deriving those factors which have been mentioned in order to compute radon flux values.

6.5 Normalisation factors between the Hybrid and HPGe activity concentrations

Normalisation factors are important because they convert the hybrid activity concentrations into absolute activity concentrations. Normalisations factors are sourced from the spots where stationary measurements were done (see Figure 5.5 step 5). So taking the activity concentrations determined using the HPGe γ-ray detector system and divide them by the activity concentrations determined by the hybrid method leads to normalisation factors for ^{238}U, ^{232}Th and ^{40}K. The relation used to determine the normalisation factors, N_f is given below and the results are presented in Table 6.3.

$$N_f = \frac{AC_{HPGe}}{AC_{Hybrid}} \tag{6.9}$$

where, AC_{HPGe} and AC_{Hybrid} represent the activity concentrations from the HPGe γ-ray detector system and the hybrid method respectively for ^{238}U series, ^{232}Th series and ^{40}K.

Table 6.3: The normalisation factors derived from the hybrid and the HPGe activity concentrations.

Spots	HPGe Activity Concentration ($Bq \cdot kg^{-1}$)			Hybrid Activity Concentration ($Bq \cdot kg^{-1}$)			Normalisation factors		
	^{238}U	^{40}K	^{232}Th	^{238}U	^{40}K	^{232}Th	^{238}U	^{40}K	^{232}Th
2	310±6	248±5	17±1	600±70	685±80	80±10	0.52	0.36	0.22
3	282±6	262±5	17±1	495±60	650±75	70±8	0.57	0.41	0.25
4	341±7	251±5	18±1	555±70	680±80	70±8	0.62	0.37	0.25
5	315±7	254±5	18±1	590±70	735±90	80±10	0.53	0.35	0.24
Average							**0.56±0.04**	**0.37±0.02**	**0.24±0.01**

Next, the MEDUSA mobile activity concentrations (indicated as step 1 in Figure 5.5) are multiplied by the appropriate average normalisation factor from Table 6.3. For example all the MEDUSA mobile activity concentrations of ^{238}U in Figure 5.5 Step 1 are multiplied by 0.56. That applies to all 4005 data points captured in the 2002 survey and to all 7961 data points captured in the 2010 survey. In a similar way, ^{40}K activity concentrations are multiplied by 0.37 and ^{232}Th activity concentrations are multiplied by 0.24 for all data points captured in the 2002 survey and the 2010 survey.

This leads to the preliminary normalised MEDUSA activity concentrations for each radionuclide (indicated as step 2 in Figure 5.5). The final normalised MEDUSA activity concentrations are obtained once the moisture content has been accounted for. Moisture has been found to influence the emanation; transport and exhalation of radon (see subsubsection 5.3.1.2). Moisture content was primarily analysed from samples collected at the stationary spots where MEDUSA measurements were performed. Thus, by applying equations 5.21-5.27, the final normalised MEDUSA activity concentrations for the radionuclides (^{238}U, ^{232}Th and ^{40}K) were generated. This is indicated as step 3 in Figure 5.5. Now it is possible to calculate the unnormalised radon flux using equation (5.13) and (5.14), since the MEDUSA mobile activity concentration (step 1) and the final normalised MEDUSA activity concentrations (step 3) are known. The unnormalised radon flux obtained is indicated as step 4 in Figure 5.5.

So up to this stage the unnormalised radon flux values have been extracted using equation (5.13) and (5.14) however, they need to be normalised as discussed next.

6.6 Normalisation of radon flux

Normalisation of radon flux at each data point is essential to ascertain the correct amount of radon flux being released from the soil surface to the atmosphere. Accurate radon fluxes are acquired when the unnormalised radon flux (see Figure 5.5 step 4) are multiplied by the normalisation constant sourced from the stationary spots (see Figure 5.5 step 5). Radon flux normalisation constants are mainly computed by applying equation (5.13) and (5.14) in combination with equation (5.2). A brief description how to work out the radon flux normalisation factors is given; otherwise subsection 5.4.1 gives a detailed discussion.

- **Radon flux normalisation constant using ^{238}U and ^{232}Th activity concentrations**

A dimensionless constant sourced from the stationary measurements is worked out using ^{238}U and ^{232}Th activity concentrations as required by equation (5.14). According to equation (5.14) the field ^{238}U and ^{232}Th activity concentrations refer to the hybrid activity concentrations derived from the stationary spots while the equilibrium ^{238}U and ^{232}Th activity concentrations refer to the HPGe activity concentrations obtained after analysing soil samples which were brought to the laboratory. This refers to step 5 in Figure 5.5. Applying equation (5.14) yields unnormalised flux depicted as step 6 in Figure 5.5).

Next, the theoretical radon flux is determined using equation (5.2) which requires the following input parameters; the diffusion length ($\ell \approx 40$ cm), the emanation coefficient ($E = 0.28$), the bulk density ($\rho_b = 1500\ \text{kg}\cdot\text{m}^{-3}$), radon decay constant ($\lambda = 2.1\times10^{-6}\ \text{s}^{-1}$) and the radium activity concentration (in Bq·kg^{-1}). The theoretical radon flux value obtained was about 0.11 Bq·m^{-2}·s^{-1} as shown in Table 6.4 and depicted as step 7 in Figure 5.5. Finally, to get the radon flux normalisation constant shown as step 8 in Figure 5.5, the theoretical radon flux value calculated using equation (5.2) was divided by the unnormalised radon flux calculated using equation (5.14). The radon flux normalisation constants obtained are shown in Table 6.4 with an average value of 4.3×10^{-4} kg·m^{-2}·s^{-1}.

Table 6.4: Determining the radon flux normalisation constant using equation (5.14).

Spot	Average HPGe activity concentration		Hybrid activity concentration		† 'Unnormalised' flux (UF)	* 'Theoretical' Flux (TF)	Normalisation constant (TF/UF)
	^{238}U	^{232}Th	^{238}U	^{232}Th			
2	310 ± 6	17 ± 1	600±70	80±10	255	0.11	0.00043
3	282 ± 6	17 ±1	495±60	70±8	231	0.10	0.00043
4	341 ± 7	18 ±1	555±70	70±8	280	0.12	0.00043
5	315 ± 7	18 ±1	590±70	80±10	254	0.11	0.00043
Average							**0.00043**

†Unnormalised flux calculated using equation (5.14).
*Theoretical flux calculated using equation (5.2).

- **Radon flux normalisation constant using ^{238}U and ^{40}K activity concentrations**

In a similar way, the procedure described above was repeated using equation (5.13) to extract the second radon flux normalisation constant from the stationary measurements when ^{238}U and ^{40}K activity concentrations are used. An average value of 6.4×10^{-4} kg·m^{-2}·s^{-1} as shown in Table 6.5 was computed. This value is important since it will be used to normalise radon flux values (indicated as step 4 in Figure 5.5) obtained when MEDUSA mobile data is processed by utilising the ^{238}U and ^{40}K activity concentrations.

Table 6.5: Determining the radon flux normalisation constant using equation (5.13).

Spot	Average HPGe activity concentration		Hybrid activity concentration		† 'Unnormalised' flux (UF)	* 'Theoretical' Flux (TF)	Normalisation constant (TF/UF)
	^{238}U	^{40}K	^{238}U	^{40}K			
2	310 ± 6	248 ± 5	600±70	685±80	165	0.11	0.00067
3	282 ± 6	262 ± 5	495±60	650±75	150	0.10	0.00067
4	341 ± 7	251 ± 5	555±70	680±80	204	0.12	0.00059
5	315 ± 7	254 ± 5	590±70	735±90	170	0.11	0.00065
Average							**0.00064**

†Unnormalised flux calculated using equation (5.13).
*Theoretical flux calculated using equation (5.2).

The theoretical radon flux value given by equation (5.2) is about 0.11 $Bq \cdot m^{-2} \cdot s^{-1}$ as shown in Table 6.5 and depicted as step 7 in Figure 5.5. The two radon flux normalisation constants (4.3×10^{-4} and 6.4×10^{-4} $kg \cdot m^{-2} \cdot s^{-1}$) are now indicated as step 8 in Figure 5.5.

Last but not least, normalised radon flux values are achieved when the unnormalised radon flux values (step 4 in Figure 5.5) are multiplied by the appropriate radon flux normalisation constant. For instance, radon flux values calculated using equation (5.13) are normalised by multiplying by 6.4×10^{-4} $kg \cdot m^{-2} \cdot s^{-1}$, while radon flux values calculated using equation (5.14) are normalised by multiplying by 4.3×10^{-4} $kg \cdot m^{-2} \cdot s^{-1}$. Normalised radon flux values are depicted as step 9 in Figure 5.5. Note that the atmospheric radon concentration discussed in subsubsection 5.4.2.3 was not taken into account because it was believed that it was low as such it could not influence the radon flux results obtained. Since equation (5.13) and (5.14) were utilised to calculated radon flux values, two sets of normalised radon fluxes were obtained which are presented in the next section.

6.7 Radon flux calculated from the hybrid activity concentrations

The results for the radon flux values obtained are presented in two forms, see Figure 6.2-6.5. The average radon flux values computed are 0.11 $Bq \cdot m^{-2} \cdot s^{-1}$ and 0.10 $Bq \cdot m^{-2} \cdot s^{-1}$ when equations (5.13) and (5.14) are used respectively.

First, tri-colour maps are used where blue colour represents low flux, yellow represents average flux and red represents high flux. In 2002 the MEDUSA survey on Kloof mine dump covered a large surface area and for the areas which were inaccessible, radon flux has been interpolated using Golden Surfer 8 software. On the other hand, in 2010 the MEDUSA survey on Kloof mine dump covered almost a third of the surface area. Since two-thirds of the surface area was not covered it was blanked out, and then the Golden Surfer 8 software was used to interpolate on the remaining surface area.

Second, radon fluxes are also represented as Gaussian distribution (Figure 6.3 and Figure 6.5) to illustrate their trends.

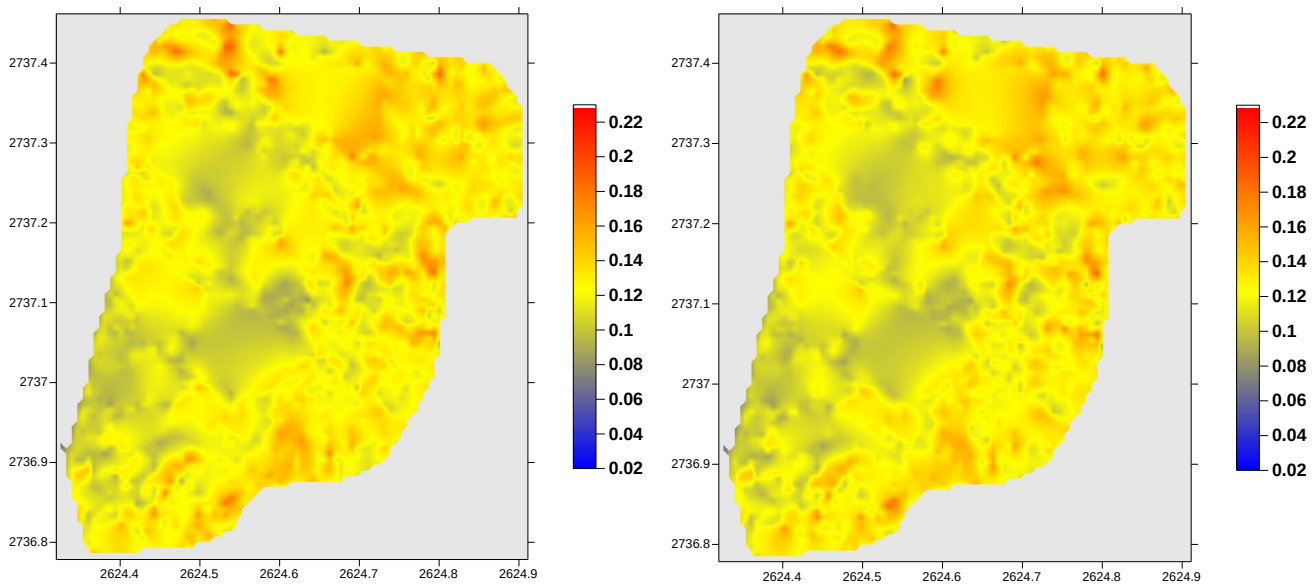

Figure 6:2: Interpolated maps generated showing radon flux values after utilising equation 5.13 (left) and equation 5.14 (right) for the 2002 survey.

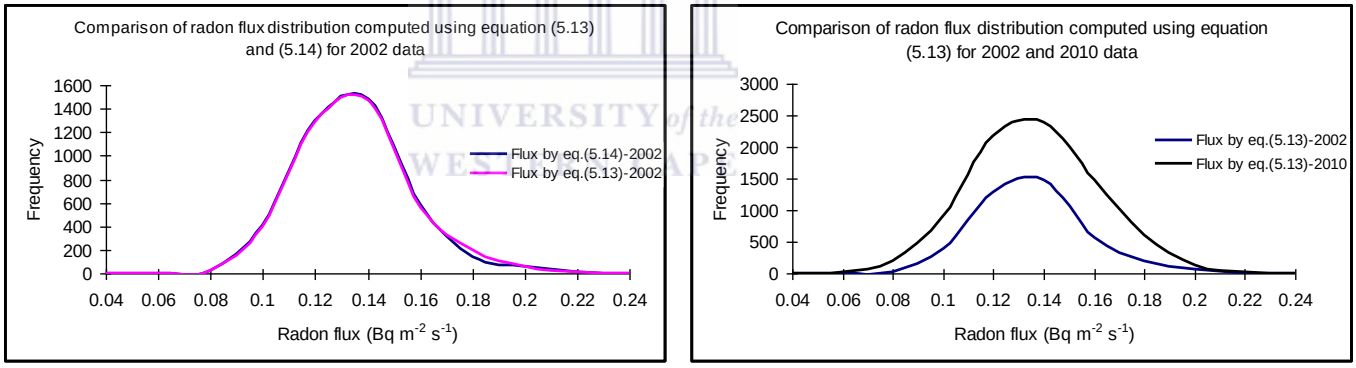

Figure 6.3: A graph showing the distribution of radon flux values calculated using equation (5.13) and (5.14) for 2002 survey (left). Another graph (right) showing a comparison of radon flux calculated using equation (5.13) only for 2002 and 2010 surveys.

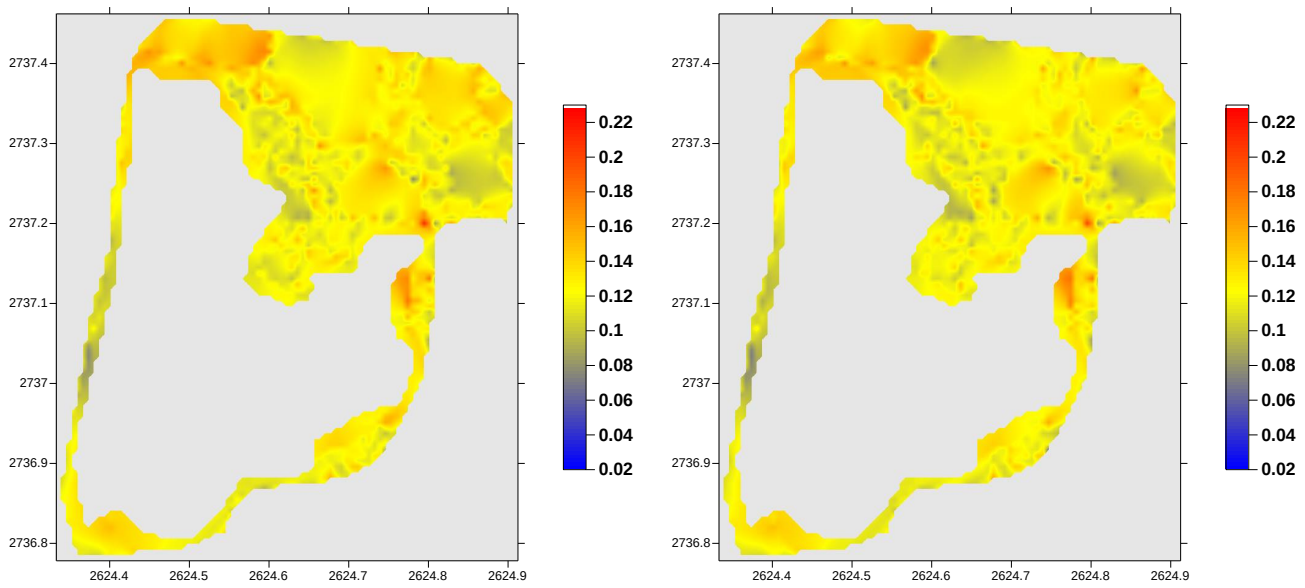

Figure 6.4: Interpolated maps generated showing radon flux values after utilising equation 5.13 (left) and equation 5.14 (right) for the 2010 survey.

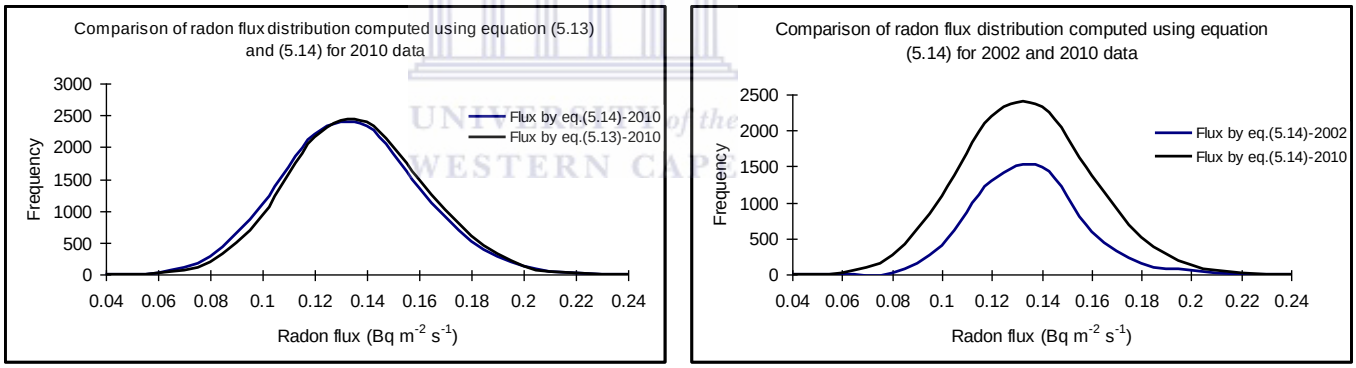

Figure 6.5: A graph showing the distribution of radon flux values calculated using equation (5.13) and (5.14) for 2010 survey (left). Another graph (right) showing a comparison of radon flux calculated using equation (5.14) only for 2002 and 2010 surveys.

6.8 Conclusion

This Chapter has explored how the hybrid method can be employed to get the effective ^{238}U, ^{232}Th and ^{40}K activity concentrations from the spots where the MEDUSA stationary measurements were conducted. The activity concentrations attained are not drastically different from the MEDUSA stationary activity concentrations at the stationary spots (see

comparison in Table 6.2). Subsequently, the derived hybrid activity concentrations in combination with the HPGe activity concentrations were utilised to establish the normalisation factors, the moisture correction factors and the radon flux normalisation constants. These factors are instrumental when the MEDUSA mobile activity concentrations are analysed to extract radon fluxes.

Thus far two main methods namely the Full Spectrum Analysis (MEDUSA detector system) and the Hybrid methods in conjunction with the traditional windows (HPGe detector system) have been utilised to extract radon fluxes from the surface of Kloof mine dump. A comparison of those methods will form part of the next Chapter.

Chapter 7

Summary, Conclusions and Recommendations

7.1 Introduction

This Chapter presents a summary and conclusions on the achievements from this study based on in-situ measurements and calculation of radon gas concentration and exhalation from a mine tailings dump. Some aspects of the project that were not tackled will be highlighted for future consideration. Radon soil gas concentration which is measured in $Bq{\cdot}m^{-3}$ was monitored using a continuous monitor, a RAD7 system. The amount of radon being released to the atmosphere which is measured in $Bq{\cdot}m^{-2}{\cdot}s^{-1}$ was extracted from the concentration of radionuclides measured using the MEDUSA γ-ray detector in combination with the HPGe γ-ray detector. The electret chambers namely the adapted H-chambers were used to measure the radon flux at three spots (see Figure 3.5 and Figure 5.15). All radon gas concentrations and flux measurements were performed at a Kloof mine dump which belongs to the Carletonville Gold field. The ensuing discussion gives a summary and conclusions from the findings of the study.

7.2 Radon soil-gas concentrations

The subject of establishing radon gas concentration levels in the ground drew considerable interest in the past as evidenced from the amount of literature published. Several authors including Bigu (1984), Speelman (2004), Manavhela (2007) and Antonopoulos-Domis (2009 investigated radon concentration levels in the soil air. Radon gas vessels [Van der Spoel, 1998; Schubert, 2002] have been constructed to monitor radon gas concentration levels at various depths as well as other factors which influence radon gas like moisture content, pressure differences, wind velocity etc. Radon gas can be detected using devices such as solid state nuclear track detectors, thermoluminescent phosphors, ionization chambers, electrets and solid state electronic detectors.

At the Kloof mine dump, a RAD7 from the Durridge Co., was used to monitor radon gas concentration in the soil air. The RAD7 is capable of measuring radon gas concentration and at the same time monitor the temperature changes and the relative humidity. Radon gas concentration was measured at depths starting from 30 cm to 110 cm at depth intervals of 20 cm. Since, only one RAD7 device was available, we utilised it by identifying five spots on the tailings mine dump where we performed our measurements. The range of radon gas concentration measured was between 26.5 $kBq{\cdot}m^{-3}$ and 472 $kBq{\cdot}m^{-3}$. The lowest radon gas concentration was extracted from spot 3 and the highest radon gas concentration was extracted from spot 5, see Table 3.2 and Figure 3.5. Radon is a decay product of radium in the uranium decay chain and in this case the weighted average activity concentration for uranium (^{238}U) which is assumed to be in secular equilibrium with its decay daughters was computed to be 308 ± 7 $Bq{\cdot}kg^{-1}$ from thirty four soil samples collected from the Kloof mine dump and then measured in the laboratory using the HPGe γ-ray detector.

Due to the difference in the strength of the sources, radon gas concentration levels in the ground have been found to vary greatly. For instance, concentrations of radon gas in soil air have been measured to a maximum of about 32.5 $kBq{\cdot}m^{-3}$ (Shweikani, 1995) when the radium content is 77 $Bq{\cdot}kg^{-1}$. Nazaroff (1992) has reported concentrations of radon gas in the soil at large depths to be about 32 $kBq{\cdot}m^{-3}$ where the ^{238}U activity used was determined to be 30 $Bq{\cdot}kg^{-1}$. Bigu (1984) reported radon gas concentrations from uranium mill tailings ranging from about 670 $kBq{\cdot}m^{-3}$ at 0.5 m to around 4 $MBq{\cdot}m^{-3}$ at 5.7 m.

The few examples mentioned above illustrate that, as expected, the amount of radon gas in the pore spaces is directly related to the radium content in the mineral grains beneath the ground. If the mineral grains contain high amounts of radium, then there is a likelihood that when radium decays, more radon gas will emanate to the pore spaces. Conversely, if the mineral grains contain less radium, when it decays less radon gas will emanate to the pore spaces. This perhaps explains the commonly observed cases where soil types like sand and clay which have less radium content yield low radon gas

concentration levels as compared to other types of soil which have high concentrations of radium, for instance the uranium bearing tailings.

It is important to determine radon gas concentration levels in soil air because they can provide an insight into the transport mechanism for radon. For instance the curves generated (see Chapter 3 Figure 3.7-3.8) show that radon concentrations in soil air decrease towards the surface as a result of diffusion and advection. The radon gas concentration depth profiles can also provide a means through which the in-situ diffusion length can be extracted as opposed to the traditional way of determining the diffusion length experimentally in the laboratory.

7.3 Activity concentrations of the primordial radionuclides

^{238}U, ^{232}Th and ^{40}K are the natural radionuclides of interest that were determined using the gamma-ray spectrometry technique. These radionuclides are characterised by long half-lives and their origin traces back to the time when the earth was formed. At the Kloof mine dump, the MEDUSA γ-ray detector was utilised to measure the activity concentrations of the ^{238}U and ^{232}Th decay products as well as the ^{40}K radionuclide. In the laboratory at iThemba LABS, the HPGe γ-ray detector system was used to identify and quantify radionuclides in the soil samples which were brought from the tailings mine dump. The windows analysis method, where the HPGe spectrum is divided into regions around the peaks of interest was used to compute the activity concentrations based on the intensity of the gamma lines given in Table 4.3. The activity concentrations determined in this way are considered to be in secular equilibrium which means that the activity of the decay product is ascribed to ^{238}U assuming that it has attained equilibrium after three weeks storage in sealed containers. On the other hand the full spectrum analysis (FSA) method was utilised to extract the activity concentrations of the radionuclides mapped using the MEDUSA γ-ray detector.

The ^{238}U, ^{232}Th and ^{40}K content in materials differ greatly. For instance Hlatshwayo (2009) reported the following activity concentrations for the sandy soil found at iThemba LABS, Western Cape, South Africa, 8-39 $Bq{\cdot}kg^{-1}$ for ^{238}U, 6-21 $Bq{\cdot}kg^{-1}$ for ^{232}Th and 30-63 $Bq{\cdot}kg^{-1}$ for ^{40}K. The vineyard soils found at Stellenbosch, Western Cape, South Africa which were investigated by Mlwilo (2010) contained 28-68 $Bq{\cdot}kg^{-1}$ of ^{238}U, 28-111

Bq·kg^{-1} of ^{232}Th and 127-227 Bq·kg^{-1} of ^{40}K. The uranium mill tailings have been quantified to have an average radium activity concentration of 15200 Bq·kg^{-1} for Australian tailings [Mudd, 2008], a range of 5081-5166 Bq·kg^{-1} for Indian uranium tailings pile [Sahoo, 2010] and 23939 Bq·kg^{-1} (647pCi/g) for Piñon Ridge, Colorado-USA uranium tailings [Golder Associates Inc., 2010].

Table 7.1 presents the average activity concentrations quantified using (1) the HGPe γ-ray detector on thirty four soil samples which were collected from the mine dump and (2) the MEDUSA γ-ray detector which was utilised on the uranium bearing tailings at the Kloof mine dump.

Table 7.1: The average activity concentrations for uranium tailings at the mine dump.

γ-ray detector	**Activity Concentrations** (Bq·kg^{-1})					
	^{238}U series		**^{232}Th series**		**^{40}K**	
	Range	Average	Range	Average	Range	Average
HPGe	240 - 354	308 ± 12	13 - 21	18 ± 1	209 - 300	255 ± 12
MEDUSA (2002)	75 - 544	309 ± 40	6 - 100	18 ± 5	33 - 762	259 ± 75
MEDUSA (2010)	117 - 551	310 ± 40	5 - 108	20 ± 5	35 - 977	260 ± 75

It can be deduced from the few examples mentioned above, that uranium bearing tailings have high radium activity concentration compared to most types of soil such as loam or sandy soil. The uranium tailings as expected, has more mineral particles with high radium content from the uranium decay than loam or sandy soil. Even though the tailings have high concentrations of ^{226}Ra, the concentration also varies across as you consider various tailings for instance when the activity concentration of tailings in India, Australia, USA and South Africa are compared they are found to differ significantly. In this particular case the activity concentration of the gold mine tailings at the Kloof mine dump were found to be less by a factor of about 50 when compared to the uranium tailings reported in Australia and the USA. This comparison applies only to the non-operational Kloof mine dump bearing in mind that South Africa has several other mine dumps which need to be investigated.

A detailed analysis of the activity concentrations using at least three techniques was performed at four stationary spots; see Figure 3.5. Note that at those spots the MEDUSA

γ-ray detector was held stationary for a period of about 30-60 minutes. A summary of the activity concentrations extracted from those spots when the windows technique (HPGe), the FSA method (MEDUSA) and the hybrid method were used is shown in Figure 7.1. The HPGe γ-ray detector was used to measure the activity concentration of soil samples collected from the stationary spots in the laboratory.

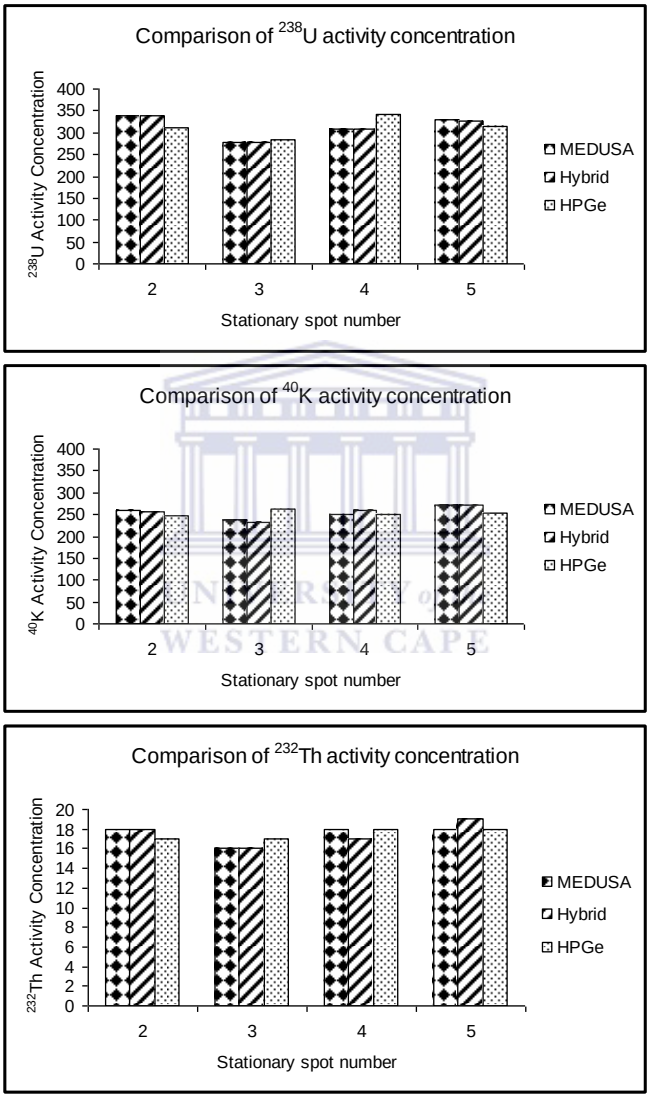

Figure 7.1: A comparison of the activity concentration of ^{238}U (top), ^{40}K (middle) and ^{232}Th (bottom) extracted using the windows (HPGe), FSA (MEDUSA) and the hybrid methods from the stationary spots.

The average activity concentrations determined by the three techniques were found to be within the range of the uncertainty calculated. The findings from the tailings at the Kloof mine dump indicate that the activity concentrations of ^{40}K and ^{238}U are high compared to that of thorium which is considerably lower (see, Table 7.1).

It is important to establish the actual activity concentrations of the three primordial radionuclides, especially uranium because it is considered to be the major source of radon. After estimating the activity concentration of uranium, models for instance the standard formula by [UNSCEAR, 1982; IAEA, 1992] can be used to predict the amount of radon released to the atmosphere after diffusing through the ground. The uranium activity concentration obtained can also be used to determine the uranium concentration at great depths as provided by equation (3.4) which in turn can be used to compute radon soil gas concentration at various depths using Comsol Multiphysics software [Comsol, 2008].

7.4 Radon flux from the Kloof mine dump

Radon gas is transported in the ground by diffusion and advection and ultimately it is released to the atmosphere. Radon gas mobility is influenced by factors such as the diffusion coefficient, the porosity, moisture content, atmospheric pressure, wind speed, temperature and the grain size. Several techniques which are described in [NCRP, 1988; IAEA, 1992; Durrani & Ilic, 1997] are available and they can be utilised to measure the amount of radon released. Although some of the techniques have been criticised [Samuelsson, 1984] because of their known shortcomings, they are still being used to measure radon release from materials such as soil, cement, building materials, rocks, and uranium tailings. Table 5.2 gives the radon exhalation rates of various materials that were determined in different regions of the world. Attempts to quantify the amount of radon released has led to the development of several models tailored towards estimating radon flux either in small or large scale as evidenced from the published literature [Nazaroff et al., 1988; Ielsch, 2002; Szegvary, 2007; Goto, 2008; Zhuo, 2008; Griffiths, 2010; Hirao, 2010].

The amount of radon released from the Kloof mine dump was mapped using the MEDUSA γ-ray detector system. The MEDUSA γ-ray detector maps the activity

concentrations of ^{40}K and the decay products of ^{232}Th and ^{238}U in the top 30 cm of the mine dump. Note that in the field the bismuth (^{214}Bi) activity concentration which is ascribed to ^{238}U is usually not in secular equilibrium with the radium (^{226}Ra) activity concentration, due to radon escape. After that the actual activity concentrations of ^{40}K, ^{232}Th series and ^{238}U series in the thirty four soil samples that were collected from the mine dump were determined in the laboratory using the HPGe γ-ray detector system.

The process of extracting the amount of radon that has escaped begins by comparing the activity concentrations of ^{40}K as recorded by both the MEDUSA γ-ray detector in the field and the HPGe γ-ray detector in the laboratory. ^{40}K activity concentration is considered because it is independent of radon escape. Then the difference obtained from the ratios of the activity concentrations measured by the MEDUSA and the HPGe γ-ray detector in combination with the calibration from the ^{40}K activity concentration, yields the amount of radon that escapes from the tailings at the Kloof mine dump. In order to achieve that the activity concentrations measured by the MEDUSA γ-ray detector were (1) normalised by normalisation factors, and (2) corrected for the moisture content present.

7.4.1 Normalisation factors

Normalisation factors were primarily utilised to convert the activity concentrations recorded by the MEDUSA γ-ray detector into absolute activity concentrations. The normalisation factors were obtained by taking the ratio of the average equilibrium activity concentrations of the five Kloof soil samples measured by the HPGe γ-ray detector to the activity concentrations measured by the MEDUSA γ-ray detector at a particular stationary spot on the mine dump, more details in subsection 5.4.1.

Normalisation factors were also investigated using soil samples collected from the iThemba LABS ground for comparison purposes. These soil samples can be classified as mainly sandy soil. Five soil samples were collected from the spot where the MEDUSA γ-ray detector is normally calibrated and after analysis an average activity concentration of 9 Bq·kg^{-1} for ^{238}U series, 9 Bq·kg^{-1} for ^{232}Th series and 59 Bq·kg^{-1} for ^{40}K, were found. A summary presented in Table 7.2 gives the normalisation factors determined between

- The HPGe γ-ray detector activity concentrations of the tailings from the mine dump and the MEDUSA γ-ray detector activity concentrations of the mine dump tailings.
- The HPGe γ-ray detector activity concentrations of the mine dump tailings and the activity concentrations determined using the hybrid method [Talha, 2009; Maleka, 2010]
- The HPGe γ-ray detector activity concentrations of the sandy soils from iThemba LABS and the MEDUSA γ-ray detector activity concentrations of the sandy soils.

Table 7.2: A comparison of the normalisation factors obtained from Kloof tailings and iThemba LABS sandy soil.

Soil type	Ratio	Normalisation factors		
		^{238}U series	^{40}K	^{232}Th series
Kloof mine dump (tailings)	HPGe/MEDUSA	0.54	0.36	0.21
	HPGe/Hybrid	0.56	0.37	0.24
iThemba LABS (sandy soil)	HPGe/MEDUSA	0.38	0.36	0.21
	HPGe/Hybrid	-	-	-

The last two columns, of Table 7.2 reveal that the normalisation factors of ^{40}K and ^{232}Th are almost constant which might suggest that the activity concentrations of ^{40}K and ^{232}Th are hardly affected by radon escape whether the tailings from the mine dump or the sandy soils from iThemba LABS ground are considered, however, that does not apply for the ^{238}U series.

It has been mentioned before that the ^{238}U activity concentration captured by the MEDUSA γ-ray detector is actually the bismuth (^{214}Bi) activity concentration which comes after radon in the uranium decay chain (see Chapter 2, Figure 2.1). Therefore the noticeable difference in the normalisation factors in the ^{238}U column especially between the mine dump tailings and the sandy soil can offer an insight into the permeability of the two types of soil. Possibly it could mean that sandy soils are more permeable as compared to the mine dump tailings, so when radon emanates from the sandy grains it diffuses quickly and in the end it is released to the atmosphere, therefore radon loss is high leading to a low normalisation factor. On the other hand the mine dump tailings are less permeable, so radon loss to the atmosphere is slower as compared to the sandy soils

yielding a high normalisation factor. Another possibility is that the sandy soils and the mine dump tailings have different emanation coefficients, leading to different normalisation factors.

7.4.2 Moisture content correction

Moisture content is an extremely important factor which cannot be ignored when determining activity concentrations. The amount of water in the pore spaces affects radon mobility in the ground which in the end affects the amount of radon released to the atmosphere. In order to take this parameter into consideration, thirty four soil samples from the Kloof mine dump were analysed for their moisture content and after that the activity concentrations measured by the MEDUSA γ-ray detector were corrected for that moisture content. Following the analysis of the moisture content from the mine dump soil samples together with the activity concentrations of the MEDUSA γ-ray detector, linear equations were developed which were used to predict the moisture correction factors for each radionuclide at every point in the field where MEDUSA was used for measurements; more details are provided in subsection 5.4.1.

7.4.3 Determination of radon flux

The amount of radon released to the atmosphere from the surface of the Kloof mine dump has been established. The approach used in this work utilised the HPGe γ-ray detector for laboratory measurements and the MEDUSA γ-ray detector for the field measurements. Because of the combination of the two γ-ray detectors the technique is called here as **ME**DUSA **L**aboratory **T**echnique (MELT). Figure 5.5 gives the necessary steps required to successfully calculate radon exhalation applying MELT.

The Kloof mine dump has been surveyed twice, first in 2002 and recently in 2010. The radon flux determined from measurements performed in 2002 ranged from 0.02-0.15 $Bq \cdot m^{-2} \cdot s^{-1}$ with an average of 0.10 ± 0.01 $Bq \cdot m^{-2} \cdot s^{-1}$ for 4005 data points that were captured during the survey. The radon flux determined from the recent survey conducted in 2010 ranged from 0.01-0.16 $Bq \cdot m^{-2} \cdot s^{-1}$ with an average of 0.10 ± 0.02 $Bq \cdot m^{-2} \cdot s^{-1}$ for 7961 data points that were captured by the MEDUSA γ-ray detector during the survey. The summary of radon flux values obtained from the mine dump are given in Chapter 5,

Table 5.8 as well as coloured maps shown by Figure 5.7-5.8 . Radon flux values from the mine dump were also calculated using the standard formula [UNSCEAR, 1982; IAEA, 1992] and the Electret ion chambers.

The standard IAEA formula (equation 5.32) is meaningfully applied when parameters such as the radium content, dry bulk density, emanation coefficient and the effective diffusion coefficient are first determined. The range of radon flux determined using the standard formula was found to be 0.03-0.20 $Bq \cdot m^{-2} \cdot s^{-1}$ with an average of 0.11 ± 0.02 $Bq \cdot m^{-2} \cdot s^{-1}$ basing it on 2002 data points while the radon flux range was 0.04-0.20 $Bq \cdot m^{-2} \cdot s^{-1}$ with an average of 0.11 ± 0.02 $Bq \cdot m^{-2} \cdot s^{-1}$ basing it on the 2010 data points.

The modified H-chambers with short-term electrets were used as another means of determining radon flux from the mine dump, more details are provided in subsubsection 5.4.2.2. The radon flux values obtained ranged between 0.02 and 0.08 $Bq \cdot m^{-2} \cdot s^{-1}$.

The radon flux values obtained using the dynamic system ranged between 0.04 and 0.20 $Bq \cdot m^{-2} \cdot s^{-1}$ with an average of 0.12 ± 0.05 $Bq \cdot m^{-2} \cdot s^{-1}$ [Manatunge, 2002].
Table 7.3 provides a summary of some techniques that have been used to assess radon flux from the mine dump.

Table 7.3: A summary of the techniques used and the radon flux values measured.

Technique	**Year**	**Kloof Radon Flux range** ($Bq \cdot m^{-2} \cdot s^{-1}$)	**Kloof Average Radon Flux** ($Bq \cdot m^{-2} \cdot s^{-1}$)
Standard formula	2002	0.03 - 0.20	0.12 ± 0.02
	2010	0.04 - 0.20	0.12 ± 0.02
Electrets	2002	0.01 - 0.11	0.06 ± 0.03
	2010	0.03 - 0.08	0.06 ± 0.02
Dynamic system	2002	0.04 - 0.20	0.12 ± 0.05
	2010	-	-
MELT	2002	0.02 - 0.15	0.12 ± 0.02
	2010	0.01 - 0.16	0.12 ± 0.02

The fourth Column in Table 7.3 gives the calculated average radon flux from the mine dump obtained using four techniques namely; the standard formula, the dynamic system, the electrets and the MEDUSA technique. The radon flux determined from the electrets seems to be lower when compared to the radon flux determined from the other

techniques. Electrets are relatively easy devices to use, however, other factors like the pressure differences during the measuring time and the period of exposure might influence the results obtained. For instance in 2002 the electrets were exposed for a period of 2.5-3 hours while in 2010 the electrets were exposed for a period of 4-8.5 hours. Electrets measurements also suffer from practical problems such as the disturbance of the soil to make a measurement and possible radon leakage between the soil and the detector. The last two rows of Table 7.3 emphasise that the new technique namely the **ME**DUSA **L**aboratory **T**echnique (MELT) was principally utilised to extract radon fluxes from the activity concentrations mapped using the MEDUSA γ-ray detector in 2002 and 2010 surveys.

The radon flux values extracted using the new technique (MELT) appear to be in between the radon flux range obtained from the other techniques as shown in Figure 7.2.

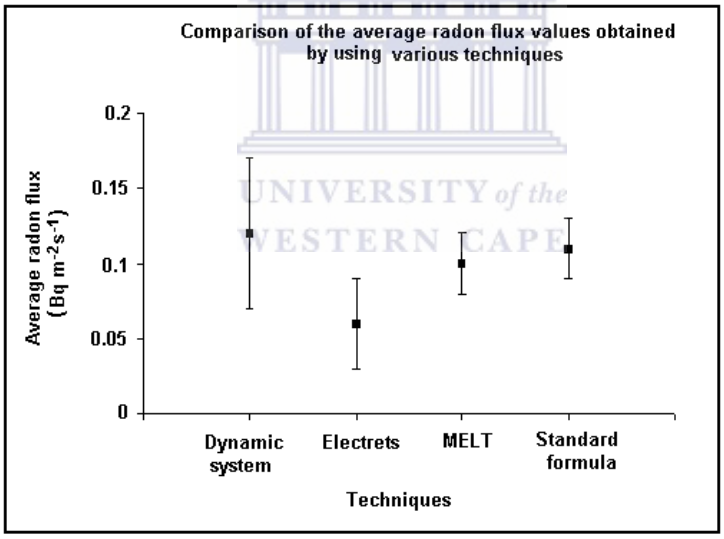

Figure 7.2: A comparison of radon flux values estimated from various techniques.

It was important to determine the amount of radon release to the atmosphere because it can help the radiation specialists to estimate the radiation dose that the communities that are in the proximity of the mine dump receive when exposed to radon. The amount of radon released from the Kloof mine dump is relatively low when compared to other uranium tailings for instance in India, Australia and USA, however it is higher than a typical soil whose ^{238}U and ^{226}Ra content is about 40 $Bq \cdot kg^{-1}$ which yields an average

measured value of 0.017 $Bq \cdot m^{-2} \cdot s^{-1}$ [NCRP, 1988]. The United Nations Scientific Committee on the effects of Atomic Radiation [UNSCEAR, 1982] has also reported that uranium tailings give much higher radon flux rates than the various soil types.

Now that the ^{238}U activity concentrations of the tailings at the Kloof mine dump have been quantified and the amount of radon that is released to the atmosphere has been estimated at every data point captured by the MEDUSA γ-ray detector, it has been found that the ^{238}U activity concentrations and the radon flux values correlate as depicted in the Figures 7.3-7.4. Note that 4005 and 7961 data points were considered for correlation in 2002 and 2010 surveys, respectively.

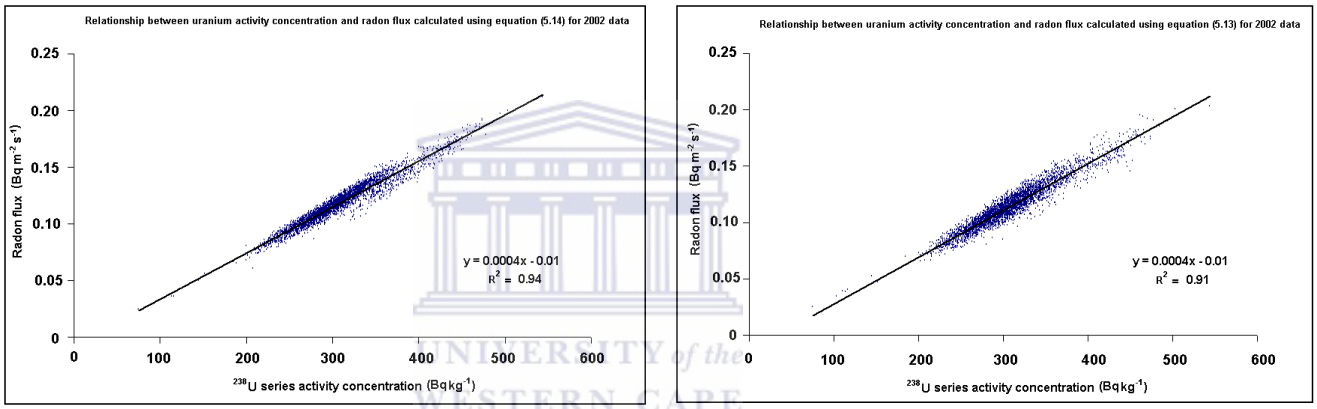

Figure 7.3: A correlation between the activity concentration of uranium and the radon flux values extracted from the 2002 survey using equation 5.14 (left) and equation 5.13 (right).

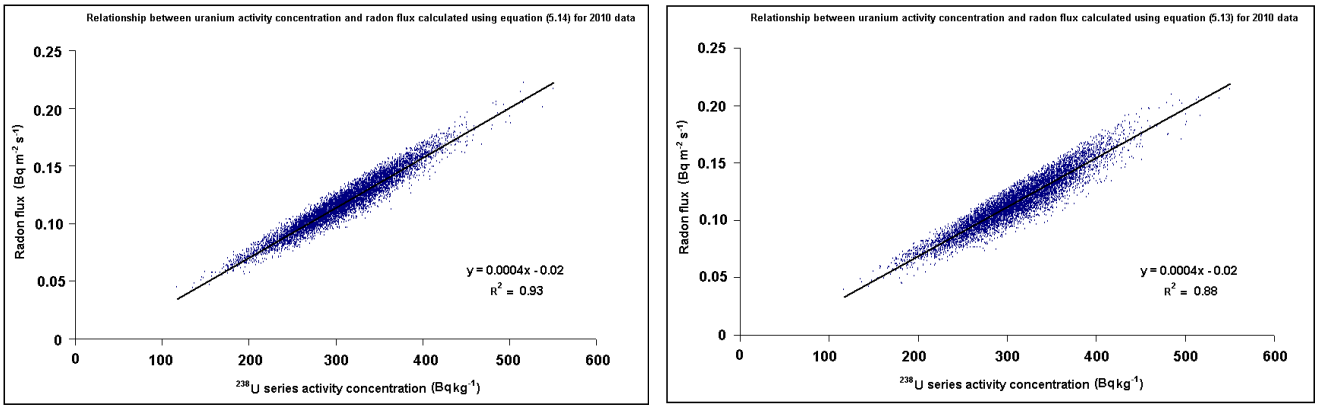

Figure 7.4: A correlation between the activity concentration of uranium and the radon flux values extracted from the 2010 survey using equation 5.14 (left) and equation 5.13 (right).

A general trend can be inferred from Figures 7.3-7.4, that the amount of radon being released to the atmosphere from the tailings surface is directly related to the radium concentration on the mine dump as expected. A uranium source with low activity concentration results in low radon flux values and vice versa. The correlation between the uranium activity concentrations and the radon flux values extracted using the new technique (Figures 7.3-7.4), indicate that the radon fluxes is distributed around the linear dependence which reflect that there is spatial variation. In practical terms it is expected because the porosity, the moisture content and the diffusion coefficient play a role in radon mobility which in the end will affect the amount of radon being released. For instance in this work linear models were developed to estimate the moisture content which was taken into consideration when extracting radon flux values. On the other hand the correlation between the uranium activity concentrations and the radon fluxes calculated using the standard IAEA formula generate straight lines. Thus, we believe that the use of ^{40}K and ^{232}Th values in equation (5.13) and (5.14), respectively, gives a better result since some correction is made for differences in attenuation.

Finally, it was found that the activity concentration of the ^{238}U series, ^{232}Th series and ^{40}K derived using the hybrid method were slightly lower than the activity concentration extracted using the Full Spectrum Analysis method (see Table 6.2). This led to a slightly lower average value for the radon flux for the mine dump. Figures 7.5-7.6 present a comparison of the radon flux values distribution for the 2002 and 2010 surveys when

- equation (5.13) and (5.14) is utilised where the activity concentration of the ^{238}U series, ^{232}Th series and ^{40}K is extracted from the measured γ-ray spectrum using the FSA method. This refers to the discussion in subsection 5.4.1 while details of the MEDUSA data processing are given in subsection 4.2.3. An average radon flux value of 0.12 Bq·m^{-2}·s^{-1} for the surveys was found.
- equation (5.13) and (5.14) is utilised where the activity concentration of the ^{238}U series, ^{232}Th series and ^{40}K is extracted from the measured γ-ray spectrum by incorporating the FSA and the traditional windows method. Since the two methods are used it is herein called the hybrid method (see Chapter 6). An average radon flux value of 0.11 Bq·m^{-2}·s^{-1} for the surveys was obtained.
- the standard formula (equation 5.32) is used to calculate the radon flux values.

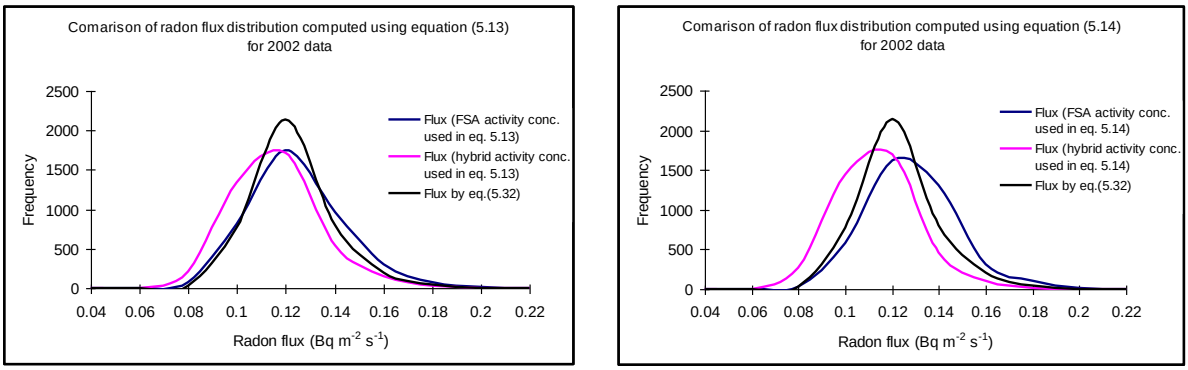

Figure 7.5: Radon flux distribution calculated using equation 5.13 (left) and equation 5.14 (right) together with equation 5.32 for the 2002 survey.

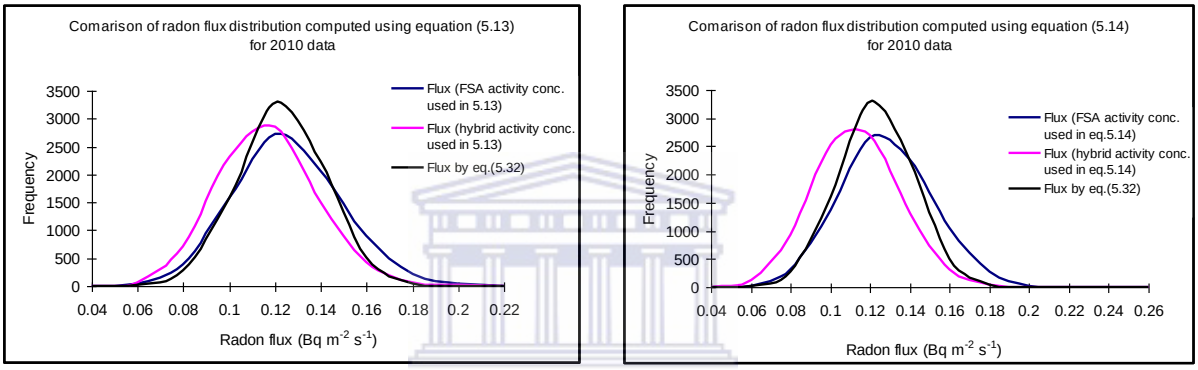

Figure 7.6: Radon flux distribution calculated using equation 5.13 (left) and equation 5.14 (right) together with equation 5.32 for the 2010 survey.

It was found that 89% of the data points have a flux distribution between 0.1 and 0.14 $Bq{\cdot}m^{-2}{\cdot}s^{-1}$ when the standard formula (equation 5.32) is utilised as compared to 78% when equation (5.13) or (5.14) is used where the activity concentrations are extracted using the FSA method. Lastly, about 68% of the data points have a flux range between 0.1 and 0.14 $Bq{\cdot}m^{-2}{\cdot}s^{-1}$ when equation (5.13) or (5.14) is used where the activity concentrations are extracted using the hybrid method.

7.5 General conclusions

In this work the MEDUSA γ-ray detector system was used

- to map the activity concentrations of the primordial radionuclides namely; ^{238}U series, ^{232}Th series and ^{40}K on tailing dumps. Mapping of the activity concentration was possible since the detector crystal has a relative high detection efficiency. Activity

concentrations were extracted using the Full Spectrum Analysis method which analyses the entire spectrum.

- to map the amount of radon being released from the mine dump surface to the atmosphere. A detailed procedure showing how to extract radon flux is given in Figure 5.5. More importantly the radon flux values extracted using this new technique (MELT) were found to be within the range of radon flux determined from other well known methods such as the one involving electrets, the dynamic system and the standard formula. The comparison of the results is shown in Figure 7.2.
- to map the amount of radon being released from a large area with reliable results. The Kloof mine dump is approximately 2 square kilometres. In 2002 and 2010 surveys, 4005 and 7961 data points were sampled respectively. The results deduced from these sample data points provide an accurate picture of the radon flux values from the mine dump unlike when a few sample points are analysed and then the results are generalised for the entire mine dump.

7.6 Recommendations and future work

- This new technique of extracting radon fluxes from measurements with the MEDUSA γ-ray detector system was applied to a non-operational Kloof mine dump which has been studied extensively. The technique could now be applied to other mine dumps to investigate the amount of radon released to the atmosphere.
- Since the study has shown that the MEDUSA γ-ray detector system can be used to map the radon flux, it could also be beneficial to model the dispersion of radon in the air with an aim of establishing the radiation dose that the surrounding communities receive if at all they are exposed to radon from the mine dump.

References

Åkerblom, G. & Mellander, H. (1997). Geology and radon. In: Durrani, S. A. & Ilić, R. (eds.), Radon measurements by etched track detectors: applications in radiation protection, earth sciences, and the environment. World Scientific Publishing Co. Pty. Ltd., pp. 21-49.

Aldenkamp, F. J., de Meijer, R. J., Put, L.W. & Stoop, P. (1992). An assessment of in situ radon exhalation measurement, and the relation between free and bound exhalation rates. Radiation Protection Dosimetry, Vol.45, No.1-4, pp. 449-453.

Andersen, C. E. (2000). Radon Transport Modelling: User's Guide to RnMod3d. Risø National Laboratory, Roskilde, Denmark.

Andersen, C. E. (2001). Numerical modelling of radon-222 entry into houses: an outline of techniques and results. The Science of the Total Environment, 272:33-42.

Antonopoulos-Domis, M., Clouvas, A. & Alifrangis, D. (2009). Experimental and theoretical study of radon distribution in soil. Health Physics, Vol. 97, No.4 (October), pp. 322-331.

Appleton, J. D. (2005). Radon in air and water. [Online]. Available from: http://www.wou.edu/las/physci/taylor/g473/med_geo/appleton_2005.pdf. [Accessed: March 20, 2012).

Arafa, W. (2004). Specific activity and hazards of granite samples collected from the Eastern Desert of Egypt. Journal of Environmental Radioactivity, 75: 315-327.

Bega, S. (2011). Residents use radioactive mud as an acne cure. [Online]. Available from: http://www.iol.co.za/saturday-star/residents-use-radioactive-mud-as-an-acne-cure-1.1178933. [Accessed on: May 2012].

BEIR VI (Committee on Health Risks of Exposure to Radon) (1999). Health Effects of Exposure to Radon: BEIR VI (Free Executive Summary) http://www.nap.edu/catalog/5499.html. National Research Council.

Bell, S. (2001). A beginner's Guide to Uncertainty of measurement Issue 2, Good Practice guide No.11, NPL, London, UK.

Bigu, J. (1984). Study of radon concentration, surface radon flux and other radiation variables from uranium mine tailings areas. Uranium 1, pp 257 - 277.

Bollhöfer, A., Storm, J., Martin, P. & Tims, S. (2003). Geographic variability in radon exhalation at the rehabilitated Nabarlek uranium mine, Northern Territory. Internal Report 465. Department of the environment and heritage, Australia.

Brajnik, D., Miklavzic, U. & Tomsic, J. (1992). Map of natural radioactivity in Slovenia and its correlation to the emanation of radon. Radiation Protection Dosimetry, 45: 273-276.

Chao, C. Y. H. & Tung, T. C. W. (1999). Radon emanation of building - impact of back diffusion and difference between one-dimensional and three-dimensional tests. Health Physics, Vol. 76, No.6, (June), pp. 675-681.

Chen, C. J., Weng, P. S. & Chu, T. C. (1993). Radon exhalation rate from various building materials. Health Physics, Vol. 64, No.6 (June), pp. 613-619.

Clements, W. E. & Wilkening, M. H. (1974). Atmospheric pressure effects on ^{222}Rn transport across the earth-air interface. Journal of Geophysical Research, Vol. 79, No. 33, pp. 5025-5029.

Collé, R., Kotrappa, P. & Hutchinson, J. M. R. (1995). Calibration of Electret-based integral radon monitors using NIST polyethylene-encapsulated ^{226}Ra/ ^{222}Rn emanation (PERE) standards. Journal of Research of the National Institute of Standards and Technology, Vol. 100, No.6, (November-December), pp. 629-639.

Comsol (2008). COMSOL Multiphysics Modeling guide version 3.5a.

Crank, J. (1975). The mathematics of diffusion. Oxford: Clarendon Press.

Croft, S. & Hutchinson, I. G. (1999). The measurement of U, Th and K concentrations in building materials. Applied Radiation and Isotopes, 51: 483-492.

Culot, M. V. J., Olson, H. G. & Schiager, K. T. (1976). Effective diffusion coefficient of radon in concrete, theory and method for field measurements. Health Physics, Vol.30 (March), pp. 263-270.

Damon, R. W. (2005). Determination of the photopeak detection efficiency of a HPGe detector, for volume sources, via Monte Carlo Simulations. MSc Thesis, University of the Western Cape, South Africa.

Daza, M. J., Quintana, B., Garcia-Talavera, M. & Fernandez, F. (2001). Efficiency calibration of a HPGe detector in the [46.54-2000] keV energy range for the measurement of environmental samples. Nuclear Instruments and Methods in Physics Research A, 470: 520-532.

Debertin, K. & Helmer, R. G. (2001). Gamma and X-ray spectrometry with semiconductor detectors. North Holland: Elsevier Science B. V.

De Groot, A. V., van der Graaf, E. R., de Meijer, R. J. & Maucec, M. (2009). Sensitivity of in-situ γ-ray spectra to soil density and water content. Nuclear Instruments and Methods in Physics Research A, 600: 519-523.

De Jong, P. et al (1996). The effect of the composition and production process of concrete on the ^{222}Rn exhalation rate. Environment International, Vol. 22, Suppl. 1, pp. S287-S293.

De Meijer, R.J. et al. (1997). Improved and new uses of natural radioactivity in mineral exploration and processing. Explor. Mining Geol. 6(1), 105-117.

De Meijer, R.J. (1998). Heavy minerals: from 'Edelstein' to Einstein. Journal of Geochemical Exploration, 62: 81-103.

De Meijer, R.J. & Lindsay, R. (2012). Department of Physics, University of the Western Cape, South Africa. Private communication.

Durrani, S. A. & Ilić, R. (eds.) (1997). Radon measurements by etched track detectors: applications in radiation protection, earth sciences, and the environment. London: World Scientific Publishing Co. Pte. Ltd.

Durridge Company Inc. (2000), Reference Manual version 6.0.1, RAD7™ Electronic Radon Detector.

EAD (2011). Effective radon diffusion coefficient. [Online]. Available from: http://web.ead.anl.gov/resrad/datacoll/radon.htm. [Accessed: November 2011].

EPA (2012), Environmental Protection Agency [Online]. Available from: http://www.epa.gov/rpdweb00/assessment/CAP88/aboutcap88.html. [Accessed: April 2012]

Escobar, V. G., Tome, F. V. & Lozano, J. C. (1999). Procedures for the determination of ^{222}Rn exhalation and effective ^{226}Ra activity in soil samples. Applied Radiation and Isotopes, 50: 1039-1047.

Ferry, C., Richon, P., Beneito, A. & Robe, M. C. (2001). Radon exhalation from uranium mill tailings: experimental validation of a 1-D model. Journal of Environmental Radioactivity, 54: 99-108.

Firestone, R.B., et al., 1996. Table of Isotopes. In: Shirley, V.S. (Ed.). John Wiley and Sons, New York.

Fleischer, R. L. (1980). Radon flux from the earth: Methods of measurement by the nuclear track technique. Journal of Geophysical Research, Vol. 85, No. C12, pp. 7553-7556.

Gadd, M. S. & Borak, T. B (1995). In-situ determination of the diffusion coefficient of ^{222}Rn in concrete. Health Physics, Vol.68, No.6 (June), pp. 817-822.

GDACE, (2008). Mining and Environmental Impact Guide. Produced by staff of Digby Wells and Associates, Growth Lab and the Council for Geoscience for the **G**auteng **D**epartment of **A**griculture, **E**nvironment and **C**onservation.

GeoDZ (2012). [Online]. Available from: http://www.geodz.com/deu/d/Witwatersrand_Gold-Uran-Seifenlagerst%C3%A4tte. [Accessed: March 2012].

Gilmore, G. R. (2008). Practical gamma-ray spectrometry. England: John Wiley & Sons, Ltd.

Golden Software, Inc., (2002). Surfer8 User's Guide, Contouring and 3D Surface Mapping for Scientist and Engineers, Colorado, USA.

Golder Associates Inc. (2010). Uranium mill tailings radon flux calculations, Piñon Ridge Project, Montrose County, Colorado. Prepared for Energy Fuels Resources Corporation. Project No. 073-81694.23. August.

Google Earth, (2012). Kloof mine dump. Available from: http://maps.google.co.za/maps?hl=en&biw=771&bih=421&q=kloof%20mine%20westonaria&um=1&ie=UTF-8&sa=N&tab=wl [Accessed: May 2011].

Goto, M. et al (2008). Estimation of global radon exhalation rate distribution. The Natural Radiation Environment - 8th International Symposium, edited by A. S. Paschoa.

Grasty, R. L. (1997). Radon emanation and soil moisture effects on airborne gamma-ray measurements. Geophysics, Vol. 62, No. 5 (September-October), pp. 1379-1385.

Graustein, W. C. & Turekian, K. K. (1990). Radon fluxes from soils to the atmosphere measured by ^{210}Pb - ^{226}Ra disequilibrium in soils. Geophysical Research Letters, Vol. 17, No.6, pp. 841-844.

Griffiths, A. D., Zahorowski, W., Element, A. & Werczynski, S. (2010). A map of radon flux at the Australian land surface. Atmos. Chem. Phys., 10, 8969-8982.

Grossi, C. et al (2011). Inter-comparison of different direct and indirect methods to determine radon flux from soil. Radiation Measurements, 46:112-118.

Hartnady, C. J. H. (2009). South Africa's gold production and reserves. South African Journal of Science 105 (9/10), pp 328–329.

Hassan, N. M. et al (2009). Radon migration process and its influence factors; review. Jpn. J. Health Phys., 44 (2), 218-231.

Hendriks, P. H. G. M., Limburg, J. & de Meijer, R.J. (2001). Full-spectrum analysis of natural γ-ray spectra. Journal of Environmental Radioactivity, 53: 365-380.

Hirao, S., Yamazawa, H. & Moriizumi, J. (2010). Inverse modeling of Asian ^{222}Rn flux using surface air 222Rn concentration. Journal of Environmental Radioactivity, 101: 974-984.

Hlatshwayo, I.N., Lindsay, R., Ndwandwe, O.M. & Newman, R.T. (2009). In-situ gamma-ray mapping of environmental radioactivity at iThemba LABS and associated risk assessment. Radioprotection, Vol. 44, No. 5, pp. 825-830.

Holford, D. J. (1994). Rn3D: A finite element code for simulating gas flow and radon transport in variably saturated, nonisothermal, porous media: User's manual, version 1.0. Pacific Northwest Laboratory.

Hosoda, M. et al (2007). Effect of soil moisture content on radon and thoron exhalation. Journal of Nuclear Science and Technology, Vol. 44, No. 4, pp. 664-672.

IAEA (1992). Measurement and calculation of radon release from uranium mill tailings. Technical Report Series No. 333. International Atomic Energy Agency, Vienna, Austria.

IAEA (2003), Guidelines for radioelement mapping using gamma ray spectrometry data. International Atomic Energy Agency, Vienna, Austria.

Ielsch, G., Ferry, C., Tymen, G. & Robe, M. C. (2002). Study of a predictive methodology for quantification and mapping of the radon-222 exhalation rate. Journal of Environmental Radioactivity, 63: 15-33.

Ingersoll, J. G. (1983a). A survey of radionuclide contents and radon emanation rates in building materials used in the U.S. Health Physics, Vol. 45, No.2 (August), pp. 363-368.

Ingersoll, J. G., Stitt, B. D. & Zapalac, G. H. (1983b). A fast and accurate method for measuring radon exhalation rates from building materials. Health Physics, Vol. 45, No.2 (August), pp. 550-552.

ISO (1992). Guide to the expression of Uncertainty in measurement. International Organization for Standardization. Switzerland.

ISU, (2011). Radioactivity in Nature. [Online]. Available from **I**daho **S**tate **U**niversity: http://www.physics.isu.edu/radinf/natural.htm. [Accessed: November, 2011].

Janssens, A., Raes, F. & Poffijn, A. (1984). Transients in the exhalation of radon caused by changes in ventilation and atmospheric pressure. Radiation Protection Dosimetry, Vol.7, No.1-4, pp. 81-86.

Jarzemba, M. S. & Blue, T. E. (1996). An in-situ method to measure a soil's undisturbed pore gas radon concentration, diffusion length for radon and air filled porosity. Health Physics, Vol.70, No.4 (April), pp. 546-551.

Jha, S., Khan, A. H. & Mishra, U. C. (2000). A study of the ^{222}Rn flux from soil in the U mineralised belt at Jaduguda. Journal of Environmental Radioactivity, 49: 157-169.

Jurza, P. et al (2005). Use of ^{214}Pb photopeaks for radon removal: utilizing current airborne gamma-ray spectrometer technology and data processing. Exploration Geophysics, 36: 322-328.

Khater, A. E. M. & Ebaid, Y.Y. (2008). A simplified gamma-ray self-attenuation correction in bulk samples. Applied Radiation and Isotopes, 66: 407-413.

Knoll, G. F. (2010). Radiation detection and measurement. 4th edition, USA: John Wiley & Sons, Inc.

Kohl, T., Medici, F. & Rybach, L. (1994). Numerical simulation of radon transport from subsurface to buildings. Journal of Applied Geophysics, 31:145-152.

Kotrappa, P., Dempsey, J. C., Hickey, J. R. & Stieff, L. R. (1988). An Electret passive environmental 222Rn monitor based on Ionization measurement. Health Physics, Vol. 54, No. 1 (January), pp. 47-56.

Kotrappa, P., Dempsey, J. C., Ramsey, W. & Stieff, L. R. (1990). A practical E-PERM^{TM} (Electret Passive Environmental Radon Monitor) system for indoor ^{222}Rn Measurement. Health Physics, Vol. 58. No. 4 (April), pp, 461-467.

Kotrappa, P. et al (1994). Measurement of the radon surface flux from undisturbed soil using Electret ion chambers. International Radon Symposium III.

Kotrappa, P., Stieff, L. R. & Bigu, J. (1996). Passive E-PERM radon flux monitors for measuring undisturbed radon flux from the ground. International Radon Symposium II.

Kotrappa, P. (2000). Review of E-PERM passive integrating Electret Ionization Chambers for measuring radon in air, thoron in air, radon in water and thoron flux from surfaces and mill tailings. International Radon Symposium.

Kotrappa, P. & Stieff, F. (2009). Radon exhalation rates from building materials using Electret Ion Chamber radon monitors in accumulators. Health Physics, Vol. 97, No.2 (August), pp. 163-166.

Kovler, K. Perevalov, A. Steiner, V. & Metzger, L. A. (2005). Radon exhalation of cementitious materials made with coal fly ash: Part 1 - scientific background and

testing of the cement and fly ash emanation. Journal of Environmental Radioactivity, 82: 321-334.

Krane, K.S., (1988). Introductory Nuclear Physics. John Wiley & Sons, Inc.

Lapp, R. E. & Andrews, H. L. (1972). Nuclear radiation physics. New Jersey: Prentice-Hall, Inc.

Lawrence, C. E. (2005). Measurement of ^{222}Rn exhalation rates and ^{210}Pb deposition rates in a tropical environment. PhD Thesis, Queensland University of Technology, Australia.

Lawrence, C. E. et al (2009). Radon-222 exhalation from open ground on and around a uranium mine in the wet-dry tropics. Journal of Environmental Radioactivity, 100: 1-8.

Laxman, C. & Dayanand, R. (2012). Mass attenuation coefficient measurements in soil sample. Research Journal of Chemical Sciences, Vol. 2(5), 17-22.

Leo, W.R. (1987). Techniques for nuclear and particles physics experiments. Germany: Springer-Verlag Berlin Heidelberg.

Lilley, J. (2005). Nuclear Physics: principles and applications. England: John Wiley & Sons, Ltd.

Limburg, J., Koomans, R. L., Tijs, M. & van der Boor, M. (2009). GAMMAN - a software tool for the analysis of gamma spectra obtained in geophysical research. The Netherlands: Medusa Explorations BV.

Lindsay, R. et al (2004a). Monitoring the radon flux from gold-mine dumps by γ-ray mapping. Nuclear Instruments and Methods in Physics Research B, 213: 775-778

Lindsay, R. et al (2004b). Measurement of radon exhalation from a gold-mine tailings dam by γ-ray mapping. Radiation Physics and Chemistry, 71: 797-798.

Lindsay, R., Newman, R. T. & Speelman, W. J. (2008). A study of airborne radon levels in Paarl houses (South Africa) and associated source terms, using Electret ion chambers and gamma-ray spectrometry. Applied Radiation and Isotopes, 66:1611-1614.

Lindsay, R. (2012). Department of Physics, University of the Western Cape, South Africa. Private communication.

Loureiro, C. O. (1987). Simulation of the steady-state transport of radon from soil into houses with basements under constant negative pressure. PhD Thesis, University of Michigan, USA.

Loureiro, C. O., Abriola, M. L., Martin, J. E., & Sextro, R. G. (1990). Three-Dimensional simulation of radon transport into houses with basements under constant negative pressure. Environ. Sci. Technol. Vol. 24, No. 9, pp. 1338-1348.

Maleka, P. P. (2010). In-situ element analysis from gamma-ray and neutron spectra using a pulsed-neutron source. PhD Thesis, Rijksuniversiteit Groningen.

Maleka, P. P. (2012). Department of Nuclear Physics, iThemba LABS, Somerset West South Africa. Private communication.

Manavhela, R. F. (2007). In-situ measurements of radon concentrations in soil gas at a site on the cape flats. MSc Thesis, University of the Western Cape, South Africa.

Manutange, S. (2002). The impact of atmospheric pathways on public exposure. MSc Thesis, University of North West, South Africa.

Markkanen, M. & Arvela, H. (1992). Radon emanation from soils. Radiation Protection Dosimetry, Vol.45, No.1-4, pp. 269-272.

Mbendi (2012). MBendi Information Services [Online]. Available from: http://www.mbendi.com/indy/ming/af/sa/p0005.htm. [Accessed: April 2012]

Melquiades, F. L. & Appoloni, C. R. (2001). Self-absorption correction for gamma spectrometry of powdered milk samples using Marinelli beaker. Applied Radiation and Isotopes, 55: 697-700.

Minty, B. R. S. (1997a). Fundamentals of airborne gamma-ray spectrometry. Journal of Australian Geology & Geophysics, 17(2), 39-50.

Minty et al., (1997b). Calibration and data processing for airborne gamma-ray spectrometry. Journal of Australian Geology & Geophysics, 17(2) : 51-62.

Misiak, R. et al (2011). Self-absorption correction and efficiency calibration for radioactivity measurement of environmental samples by gamma-ray spectrometry. Nukleonika, 56(1):23-28.

Mlwilo, N. A. (2010). Radiometric characterization of vineyard soils, Western Cape, South Africa. PhD Thesis, University of the Western Cape, South Africa.

Motlhabane, T. G. K. (2003). Critical assessment of the MEDUSA gamma ray detection system for radon flux measurement on a tailings dam. MSc Thesis. University of North West, South Africa.

Mudd, G. M. (2007). Global trends in gold mining: Towards quantifying environmental and resource sustainability. Resources Policy 32: 42-56.

Mudd, G. M. (2008). Radon sources and impacts: a review of mining and non-mining issues. Rev. Environ. Sci. Biotechnol., 7: 325-353.

Nazaroff, W. W., Moed, B. A. & Sextro, R. G. (1988). Soil as a source of indoor radon: Generation, migration, and entry. In: Nazaroff, W.W. & Nero, A. V. (eds.), Radon and its decay products in indoor air. John Wiley and Sons, Inc., pp 57-112.

Nazaroff, W. W. (1992). Radon transport from soil to air. Reviews of Geophysics, 30, No.2 (May), pp. 137-160.

NCRP (1988). National Council on Radiation Protection and Measurements. Measurement of radon and radon daughters in air, NCRP Report No. 97. National Council on Radiation protection and Measurements, Bethesda, Maryland.

Nero, A. (1989). Earth, air, radon and home. Physics Today. April, pp. 32-38.

Newman, R. T. et al (2008). Determination of soil, sand and ore primordial radionuclide concentrations by full-spectrum analyses of high-purity germanium detector spectra. Applied Radiation and Isotopes, 66: 855-859.

Nielson, K. K. et al (1994). The RAETRAD model of radon generation and transport from soils into slab-on-grade houses. Health Physics, Vol.67. No.4 (October), pp. 363-377.

Ogundare, F. O. et al (2012). Low-energy broad-beam photon shielding data for constituents of concrete. Journal of Applied Clinical Medical Physics, Vol. 13 (2): 176-182.

Oufni, L. (2003). Determination of the radon diffusion coefficient and radon exhalation rate in Moroccan quaternary samples using the SSNTD technique. Journal of Radioanalytical and Nuclear Chemistry, Vol. 256, No. 3, pp. 581-586.

Owczarski, P. C., Holford, D. J., Gee, G. W., Freeman, H. D. & Burk, K. W. (1990). Radon transport from the subsurface: The role of certain boundary conditions at subsurface/environment boundaries. Pacific Northwest Laboratory.

Pearson, J. E. & Jones, G. E. (1966). Soil concentrations of emanating radium-226 and the emanation of radon-222 from soils and plants. Tellus, XVIII, 2.

Pires, F. L., Bacchi, O. O. S. & Dias, N. M. P. (2006). Gamma-ray beam attenuation to assess the influence of soil texture on structure deformation. Nukleonika, 51(2):125-129.

Quindós, L. S. et al (2006). Correction by self-attenuation in gamma-ray spectrometry for environmental samples. Journal of Radioanalytical and Nuclear Chemistry, Vol. 270, No.2, pp. 339-343.

Rad Elec Inc. (1994), Reference Manual, Radon and Radiation Measurements.

Rogers, V. C. & Nielson, K. K. (1991a). Multiphase radon generation and transport in porous materials. Health Physics, Vol. 60, No.6 (June), pp. 807-815.

Rogers, V. C. & Nielson, K. K. (1991b). Correlations for predicting air permeabilities and 222Rn diffusion coefficients of soils. Health Physics, Vol.61, No.2 (August), pp. 225-230.

Rosnick, R. (2007). CAP88-PC Version 3.0 User Guide. Washington (USA): Trinity Engineering Associates, Inc.

Sahoo, B. K. et al (2007). Estimation of radon emanation factor in Indian building materials. Radiation Measurements, 42: 1422-1425.

Sahoo, B. K. (2010). Radon exhalation studies in an Indian uranium tailings pile. Radiation Measurements, 45: 237-241.

Samuelsson, C. & Pettersson, H. (1984). Exhalation of ^{222}Rn from porous materials. Radiation Protection Dosimetry, Vol.7, No. 1-4, pp. 95-100.

Scheele, F., de Haan, E. & Wilde-Ramsing, J. (2011). Uranium from Africa Mitigation of Uranium mining impacts on society and environment by industry and governments. WISE & SOMO, Amsterdam.

Schery, S. D. & Petschek, A. G. (1983). Exhalation of radon and thoron: the question of thermal gradients in soil. Earth and Planetary Science Letters, 64: 56-60.

Schery, S. D., Gaeddert, D. H. & Wilkening, M. H. (1984). Factors affecting exhalation of radon from gravelly sandy loam. Journal of Geophysical Research, Vol. 89, No. D5, pp. 7299-7309.

Schery, S. D., Whittlestone, S. & Hill, S. E. (1989). The flux of radon and thoron from Australian soils. Journal of Geophysical Research, Vol.94, No.D6 (June), pp. 8567-8576.

Schubert, M. & Schulz, H. (2002). Diurnal radon variations in the upper soil layers and at the soil-air interface related to meteorological parameters. Health Physics, Vol. 83, No.1 (July), pp. 91-96.

Schumann et al (1988). Weather factors affecting soil-gas radon concentrations at a single site in the semiarid western U.S. [Online]. Available from:

http://www.aarst.org/proceedings/1988/1988_54.

Schumann, R.R., Gundersen, L.C.S. & Tanner, A.B. (1994). Geology and occurrence of radon. In Radon: Prevalence, measurements, health risks and control. Editor N.L. Nageda, pp. 83 - 96.

Shweikani, R., Giaddui, T. G. & Durrani, S. A. (1995). The effect of soil parameters on the radon concentration values in the environment. Radiation Measurements, Vol. 25, No.1-4, pp. 581-584.

Speelman, W. J. (2004). Modelling and measurement of radon diffusion through soil for application on mine tailings dams. MSc Thesis. University of the Western Cape, South Africa.

Stranden, E. (1983). Assessment of the radiological impact of using fly ash in cement. Health Physics, Vol. 44, No.2 (February), pp. 145-153.

Stranden, E., Kolstad, A. K. & Lind, B. (1984). Radon exhalation: moisture and temperature dependence. Health Physics, Vol. 47, No.3 (September), pp. 480-484.

Strong, K. P. & Levins, D. M. (1982). Effect of moisture content on radon emanation from uranium ore and tailings. Health Physics, Vol. 42, No.1 (January), pp. 27-32.

Szegvary, T., Leuenberger, M. C. & Conen, F. (2007). Predicting terrestrial ^{222}Rn flux using gamma dose rate as a proxy. Atmos. Chem. Phys., 7: 2789-2795.

Talha, S. A. A. (2009). Measurements and applications of radon in South African aquifer and river waters. PhD Thesis, University of the Western Cape, South Africa.

Tanner, A.B. (1980) Radon migration in the ground: A supplementary review. Proceedings of Natural Radiation Environment III: Springfield, US DOE Report CONF-780422, Vol. 1, pp. 5-56.

Tsela A. S. & Brits R.J.N. (1998). A theoretical study of the effect of various parameters on radon exhalation from mine tailings. SARPA Conference.

Turhan, S. (2008). Assessment of the natural radioactivity and radiological hazards in Turkish cement and its raw materials. Journal of Environmental Radioactivity, 99: 404-414.

UKAS (2007). The Expression of Uncertainty and Confidence in Measurement, M3003. United Kingdom Accreditation Service. Middlesex, UK.

UNSCEAR (1982). Ionizing radiation: Sources and biological effects Annex D. United Scientific Committee on the Effects of Atomic Radiation. 1982 Report to the General Assembly, with annexes. United Nations publications.

Van der Spoel, W. H., van der Graaf, E. R. & de Meijer, R. J. (1997). Diffusive transport of radon in a homogeneous column of dry sand. Health Physics, Vol. 72, No. 5 (May), pp. 766-778.

Van der Spoel, W. H., van der Graaf, E. R. & de Meijer, R. J. (1998). Foil coverage of a crawl-space floor: measurements and modelling of radon entry. Health Physics, Vol.74, No.5 (May), pp.581-593.

Van der Spoel, W. H., van der Graaf, E. R. & de Meijer, R. J. (1999). Diffusive transport of radon in a column of moisturized sand. Health Physics, Vol.77, No. 2 (August), pp. 163-177.

Venema, L. B. & de Meijer, R. J. (2001). Natural radionuclides as tracers of the dispersal of dredge spoil dumped at sea. Journal of Environmental Radioactivity, 55: 221-239.

Watterson, J. I. W., Makhabane, J. H. & Kala, B. R. (1993). Radon emission from tailings dumps. Report to Richard's Bay Minerals (TISAND). Report No. SRCNS 93/05. University of the Witwatersrand, Johannesburg. Scholand Research Centre for Nuclear Sciences.

Wikipedia1: The Free Encyclopedia (2012). Mining industry of South Africa. [Online]. Available from: http://en.wikipedia.org/wiki/Mining_industry_of_South_Africa#cite_note-cia-7. [Accessed: April 2012].

Wikipedia2: The Free Encyclopedia (2012), Radon. [Online]. Available from: http://en.wikipedia.org/wiki/Radon. [Accessed: March, 2012].

Winde, F. (2010). Uranium pollution of the Wonderfonteinspruit, 1997-2008. Part 2: Uranium in water - concentrations, loads and associated risks. Water SA, Vol. 36 No.3. Also Available from: http://www.wrc.org.za/Pages/Preview.aspx?ItemID=8677&FromURL=%2fPages%2fDisplayItem.aspx%3fItemID%3d8677%26FromURL%3d%252fPages%252fDefault.aspx%253f [Accessed: April, 2012].

WISE, (2012). World information Service on Energy Uranium Project. Uranium Mill Tailings Radon Flux Calculator. [Online]. Available from: http://www.wise-uranium.org/ctb.html?unit=c. [Accessed: April, 2012].

WHO (2009). World Health Organization. WHO handbook on indoor radon: A public health perspective. WHO press, Geneva.

Yakovleva, V. S. (2005). A theoretical method for estimating the characteristics of radon transport in homogeneous soil. Annals of Geophysics, Vol. 48, No.1 (February), pp. 195-198.

Yucel, H., Cetiner, M. A. & Demirel, H. (1998). Use of the 1001 keV peak of ^{234m}Pa daughter of ^{238}U in measurement of uranium concentration by HPGe gamma-ray spectrometry. Nuclear Instruments and Methods in Physics Research A, 413: 74-82.

Zhuo, W., Iida, T. & Furukawa, M. (2006). Modeling radon flux density from the earth's surface. Journal of Nuclear Science and Technology, Vol. 43, No. 4, pp. 479-482.

Zhuo, W., Guo, Q., Chen, B. & Cheng, G. (2008). Estimating the amount and distribution of radon flux density from the soil surface in China. Journal of Environmental Radioactivity, 99: 1143-1148.

APPENDICES

Appendix A

Interpolation using Surfer® 8

Surfer® is a grid based graphics program. Surfer interpolates irregularly spaced XYZ data into a regularly spaced grid. The term "irregularly" spaced means that the points follow no particular pattern over the extent of the map, so there are many "holes" where data are missing. The grid is then used to produce different types of maps including contour, vector, wireframe, image, shaded relief, and surface maps [Golden Software, Inc., 2002].

In order to progress from a XYZ data set to a finished, grid-based map the following steps are followed as illustrated by the flow chart in Figure A.1 and explained briefly as

1. Create a XYZ data file. This file can be created in a **Surfer** worksheet window or outside of **Surfer** (using an ASCII text editor or Excel, for example).
2. Create a grid [.GRD] file from the XYZ data file using the **Grid | Data** command.
3. To create a map, click the **Map | New** command, select a map type, and use the grid file from step two. Grid-based maps include contour, image, shaded relief, vector, 3D wireframe, and 3D surface maps.
4. Use the **File | Save** command to save the project as a **Surfer [**.SRF] file which contains all of the information needed to recreate the map.

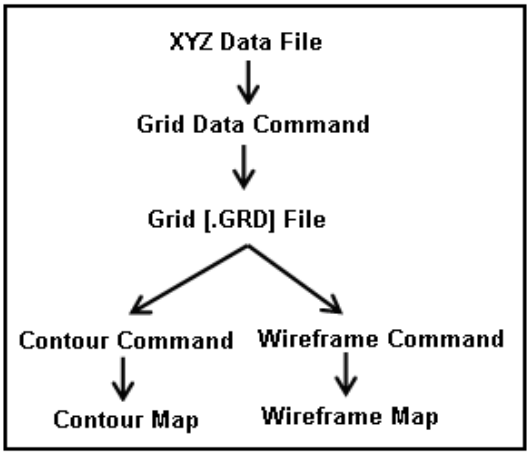

Figure A.1: The flow chart illustrates the relationship between XYZ data files, grid files, contour maps, and wireframes.

Surfer uses several methods for gridding such as; Inverse Distance to a power, Kriging, Minimum Curvature, Modified Shepard's Method, Natural Neighbour, Nearest Neighbour, Polynomial Regression, Radial Basis Function, Triangulation with Linear interpolation, Moving Average Data Metrics and Local Polynomial. These methods are displayed on the left hand side of Figure A.2. These gridding methods produce a regularly spaced, rectangular array of Z values from irregularly spaced XYZ data at each grid node by interpolating or extrapolating the data values.

While analysing data an appropriate gridding method can be chosen depending on the data being processed and the method which produces the best expected results.

In this study, the **Natural Neighbour** gridding method was used, (see right hand side of Figure A.2. The X and Y data represent the latitude and the longitude respectively. The Z data was ascribed as either the activity concentrations of the radionuclides or the total counts of the radionuclides or the radon flux.

As an example Figure A.2 on the right hand side shows that the **Natural Neighbour** gridding method was used to interpolate the radon flux for the Kloof mine dump survey of 2002 where a total of 4005 points were captured.

The Natural Neighbour gridding method uses an interpolation algorithm which uses a weighted average of the neighbouring observations, where the weights are proportional to the "borrowed area". The details of the other gridding methods can be found in the Surfer®8 Manual [Golden Software, Inc., 2002].

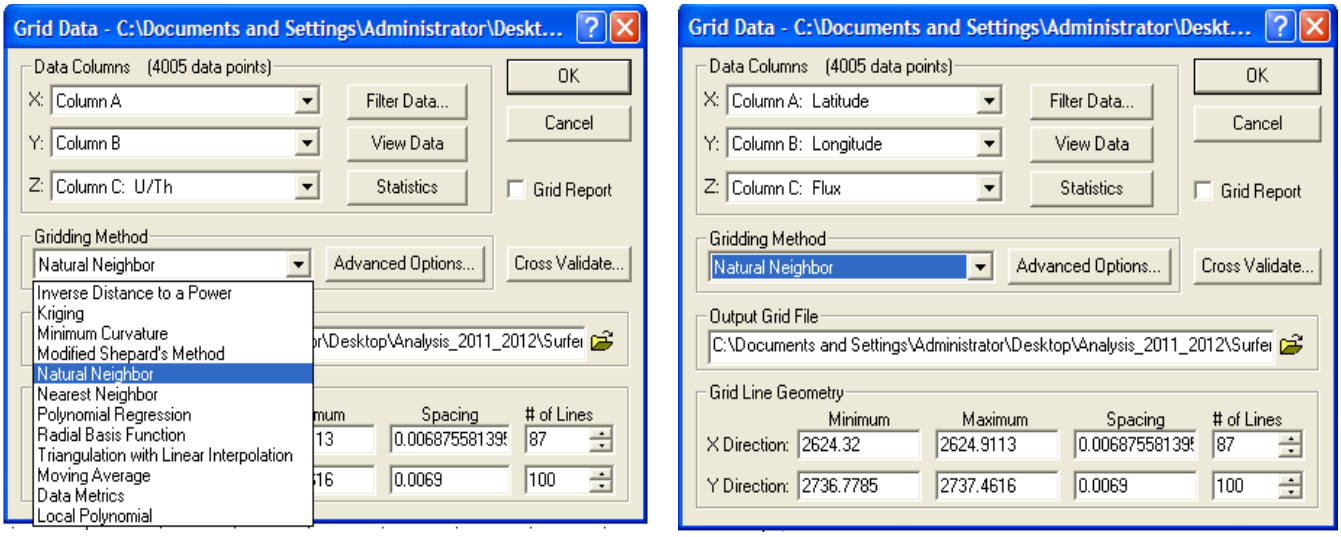

Figure A.2: The Dialog box on the left shows the gridding methods while the dialog box on the right shows the gridding method chosen for this study.

Appendix B

Determining the uncertainty of the MEDUSA activity concentration

The activity concentrations of the radionuclides ^{40}K and in the decay series of ^{238}U and ^{232}Th on the Kloof mine dump were determined using the MEDUSA γ-ray detector. The set-up and the extraction of the activity concentrations are discussed at length in Chapter 4 section 4.2. The MEDUSA γ-ray detector detects radionuclides in the ground up to a depth of 30 cm. This limitation is as a result of self-absorption of the γ-rays within the soil.

The activity concentrations are extracted using the MEDUSA Post Analysis (MPA) software using a process based on the least squares method which minimizes the chi-squared (χ^2). The activity concentrations were then exported to Microsoft Excel for further analysis for instance the activity concentrations were normalised using appropriate normalisation factors (see Chapter 5 Table 5.4). After that the averages of the normalised activity concentrations were determined as well as their uncertainties as described next.

B.1 Types of uncertainty

Uncertainty can be categorised as Type A and Type B. Type A uncertainties are determined by repeated measurements to assess the magnitude and distribution of the parameter. Type B uncertainties are those determined by any other means for example information can be obtained from the literature or based on experience etc [Gilmore, 2008].

B.2 Evaluating Type A uncertainty

Type A uncertainty (σ_A) was derived from the activity concentration measurements which were performed on the same path on the Kloof mine dump. The path is indicated by a circle on the maps shown in Figure B.1. The activity concentrations along that path were measured on three different days but at approximately the same time each day. After the activity concentrations for each radionuclide was extracted using the MEDUSA

Post Analysis software the standard deviation for each radionuclide was divided by $\sqrt{3}$ to give the standard uncertainty (u) which is given by

$$u = \frac{s}{\sqrt{n}} \qquad \text{(B.1)}$$

where, s is the standard deviation and n is the number of measurements performed and in this case it is 3. The activity concentrations along that path were measured assuming that the path (or geometry) and other meteorological factors will be almost the same because it was measured at approximately the same time of the day.

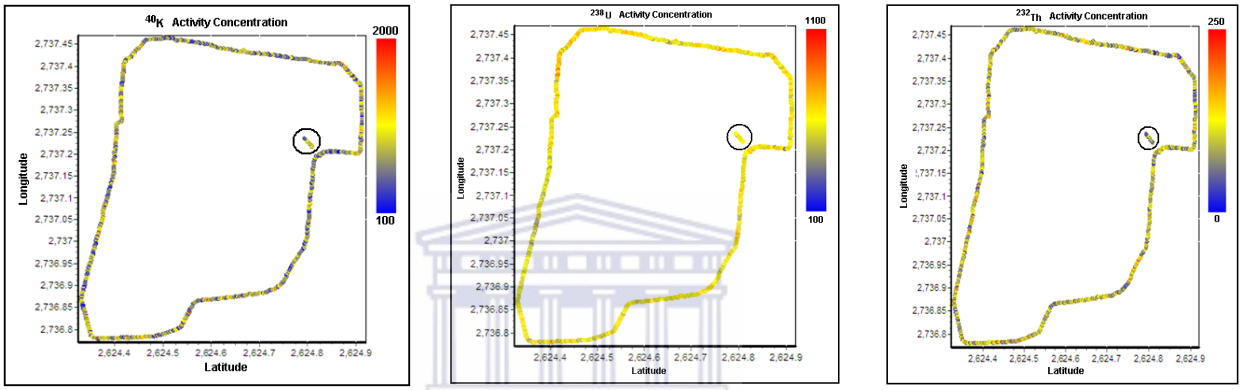

Figure B.1: Maps showing the path where the activity concentrations for ^{40}K, ^{238}U series and ^{232}Th were measured.

B.3 Evaluating Type B uncertainty

Type B uncertainty (σ_{B1}) was evaluated by considering the standard deviation computed on one part indicated in Figure B.2 of the Kloof mine dump for 2002 and 2010 surveys. The average activity concentrations for ^{40}K and the decay series of ^{232}Th and ^{238}U for that part of the mine dump were computed as well as the standard deviations. In Chapter 5 the bar graphs of Figure 5.9-5.10 indicate that there is a normal distribution of the radon fluxes in the mine dump. Therefore, assuming that the activity concentrations will be distributed normally then the magnitude of the standard deviation calculated for the radionuclides will be divided by 2 [Bell, 2001].

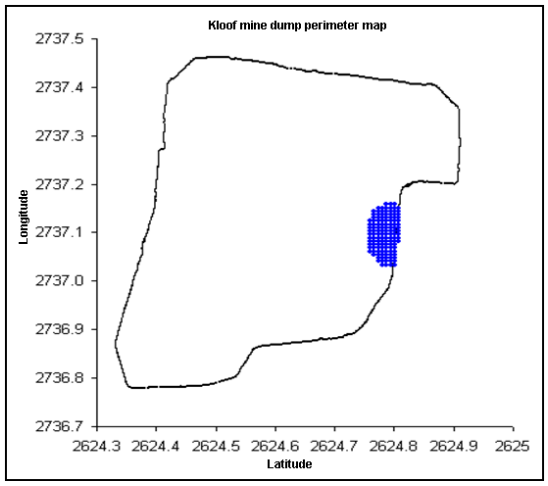

Figure B.2: A map showing the Kloof mine dump perimeter plus the part which was analysed for Type B uncertainty

B.4 Further evaluation of Type B uncertainty

This type of uncertainty designated as σ_{B2} was derived from measurements which were performed when the iThemba MEDUSA γ-ray detector was first tested in June 2002.

According to the records available at iThemba LABS it was tested on drums which contained silversand, monazite and KCl+silversand [Maleka, 2012]. Therefore taking the lowest percentage of uncertainty recorded when those measurements were performed and then dividing them with a coverage factor, k=1.645 gives an indication of the uncertainty during that time it was manufactured (or tested) [ISO, 1992]. That yields a percentage uncertainty of 1% for ^{40}K, 2% for ^{238}U and 2% for ^{232}Th.

Table B.1: Coverage factors and the associated degree of confidence[*].

Coverage factor	Area within confidence limits (%)
1.0	68.3
1.645	90.0
1.96	95.0
2.0	95.5
2.326	98.0
2.576	99.0
3.0	99.9

[*]Confidence limit = Coverage factor × Standard Uncertainty

B.5 Combining the standard uncertainty

The uncertainties mentioned above were combined as shown below and the results are given in Table B.2.

$$\sigma_{Total} = \sqrt{(\sigma_A)^2 + (\sigma_{B1})^2 + (\sigma_{B2})^2} \quad \text{(B.2)}$$

Table B.2: Uncertainty budget for ^{40}K, ^{238}U series and ^{232}Th series.

Source of uncertainty	Uncertainty Magnitude (%)			Probability Distribution	††Divisor	+Standard uncertainty (%)		
	^{40}K	^{238}U	^{232}Th			^{40}K	^{238}U	^{232}Th
Type A Due to repeatability of measurements	16	7	15	Normal	1	16	7	15
Type B Due to measurement done on different years	9	4	11	Normal	1	9	4	11
Uncertainty attributed to when the MEDUSA detector was first tested	2	4	3	Normal	2	1	2	2
$\sigma_{Total} = \sqrt{(\sigma_A)^2 + (\sigma_{B1})^2 + (\sigma_{B2})^2}$						18	8	18
**Expanded uncertainty (90% uncertainty; coverage factor (k) = 1.645)						29	13	29

+Standard uncertainty = Uncertainty Magnitude/divisor
††Divisors are given in Table B.3.
**Expanded uncertainty = Standard Uncertainty × 1.645

Table B.3: Calculation of standard uncertainty for different distributions.

Distribution	Parameter	Divisor
Normal	68% confidence limit(1σ)	1
Normal	95% confidence limit (2σ)	2
Rectangular	Half-range	√3
Triangular	Half-range	√6
U-shaped	Half-range	√2

Appendix C

Exhalation of radon from a mine tailings dump by measuring the gamma radiation from the dump

(Developed from unpublished report [De Meijer & Lindsay, 2012]).

Consider a semi infinite homogeneous layer of consolidated dry sand. The sand with specific density of ρ_s (which can be approximated fairly accurately by the density of sand made of SiO_2 that equals 2.6 g·cm^{-3}) contains C_{Ra} Bq·kg^{-1} of ^{238}U (as measured in the HPGe at iThemba LABS) which is in secular equilibrium with ^{226}Ra. A fraction ε per unit volume is filled with air (porosity ε), hence the grains occupy (1-ε) of the volume. Ignoring the mass of the air, the bulk density of the layer is given by

$$\rho_b = (1-\varepsilon)\,\rho_s \qquad \text{(C.1)}$$

For every m^3 of layer, $C_{Ra}\rho_b$ Bq of ^{226}Ra is present. (ρ_b was measured at UWC based on the mass of material brought from the dump).

Due to nuclear decay, ^{226}Ra will turn into ^{222}Rn (radon). A fraction, E, will leave the grains and enter the air-filled void space. Since each Bq of ^{226}Ra produces one Rn atom, per second, the number of radon atoms entering the void space per second per m^3 equals

$$N_{Rn} = E\,C_{Ra}\,\rho_b \qquad \text{(C.2)}$$

In secular equilibrium, the total number of radon atoms in the pore space per m^3 of layer follows from the condition that production equals decay:

$$E\,C_{Ra}\,\rho_b = \lambda_{Rn}\,N = A_{Rn}^{air} \text{ per m}^3 \text{ of layer} \qquad \text{(C.3)}$$

The activity concentration of Rn in the air-filled pore space becomes:

$$C_{Rn}^{air} = \frac{E\,C_{Ra}\,\rho_b}{\varepsilon}\ \text{Bq/m}^3 \qquad \text{(C.4)}$$

In the grain filled part of the layer, the radon production is $(1-E)C_{Ra}\rho_b$ atoms per second and hence the volumetric concentration becomes

$$C_{Rn}^{grain} = \frac{(1-E)\,C_{Ra}\,\rho_b}{(1-\varepsilon)}\ \text{Bq/m}^3 \qquad \text{(C.5)}$$

Note: The total radon concentration under secular equilibrium conditions (only radon is disappearing by nuclear decay)

$$C_{Rn}^{total} = \varepsilon C_{Rn}^{air} + (1-\varepsilon)\ C_{Rn}^{grain} = E\ C_{Ra}\ \rho_b\ +\ (1-E)\ C_{Ra}\ \rho_b\ =\ C_{Ra}\ \rho_b \qquad (C.6)$$

as to be expected.

So at great depth, we know the partitioning between radon in the grains and radon in the pore space.

Near the surface, radon will diffuse to the surface and exhale into the air. We assume that the radon concentration profile for the air-filled pore space can be written as (see derivation in Chapter 3 equations (3.5)-(3.8))

$$C(z) = C^{\infty}(1-e^{-z/\ell}) \qquad (C.7)$$

where C^{∞} is the volumetric concentration of radon in the pore space at large depth and $\ell = \sqrt{D/\lambda_{Rn}}$ is the diffusion length with D the effective diffusion constant for radon and λ_{Rn} is the radon decay constant.

According to equation (C.4):

$$C^{\infty} = \frac{E}{\varepsilon} C_{Ra}\ \rho_b \qquad (C.8)$$

The exhalation per unit of surface is often defined as

$$J = \varepsilon D \frac{\partial C}{\partial z} \quad \text{at } z = 0$$

$$J = \frac{\varepsilon D}{\ell} C^{\infty} = \frac{E D}{\ell} C_{Ra}\ \rho_b \qquad (C.9)$$

from equation (C.7) which is similar to equation (5.32).

Radon in the soil decays further into the gamma-ray producing nuclei ^{214}Pb and ^{214}Bi which are assumed to be in equilibrium with respect to each other and to the ^{222}Rn concentration. At depth z, the volumetric concentration of the 214 nuclei follows from the radon concentration in the grains, which is independent of z, and the z dependent radon concentration in the air filled pore space

$$C^{214}(z) = (1-\varepsilon) C_{Rn}^{grain} + \varepsilon C_{Rn}^{air} = (1-E)\ C_{Ra}\ \rho_b + E\, C_{Ra}\ \rho_b\ (1-e^{-z/\ell})$$

$$C^{214}(z) = C_{Ra}\ \rho_b\ [1-E\, e^{-z/\ell}] \qquad (C.10)$$

Consider again a semi infinite layer of homogeneous material with density ρ and activity concentration of C (Bq/kg). Assume that per decay the gamma-rays are emitted isotropically.

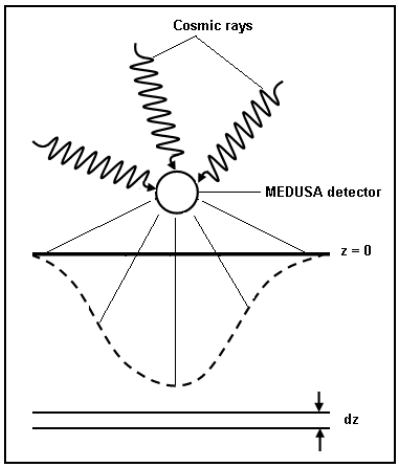

Figure C.1: A sketch showing the MEDUSA detector above the ground detecting gamma-rays emitted from the ground.

We simplify the picture by assuming that all gamma-rays are emitted perpendicular to the surface. On top of the surface we place a detector with surface A_{det} and efficiency 1. The correction for the real efficiency will be made later.

The number of gamma-rays emitted towards the detector per unit of volume is set to I_0, hence for a layer with thickness dz the number is given by

$$I_0\, dz = \frac{1}{2}\, C \rho\, dz \qquad \text{(C.11)}$$

At the detector, due to absorption one has a count rate due to this layer

$$I(z)\, dz = A_{det}\, I_0\, e^{-(\mu/\rho)\rho z}\, dz \qquad \text{(C.12)}$$

where μ/ρ is the mass-attenuation coefficient and A_{det} is the area of the detector.

If $C(z)$ is constant, the number of gamma-rays at the detector follows from the integration:

$$I^{tot} = \frac{1}{2}\, A_{det}\, C_{Ra}\, \rho_b \int_0^{\infty} e^{-(\mu/\rho)\rho z}\, dz = \frac{1}{2} A_{det} \frac{C_{Ra}\, \rho_b}{\mu} \qquad \text{(C.13)}$$

This result can be applied to the case for radon. So in the case that no radon escapes from the soil, we may write

$$I^H = \frac{1}{2} A_{det} \frac{C_{Ra}\,\rho_b}{\mu} \tag{C.14}$$

In case of radon exhalation by the surface, I_0 is no longer a constant and equation (C.11) becomes

$$I_0(z)\ dz = \frac{A_{det}}{2} C(z)\,\rho\ dz \tag{C.15}$$

where $C(z)$ is given by equation (C.10). This results in

$$I_0(z)\ dz = \frac{A_{det}}{2} C_{Ra}\,\rho_b\,(1 - E\,e^{-z/\ell})\,dz \tag{C.16}$$

The total number of gamma counts in the detector then becomes, if equation (C.12) is used.

$$I = \int_0^\infty I_0(z)\ dz = \frac{A_{det}}{2} C_{Ra}\,\rho_b \left[\int_0^\infty (e^{-(\mu/\rho)\rho z} - E\,e^{-(\mu+1/\ell)z})dz\right] \tag{C.16a}$$

$$I = \frac{A_{det}}{2} C_{Ra}\,\rho_b \left[\frac{1}{\mu} - \frac{E}{\mu + 1/\ell}\right] \tag{C.17}$$

The first term in the bracket results from the radon in the grains and the second term from the decay of radon in the pore space. From equation (C.17) and (C.14),

$$I = I^H \left[1 - \frac{E\,\mu\,\ell}{\mu\,\ell + 1}\right]$$

$$\frac{I}{I^H} = \left[1 - \frac{E\,\mu\,\ell}{\mu\,\ell + 1}\right] \tag{C.18}$$

This equation implies that if E is measured in the laboratory, the value of ℓ (and hence the exhalation rate) follows from the ratio $\frac{I}{I^H}$.

Since I is linearly dependent on the concentration of radium, C_{Ra},

$$\frac{I}{I^H} = \frac{C_{Ra}^M}{C_{Ra}^H} \tag{C.19}$$

The ratio in equation (C.19) can be obtained as follows; the C_{Ra}^H values are found from the sample measurements in the laboratory and (C_{Ra}^M) from the measurements in the field.

Determination of the attenuation coefficient (μ)

The attenuation coefficient is important so that the fraction of radon that escapes at the stationary spots can be determined. It is one of the input parameters required for equation (C.18) or equation (5.12). The attenuation coefficient was determined at the Physics Department of the University of Western Cape using a ^{137}Cs source, soil samples of various thicknesses, Sodium Iodide detector and a Multichannel analyser. Note that when determining the value of the attenuation coefficient it depends on the energy as well as the detection efficiency. In the field, radiation energy greater than that emitted from a ^{137}Cs source can be detected. Since ^{137}Cs was available in the laboratory it was used as a source of radiation. The schematic diagram for measuring the attenuation coefficient of the soil sample is shown in Figure C.2.

The decrease in intensity of radiation as it passes through an absorber, in this case through a soil sample is given by

$$I = I_O e^{-\mu x} \qquad \text{(C.20)}$$

where, I is the intensity of the radiation after the absorber is placed between the source of radiation (^{137}Cs) and the 2-inch $\times$ 2-inch NaI(Tl) detector. In this experiment, the intensity (I) was measured as the net counts in the photopeak divided by the elapsed live time (600 seconds). I_O is the intensity measured without the absorber, x is the thickness of the absorber in cm and μ is the linear absorption coefficient in cm^{-1}. This expression can be written in linear form as,

$$\ln I = -\mu x + \ln I_O \qquad \text{(C.21)}$$

$$\ln\left(\frac{I_O}{I}\right) = \mu x \qquad \text{(C.22)}$$

Equation C.22 implies that if a graph of $\ln(I_O/I)$ against the thickness (x) of the soil samples is plotted a straight line is obtained where the slope is the attenuation coefficient of the soil sample (see Figure C.3). The parameters for determining μ are given in Table C.1. The attenuation coefficient for Kloof soil sample was found to be about 0.42 cm^{-1}. This value is in agreement with values obtained for soil samples of the same

density as investigated by other researchers such as Pires et al. (2006), Laxman & Dayanand (2012), and Ogundare et al. (2012).

Table C.1: Parameters for determining the attenuation coefficient.

Thickness (cm)	Counts	I = (counts/600)	ln (Io/I)
0	195139	325	0
1.42	182172	304	0.07
2.46	109888	183	0.57
3.80	68388	114	1.05
5.80	34147	57	1.74
6.97	14991	25	2.57

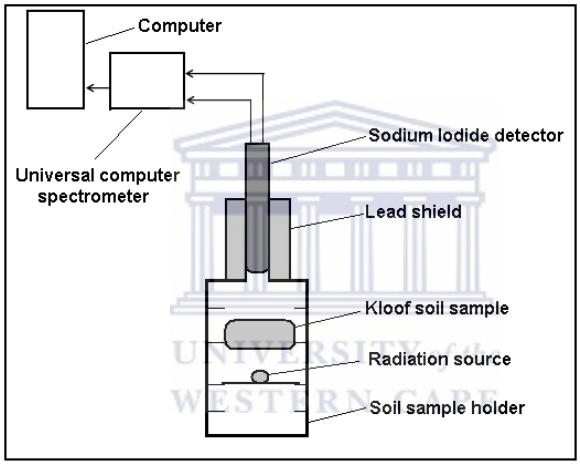

Figure C.2: Schematic diagram for measuring the attenuation coefficient.

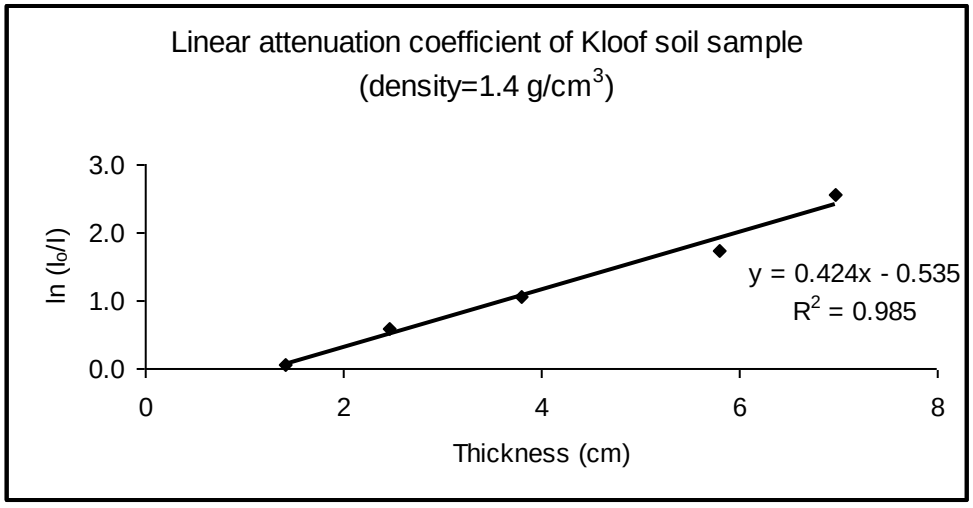

Figure C.3: A graph showing the slope (attenuation coefficient) of the soil sample.

Appendix D

Measurement of Radon emanation coefficient

The measurement of the Radon Emanating ^{226}Ra Concentration (RnERaC) can be determined from the expressions given by Collé et al. (1995), Kotrappa (1994) and Speelman (2004).

If an accumulator jar (see Chapter 5 Figure 5.18) which has a volume (V_a) contains a thin layer of soil with mass (m), then the ^{222}Rn activity concentration ($\overline{C}_{Rn}$) inside the closed jar will grow according to the relation below

$$\overline{C}_{Rn} = \frac{E\, C_{Ra} m}{V_a}(1-e^{-\lambda t}) + \overline{C}^{0}_{Rn} e^{-\lambda t} \qquad (D.1)$$

where, E is the radon emanation coefficient, C_{Ra} is the radium activity in Bq·kg^{-1}, m is the mass of the soil sample in grams, V_a is the air volume in the accumulator jar in litres, λ is radon decay constant (0.1813 days^{-1}), $\overline{C}^{0}_{Rn}$ is the initial radon concentration in the jar (0 Bq·m^{-3}) and t is the accumulation time.

The integrated radon activity concentration (I_{Rn}) from $t = 0$ to $t = T_a$ will be given as

$$I_{Rn} = \int_0^{T_a} \overline{C}_{Rn} dt \qquad (D.2)$$

$$= \frac{E\, C_{Ra} m}{V_a} \int_0^{T_a} (1-e^{-\lambda t}) dt \qquad (D.3)$$

$$= \frac{E\, C_{Ra} m}{V_a} \left[T_a - \left(\frac{1}{\lambda}\right)(1-e^{-\lambda T_a}) \right] \qquad (D.4)$$

From equation (D.4) the time averaged ^{222}Rn activity concentration (C_{Rn}) is

$$C_{Rn} = \frac{I_{Rn}}{T_a} \qquad (D.5)$$

$$= \frac{E\, C_{Ra} m}{V_a}\left[1 - \frac{(1 - e^{-\lambda T_a})}{\lambda T_a}\right] \qquad (D.6)$$

$$E = \frac{C_{Rn} V_a}{C_{Ra} m}\left[1 - \frac{(1 - e^{-\lambda T_a})}{\lambda T_a}\right]^{-1} \qquad (D.7)$$

The ratio of the RnERaC [Rad Elec Inc., 1994] and the C_{Ra} gives the radon emanation coefficient (E) as follows

$$E = \frac{RnERaC}{C_{Ra}} \qquad (D.8)$$

Re-arranging equation (D.8) and substituting equation (D.7) the RnERaC becomes

$$RnERaC = \frac{C_{Rn} V_a}{m}\left[1 - \frac{(1 - e^{-\lambda T_a})}{\lambda T_a}\right]^{-1} \qquad (D.9)$$

If we let,

$$K = \left[1 - \frac{(1 - e^{-\lambda T_a})}{\lambda T_a}\right]^{-1} \qquad (D.10)$$

then,

$$RnERaC = \frac{C_{Rn} V_a}{m} K \qquad (D.11)$$

The final RnERaC values for the soil samples can be determined using either equation (D.9) or (D.11).

Appendix E

Determining the activity concentration of radon using calibration equations and error analysis for electrets

E.1 Radon concentration calculation

Electret ion chamber for monitoring radon [Kotrappa, 1990] consists of an electret (electrically charged Teflon' disc) mounted inside an electrically conducting chamber. The electret serves as a source of the electric field and as a sensor. The air containing radon diffuses into the monitoring chamber through the filtered inlets. When radon decays inside the chamber the ions produced are collected by the electret. The decrease in charge of the electret is related to total ionisation during the period of exposure. This charge decrease is measured using a battery operated electret reader where the initial voltage (I) is read before the exposure and the final voltage (F) is read after the exposure. Using the appropriate experimentally determined calibration factors (CF) and the exposure time, the radon concentration in air is calculated as follows

$$RnC = \frac{I - F}{CF \times T} - BG \qquad \text{(E.1)}$$

where RnC is the radon concentration in Bq m^{-3}, I is the initial electret voltage in volts, F is the final electret voltage in volts, CF is the calibration factor drop in volts in Volts/(Bq/$m^3 \times$ days), t is time in days and BG is the environmental background correction in Bq·m^{-3}.

E.2 Calibration equations

The calibration factors for E-PERM are defined as the decrease in electret voltage when a specific E-PERM configuration is exposed to a known radon concentration. Electrets discharge their surface voltages when exposed to ionising radiation. There is a nearly linear relationship between the calibration factor and the electret voltage in a range of about 150-750 Volts [Rad Elec Inc., 1994]. The calibration equations vary for all

combinations of chambers and electret types because of the varying voltage drops for each configuration.

In this study, blue labelled short-term electrets fitted to S chambers (SST) and H chambers (HST) were used. The calibration equation used to calculate the calibration factor (CF) required in equation (E.1) for the S chamber (see Figure 5.19) is given by

$$CF = 1.69776 + 0.00057420 \times \frac{I + F}{2} \qquad (E.2)$$

and the CF for the H chamber (see Figure 5.18) is given by

$$CF = 7.2954 + 0.004293 \times \frac{I + F}{2} \qquad (E.3)$$

where, I and F are the initial and final voltages respectively. The calibration factors that are equations (B.2) to (B.4) are given in pCi/L units. The calibration factor (CF) is used in equation (B.1) as is, but the final answer should be multiplied by 37 to get the result in $Bq \cdot m^{-3}$ (1 pCi/L = 37 $Bq \cdot m^{-3}$).

E.3 Background corrections

The environmental background should be subtracted from the apparent radon concentration. The only source of gamma radiation is from the natural background, unless the E-PERM detectors are exposed to a source emitting gamma radiation. For instance, the response for gamma radiation for the S chamber has a radon concentration equivalence of 3.2 $Bq \cdot m^{-3}$ for every 1 μR/h [Rad Elec Inc., 1994]. The radon concentration equivalence of 1 μR/h for the H chamber is 2.6 $Bq \cdot m^{-3}$. A typical range for gamma radiation varies from about 6 to 12μR/h. The effects of gamma radiation can also be measured using E-PERM detectors.

E.4 Error analysis for E-PERMs

The three sources of errors associated with E-PERM are

(1.) The error due to faults in the system components ($E1$). This arises due to uncertainties in the volumes of the chambers, the thickness of the electrets and other possible problems like how tight the electret fit into the chamber. The contribution is about 5%.

(2.) The error due to the electret voltage reading ($E2$).The electret readers have an accuracy of ±1 Volt [Rad Elec Inc., 1994]. The error when reading the initial voltage and the final voltage can be interpreted as the square root of the sum of the two 1 Volt errors which will give a contribution as

$$E_2 = \frac{100 \times 1.4}{I - F} \tag{E.4}$$

(3.) The uncertainty of the gamma background reading contributes to the error component ($E3$). Normally in correcting for the environmental gamma background, a background correction factor is introduced. This is obtained from a compilation of average background data. When using the average contribution, the error is about

$$E_3 = \frac{100 \times 7}{RnC} \tag{E.5}$$

where the 7 $Bq \cdot m^{-3}$ arises from the background correction and RnC is the radon concentration.

Therefore the total error from the contributions add up to the following

$$E_{Total}(\%) = \sqrt{(E_1)^2 + (E_2)^2 + (E_3)^2} \tag{E.6}$$

or

$$E_{Total}(\%) = \sqrt{(5)^2 + \left(\frac{100 \times 1.4}{I - F}\right)^2 + \left(\frac{100 \times 7}{RnC}\right)^2} \tag{E.7}$$